

Realization and characterization of two unconventional ultracold mixtures

DISSERTATION

by

Slava M. Tzanova, MSc.

submitted to the Faculty of Mathematics, Computer Science, and
Physics of the University of Innsbruck, in partial fulfillment of the
requirements for the degree of Doctor of Philosophy (PhD)

Innsbruck, June 2020

Advisor:

Univ.-Prof. Dr. Rudolf Grimm

Co-advisor:

Prof. Dr. Florian E. Schreck

Introduction

This thesis describes the realization and characterization of the ultracold mixtures Sr-Rb and Dy-K as novel platforms for analogue quantum simulation. The solution of challenging questions in modern physics often relies on a better understanding of collective quantum behavior. Real-world quantum systems and in particular strongly correlated systems are difficult to simulate with a classical computer, yet many of them can be investigated with ultracold quantum gases. At temperatures close to absolute zero the quantum nature of matter becomes important in the atomic clouds. These well-controlled quantum systems can be used to simulate and thus understand other quantum systems and test analytical and numerical theoretical predictions.

This thesis presents two complex systems, Sr-Rb and Dy-K. Each of the experiments is breaking new ground in heteronuclear molecules and mass-imbalanced Fermi-Fermi mixtures, respectively. We expand the realm of experimental ultracold research by mixing alkali atoms with alkaline-earth or lanthanide elements. The RbSr molecules are open-shell polar molecules. They have an electric and a magnetic dipole moment and are therefore well suited for quantum simulation. The Dy-K ultracold mixture offers isotopic diversity and is conveniently imbalanced in mass and optical polarizability for the targeted strongly interacting fermionic mixture experiments. Moreover, dysprosium is a magnetic atom, which brings anisotropic properties to the system and allows for various research directions.

My contributions to both experiments are to the experimental preparation and to the characterization of the properties of the novel mixtures. In the Sr-Rb experiment I contributed to the realization of a double BEC and to the initial photoassociation investigations of the RbSr molecular potential. Both experimental objectives were published. The Dy-K experimental apparatus was designed and constructed from scratch in the course of my thesis. My contributions to the experimental setup have the stability as well as the flexibility of the experiment in mind. After setting up the apparatus, I took part in the initial measurements with thermal samples of Dy-K for the determination of the dysprosium polarizability and later on investigated the elastic and inelastic interaction of a Bose-Fermi Dy-K mixture. Both subjects are necessary findings towards the investigation of strongly interacting Fermi-Fermi mixtures.

This thesis is structured in three parts. The first part introduces the field of ultracold atoms and deals with the similarities between both unconventional mixtures. The second part is dedicated to the Sr-Rb experiment and my contributions towards the formation of RbSr open-shell molecules. The third part presents the novel Dy-K experimental apparatus and the first measurements characterizing the properties of this species mixture. I will use the opportunity of reporting on two different mixtures of ultracold gases to highlight the experimental perspectives in this research field. The preparation, manipulation, control and detection of quantum systems are the basic building blocks of quantum simulation. It is important to continue developing the experimental platforms and widen the horizon of available quantum systems for quantum simulations.

Contents

Introduction	2
I. New platforms for quantum simulation	6
1. Quantum simulation with ultracold mixtures	8
1.1. Quantum simulation	8
1.2. Ultracold mixtures	10
1.2.1. Historical perspective	10
1.2.2. Research line: Polar molecules	13
1.2.3. Research line: Fermi-Fermi systems	15
2. Experimental realization of quantum systems with ultracold atoms	17
2.1. Ultracold neutral atoms	17
2.2. Interactions between ultracold atoms	18
2.2.1. s -wave scattering length a	19
2.2.2. Dipole-dipole interactions	19
2.2.3. Feshbach resonance	20
2.2.4. Atom loss and inelastic collisions	21
2.3. Making and probing ultracold atomic gases	22
2.3.1. Laser cooling	22
2.3.2. Narrow lines are cooler	25
2.3.3. Optical trapping	27
2.3.4. Detection	30
3. Outlook on the mixtures in this thesis	33
3.1. RbSr open-shell polar molecules	33
3.1.1. Two-dimensional lattice-spin models	33
3.1.2. Interaction tuning in open-shell molecules	34
3.2. Dy-K quantum mixtures	35
3.2.1. Mass-imbalanced Fermi-Fermi	35
3.2.2. Dipolar fermionic systems	37
3.2.3. Dy-K in an optical lattice	38
II. Sr-Rb mixtures	39
4. Properties of Sr and Rb	41
4.1. Why Sr?	41
4.2. Why Rb?	43
4.3. Sr-Rb interactions	44

5. Sr-Rb machine	46
5.1. Vacuum setup and precooling	46
5.2. Magnetic field coils and control	49
5.3. Laser systems	50
5.3.1. Rb lasers	50
5.3.2. Sr lasers	50
5.3.3. TA comb for spectroscopy	51
5.3.4. Infrared and green optical traps	52
5.4. Loading into traps	52
6. Publication: Quantum degenerate mixtures of strontium and rubidium atoms	53
6.1. Introduction	54
6.2. Overview of the experimental strategy	55
6.3. Preparation of an ultracold sample of rubidium and strontium	55
6.4. Sympathetic narrow-line laser cooling	57
6.5. Evaporation to alkali/alkaline-earth double BECs	60
6.5.1. ^{88}Sr - ^{87}Rb double BEC	61
6.5.2. ^{84}Sr - ^{87}Rb double BEC	61
6.6. Conclusion and outlook	64
7. Experimental steps towards ground-state RbSr molecules	66
7.1. Photoassociation spectroscopy	66
7.2. Molecule creation	69
7.3. Conclusion on the Sr-Rb results	71
III. Dy-K mixtures	73
8. Properties of Dy and K	75
8.1. Why Dy?	75
8.2. Why K?	77
8.3. Dy-K interactions	78
9. Dy-K machine	81
9.1. Design of the experimental setup	81
9.1.1. Main chamber	83
9.1.2. Stability	85
9.1.3. Control	86
9.2. Cold atomic beams: 2D MOT and Zeeman slower	87
9.2.1. Potassium 2D MOT design	87
9.2.2. Dy cold-atom-source	90
9.3. Main coils	94
9.4. Resonant laser systems	101
9.4.1. K lasers	101
9.4.2. Dy lasers	103
9.5. Experimental outlook	107
9.5.1. Trapping beams and geometry	107
9.5.2. High-resolution imaging	108
9.5.3. Future Science Cell	108

10. Experimental results	109
10.1. MOTs	109
10.1.1. Potassium MOT	110
10.1.2. Dysprosium MOT	113
10.2. Optical dipole traps	117
10.2.1. Loading of ODTs	118
10.2.2. Determination of Dy polarizability (Publication)	120
10.3. ^{162}Dy - ^{40}K interactions	121
10.3.1. Feshbach scans	121
10.3.2. ^{162}Dy - ^{40}K two-body collisions and thermalization	124
10.3.3. Three-body loss in ^{162}Dy - ^{40}K	132
Appendices	139
A. Publication: Tapered amplifier laser with frequency-shifted feedback	139
A.1. Introduction	140
A.2. Experimental setup	140
A.3. Properties of the laser	142
A.3.1. Broadband modeless laser	142
A.3.2. Externally seeded laser	143
A.4. Conclusion and outlook	146
B. 421 nm laser system for Dy	147
B.1. Laser source	147
B.2. Laser stabilization	149
C. Overlap density	151
Bibliography	153
Acknowledgments	171

Part I.

New platforms for quantum simulation

Ultracold mixtures of quantum gases are a unique testbed for fundamental physics. Dilute atomic samples are prepared by means of laser light and magnetic fields at very low temperatures. The experimentalists have exquisite control over internal and external states of the atoms and their trapping geometry. A substantial strength of ultracold gases compared to other quantum systems is the ability to tune the inter-particle interactions. The capabilities of creating and manipulating many-body states that are effectively isolated from the environment have been developed mainly in single-species experiments and are also being transferred to mixtures of species, which offer further degrees of freedom. The systems of ultracold atoms address (many-body) problems from nearly all areas of physics: atomic and molecular physics, condensed matter physics, nuclear (high-energy) physics, quantum information science, quantum chemistry and even general relativity. The realization of such fundamental research in a table-top experiment is what makes ultracold gases a prominent choice for analog quantum simulation.

The first chapter of this opening part introduces the field of ultracold mixtures in the context of analog quantum simulation. I give a historical review of the existing species mixtures of ultracold gases and point at typical research directions. Then the focus is laid on the two research lines that are most relevant for Sr-Rb and Dy-K: polar molecules and Fermi-Fermi mixtures, respectively. In the second chapter I present the basic properties of ultracold gases as well as the main experimental tools to produce and probe them. The emphasis there falls on the interactions between atoms and the main cooling techniques. The last chapter of this part presents the motivation for the two mixtures in this thesis and is also the long-term outlook for Sr-Rb and Dy-K.

Quantum simulation with ultracold mixtures

1.1. Quantum simulation

Many open questions in various fields of physics, chemistry, and even biology require a deeper understanding of strongly correlated or strongly interacting many-body quantum systems. As pointed out by R. Feynman in 1982 [1], scientists could better tackle many of these open questions using a simulation machine that can itself take advantage of quantum mechanical phenomena, a so-called quantum simulator. The experimental progress in quantum simulation in the last decades has been extraordinary and one can distinguish between two main types of quantum simulators: digital and analog [2–4]. Digital quantum simulators (DQSs) are circuit-based, they rely on quantum mechanical phenomena to carry out algorithms and should be programmable to solve almost any physical problem. analog quantum simulators (AQSs) are specifically designed quantum many-particle systems that can simulate a (set of) complex quantum phenomena to solve a particular type of problem. Well-controlled quantum systems such as ultracold gases show great potential as AQS for obtaining insights into interacting many-body systems [5–7].

A quantum simulator should fulfill the following criteria [8]:

- *Quantum system ('Hardware')* A quantum system with a large number of degrees of freedom, which can be manipulated (at will) using external fields. The quantum system should be isolated from the environment to avoid decoherence. A DQS typically consists of two-level quantum subsystems (qubits). For an AQS that tackles many-body problems the quantum system can be composed of bosons or/and fermions, or spin representatives.
- *Initialization* Preparation of the quantum system in a well-defined quantum state. Ideally the initial state should be a pure state, but a mixed state can be also used to study the dynamics of the system or for the simulation of open quantum systems, which interact with a bath.
- *Hamiltonian engineering ('Software')* Design a set of adjustable interactions (either local or long-range) with external fields or between different particles. The accessible Hamiltonians of the system should range between problems that cannot be solved (yet or easily) by classical techniques and problems that have a known solution to allow the quantum simulator to be calibrated. The *Hamiltonian engineering* requirement sets the difference between digital and analog quantum simulators: a DQS may be used

to implement a wide range of Hamiltonians, while an AQS is less versatile and the accessible Hamiltonians are strongly limited by the specific ‘*Hardware*’.

- *Detection* Measure relevant observables with sufficient fidelity. For destructive measurement techniques the requirement is to have a high repeatability.
- *Verification* To increase the confidence in a result for a classically unsolvable problem, the quantum simulator should be benchmarked with problems with known solutions. For adiabatic algorithms it should be possible to implement the dynamics in reverse to check if the initial state is recovered. Most importantly, different quantum simulation platforms should deliver consistent results for the same classically unsolvable problem.

In the last decades, researchers have achieved exquisite control over different quantum systems, which can be used as platforms for quantum simulation [2–4]. There are atomic, photonic, semiconductor-based systems and also hybrid systems. Some systems are more suitable than others for digital or analog quantum simulation. Digital quantum simulation requires a discretization in space and time in order to apply unitary transformations to a qubit. In addition, long-range interactions are necessary to engineer fast logic gates between remote qubits. Nowadays small-scale DQs are being developed [9, 10], but the size of such quantum circuits is limited by noise in the quantum logic gates [11]. Among the atomic quantum simulation platforms the ones that exhibit promising long-range interactions are trapped ions [10], Rydberg atoms [12] and polar molecules [13, 14]. A great advantage of cold atoms and molecules, Rydberg atoms and trapped ions relative to other quantum simulation platforms regarding the *Verification* requirement is that the basic quantum system is made by nature and the atoms of a certain isotope are identical all over the world. This is in contrast to man-made quantum systems like superconducting circuits [9] or quantum dots [15].

Ultracold quantum gases and mixtures thereof are a prominent platform for analog quantum simulation [5–7]. They belong to the largest quantum systems currently available with few thousands to millions of constituent particles. All other quantum simulation platforms are so far limited to about 50 qubits [16–18]. The assortment of laser-cooled atoms has quickly grown in the last decades and features bosons and fermions with various optical and magnetic properties. Experiments with ultracold atoms can take place in a bulk (as in continuum) or in an optical lattice (as in an artificial crystal). Bulk systems are important mostly for analog quantum simulation of complex many-body problems [8]. Atomic systems in optical lattices, on the other hand, allow for quantum simulation of various problems in condensed matter physics [19], as well as tailored investigations of few-body problems [20]. The unique control over interactions and confinement in systems of ultracold gases is the key for the experimental breakthroughs in the realization of fundamental quantum phases and phase-transitions as illustrated by the BEC-BCS crossover in two-component Fermi gases [21] and the superfluid to Mott-insulator transition of bosons in an optical lattice [22].

Mixtures of atomic species provide further degrees of freedom to the AQS-hardware. The components can have widely different intrinsic properties like differing spins, scattering properties, masses and polarizabilities. This enables the study of the interplay of diverse populations [23], dimensions [24] and quantum statistics [25]. A direct consequence of species mixtures is the mass imbalance in the ultracold system, which leads to the emergence of new few-body [26] and many-body effects [27]. Moreover, an ultracold mixture of atomic species can be the starting point for the production of ultracold polar diatomic molecules [13]. The differing number of protons in the atomic nuclei of a heteronuclear ground-state molecule is the source of an electric dipole moment in the molecular frame of the dimer. The resulting

long-range anisotropic dipole-dipole interaction (DDI) opens the path towards digital quantum simulation with neutral ultracold gases [28]. Moreover, ultracold polar molecules are an excellent platform for analog quantum simulation of intriguing many-body phenomena [29–32] and quantum chemistry [13, 33].

Strong interactions as well as long-range interactions are among the key topics that are studied with ultracold quantum mixtures. The pairwise interactions between many atomic species can be tuned in strength and sign via magnetic Feshbach resonances [34]. An additional possibility is to use an optical lattice to tune the strength of interactions by changing the effective mass of the particles in the periodic potential of variable depth [35]. Whether in a lattice or in a bulk gas, the range of the strong interatomic interactions remains relatively short. So far effects of the long-range dipole-dipole interaction have been observed between electric dipoles with heteronuclear ground-state dimers [36] and between magnetic dipoles with highly magnetic atoms [37]. Further developing the tools for the experimental implementation of long-range or strong interactions are the topics of this theses and the mixtures therein.

1.2. Ultracold mixtures

Both experimental platforms presented in this thesis, Sr-Rb and Dy-K, are mixtures of atomic species belonging to different groups of the table of elements. The following brief overview of the research field will thus concentrate on mixtures keeping analog quantum simulation in mind. In ultracold gases one can distinguish between combinations of different spin-states of the same element and isotope (spin mixture), mixtures of isotopes of the same chemical element (isotopic mixture), and mixtures of chemically different elements (species mixture). This section presents the history of species mixtures, which is intertwined with that of single-species quantum gases, and the experimental achievements of the nowadays available mixtures. Ultracold mixtures already offer multiple examples of valuable analog quantum simulation. Furthermore, the two prominent research lines of polar molecules and Fermi-Fermi mixtures will be highlighted, as these are the directions in which research will be pursued with Sr-Rb and Dy-K, respectively.

1.2.1. Historical perspective

The history of ultracold mixtures is closely related to the quest of obtaining degenerate quantum gases as well as the available technology needed to create these gases. The very first achievements of a Bose-Einstein condensate in a dilute gas (BEC) in 1995 were accomplished by removing all but one spin-state from the respective atomic ensemble [38–40]. In contrast, for the production of the first degenerate Fermi gas (DFG) in 1999 a mixture of two spin-states was imperative [41]. These successful experiments brought ultracold gases to the forefront of atomic physics research at the dawn of the 21st century. The seminal experiments on BEC and DFG relied on laser cooling, followed by evaporative cooling in a magnetic trap. The subsequent development of ultracold gas experiments with a single species or a mixture strongly benefited from the implementation of optical dipole traps (ODTs) [42] and on the tunability of interactions between atoms via Feshbach resonances [34]. Feshbach resonances allow experimentalists to control the short-range interactions between particles by tuning a magnetic field. Interaction tuning and confinement engineering quickly became invaluable tools for creating ultracold gases and mixtures thereof [43].

Mixing of atomic isotopes and species was primarily introduced to simplify the cooling towards quantum degeneracy of indistinguishable fermions in magnetic traps. Magnetic traps enable efficient evaporative cooling but are state-selective and inconvenient for the application of homogeneous magnetic fields for interaction tuning (Feshbach resonances). Sympathetic evaporative cooling happens when only one component of a mixture is evaporatively cooled and then thermalizes with the other component in the trap. In 1997 a bosonic mixture of two spin-states of Rb [44] was brought to quantum degeneracy by sympathetic evaporative cooling. Then, using sympathetic cooling in 2001 the first double-species BEC was achieved with ^{39}K - ^{87}Rb [45]. In the early 2000s interspecies sympathetic cooling of fermions was successfully implemented in ^7Li - ^6Li [46], Li-Na [47] and Li-Rb [48]. Even a mixture of fermionic Li and K has been sympathetically cooled by Rb [49] in 2008. Sympathetic cooling with a well-controlled bosonic species is a valuable cooling step in experiments with fermionic atoms, e.g. in the investigations of the Fermi-Hubbard model in an optical lattice from the mid 2010s [50, 51]. Sympathetic evaporative cooling in any type of trap continues to be an essential experimental tool in the work with ultracold mixtures.

The successful achievement of fermionic quantum degeneracy for the first time in 1999 was reached using a spin mixture of ^{40}K [52]. Both spin states were evaporated and the mixture was necessary to allow for elastic collisions between the non-identical fermions in order to rethermalize the gas. The simultaneous evaporation from a magnetic trap is tricky but the collisional properties of ^{40}K turned out to be favorable [53]. The observation of a strongly interacting Fermi gas was first achieved in a spin mixture of ^6Li in 2002 [54]. This double DFG was achieved by simultaneous evaporation in an ODT from a CO_2 laser and using interaction tuning by magnetic fields. This approach established itself for the major investigations with DFGs in a bulk system [21, 55, 56] (see Sec. 1.2.3).

The investigation of interspecies interactions and their tunability advanced tremendously in the 2000s with the common implementation of near-infrared ODTs in addition to (or instead of) magnetic traps. Optical traps allow to freely chose any magnetic field to explore and to manipulate the collisional properties of an ultracold gas without changing the trap itself [42]. Moreover, under appropriate conditions an optical potential can trap any magnetic sub-level of the ground-state manifold of one or more atomic species. One of the early optical trapping of a species mixture (^{133}Cs - ^7Li) was performed in 2001 in a very-far-detuned ODT [57] from a CO_2 laser with a wavelength around $10.6\ \mu\text{m}$. Soon after, far-detuned ODTs were implemented using solid-state lasers (Nd:YAG) and later on fiber lasers with a wavelength around $1064\ \text{nm}$ and high optical power. The shorter wavelengths allow for the use of glass-based instead of purely metallic optical elements and thus facilitate the implementation of optical trapping potentials of diverse geometry [42]. In particular, an artificial crystal of arbitrary spacial dimension can be simulated with ultracold atoms when the interference pattern of multiple beams forms a lattice of periodic micropotentials [35].

The possibility to tune the interspecies interactions as well as the optical trapping potential lead to many novel theory proposals of research with atomic mixtures. One of them was a promising alternative path for the production of an ultracold gas of polar molecules from 2003 [58], which suggests the (photo)association of heteronuclear atomic pairs to deeply-bound dimers in a low-entropy sample confined in an optical lattice (see Sec. 1.2.2). Other promising theoretical proposals from the mid 2000s were oriented towards the observation of quantum effects in Bose-Fermi mixtures in an optical lattice [25, 59]. Atomic mixtures with tunable interactions allow for investigations of strong correlations and diverse pairing mechanisms in different dimensions.

Two of the early significant bi-alkali mixtures under investigation were the Bose-Fermi

mixture Rb-K and the Fermi-Fermi and Fermi-Bose mixtures of Li-K. In 2006 the mixture of ^{87}Rb and ^{40}K was for the first time loaded into an optical lattice [60]. In the lattice the interplay between the species and their quantum statistics has been measured as the transition from BEC to Mott insulator phase of Rb is shifted to lower lattice depths in the presence of the fermionic impurities [61]. A further prominent example of an AQS of impurity physics is the Li-K mixture. In the mid 2010s the response of a ^6Li Fermi sea to a suddenly introduced heavy impurity (^{40}K) was thoroughly investigated and brought unprecedented insight into the physics of the Fermi polaron [62–64] (see Sec. 1.2.3). As a technical example of the analog character of quantum simulation with cold gases, in the Li-K experimental setup exchanging the fermionic ^{40}K isotope for the bosonic ^{41}K allowed to probe the thin interface between a phase-separated state of a small BEC in a large Fermi sea of ^6Li [65].

Another example of analog quantum simulation in Bose-Fermi systems is given by species mixtures of different alkali metals with ^6Li . In 2016 the phononic Lamb shift was demonstrated in ultracold gases [66]. Using the different polarizability of Li and Na in order to pin the Li atoms in a species-selective optical lattice, the interactions with the phonons of the surrounding BEC of Na were measured. In this quantum system the BEC plays the role of the quantum vacuum as it allows for creation and annihilation of excitations. Notably, in such analog simulation the ‘quantum vacuum’ can be switched on and off.

In addition to investigations of many-body systems, bulk systems of species mixtures have provided insight into few-body effects like the Efimov states. The Efimov quantum effect predicts a universal sequence of three-body bound states for resonant two-body interaction between identical bosons [67], regardless of the specific nature of the short-range forces (van-der-Waals interaction between neutral atoms or the strong interaction between nucleons). The universality of the Efimov effect [68] boosts the interest in analog quantum simulation with ultracold atoms. The very first evidence for Efimov states came in an experiment with single-species ultracold Cs [69] in 2006. However, the exploration of the distribution of Efimov states with a single-species is experimentally challenging. Two consecutive Efimov resonances were observed in 2009 in a three-component Fermi gas [70] and in 2014 in a bosonic system [71]. The discrete scaling symmetry of the Efimov effect was confirmed in 2015 with an ultracold mixture of Cs and Li by the measurement of three consecutive Efimov resonances [72]. In a species mixture with a strongly asymmetric mass ratio the distribution of Efimov states is more dense and the detection of multiple resonances allows for model-independent tests [26, 73, 74].

During the years, many experiments have been setup providing a wealth of different species mixtures. They each offer unique properties for experimental study and analog quantum simulation. Table 1.1 summarizes the species mixtures, which are under investigation nowadays¹. The upper part shows that all bi-alkali combinations are part of the current research, while the lower part lists the available mixtures with non-alkali elements. The relatively easy cooling procedure for Rb makes it a good candidate for species mixtures and also atoms with a fermionic isotope are being favored. The latter is because the Pauli exclusion principle between identical fermions provides stability against inelastic losses at high atomic/molecular densities [75, 76]. Typically, the routes to quantum degeneracy are established for both species individually or one of the species is implemented as a sympathetic coolant.

A rich phase diagram is the motivation for many of the here presented implementations of ultracold mixtures. The predicted rich (quantum-) phase diagrams often require interac-

¹ Table 1.1 consists of representative publications from different experiments and does not claim to be an exhaustive presentation of all available species mixtures.

	Li	Na	K	Rb	Cs
Na	[66, 77]				
K	[64, 78, 79]	[80–82]			
Rb	[83, 84]	[85]	[61, 86, 87]		
Cs	[72]	[88]	[89]	[90, 91]	
<hr/>					
Cr	*[92]				
Sr	*[93]			[94], Part II	
Dy			[95], Part III		
Yb	[96, 97]			[98]	[99]
	also Dy-Er [100], Hg-Rb *[101]				

Table 1.1.: Existing mixtures of ultracold atomic species. The references show examples of representative publications towards a quantum-degenerate mixture, molecule production or mass-imbalanced few-body effects. The mixtures, for which only a double-species MOT is reported, are marked with *. The empty row separates the bi-alkali mixtures from mixtures including non-alkali atoms. The elements in **bold** have a fermionic isotope. The pink cells indicate the mixtures presented in this thesis.

tion tunability and reveal themselves at very low temperatures. This is one of the reasons to upgrade the bi-alkali mixtures by introducing two-electron systems with relatively easy cooling procedures (see Sec. 2.3.2). Among the many research directions with ultracold mixtures, two of the most prominent are the research lines of polar molecules and Fermi-Fermi mixtures, to which we hope the mixtures of this thesis to contribute.

1.2.2. Research line: Polar molecules

A common goal for almost all bi-alkali mixtures is the production of a quantum-degenerate gas of ground-state polar molecules. A quantum gas of polar molecules would enable investigations of long-range anisotropic interactions in systems of thousands or more particles [13, 14]. Heteronuclear ground-state dimers exhibit a permanent electric dipole moment in the molecular frame, which arises from the separation between the barycenter of positive and negative charges. In the laboratory frame the molecule can be polarized in an external electric field. Furthermore, the strength of the dipole moment can be tuned by the external field from zero to the maximal value along the interatomic axis.

Formation of ultracold polar molecules out of a mixture of ultracold atomic gases is a powerful alternative to direct cooling of large ensembles of molecules [13, 14]. The direct cooling of polar molecules was boosted by the successful production of atomic BECs. In 1998 the first magnetic trapping of CaH was achieved [102]. A decade later laser-cooling of diatomic molecules was pioneered with SrF [103]. In 2018 CaF molecules were laser-cooled in an ODT to reach the so far lowest phase-space density (PSD) of 2×10^{-9} for direct cooling of molecules [104]. The cooling techniques for molecules are motivated by the successful techniques for atoms, but are challenging due to the far more complex level structure of the compounds. Therefore, the production of polar molecules from (nearly) quantum-degenerate atoms at $\text{PSD} \sim 1$ is a prominent research direction in ultracold mixtures.

The association of ultracold atoms of different species into an ensemble of dimers is an alternative approach towards a quantum-degenerate gas of polar molecules. The bi-alkali mixtures of Li-Na, Na-K, K-Rb, Na-Rb, Na-Cs, and Rb-Cs are all using the following bottom-up procedure for the formation of ground-state polar molecules. At first, weakly bound

molecules are produced by Feshbach association [105]. Ramping the magnetic field across a Feshbach resonance results in the conversion of the free colliding atoms to weakly bound molecules ideally without an increase in temperature. In a second step these huge molecules can be optically transferred to the ground state. A successful method of transferring weakly bound molecules to strongly bound deeper states is STIRAP [106]. It stands for stimulated Raman adiabatic passage and is a method of full population transfer in a three (or more) level system. The process uses two strong laser pulses partially overlapping in time to couple the initial and final states to an intermediate dark state, which remains unpopulated. Dipole selection rules and expected transition rates between the Feshbach state and the intermediate state as well as between the intermediate state and the rovibrational ground-state determine the choice of intermediate state. The crucial aspect of the transfer then is the adiabaticity, which is assured by long-lived states and high Rabi frequencies.

With the work on the Bose-Fermi mixture of ^{87}Rb and ^{40}K one can track the historical evolution in mixtures of atomic species towards polar molecules. After the sympathetic cooling to quantum degeneracy in 2002 [86], Feshbach resonances in a thermal mixture of K-Rb were first discovered in 2004 [107]. Two years later the interaction tuning was confirmed with quantum-degenerate K-Rb [108]. Feshbach association of the K-Rb mixture into heteronuclear molecules was demonstrated in Ref. [109]. Then, with the advancement of optical association (initially shown for RbCs [110]), heteronuclear ground-state KRb molecules were produced in a bulk and their electric dipole moment was measured [111]. Due to the required finesse in the production of polar molecules it took the experimentalist more than ten years to close the gap in temperature and realize a quantum-degenerate gas of polar molecules [87]. The work on the K-Rb system presents the essential building blocks and difficulties in ultra-cold species mixtures: the intra- and interspecies interactions are of major importance next to the laser-cooling and trapping options for each of the species.

A current challenge in the field of polar molecules is the decay of the ensemble of ground-state molecules [112]. The decay is observed throughout chemically reactive [111], but also nonreactive dipolar gases of bosonic [85, 90] as well as fermionic [80] molecules. On the one hand inelastic molecular collisions [113, 114] complicate the experimental formation of quantum-degenerate polar gases and on the other hand they are the actual subject of quantum chemistry investigations [13, 115]. The newest achievement in the field of polar molecules is the creation of a degenerate Fermi gas of KRb molecules [87], where the Fermi pressure suppresses chemical collisions. However, a quantum-degenerate gas of polar molecules has not yet been loaded into an optical lattice. Nevertheless, recently a general scheme has been established that only requires a suitable interspecies Feshbach resonance, which delivers weakly bound molecules with a high filling in a quadratic optical lattice [91]. The lattice protects the molecules from lossy collisions before and after the final ground-state transfer. In addition a low-entropy gas in an optical lattice is the desired final geometry of most experiments with polar molecules and would be the initial step towards a new platform for digital quantum simulation [13].

The different bi-alkali ground-state molecules can have a large electric dipole moment ranging from 0.6 D to 5.5 D [113] (1 Debye $\simeq 3.335 \times 10^{-30}$ C m) but they do not have a magnetic moment. A bi-alkali molecule can have a magnetic moment in the triplet state at the cost of reducing the electric dipole moment and increasing the collisional instability [116]. Fermionic LiNa in the triplet state has an electric moment of 0.2 D and a magnetic moment of $2\mu_B$ and the ensemble of 10^4 molecules in a trap is extraordinary stable with a lifetime of little less than 5 s [77]. The formation of the LiNa molecules is relatively inefficient with a Feshbach molecule association rate of only 3% (followed by STIRAP with 86% efficiency),

which is a hindrance for the initialization and detection of the quantum system in the context of an AQS.

The more recent approach in the production of polar molecules with a magnetic moment is the merging of an alkali and a non-alkali element. The experimental development towards such open-shell molecules is still in its youth compared to the heteronuclear alkali molecules. Many of the experiments with a mixture of an alkali and a non-alkali element are still investigating the interspecies scattering properties or are at a stage of a double-species MOT (see lower part of Table 1.1). The Sr-Rb experiment presented in Part II of this thesis has reached many of the preparation steps towards the formation of open-shell polar ground-state molecules. A major challenge in the production of open-shell molecules is the lack of broad interspecies Feshbach resonances, as will be discussed in detail for the case of Sr-Rb in Chapter 7.

1.2.3. Research line: Fermi-Fermi systems

A well-controlled many-body system with fermionic quantum statistics can be studied with mixtures and is irreplaceable for analog quantum simulation of large and complex fermionic systems. Fermions with strong interactions are essential for the study of strongly correlated electrons in condensed matter systems [117, 118] and the investigation of ultracold fermionic mixtures can help to grasp the physics behind less accessible systems like neutron stars [119, 120] and quark-gluon plasma [6]. In this context, if suitable interaction tuning is available, mass-imbalanced Fermi-Fermi systems provide a unique and rich platform for analog quantum simulation. Because identical fermions with short-range interaction do not collide at very low temperatures, cooling them to a DFG requires mixtures. Moreover, in a two-component fermionic gas at large scattering lengths the inelastic collisions are strongly suppressed by the Pauli exclusion principle [75, 76], while for bosons the experimental observations in the strongly interacting regime consist of immense loss.

The importance of ultracold fermions is best illustrated by the BEC-BCS crossover, which provides a physical link between superfluidity and superconductivity. The BEC-BCS crossover gives key insights into different few-body and many-body effects as the interparticle interactions in a fermionic mixture are tuned across a Feshbach resonance. At sufficiently low temperatures and weak attractive interactions the many-body system favors the formation of Cooper pairs in momentum space, in analogy to the pairing of electrons in a type-I superconductor. On the repulsive side of the resonance the molecular potential contains at least one bound state and two non-identical fermions can form a bosonic molecule. These composite bosons then form a BEC below a critical temperature T_c . The pairing mechanism between the fermions undergoes a smooth transition between the BCS and the BEC regime and the physics behind it is not yet fully understood [117]. Across the Feshbach resonance the ground state of the many-body system at zero temperature remains a superfluid. A special region of interest in the BEC-BCS crossover is the unitarity regime of strong interactions, where the scattering length diverges [121, 122]. There, the strong interactions do not explicitly enter into any thermodynamic quantity, so that the physics in this regime is independent of the type of interacting particles and is thus universal.

The BEC-BCS crossover has been extensively investigated with a spin mixture of ${}^6\text{Li}$ [21, 55, 56], thanks to the exceptionally broad Feshbach resonance around 834 G. Also the thermodynamics of a universal gas, i.e. its equation of state, have been explored in depth with the same fermionic system [123, 124]. The experimental achievements so far allow to distinguish between theoretical approaches for the many-fermion studies [122]. Nonetheless,

the strongly interacting regime remains a challenging problem in theoretical physics due to its non-perturbative nature. Investigations of fermionic mixtures with population imbalance [125, 126] and also mass-imbalance [27, 127, 128] could shine new light on strongly correlated fermionic systems (see Sec. 3.2.1).

The prime system of mass-imbalanced Fermi-Fermi mixtures consists of the fermionic alkali-metals ${}^6\text{Li}$ and ${}^{40}\text{K}$. The ${}^6\text{Li}$ - ${}^{40}\text{K}$ mixture has served for the investigation of the striking effects of mass imbalance at the few-body level [129]. With a mass ratio of 6.7, Li-K is below the threshold of 13.6, for which the subsystem of one light and two heavy fermions can exhibit the Efimov effect [74, 130]. In the ${}^6\text{Li}$ - ${}^{40}\text{K}$ system at very low collision energies in the regime of near-resonant atom-dimer interactions based on s -waves alone one would naively expect a strong repulsion. Yet, a substantial attraction results from the contribution of higher partial waves (mainly p -wave) [129]. The phenomenon can be understood as a three-body effect in which two heavy fermions exchange the light atom, leading to attraction in odd partial wave channels in analogy to the H_2^+ cation. Such effects are not present in mass-balanced fermionic mixtures and show how a mass-imbalanced ultracold Fermi-Fermi mixture is an important quantum simulation platform for the understanding of fundamental questions.

By creating a population imbalance in the mixture and thanks to the experimental capability to tune interparticle interactions, the ${}^6\text{Li}$ - ${}^{40}\text{K}$ system also provided essential insights into impurity physics in Fermi systems. The response of a ${}^6\text{Li}$ Fermi sea to a suddenly introduced heavy impurity (${}^{40}\text{K}$) was investigated on different timescales [63, 64]. This was possible thanks to the large Fermi time of approx 3 μs in atomic quantum gases, compared to 100 as for electrons in copper. The Fermi time gives the time scale of the shortest collective response of a fermionic many-body system. The non-equilibrium dynamics revealed the real-time quasiparticle (fermionic polaron) formation and its time evolution, which are otherwise not accessible in condensed matter systems. Furthermore, the response of the Fermi system to an impurity with very strong interactions in the unitarity regime was characterized in the energy [62] and time [63, 64] domains.

Mass-imbalanced Fermi-Fermi mixtures are promising candidates for the exploration of unconventional pairing mechanisms in the strongly interacting regime [27, 127]. Unfortunately, the only tunable mass-imbalanced fermionic system so far does not provide the necessary collisional stability in the strongly interacting regime: In the ${}^6\text{Li}$ - ${}^{40}\text{K}$ system the Feshbach resonances are closed-channel dominated, i.e. the resonances are narrow with strong three-body losses [131, 132]; In addition, two-body loss is present because the spin states of ${}^{40}\text{K}$ involved in the experimentally manageable Feshbach resonances are not the lowest Zeeman sub-level of the ground state. Nonetheless, measurements of the lifetime of weakly bound Li-K dimers showed that even for such narrow Feshbach resonances the Pauli exclusion principle contributes to a suppression of collisions between dimers [132]. Although collisional Pauli suppression is much stronger for broad (open-channel dominated) Feshbach resonances [76], Ref. [132] gives a guide for identifying suitable narrow Feshbach resonances with sufficient collisional stability. The Fermi-Fermi mixtures of Dy-K and Cr-Li with mass-ratios of 4 and 8.8, respectively, could exhibit more favorable Feshbach resonances and are promising candidates for the investigation of strong interactions in fermionic mass-imbalanced mixtures [132]. A specific outlook on Dy-K is presented in Sec. 3.2, while the investigations on the interaction tunability of a Bose-Fermi Dy-K mixture are the main results of Part III.

Experimental realization of quantum systems with ultracold atoms

The supreme control over the internal and external states of quantum-degenerate atomic ensembles opens the path towards numerous realizations of quantum simulation. The great progress within the field of ultracold gases relies on the continuous development of scientific techniques as well as available technology. This chapter aims to give insight into the complexity of ultracold quantum gas experiments by briefly reviewing the properties of the atoms (Sec 2.1), their interactions (Sec 2.2) and the tools that are used to control and manipulate them (Sec 2.3). The ability to control a given atomic species ultimately defines the range of physical problems that can be tackled with an ultracold gas experiment.

2.1. Ultracold neutral atoms

The basic building blocks of the quantum systems that we manipulate towards quantum simulation are the atoms. They are neutral particles since the number of electrons surrounding the nucleus is the same as the number of protons in it. According to the total spin of an atom, which depends on the number of protons, neutrons and electrons, the atom is either a boson or a fermion. Close to the absolute zero temperature identical bosonic or fermionic particles have fundamentally differing quantum statistics and therewith the consequences of quantum degeneracy are different. Identical bosons undergo a phase transition at the critical temperature T_c to the BEC phase, which is the macroscopic occupation of the ground-state. Identical fermions, on the other hand, avoid each other due to the Pauli exclusion principle and fill all available energy states up to the Fermi energy E_F , which is the chemical potential of a closed system at $T = 0$. The occurrence of a superfluid phase in a Fermi gas can only be due to the presence of interactions [133]. The availability of bosonic or fermionic stable atoms is given by nature. A trick the experimentalist can apply to manipulate natural statistics is to associate two non-identical fermions into a composite boson.

Within ultracold gas experiments the atoms are in the state of a dilute gas, unless the range of interactions of the interatomic forces is larger than the interparticle distance. Typical atom number densities n in ultracold experiments are in the range from 10^{11} cm^{-3} to 10^{15} cm^{-3} . The gas is ‘quantum’ when the interparticle distance $n^{-1/3}$ is on the order of the thermal deBroglie wavelength λ_{dB} . An important parameter for the atomic cloud is the phase-space density (PSD) given by $\mathcal{D} = n\lambda_{\text{dB}}^3$. It compares the wave packet size and the interparticle distance in a gas. For a thermal gas $\mathcal{D} \ll 1$, while Bose-Einstein condensation

and collective quantum phenomena start to be observable at $\mathcal{D} \approx 1$. The atomic systems are usually brought to the quantum regime using laser cooling and subsequent evaporation in an electromagnetic trap inside a UHV chamber.

The typical and vastly implemented ultracold atoms are the alkali metals from the first group of the table of elements. The alkali elements have limited isotopic diversity due to the uneven number of protons and nearly all stable isotopes are bosons apart from ${}^6\text{Li}$ and ${}^{40}\text{K}$, which are fermions. The alkali metals are hydrogen-like atoms with completely filled shells except for the outermost single-electron s -shell. In their ground state all alkali metals have a magnetic moment on the order of $1 \mu_B$ (Bohr magneton), therefore they are sensitive to magnetic fields and tuning of inter-atomic interactions via magnetic fields is possible [34] (see Sec. 2.2.3). The relatively simple electronic configuration of the elements of the first group allows for theoretical predictions of atom-light interactions and interatomic potentials.

Beside the alkali metals, further elements that can be readily laser cooled on (almost) closed optical transitions are the alkaline-earth element Sr [134] and the lanthanides Dy [135], Er [136] and Yb [137]. They all carry two electrons in their outermost s -shell and exhibit a rich electronic structure with similar optical transitions for efficient laser cooling (see Sec. 2.3.2). Further, these four heavy elements have many stable isotopes due to the even number of protons and some of them are fermions with decent natural abundance. These ‘two-electron systems’ have utterly differing magnetic properties compared to the alkali elements. Sr and Yb have a highly symmetric ground state with zero angular momentum, since all electronic levels are full. In contrast, the lanthanides Dy and Er have a partially filled f -shell underneath the full outermost s -shell, which results in a high angular momentum of the ground state. While the highly symmetric ground state of Sr and Yb allows for relatively simple calculations of intra and inter-atomic scattering properties, the forest of electronic levels in the magnetic lanthanides turns them into a challenge for theoreticians. For other elements like He, Cr, Ca or Hg the laser-cooling techniques are more involved due to the use of a metastable state, numerous decay channels or much narrower optical transitions than for the elements presented so far. Therefore complex analogue quantum simulation seems better manageable with the alkali elements, strontium and the laser-cooled lanthanides.

2.2. Interactions between ultracold atoms

The scattering properties of an atomic species are of great importance for quantum gas experiments [34]. Elastic collisions between atoms are essential for reaching thermal equilibrium in the atomic ensemble and thus for cooling to quantum degeneracy, while state-changing collisions usually lead to loss of atoms and increased temperatures in the atomic ensemble. The atomic state is essential for the collisional properties. In spin-exchange collisions the released energy is usually large enough for the atoms to leave the trap. Thus, it is important to prepare the atoms in their hyperfine ground state or a state, which prohibits such an exothermic spin relaxation. If a different atomic state is needed, the timescale of the experiment will be limited by the losses. To escape the trapping potential an ultracold atom can collide with the background gas, it can be associated to another atom by light-assisted collisions or it can undergo a three-body collision. Furthermore, at low temperatures in the quantum-degenerate regime the interactions between atoms determine the equation of state and therewith again the thermalization time for cooling.

2.2.1. *s*-wave scattering length a

In dilute quantum gases the neutral atoms interact typically pairwise through a short-range isotropic potential, like the van-der-Waals potential. The interatomic potential is often simplified to a δ -potential and thus the interaction between atoms is called ‘contact’ interaction. At ultra-low temperatures the kinetic energy in a collision of two particles approaches zero and the number of partial waves contributing to the scattering problem is reduced to the *s*-wave. The contact interaction is then entirely characterized by the *s*-wave scattering length a , defined as [138]

$$a = -\lim_{k \rightarrow 0} \left(\frac{1}{k \cot \eta_0} \right), \quad 2.1$$

where $k = 2\pi/\lambda_{\text{dB}}$ is the wave number, λ_{dB} is the de Broglie wavelength of the reduced mass particle, and η_0 is the *s*-wave phase shift due to the scattering potential. The scattering length a depends on the location of the last bound state of the scattering potential and is given by nature. Between identical particles, spin mixtures, isotope or species mixtures it can have any value, $-\infty < a < +\infty$. Effective interactions are attractive if $a < 0$ and repulsive if $a > 0$. The scattering length is typically given in units of the Bohr radius a_0 . For identical fermions the *s*-wave scattering length is absent, since their wavefunction is antisymmetric under exchange of the colliding partners. Thus, an ultracold sample of identical fermions with only short-range interactions represents an ideal gas.

2.2.2. Dipole-dipole interactions

Most ground-state atoms have a magnetic moment, which can give rise to magnetic dipole-dipole interactions (DDI). For ground-state alkali metals with a maximum magnetic moment of about $1 \mu_B$ the interparticle magnetic dipole interaction is small compared to the contact interaction. Nevertheless, the magnetic dipole of the alkali elements can be used for magnetic trapping and is responsible for spin-changing collisions in an unpolarized sample. The DDI becomes significant for laser-cooled magnetic atoms like Dy, Er, Cr, which have a magnetic moment $\mu > 5 \mu_B$. The coupling constant for magnetic dipoles is $C_{\text{dd}} = \mu_0 \mu^2$ with μ_0 the permeability of vacuum. For a spin-polarized sample the DDI potential¹ U_{dd} is given by [139]

$$U_{\text{dd}} = \frac{C_{\text{dd}}}{4\pi} \frac{1 - 3 \cos^2 \theta}{r^3}, \quad 2.2$$

where θ is the angle between the dipole orientation and the relative position of the particles r . The interaction is repulsive for $\theta = 0$ and it is attractive for $\theta = \pi/2$. At large interatomic distances or at low or forbidden *s*-wave scattering, the weak magnetic DDI becomes important relative to the negligible contact interaction. A representative example of dipolar scattering in absence of *s*-wave scattering is the evaporation of a spin-polarized cloud of fermionic erbium to quantum degeneracy [140]. The anisotropic character of the DDI is not only relevant at long-range ($\sim 1/r^3$), but in the lanthanides Dy and Er with a submerged *f*-shell, the van-der-Waals interaction becomes also slightly anisotropic [141]. The DDI is a relatively new component in ultracold gases and already a very prominent one. In the quantum-degenerate state the anisotropic interaction brings new physical effects shown

¹ The DDI potential between particles with electric dipole moment d is also given by Eq. 2.2, just the coupling constant is $C_{\text{dd}} = d^2/\epsilon_0$ with ϵ_0 the permittivity of vacuum.

already with Cr [142], Dy [143] and Er [144].

2.2.3. Feshbach resonance

An essential property in many ultracold systems is the capability to tune the short-range interactions via magnetic Feshbach resonances [34]. The effect is a resonance as it relies on a level crossing between the entrance scattering state and a bound state of the molecular potential. For magnetic Feshbach resonances to occur the difference between the magnetic moment of the separated atoms and the magnetic moment of the bound state must be nonzero, i.e. $\delta\mu \neq 0$. A homogeneous magnetic field changes the energy of the last bound state in the scattering potential between the two (magnetically sensitive) atoms. Since the scattering length a depends on the location of this last bound state, the experimentalist is able to tune the contact interaction of the ultracold cloud as a function of the magnetic field B . A magnetic Feshbach resonance can be described by [34]

$$a(B) = a_{\text{bg}} \left(1 - \frac{\Delta}{B - B_0} \right), \quad 2.3$$

where a_{bg} is the off-resonant (background) value of the scattering length, Δ is the resonance width, and B_0 gives the position of the resonance. This formula displays the main strengths of a Feshbach resonance: The scattering length diverges for $B = B_0$, it changes sign across the resonance, and it vanishes for $\Delta = B - B_0$. Thus, with a given Feshbach resonance we can turn off the interactions ($a = 0$) and have an ideal gas, we can change from a repulsive gas ($a > 0$) to an attractive one ($a < 0$), and we have the possibility to study a regime of strong interactions and correlations ($a \rightarrow \infty$). Furthermore, it is possible to associate pairs of ultracold atoms into molecules and vice versa just by sweeping the homogeneous magnetic field [105].

The practical application of Feshbach resonances depends strongly on the width of the resonance. On the one hand, there is the technical implementation of homogeneous magnetic fields and the achievable precision at given field values, i.e. magnetic field resolution. On the other hand, similar magnitudes of the width Δ do not necessarily have the same physical significance. In order to have a usable Feshbach resonance the atomic and molecular levels not only need to cross, but there must be also a strong enough coupling between them. Therefore a distinction between broad and narrow resonances can be made with a dimensionless resonance strength parameter that depends on Δ , $\delta\mu$ and a_{bg} . With it the resonances can be classified in open-channel or closed-channel dominated resonances, but there are also resonances with mixed character [34]. The strength of the Feshbach resonance together with the experimental control of the magnetic field define the applicability of the resonance for interaction tuning and also influence the efficiency in the association of atoms to weakly bound molecules.

The availability of Feshbach resonances varies strongly among the different laser-cooled atoms and isotopes. All isotopes of the alkali elements exhibit magnetic Feshbach resonances below 1200 G. The very broad open-channel dominated resonance in ^6Li is an exception to the typically narrow or moderate resonances in the rest of the alkali elements [34]. The alkaline-earth atoms together with Yb have a highly symmetric ground state with zero electron spin. Their fermionic isotopes have a small nuclear magnetic moment, which could allow for (extremely) narrow Feshbach resonances between ground-state atoms to emerge, and is responsible for orbital Feshbach resonances between atoms in different electronic states, as shown for ^{173}Yb [145, 146]. The bosonic isotopes of the closed-shell atoms do

not exhibit any magnetic Feshbach resonances. In contrast, for lanthanides with relatively strong DDI, which involves all even/odd partial waves in the scattering for bosons/fermions at low temperatures, the density of Feshbach resonances is very high and they are randomly distributed, which can be described as chaotic scattering [147–149].

In mixtures of atomic species magnetic Feshbach resonances are also present between the heteronuclear atoms. Accurate predictions of the location of interspecies resonances requires precise knowledge of the respective molecular potentials. Nonetheless, the density of Feshbach resonances in species mixtures can be theoretically well estimated. For mixtures of alkali elements the location of interspecies resonances can be predicted with relatively low uncertainties, because the alkali atoms are well studied and usually experimental data serves as a reliable input to the theoretical models. Typically, the bi-alkali mixtures have similar resonance densities as single-species alkali systems. In contrast to the complete lack of Feshbach resonances in bosonic closed-shell atoms, a mixture of an alkali element with a closed-shell atom does exhibit few narrow Feshbach resonances [150]. Finding the exact location of those sparsely distributed narrow resonances requires supportive optical investigation, such as photoassociation spectroscopy, of the molecular potential (see Sec. 7.1 in Part II). Recently the Feshbach spectrum between closed-shell atoms and magnetic lanthanides has attracted the attention of theoreticians [151, 152]. Also in these systems the anisotropy of the magnetic lanthanides is responsible for the emergence of chaos in the positions of near-threshold bound states and thus in magnetic Feshbach resonances [151]. Yet, the density of resonances in Er-Yb (or similar) remains an order of magnitude lower than between open-shell lanthanides alone. Another order of magnitude lower is the density of Feshbach resonances between the lightest alkali atom, Li, and the open-shell lanthanide, Er [153]. Moreover, the predicted distribution of Feshbach resonances in Li-Er is not chaotic. Lastly, for tuning of interactions within a mixture, the experimentalist should be aware that the interspecies resonances might (partly) overlap with an intraspecies resonance.

2.2.4. Atom loss and inelastic collisions

Atom loss is on the one hand a hindrance for an ultracold experiment and on the other hand it is an essential tool for characterizing interactions. Beside being main pointers for the position of a Feshbach resonance [34] or the lifetime of a certain state, inelastic collisions and corresponding decay rates give the most insight into the scattering potential [138, 154]². Loss measurements can further reveal crucial physical parameters in the so-called universal regime of strong interactions in the context of the Efimov quantum effect [68]. In general, inelastic loss is a fundamental observable, which needs to be treated with caution, since it can have multiple origins.

In inelastic three-body collisions two of the scattering atoms form a weakly bound molecule, while the third atom takes care of the energy and momentum conservation. If the energy that is released from the change in internal state of the colliding atoms is larger than the trapping potential depth, atom loss will be observed. The formed molecules can collide with other atoms, decay into deeper lying states and induce further losses. Such three-body loss collisions depend on the scattering length, but more importantly on the statistical properties of the atoms. The Pauli principle strongly suppresses losses in fermionic samples [75, 76].

² Here I refer mainly to photoassociation spectroscopy, which is a basic tool for probing interatomic potentials. The experimental observation in one-color photoassociation spectroscopy is atom loss or reduction of atom loss in two-color photoassociation spectroscopy.

2.3. Making and probing ultracold atomic gases

The main experimental tools for controlling the atom's external and internal degrees of freedom are resonant or near-resonant laser light and magnetic fields. From a historical point of view the laser era revolutionized atomic physics [155]. The development of methods to cool and trap atoms with laser light was acknowledged by the 1997 Nobel prize in physics [156–158]. Here I will introduce some of the basic parameters for laser cooling (Sec.2.3.1) with an emphasis on narrow-line cooling (Sec.2.3.2), followed by optical trapping (Sec.2.3.3) and finally detection (Sec.2.3.4) of ultracold atoms. More in-depth reviews of atom-light interaction towards production of ultracold gases can be found in older books [159] or review articles [160], as well as in more recent ones [155, 161].

2.3.1. Laser cooling

To obtain ultracold gases the atoms are cooled using (near-) resonant laser light. Laser cooling of atoms at low densities can be characterized in a single-atom picture. The theoretical description of atom-light interactions often reduces the atom to a two-level system [155]. However, the actually complex atomic structure is the reason for the richness of physical effects that can be investigated with ultracold atoms. The diversity of physical phenomena that can be probed with the multilevel atoms ranges from effects like the sub-Doppler cooling [162] to the examination of artificial gauge fields [163]. The specific properties of each laser-cooled atomic species and isotope eventually set the scope of possible interrogations in a given experiment.

The thermodynamic ‘temperature’ as a parameter describing the state of a closed system in thermal equilibrium with its surroundings is not directly applicable to laser cooling mostly due to the lack of thermal equilibrium with the environment [159]. Nonetheless, we use the notion of temperature as a measure of the average kinetic energy of an atomic sample with a Boltzmann velocity distribution. The ultracold gas is cooled when the average kinetic energy of an atomic sample as well as the width of the velocity distribution are lowered.

In the presence of a (near-)resonant laser field an atom with an (almost) closed optical transition experiences a multitude of absorption and re-emission processes. The transferred momentum from the absorption is in the direction of the laser beam, while spontaneous emission is isotropic and its momentum transfer averages to zero after a large number of events. When a single photon with wavelength λ is absorbed or emitted by an atom of mass m the recoil energy of the atoms is

$$E_{\text{rec}} = \hbar^2 k^2 / 2m \tag{2.4}$$

with the reduced Planck constant \hbar and the wave number $k = 2\pi/\lambda$. In a simple energy conservation picture the atom should absorb less energy than it emits in order to be cooled, which is only possible thanks to the nonzero linewidth of the optical transitions. The laser-cooling techniques rely on a direct change of the kinetic energy of the atom (Doppler cooling) or on an additional change in the potential energy of the atom from polarization gradients or trapping potential (sub-Doppler cooling).

Doppler cooling

The Doppler effect plays an important role in laser cooling and hence the name Doppler cooling. If the frequency of the laser is slightly red-detuned from the atomic transition, the

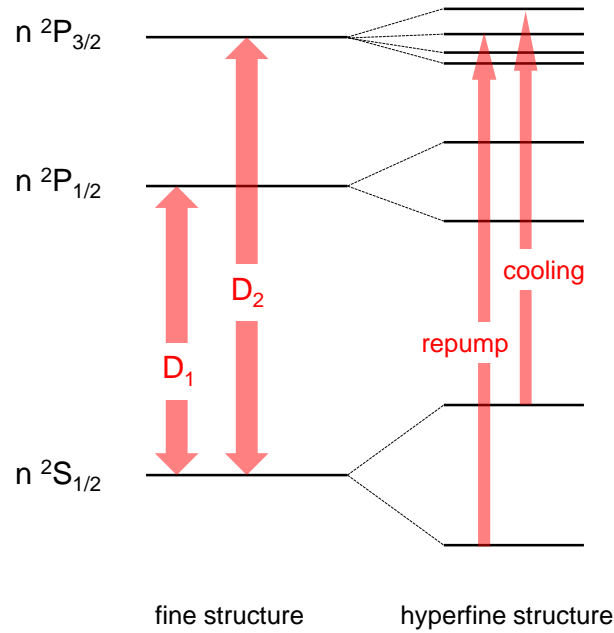


Figure 2.1.: Concept of the electronic level scheme of alkali elements and the typical optical transitions for laser cooling. The principle quantum number n goes from 2 to 6 for the alkali metals. The fine structure splitting of the ${}^2\text{P}$ level gives rise to the D1 and D2 optical transitions. The hyperfine states of the atomic levels with total electronic angular momentum $J = 1/2$ are doublets for all alkali elements. The hyperfine energy splitting of the ground state ${}^2\text{S}_{1/2}$ is typically an order of magnitude larger than the one of the ${}^2\text{P}_{1/2}$ level. The hyperfine splitting of the ${}^2\text{P}_{3/2}$ state results in four levels for all alkali isotopes apart from ${}^6\text{Li}$, which has three hyperfine levels. The exemplary cooling and repumping transitions are given for the alkali isotopes with nuclear spin $I = 3/2$.

atom moving towards the light source can be slowed down on average. In a two-level system with a given linewidth of the optical transition Γ_λ laser cooling is limited to the Doppler temperature [164]

$$T_D = \frac{\hbar\Gamma_\lambda}{2k_B}. \quad 2.5$$

Most properties of laser cooling depend on Γ_λ .

For the alkali metals the main optical transition for cooling is at a wavelength λ in the range from 589 nm to 895 nm with a linewidth $\Gamma_\lambda/2\pi$ in a range of 5 MHz to 10 MHz and therewith T_D is around 150 mK. The electronic configuration of the alkali metals yields similar laser cooling properties for all the elements of the first group, as shown in Figure 2.1. The principle quantum number n equals 2 for Li, 3 for Na, 4 for K, 5 for Rb, and 6 for Cs. The fine-structure splitting leads to two P states, ${}^2\text{P}_{1/2}$ and ${}^2\text{P}_{3/2}$, and the main optical transitions from S to P are called D1 and D2 line (legacy of Fraunhofer sun spectrum), respectively. The ground state ${}^2\text{S}_{1/2}$ has a hyperfine splitting, which typically hinders the existence of a closed optical transition needed for laser cooling. Thus, for alkali elements two frequencies are needed to create a cycling transition, the so-called pump and repump frequencies. The hyperfine splitting of the excited states is usually well resolved relative to the linewidth of the optical transition, but it can also be narrower than $\Gamma_\lambda/2\pi$, as for Li, Na and bosonic K.

Sub-Doppler cooling

The actual multi-level character of the atoms allows us to laser cool them below T_D . Already the Nobel prize in 1997 [156–158] was partly for sub-Doppler cooling with D2 molasses based on laser polarization gradients [165, 166]. Since then, different cooling techniques with polarization of the light and frequency detuning have been developed [167]. In alkali elements like K, Na or Li, where the hyperfine structure of the optically excited state is not resolved relative to Γ_λ , sub-Doppler laser cooling on the D1 line has been established [78, 168–170]. With the combination of magnetic fields and optical lattices (1D is enough) one can reach low temperatures and a spin-polarized sample via degenerate Raman sideband cooling [171, 172], which is a laser cooling technique ‘borrowed’ from trapped ions [173].

Recoil limit

After crossing the limit of the Doppler temperature, the next fundamental limit in laser cooling towards the absolute zero is the recoil temperature

$$T_{\text{rec}} = \frac{2E_{\text{rec}}}{k_B} = \frac{\hbar^2 k^2}{mk_B}. \quad 2.6$$

Every spontaneous absorption and emission of a photon can change the kinetic energy of the atom and thus the temperature achieved by laser cooling with (near-)resonant light is always a balance between heating and cooling. At sufficiently low temperatures of about $T < 10T_{\text{rec}}$, the (near-)resonant light, which up to then was on average removing entropy from the atomic system, can become an essential heat source for the atomic cloud. The straightforward solution is to turn off the resonant light and the usual approach is to continue with evaporative cooling (see Sec. 2.3.3). For the alkaline earth atom strontium with an optical transition where $T_D < T_{\text{rec}}$, the recoil limit can be overcome by shifting the colder atoms out of resonance as shown in Ref. [174], which is a different way of turning off the resonant light. Recently rubidium, the most common laser cooled alkali metal, was brought to quantum degeneracy using only laser cooling by effectively reducing the recoil momentum in a Raman cooling scheme with far-off-resonant light [175].

Magnetic fields

An important ingredient for laser cooling is the additional control by magnetic fields, since they can shift the energy of the atomic levels. The use of a spatially varying magnetic field with a single frequency laser beam is the principle idea behind a Zeeman slower (ZS) [176]. This typical cooling stage in an ultracold gas machine decelerates and cools atoms from the high oven temperature to less than 1 K: not only is the average velocity lower, but also the spread of velocities is narrower. Another possibility for precooling³ is a two-dimensional magneto-optical trap (2D MOT) [177], where the magnetic field gradient makes the light force velocity dependent. Similarly, a spherical quadrupole magnetic field defines the middle of the 3D MOT [138], which is a dissipative trap. The same quadrupole magnetic field can be used alone as a conservative magnetic trap for low-field seeking atomic states [178] or for additional levitation in an optical trap. More elaborate magnetic field configurations [179] can be designed for purely magnetic trapping of atoms. Nonetheless, we will concentrate in

³ Throughout this work I will refer to the initial cooling of atoms from oven to 3D MOT as precooling.

the following on the more general optical traps, as they free up the magnetic field to be used for interaction tuning.

2.3.2. Narrow lines are cooler

This section is dedicated to laser cooling in narrow-line magneto-optical traps, which are representative for the non-alkali atoms. The cooling dynamics with a narrow optical transition is the major difference from the general method of cooling alkali elements. The presence of a closed intercombination line⁴ in strontium and dysprosium allows us to describe them together, although these non-alkali elements belong to different families of atoms and have partly contrasting properties. Narrow cooling transitions provide very low Doppler temperatures and under appropriate conditions a spontaneous spin polarization of the atomic ensemble, thus offering advantageous starting conditions for evaporative cooling towards quantum degeneracy. Simple laser cooling to even lower temperatures is very important for precision measurements with optical clocks or atomic fountains, where just a cold but not quantum-degenerate gas suffices. Thus, already in 1998 Katori et al. reported on a narrow-line MOT of Sr with a very high phase-space density and a temperature close to the recoil limit [134].

To demonstrate that narrow lines are cooler, six basic laser-cooling parameters can be compared. These parameters, following Ref. [180], are summarized in Table 2.1 for potassium, rubidium, strontium and dysprosium. The table shows the optical transitions at wavelength λ , the linewidth of the excited state Γ_λ , the Doppler temperature T_D (see Eq. 2.5), the recoil temperature T_{rec} (see Eq. 2.6), the ratio between Γ_λ and the single photon frequency shift $\omega_{\text{rec}} = \hbar k^2/2m$, and the ratio between gravitational and light force $R = \hbar k \Gamma_\lambda / 2mg$ with the gravitational acceleration g . For the mass m of the chemical elements a mean value of the most abundant isotopes was taken. For the alkali elements the properties of the closed transitions at the respective D2 line are given, as well as an example of a narrower open transition such as the $4S_{1/2} \rightarrow 5P_{3/2}$ at 405 nm for potassium⁵. For strontium and dysprosium the main cooling transitions used for ZS and 3D-MOT are given. The ratio $\Gamma_\lambda/\omega_{\text{rec}}$ compares the Doppler temperature T_D to the recoil temperature T_{rec} and a true narrow-line transition is when $\Gamma_\lambda/\omega_{\text{rec}} \approx 1$ or less, or in other words when $T_D \leq T_{\text{rec}}/4$ [180]. This means that the simple laser cooling on a narrow-line transition is not limited by the Doppler temperature, but by the photon recoil.

With such narrow transitions as at 689 nm for Sr or at 741 nm for Dy, the intensity I of the (near-) resonant light plays a major role next to the detuning in the cooling dynamics [180]. The linewidth Γ_λ determines also the saturation intensity $I_{\text{sat}} = 2\pi^2 \hbar c \Gamma_\lambda / 3\lambda^3$ and therewith the saturation parameter $s = I/I_{\text{sat}}$. For $s \gg 1$ the effective transition linewidth $\Gamma_E = \Gamma_\lambda \sqrt{1+s}$ is much larger than ω_{rec} and the atoms are in a standard cooling regime similar to the alkali metals. For moderate saturation and large detuning the shape of the MOT changes, as it is governed by the balance between gravitational and radiative force. In the very low intensity regime at $s \approx 1$ the cooling is determined by single photon recoils, is purely quantum mechanical, and the limit temperature is only half of T_{rec} [180]. There, the lifetime of the MOT is limited by gravitational leaks from the trap, because with the

⁴ The intercombination line is an optical transition between a singlet and a triplet state. Note that ‘singlet’ and ‘triplet’ states are not accurate general descriptions for the electronic states in lanthanides except for Yb and No, since the total angular momentum of the ground state of each element depends on the number of unpaired electrons in the submerged shell.

⁵ The linewidth of the $4S_{1/2} \rightarrow 5P_{3/2}$ transition in potassium is $2\pi \times 185$ kHz, yet in Table 2.1 we use the linewidth broadened by multiphoton decay channels [181].

	Potassium		Rubidium	Strontium		Dysprosium		
λ (nm)	767	405	780	461	698	421	626	741
$\Gamma_\lambda/2\pi$ (kHz)	6035	1190	6067	30500	7.4	32200	136	1.7
T_D (μ K)	145	29	146	732	0.18	773	3.3	0.04
T_{rec} (nK)	815	2919	366	1036	464	665	301	215
$\Gamma_\lambda/\omega_{\text{rec}}$	711	39	1592	2830	1.5	46500	43	0.8
$R = \hbar k \Gamma_\lambda / 2mg$	25200	9400	11600	97200	16	60200	171	2
Ref.	[182]	[181]	[183]	[184]	[185]	[186]	[187]	[186]

Table 2.1.: Comparison of atomic properties and main laser-cooling parameters between the alkali metals potassium and rubidium and the two-electron systems strontium and dysprosium.

narrow transition comes also a low scattering rate, due to which atoms can fall out of the MOT before interacting with a photon⁶. In Table 2.1 the ratio between gravitational and light force $R = \hbar k \Gamma_\lambda / 2mg$ shows the substantial difference between broad and narrow cooling transitions. With dysprosium the narrow closed transition around 741 nm demands for an unusual blue-detuned MOT to overcome gravity [188] and can be referred to as an ultranarrow transition. The commonly used closed transition for a dysprosium MOT is around 626 nm and for large red detuning the 626 nm-MOT shares the properties of a ‘true’ narrow-line MOT in the regime of moderate intensity [189].

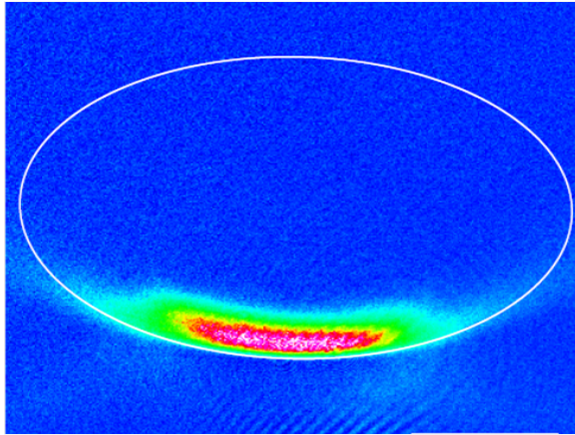


Figure 2.2.: Representative image of the shell-like narrow-line MOT of Sr. It is an *in situ* absorption image of an atomic sample of ^{88}Sr in the horizontal direction showing about 1.3×10^6 atoms. The white ellipse is a guide to the eye along a constant magnetic field underlining the shell-like extent of the narrow-line MOT. From Ref. [190].

In the quadrupole magnetic field of a narrow-line MOT the velocity and detuning dependent resonance condition is met only along a thin ellipsoid shell. The atoms move in a free flight between the boundaries of that shell while only in one direction there is gravity. Thus, the atoms sag to the bottom of the trap, where they interact almost exclusively with the MOT beam directed up. This shell-like MOT shape is a signature of narrow-line MOTs and can be observed for strontium in Figure 2.2. A useful side effect of the shell-like MOT is the spontaneous spin polarization in the MOT [189]. Bosonic strontium and ytterbium do not

⁶ Very low temperatures can be safely reached with laser cooling on a narrow transition in an optical dipole trap. What needs to be considered there are eventual shifts of the ground and excited electronic energy levels due to the strong electric field of the trapping light (differential AC Stark shift).

have a hyperfine splitting in the ground state, but the fermionic isotopes and the magnetic lanthanide atoms do. The beneficial spin polarization in the shell-like MOT can be shown through Stern-Gerlach investigation of the spin composition of the atomic sample.

To load a narrow-line MOT, typically power broadening of the transition linewidth Γ_E or broadband frequency modulation of the cooling light is used [134, 135]. The frequency modulation temporarily introduces additional frequency components, preferably further detuned to the red, and drastically increases the capture velocity of the MOT at the expense of temperature. Notwithstanding, the radiation pressure on the narrow transitions is not strong enough to capture atoms directly from hot atomic vapour, as it can be the case for alkali metals on the D2 line. The narrow-line MOT offers high PSD without complex sub-Doppler cooling schemes, however it requires also efficient precooling of the atoms.

Precooling on a broad blue line

The precooling of strontium and dysprosium before they can be captured by the respective narrow-line MOT happens on the more than 30 MHz-broad transitions in the blue/UV spectrum (see Table 2.1). The maximum deceleration of those broad blue lines is ten times larger than in alkali for comparable atomic mass. Such a blue transition can be used for efficient precooling thanks to its very strong radiation pressure. Even if these strong blue optical transitions have a branching ratio to states other than the ground state of about 1 : 100000 and are thus ‘almost’ closed, they can be successfully implemented in a Zeeman slower, in a 2D MOT [191] or in a short lived 3D MOT. Transverse cooling is also very efficient with blue light and usually increases the loading rate of a MOT almost by an order of magnitude.

Depending on the capture velocity of a narrow-line MOT, even with line-broadening, a blue collector MOT is needed for some elements. In the case of strontium a direct loading of a MOT operating at the narrow intercombination line is not possible, so the atoms from the Zeeman slower are collected in a blue MOT first. That is also the case for dysprosium, if the MOT operates at 741 nm [186]. For a dysprosium MOT operating at 626 nm, on the other hand, the capture velocity is high enough to omit the blue collector MOT [135].

Apart from precooling, the broad blue line gives also a new opportunity for imaging. Despite the smaller absorption cross section due to the lower wavelength compared to alkali metals, the higher scattering rate due to the larger transition dipole moment and the higher optical resolution thanks to the low wavelength allow for faster and better resolved imaging.

2.3.3. Optical trapping

Optical trapping of neutral particles is achieved in the intensity gradient of a laser field. The impact of the so-called optical tweezers beyond atomic physics was recognized with half of the 2018 Nobel prize in physics [192]. Optical dipole traps (ODTs) are conservative traps with typical trap depths below 1 mK, which is about 100 times lower than for magnetic traps. ODTs are widely used ultracold gas experiments [42] because they can be operated at arbitrary external magnetic fields allowing for interaction tuning. Furthermore, the optical dipole potentials created by focused off-resonant laser light can be independent of the particular magnetic sub-level of the electronic ground state manifold for appropriate atomic polarizability. This makes the ODTs very versatile in their use in comparison to magnetic trap, especially since they also give freedom in the confinement geometry. Besides spatial control, optical potentials allow the experimentalist for more precise temporal manipulation of the confinement of ultracold atoms than magnetic fields.

Typically ODTs are used to capture the atoms from the MOT stage and further cool the atomic gas by evaporative cooling. Here I will first introduce the properties of the ODT and then briefly explain forced evaporative cooling. The section ends with a discussion of optical lattices and geometrical confinement.

Optical dipole traps

The properties of the ODT are determined by the polarizability of the atoms $\alpha(\omega_L)$ at a given laser frequency ω_L , since the dipole potential U_{dip} stems from the interaction of the driving laser field \mathbf{E} with the induced electric dipole moment \mathbf{p} in the atom [42]

$$U_{\text{dip}} = -\frac{\langle \mathbf{p}\mathbf{E} \rangle}{2} = -\frac{2\pi a_0^3}{c} \text{Re}(\alpha(\omega_L))I, \quad 2.7$$

with the angular brackets denoting the time average over the rapid oscillating terms. The right hand-side of Eq.2.7 includes the local intensity of the laser field I and the real part of the polarizability $\alpha(\omega_L)$ in Hartree atomic units⁷. While the potential energy of the atom in the laser field is proportional to the real part of $\alpha(\omega_L)$, the imaginary part of $\alpha(\omega_L)$ determines the scattering rate at ω_L [42]. Both, the dipole potential and the scattering rate, are proportional to the laser field intensity, but the scattering decreases faster with detuning from the frequency of the strongest optical transition in the atom. A red-detuned ODT beam attracts atoms, while a blue-detuned focused laser beam repels them. Since the strongest optical transition for the alkali elements is in the range $\lambda = 589 \text{ nm}$ to 895 nm and for strontium and dysprosium it is in the blue visible spectrum (see Table 2.1), an attractive dipole potential is typically produced by a focused infrared (IR) beam.

A harmonic trapping potential can be easily characterized and allows for straightforward extraction of physical quantities. The typical ODT consists of a focused Gaussian beam, which can be well approximated to a harmonic potential in its center. The radial trap frequency of a single Gaussian beam ODT is calculated by

$$\omega_r = \sqrt{\frac{16a_0^3 P \text{Re}(\alpha(\omega_L))}{cw_0^4 m}}, \quad 2.8$$

where the laser parameters are the frequency ω_L , power of the laser beam P and its waist w_0 and the atomic properties are the mass m and the polarizability $\alpha(\omega_L)$ in Hartree atomic units. The weak axial trapping in a single-beam ODT can be compensated by an additional confinement from a second (usually perpendicular) beam, forming a crossed ODT.

The loading of an atomic cloud into an ODT depends on the spatial overlap of the dissipative (MOT or optical molasses) and the conservative traps. However, it is not a generally established procedure, but rather depends on the experimental setup as well as on the atomic species. After the 3D-MOT cooling stage the atomic clouds are typically loaded into a conservative trap (optical, magnetic or a mixture of both) from a compressed MOT. If the atomic species and the experimental setup allow it, the loading of the atomic cloud into an ODT from a magnetic trap is usually more efficient than direct loading from a MOT. Typical loading efficiencies into an ODT directly from a MOT are about 10%⁸. In an ultracold mix-

⁷ The Hartree atomic unit for electric polarizability is $1 \text{ a.u.} = e^2 a_0^2 / E_h$ with the electron charge e , the Bohr radius a_0 and the Hartree energy E_h .

⁸ With the narrow optical cooling transition of strontium S. Stellmer reports on the exceptional 50% loading efficiency into an ODT from a single-frequency MOT [190].

ture of atomic species the loading of both species into the same dipole trap is experimentally challenging and can be sequential. Once in the conservative trap, the atomic ensemble can be further cooled optically or by evaporative cooling.

Forced evaporation

In forced evaporative cooling, the ultimate atom cooling procedure, the atoms with the highest potential energy are removed from the trap and the remaining atoms thermalize to a lower temperature. Evaporative cooling requires atoms interacting mutually with a moderate strength, such that thermalization happens on a reasonable timescale while inelastic collisions stay low. As long as there are enough atoms in the high energy tail of the thermal distribution, which can be removed from the ensemble, forced evaporation leads to an increase of density and more importantly PSD while the number of atoms considerably decreases.

For some elements with broad enough Feshbach resonances we can tune the interactions to optimize the evaporative cooling. This procedure is easily applicable in an ODT while it is only seldom available for the magnetically trappable low-field seeking states [34] and requires a specialized magnetic field setup for a magnetic trap (e.g. ‘baseball’ trap [193]). Note that identical fermions with only short-range interactions do not collide at low temperatures, therefore mixtures of spins [52], isotopes [46], or elements [86] are used for evaporation. The best example of favourable scattering properties is the most commonly used alkali metal ^{87}Rb with a scattering length of about $100 a_0$, which allows for efficient evaporative cooling in magnetic and optical traps. Next to the atomic scattering properties, the type of conservative trap and the corresponding method of removing ‘hot’ atoms are important considerations.

Removing the high energy tail of the atomic thermal distribution requires different approaches depending on the type of trap. From a magnetic trap, on the one hand, one can selectively remove velocity classes using RF-induced spin flips [194]. On the other hand, for forced evaporation in an ODT the entire trap depth is lowered by reducing the power of the trapping laser. This leads to a reduction in trapping frequency and atom density as well and slows down the evaporation. Thus, for efficient evaporative cooling in an ODT, the necessary large initial particle numbers together with a convenient particle density for a good ratio of elastic to inelastic collisions typically require more than one optical trapping beam. Usually there is a larger ‘reservoir’ ODT⁹ for loading from the previous cooling stage (compressed MOT, optical molasses or else), which is later on overlapped with a tighter or crossed ODT for final evaporation [195]. The notion of a ‘dimple’ trap describes an additional tight trapping potential on top of a larger trap. In the ‘dimple’ only the particles with the lowest kinetic energy are confined, resulting in a high PSD and eventual quantum degeneracy.

Geometrical confinement and optical lattices

Trapping atoms with intensity gradients of light allows for almost arbitrary geometries of the trapping potentials: from optical lattices for the simulation of condensed matter systems [19], through transport channels between atomic reservoirs for the exploration of quantized conductivity [196], to random potentials for Anderson localization experiments [197]. The geometrical confinement of ultracold atoms is virtually unlimited thanks to modern optical technologies like spatial light modulators (SLM) [198] and high resolution microscope

⁹ FORT as in far-off-resonant (optical) trap is also a notion in the ultracold community.

objectives in the vicinity of the atoms [199]. The quantum gas microscope allows to image and address single atoms in optical lattices [19, 200, 201], as well as to imprint specific trapping potentials for transport measurements of fermions through a very thin tunnel [202]. The current limiting factor in the available trapping geometries and also for the light used for single-atom-manipulation is the diffraction limit and the corresponding ‘speckles’. The diversity in optical trapping potentials and especially the optical lattice can be used to simulate a specific Hamiltonian or they can be applied as an experimental tool for precise manipulation of the atomic ensemble.

Optical lattices are interference patterns of off-resonant laser light that realize a periodic trapping potential. The usual interference pattern formed by a standing wave of wavelength λ has a periodicity of $\lambda/2$. Depending on the atomic polarizability at a given lattice wavelength the atoms can be trapped in an intensity maxima or minima of the periodic light structure. In an ultracold mixture the lattice can be species specific [24]. Typical laser wavelengths for lattices are 1064 nm and 532 nm.

Optical lattices are widely used for simulating different quantum periodic structures, in particular the Hubbard model and variations thereof [203–205]. A prominent quantum simulation achievement with ultracold gases in optical lattices is the realization of the quantum phase transition from a superfluid to a Mott insulator phase for bosons [22] as well as for fermions [206]. Realizing such strongly correlated systems in optical lattices of diverse dimensionality opens a separate lattice-based quantum simulation field in ultracold quantum gases [19].

In addition, an optical lattice can be used as a tool by the experimentalist for a controlled manipulation of the atoms. The lattice can be used to transport [207] or pin the atoms. The precise number of atoms per lattice site in the Mott insulator phase is a crucial preparation step for homonuclear molecule creation without Feshbach resonances [208] or for protection against inelastic losses during and after the association of heteronuclear molecules [91], as will be discussed later in Sec. 7.2.

2.3.4. Detection

Ultracold atoms are usually detected with the same resonant light that is used for laser cooling. To assess physical quantities both precision and stability in the experiment as well as a good understanding of the investigated many-body systems are needed. One can distinguish between fluorescence, absorption and dispersive imaging techniques of which absorption imaging is the most commonly used and will be discussed in more detail below.

Fluorescence imaging In fluorescence imaging the trapped atoms are illuminated with resonant light and the photons that are scattered by the atoms over a solid angle given by the imaging optics are detected. Fluorescence imaging is widely used to characterize a MOT, since the atomic cloud readily scatters photons from the MOT beams. In addition, fluorescence imaging is a powerful tool in quantum gas microscopes for single-site and single-atom imaging in an optical lattice [209]. A drawback of fluorescence imaging is that it is difficult to obtain absolute atom numbers either in a bulk atomic cloud or in a lattice¹⁰.

Absorption imaging The absolute atom number is most commonly determined using absorption imaging. Resonant light is shone on the atoms and the detected shadow is analyzed.

¹⁰ Fluorescence imaging detects only the parity of the occupation number on a lattice site because of pairwise light-assisted collisions.

The shadow is a two-dimensional image of the optical density of the atomic cloud. In the ideal case of linear scattering from the atoms in a single initial internal state, the intensity detected on the camera is a magnified image of the transmitted intensity $I_t(x, y)$ of the probe pulse following Beer-Lambert's law

$$I_t(x, y) = I_i(x, y)e^{-\sigma_{\text{ph}} \int n(x, y, z) dz} = I_i(x, y)e^{-OD(x, y)}, \quad 2.9$$

where $I_i(x, y)$ is the initial intensity, σ_{ph} is the photon absorption cross section of the atoms, $\int n(x, y, z) dz$ is the column density of the atoms along the imaging axis (here z) and $OD(x, y)$ is the optical depth of the gas. The parameter $I_i(x, y)$ is obtained by taking a reference image without atoms in the field of view. With a well-known σ_{ph} for a given atomic initial state, probe-light polarization, and detuning we can determine the total atom number by integrating the column density along both image axes.

For dense atomic samples, however, absorption imaging has limited use. On the one hand, for $OD \gg 1$ the detected image is mostly black and thus dominated by noise. On the other hand, at high atomic densities there is photon reabsorption and multiple scattering in the atomic cloud, for which Eq. 2.9 breaks down. To circumvent these limitations further detuned probe light for *in situ* (in trap) measurements can be used. Another method is to release the gas from the trap and let it expand for a certain time t_{TOF} (TOF stands for time of flight) before taking the absorption image at $OD \approx 1$.

The utility of the time-of-flight (TOF) detection technique goes beyond reduction of the atomic density. Provided that the interactions between atoms can be neglected during the expansion, for a large enough¹¹ t_{TOF} the spatial distribution of the atoms is proportional to the initial momentum distribution in the trap. For quantum-degenerate gases the atomic density distribution depends on the quantum gas statistics, the temperature (or condensate fraction) and the strength of interactions between the trapped atoms and can be characterized for different regimes [210, 211]. For a partly Bose-condensed bosonic sample with non-negligible interactions the density distribution is bimodal [210]. In a TOF image from a harmonic trap the condensate has a parabolic density profile (Thomas-Fermi distribution), which can be usually clearly distinguished from the Gaussian density profile of the non-condensate (thermal) fraction of the atoms. The determination of the BEC to thermal fraction from the wings of the total density distribution is important for temperature determination, since temperature is not defined in a pure BEC¹². Fermionic quantum degeneracy, on the other hand, manifests itself in subtle changes of the momentum distribution [211]. Pauli blocking limits the occupation of low momentum states to one fermion per state, leading to a flatter and wider momentum distribution than expected classically. This change in shape is evident in the azimuthally averaged time-of-flight density distributions. Other ways to detect quantum degeneracy in an ultracold gas is to look for 'smoking guns' of superfluidity like vortices in a rotating superfluid or the second sound in the propagation of thermal excitations. In the early stage of an experiment, for characterization of the atomic system, one typically works with thermal atomic samples. There the temperature of the ensemble can be deduced from the Gaussian cloud size σ_{TOF} using

$$\sigma_{\text{TOF}}^2 = \frac{k_B T}{m} t_{\text{TOF}}^2. \quad 2.10$$

¹¹ The expansion time is large when $t_{\text{TOF}} \gg 1/\omega_x, 1/\omega_y, 1/\omega_z$, where ω_i are the trap frequencies along the i -th direction.

¹² If all the atoms are in the lowest energy level, then temperature, in the usual sense of a distribution amongst energy levels, loses its meaning

Absorption imaging is the main investigative tool for ultracold atoms and it imposes a major restriction to the experiments. Absorption imaging is namely a destructive type of detection, so after each measurement the atomic sample is discarded and a new one has to be prepared. The destructive imaging technique requires best possible repeatability and thus stability in the experiment, in order to examine the dependence on a scanned parameter or detect the time evolution of the atomic system.

Dispersive imaging A workaround option for the destructive detection and also for imaging dense samples is the implementation of dispersive imaging. Dispersive imaging is a non-destructive detection method which can also be used for dense atomic samples. This imaging technique uses far-detuned imaging light and relies on the fact that the dense atomic cloud is a medium with a refractive index. The experimental difficulty is to collect only the refracted light, in order to measure a polarization change or a of phase shift of the imaging light, whereas the transmitted imaging beam is blocked. Since the imaging light is off-resonant, the atomic sample is not immediately destroyed and one can take several images of the same atomic cloud [212]. Dispersive imaging is a valuable experimental perspective for the future ‘science cell’ in the Dy-K experiment (see Sec. 9.5).

Outlook on the mixtures in this thesis

The work presented in this thesis covers the realization and characterization of the Sr-Rb and the Dy-K mixtures. The motivation for the experimental investigation of these two mixtures is also the outlook for the near future. The Sr-Rb and Dy-K mixtures embody two prominent research directions with ultracold gases: dipolar molecules and Fermi-Fermi mixtures. Some specific goals for each mixture will be presented in the following. A more general outlook for the intended complex quantum systems of this thesis is to deploy them as analogue quantum simulators that can verify the results of an eventually available quantum computer for classically unsolvable problems.

3.1. RbSr open-shell polar molecules

The aim of the Rb-Sr mixture is to create open-shell polar molecules to perform quantum simulation. This system is promising because a ground-state open-shell molecule has an unpaired electron as compared to a ground-state heteronuclear bi-alkali molecule. The unpaired electron provides additional degrees of freedom, which can be of vital importance for complex quantum simulation schemes such as lattice-spin models and for interaction tuning between the molecules.

3.1.1. Two-dimensional lattice-spin models

Two-dimensional lattice-spin models can give rise to topologically ordered states, which are robust to perturbations and would allow fault tolerant quantum computation. Creating such a system in a laboratory is highly non-trivial, but open-shell polar molecules can enable the construction of Hamiltonians with the necessary anisotropic two-spin interaction with engineered range and long coherence times, as proposed in Ref. [213]. Figure 3.1 shows a possible configuration for an experiment based on strong correlations in the quantum system. The spin (or qubit) is given by the single electron in the open shell in its rotational ground state, which is doubly degenerate. Due to spin-rotation coupling and the strong coupling of the rotational motion of the molecules through the dipole-dipole interaction (DDI), the DDIs become spin-dependent on top of being anisotropic and long-range. Hence there is effective coupling of internal states at moderate distances, achievable in a 3D optical lattice.

Such coupling has been shown with the bi-alkali KRb molecules [36], but there the missing spin has to be simulated by rotational levels. This system is thus liable to differential AC stark shifts from the lattice. In the open-shell molecules ground and excited spin-states see

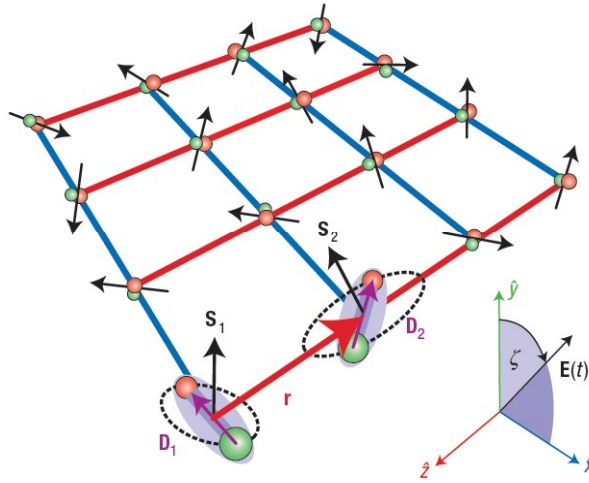


Figure 3.1.: Example of a 2D spin-lattice model. ‘Effective interactions between the spin \mathbf{S}_1 and \mathbf{S}_2 of the molecules in their rovibrational ground states are generated with a microwave field $\mathbf{E}(t)$ inducing dipole-dipole interactions between the molecules with dipole moments \mathbf{D}_1 and \mathbf{D}_2 , respectively.’ From Ref. [213]

the same trapping potentials up to tensor shifts, hence decreasing decoherence rates [13]. An additional advantage of RbSr is that the outer-shell electron can be optically activated and has much longer lifetimes than an excited rotational state. This direct and more robust control of $^2\Sigma$ molecules in contrast to alkali dimers is a strong motivation to create an ultracold dense ensemble of ground state RbSr molecules.

3.1.2. Interaction tuning in open-shell molecules

Most proposed quantum simulations require a degenerate quantum gas of polar molecules as a starting point. Although ultracold molecule formation starts with a mixture of quantum degenerate gases, the final product was until recently [87] not quantum degenerate due to inevitable imperfections in the association process. Evaporative cooling of the molecular gas has been limited so far by strong losses. Some molecules like KRb or RbSr are chemically unstable against two-body collisions. Even the chemically stable ones as RbCs or NaK have short lifetimes in a gas. One of the proposed explanations is that scattering events with formation of long-lived collision complexes, so-called ‘sticky collisions’, enhance the three-body loss in the sample [214]. Meanwhile it was measured that on an even shorter timescale the near-infrared trapping laser excites those collision complexes and thus strongly enhances the two-body loss [112, 215]. A possibility to alleviate those strong losses is to have interaction control in order to tune the ratio of elastic to inelastic collisions between the bosonic molecules. For fermionic ground-state molecules such as KRb the Pauli suppression in the quantum degenerate Fermi gas keeps the molecules stable [87]. Nevertheless, interaction tuning is always of interest.

One main prospect in suppression of inelastic collisions is the use of strong electrostatic fields, as proposed in Ref. [216]. At high E-fields rotational levels of opposite parity become degenerate and can alter the scattering Hamiltonian for neighboring rotational states. Colliding molecules exert forces on one another that are second order in the dipole-dipole

interaction. When two levels are about to cross, the sign of this effective van-der-Waals interaction changes and results in a barrier in the interaction potential of the colliding molecules. This barrier is at long range and provides collision shielding up to a certain entrance energy. For KRb such suppression is predicted with a potential barrier of 1 mK [217], however for fields (≈ 12 kV/cm) larger than the currently attainable in the experiment at JILA (5 kV/cm, from Ref. [218]).¹

For RbSr the same collision shielding effect exists and is predicted at much lower and attainable fields, namely 2 kV/cm [219]. Moreover, the region of suppressed collisions extends to a larger field range, because the additional spin states in the open-shell molecule provide many more states of opposite parity. By simply exciting the ground state molecules into the next rotational level, a shielding potential of 15 mK can be generated, which is more than enough to allow for evaporative cooling. One could even try to design the STIRAP process such that it directly creates the molecules in this protected state. The open shell molecules have the magnetic degree of freedom too, which might also be useful in tuning the intermolecular interactions. Since the loss shielding comes from crossing of energy levels, there might be a similar mechanism with magnetic levels. The importance and possible advantages of such magnetic tuning are under investigation, as pointed out the conclusion of Ref. [219].

The novel properties of the open-shell molecules favor experimentally interesting ways to engineer repulsive van-der-Waals interactions between molecules. This tuning option would allow for evaporative cooling of ground-state molecules. Protecting ground-state molecules from three-body loss and also cooling of bosonic ground-state molecules to quantum degeneracy has never been achieved, but with RbSr these goals are becoming realistic.

3.2. Dy-K quantum mixtures

The Dy-K system is a promising platform for analogue quantum simulation as it offers multiple possibilities to investigate species mixtures of different properties. Each element has bosonic and fermionic isotopes that are readily laser-cooled to the *s*-wave regime. Our interest falls on explorations of Fermi-Fermi and Bose-Fermi mixtures. The Dy-K mixture represents an important novelty compared to bi-alkali mixtures. It not only shows a moderate mass imbalance, but in addition the magnetic moments of Dy and K differ by an order of magnitude. Thus, experiments with the Dy-K mixture could shed light on more complex many-body phases and go beyond the research done with bi-alkali mixtures.

3.2.1. Mass-imbalanced Fermi-Fermi

Experiments with fermionic atomic gases make it possible to realize an accurate setting to explore highly correlated quantum systems and offer unique opportunities for precision investigation of quantum many-body phenomena [117]. Ultracold mass-imbalanced Fermi systems like Dy-K can provide an additional platform to test some of the non-perturbative theoretical approaches in the direction of unconventional superfluids and superconductors. The phase diagrams of different classes of unconventional superconductors look similar, but an accepted general theory of superconductivity is still elusive [118]. For example, the problem of an ultracold Fermi system with unequal spin populations is analogous to the

¹ In addition, their glass cell charges itself and limits the E-field control. The latter needs to be excellent, because the region of collision suppression is rather narrow.

physics of a superconductor that is under the influence of an external magnetic field, which causes a chemical potential difference between the two spin-states. In the regime of strong interactions between the two spin-states exotic quantum phases can emerge. With a mass imbalance in the fermionic mixture the expected exotic superfluid phases should be better pronounced, more stable and thus more probable to observe and investigate [27, 128]. The key factor for the successful investigation of such phases with a mass-imbalanced Fermi mixture is the availability of a relatively broad Feshbach resonance that can provide collisional stability in the strongly interacting regime [76, 130, 132].

To understand complex strongly interacting fermionic systems, it is important to know how pairing happens. When the mass and density of the two components in a Fermi mixture are identical (in the so-called symmetric case), at low temperatures a weak attractive interaction between two fermions with equal and opposite momenta at their Fermi surface leads to the formation of Cooper pairs. The Fermi mixture is then superfluid according to BCS theory. Furthermore, the ground state at zero temperature of a symmetric Fermi mixture remains a homogeneous superfluid throughout the BEC-BSC crossover (see Sec. 1.2.3). In the case of an asymmetry in density or mass of the two components their Fermi surfaces move apart, the well-understood Cooper pairing becomes more difficult and exotic pairing mechanisms or mixed phases could be observed for weak and strong interactions [27, 120, 126, 127, 220, 221]. The Fermi surface and corresponding deformations depend on the spatial dimension and periodicity of the quantum system. Here, I will concentrate on the three-dimensional homogeneous case².

A special motivation for the mass-imbalanced fermionic Dy-K mixture is the observation of inhomogeneous superconductivity. When the Fermi surfaces of the two components are separated, the formation of Cooper pairs with a nonzero total momentum should be possible. For this reason the pairing condition would vary in space, the ground-state is inhomogeneous and thus a periodic structure might be formed (a form of supersolid or a pair-density wave). Larkin and Ovchinnikov proposed such exotic pairing in 1964 [222], so it is sometimes referred to as LO state. At the same time Fulde and Ferrel considered a slightly different inhomogeneity [223], which is referred to as FF state. Often the resulting inhomogeneous state is described as a whole as an FFLO or LOFF state [126, 224]. The theoretical predictions on the existence and the stability of the FFLO phase in three-dimensions and on the type of phase transition to the FFLO phase differ depending on the calculation approach [120, 126, 128, 221, 224]. Since the interactions are strong, there is no exact analytical solution to the many-body problem, especially at $T \neq 0$. The numerical calculations are thus based on different approximations, like the mean-field model or density functional theory, and do not always agree with each other. Because the pairing of strongly interacting imbalanced Fermi gases is closely related to superconductivity [118, 225] and studies of quark and nuclear matter [119, 120], it is important to provide experimental access to this field.

The FFLO phase is expected to occupy only a thin layer of parameter space (if at all), so the experimental detection is quite challenging. The search for an experimental observation in equal-mass spin-mixtures is so far limited mostly by temperature [27, 226], but also by the use of a harmonic trapping potential, where a valid local-density approximation needs to be applied in order to compare to predictions for a homogeneous gas [126]. In mass-imbalanced mixtures with a majority of heavy fermions the parameter space for inhomogeneous pairing is supposed to be larger than for mass-balanced mixtures [27, 128, 227]. In addition, in

² Some of the theoretical predictions in this section do not consider the typical harmonic trap for the atomic ensemble.

the unitarity regime for a Fermi mixture with a mass ratio of four the superfluid transition temperature to the FFLO phase is expected to be higher than for the equal-mass mixture by at least a factor of two [227]. Moreover, one of the theoretical estimations states that an inhomogeneous superfluid phase can only exist in a mass-imbalanced Fermi mixture with a mass ratio > 3.2 [128]. The detection of an FFLO state would rely either on measuring the finite momentum of the Cooper pairs [228] or detection of periodic number density fluctuations of the minority component [224].

One of the other exotic superfluid phases predicted in an imbalanced (in other words polarized) Fermi mixture is the Sarma phase (also called breached-pair or interior-gap phase) [220, 229–231], where the superfluid and excess fermionic states phase-separate in momentum space. For a specific momentum range, which depends on the asymmetry in the system, the pairing does not decrease the many-body ground-state energy and the fermions in this momentum range (or momentum gap) remain a Fermi liquid. For the case of only spin-imbalance in the Fermi-Fermi system the Sarma phase exists only above $T = 0$ [230, 232], where the expected multiple Fermi surfaces would be smoothed away and the observation of the remaining bumps and dips in the momentum distribution is questionable. With a mass-imbalanced Fermi mixture, the Sarma phase can be stable down to $T = 0$. Moreover, with growing mass-ratio the region of the Sarma phase in the phase diagram expands to a broader interaction range [233] and its detection becomes realistic using noise correlations.

A different type of phase separation at unitarity (very strong interactions) is also predicted for a mass ratio > 3.95 [233], as in the case of Dy-K. For a sufficiently small polarization of the Fermi condensate the superfluid phase can occupy a shell region sandwiched between a normal inner core of the heavy species and a normal phase outer shell of the light species. This happens if each species experiences the same trapping potential and the local density approximation can be applied. Depending on the temperature and the polarization of the Fermi gas, the boundaries between the superfluid and the normal phases can be of the second or first order.

3.2.2. Dipolar fermionic systems

Dysprosium is the most magnetic atom and introduces dipolar properties into the Dy-K experiment. The long-range and anisotropic character of the magnetic dipole-dipole interactions can affect the properties of the quantum system on a many-body, as well as on a few-body level. The focus falls again on fermionic systems due to the suppression of inelastic collisions for strong short-range interactions [75, 76, 130]. Generally in a harmonic trap, dipolar fermions experience a deformation of the Fermi surface into an ellipsoid, as shown initially for Erbium [234]. Although the deformation of the Fermi surface is small [235], it could influence the exotic pairing mechanisms in the Dy-K fermionic mixture discussed above.

On a few-body level the Dy-K system is an interesting platform to study the interactions between heavy and light fermions and/or bosons. With a sufficiently broad interspecies Feshbach resonance one could associate the light fermion in our system, ^{40}K , with a heavy bosonic (fermionic) Dy into a weakly bound fermionic (bosonic) molecule and then investigate atom-dimer and dimer-dimer scattering properties [76, 130]. The strong magnetic moment of Dy introduces anisotropy in the Dy-K system and is interesting to compare the few-body effects to the non-dipolar Li-K system [129]. Furthermore, if the ensemble of weakly bound fermionic DyK molecules happens to be collisionally stable, one could attempt to reach quantum degeneracy with this dipolar system similar to the achievement of molecular

BEC [236]³.

Another outlook for investigations of fermionic systems would be the mixture of the two fermionic isotopes of dysprosium. Since identical dipolar fermions can form a p-wave BSC state [237], in a mixture of dipolar fermions with tunable interspecies s-wave interaction, it should be possible to observe the transition of the ground state of the system from two intraspecies p-wave superfluids (for $a = 0$) to one interspecies s-wave superfluid (for $a > 0$) [238]. The singlet and triplet pairs may also coexist. Up to now, a quantum mixture of dipolar fermions has been achieved with two spin-states of Erbium [239]. It was shown that despite the high density of Feshbach resonances the short-range interactions between the two spin-states can be tuned. However, the mixture has to be protected against dipolar relaxation by an optical lattice, for example. In a mixture of ^{161}Dy and ^{163}Dy in their lowest spin-states, dipolar relaxation is forbidden. With the appropriate experimental setup both Dy fermionic isotopes in their lowest spin-state can be simultaneously cooled and would thus allow for the investigation of dipolar fermionic superfluids.

3.2.3. Dy-K in an optical lattice

The ability to change the confinement of an ultracold gas with optical potentials provides further opportunities for the Dy-K system. The analog quantum simulation of condensed matter systems in optical lattices [19, 25] is possible with this mass-imbalanced mixture of fermions or bosons thanks to the multiple isotopes. The Dy-K mixture can become a platform for the investigation of the Bose-Fermi Hubbard model as well as for the asymmetric Hubbard model with light and heavy fermions [25]. Furthermore, an imbalance in the hopping amplitude between lattice sites due to the different mass of the fermions is suggested to increase the transition temperature to the antiferromagnetic phase in the Fermi-Hubbard model [240]. Additionally in our mixture, the magnetic moment of Dy opens the path towards dipolar systems and an extended Hubbard model, where the interaction is not limited to the nearest neighbor in the lattice [29], even if the magnetic dipole-dipole interaction is weaker than between electric dipoles of polar molecules, for example. And finally, for a dilute Fermi gas in an optical lattice the effective masses of the two species could be tuned independently with the lattice depth, which would allow for continuous variation of the mass ratio and can provide a platform for testing the many-body as well as the few-body theories described in the sections above. Although the investigation of quantum dynamics in optical lattices is not the main research motivation for the Dy-K experiment, a tunable optical confinement is technically available and can be used at any stage of the experimental procedure.

³ Producing open-shell molecules out of Dy and K is not a realistic goal, because the potential energy curves of DyK seem inscrutable, given the forest of energy levels in Dy.

Part II.

Sr-Rb mixtures

This part of the thesis presents my contribution to the research with the Sr-Rb experiment towards RbSr open-shell dipolar molecules. Important steps in the quantum engineering of RbSr molecules are developing appropriate cooling and trapping techniques and studying the scattering properties of the mixture. A major interest in this part falls on the highly efficient sympathetic narrow-line laser cooling of Rb by Sr, which led to the publication *Quantum degenerate mixtures of strontium and rubidium atoms* *Phys. Rev. A* **88**, 023601 (2013), Ref. [241]. It is a core component of the experimental procedure and shows the importance of interactions between the species. For the coherent creation of ground-state RbSr molecules via magnetic or optical association best possible knowledge of the molecular potential energy curves (PECs) is required. The investigation of the long-range side of the PEC of the RbSr ground-state using photoassociation (PA) spectroscopy is a major part of the publication *The RbSr $2\Sigma^+$ ground state investigated via spectroscopy of hot & ultracold molecules*, *Phys. Chem. Chem. Phys.* **20**, 26221 (2018), Ref. [242]. Further, we have developed a frequency-shifted feedback laser based on a tapered amplifier and an acousto-optic modulator, which can be implemented as a tool for efficient spectroscopic measurements on RbSr. This laser is presented in Ref. [243] and it would facilitate the search for a suitable STIRAP path to the absolute ground state of RbSr.

In Chapter 4 I will motivate the choice of the alkaline-earth element strontium and the alkali element rubidium for the experimental generation of open-shell polar molecules. The experimental setup is then presented in Chapter 5 with focus on specific features in the context of designing a generic experiment for well laser-cooled species of unlike properties. These features include the vacuum setup, the main cooling and trap-loading strategies and a summary of the frequency-shifted feedback laser as a spectroscopic tool. Chapter 6 consists of our publication on the experimental procedure for creating a Sr-Rb double BEC. In Chapter 7 the one and two-color PA spectroscopy measurements in a thermal sample of Sr and Rb are outlined. The newly determined interspecies scattering behavior is discussed regarding cooling and molecule production in the quest for a performable Sr-Rb isotopic mixture. Finally, the current procedure for the association of Sr and Rb to RbSr molecules is briefly presented⁴.

⁴ Since the Sr-Rb experimental setup moved in 2014 to the University of Amsterdam (UvA) from IQOQI Innsbruck, I continue to be up-to-date with the measurements on the Sr-Rb experiment and the current experimental work of the Sr-Rb team.

Properties of Sr and Rb

The main motivation for the Sr-Rb experiment is to explore RbSr dipolar molecules. We wish to produce an ultracold ensemble of open-shell polar molecules as a basis for quantum computing and investigations of novel quantum states. Strontium persuades with excellent laser-cooling properties and rubidium is the prevalent species in ultracold experiments. The interactions between the Sr and Rb atoms and the RbSr molecules are non-trivial, yet essential for the realization of quantum degenerate gases of open-shell polar molecules.

4.1. Why Sr?

Strontium is an alkaline-earth element with favorable laser cooling properties. In Fig. 4.1 we see the strontium level scheme, which is on the one hand rich with singlet and triplet states and on the other hand simple, due to the highly symmetric ground state. The intercombination line of strontium is near 689 nm and delivers the foundation of narrow-line magneto-optical traps (MOTs) (see Sec. 2.3.2). The broad singlet optical transition is near 461 nm, which is a more advantageous wavelength for lasers and optics than the UV transitions of other alkaline-earth elements like calcium or barium. Another good candidate, similar to strontium, is ytterbium. However, we choose Sr as the narrow-line MOT of Yb uses a broader optical transition ($\Gamma_{556} = 2\pi \times 182$ kHz vs. $\Gamma_{689} = 2\pi \times 7.4$ kHz in strontium) near 556 nm, which leads to higher MOT temperatures and for which diode lasers are not available.

Strontium has many isotopes with different natural abundance. The bosons ^{84}Sr , ^{86}Sr and ^{88}Sr are non-magnetic in the ground state, hence there are no intraspecies magnetic Feshbach resonances. The hyperfine structure of the fermionic isotope ^{87}Sr could deliver extremely narrow Feshbach resonances [190], but the main tool for interaction tuning is to use isotopic mixtures [245]. Simultaneous work with two or more isotopes is possible even with a single laser system thanks to the small isotope shifts of the main optical transitions (see Sec 5.3.2). Note that the small isotope shift of less than 270 MHz in the 461 nm-transition in Sr contrasts the situation with the alkali atoms. In Li, for example, the isotope shift in the D2 and D1 lines between ^6Li and ^7Li is about 10 GHz [246] and separate laser systems are needed for simultaneous work with both isotopes.

Nowadays we can refer to strontium as a well-known laser-cooled species. A lot of the groundwork on techniques to cool strontium to quantum degeneracy and further investigation of the properties of all stable Sr isotopes has been performed by our group on the same apparatus now used for Sr-Rb mixtures [190, 245, 247]. A recapitulation on all cooling techniques for strontium can be found in the review [245].

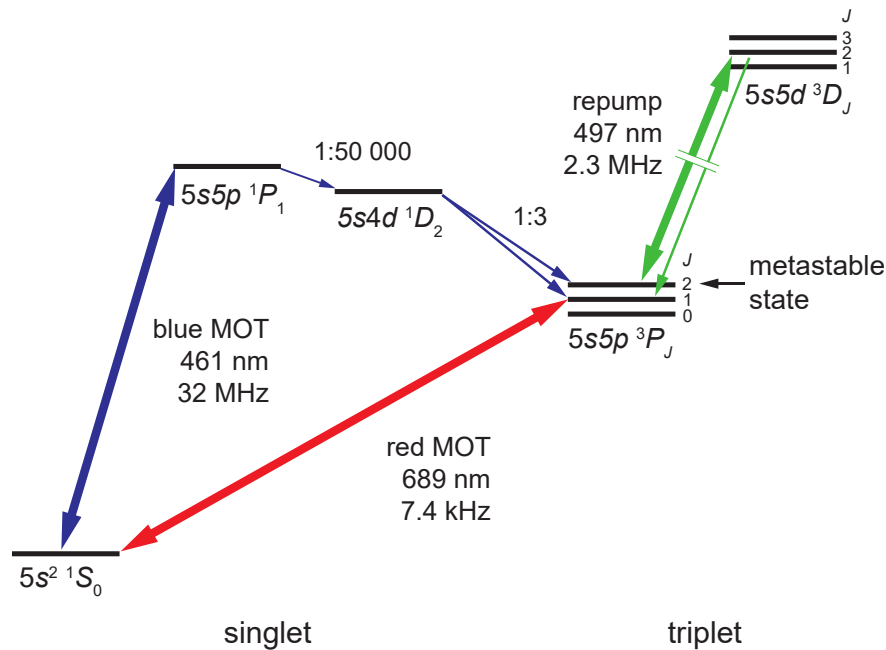


Figure 4.1.: Sr level scheme. The laser-cooling from oven to MOT operates near 461 nm. The decay channel from the blue MOT to the triplet states allows to collect atoms in the metastable state in a magnetic trap. Those atoms are afterwards optically pumped with a green pulse of light near 497 nm into the narrow-line MOT at 698 nm. From Ref. [244].

An important step in the laser cooling of strontium is the magnetic atom reservoir filled during the blue MOT stage. The blue MOT cycle is not closed. Decay channels lead to the metastable 3P_2 state (see Fig. 4.1), which has magnetically trappable sub-states. Atoms in these states do not interact with the MOT light and accumulate until the end of the blue MOT phase. A narrow-line red MOT, applied after repumping the reservoir atoms into the ground state, delivers higher atom numbers than a red MOT after a continuously repumped blue MOT [248]. The other crucial step in the production of degenerate quantum gases of strontium is the choice of isotope. Evaporative cooling of strontium to quantum degeneracy was first achieved with the least abundant isotope ^{84}Sr , which is the only strontium isotope with favorable scattering length for efficient evaporation ($a_{s^{84}\text{Sr}} = 123 a_0$) [244]. The natural abundance of $< 1\%$ highlights again the importance of the magnetic reservoir between the two MOT stages.

For ^{84}Sr the narrow 689 nm-line and the favorable scattering properties have allowed for the production of a BEC by using only laser-cooling to remove the entropy from the gas [174]. Strontium has also been loaded into an optical lattice where ground-state Sr_2 molecules have been created via photoassociation [249]. The Sr_2 molecule production has been later on optimized [208]. This technique shows the possibility of purely optical molecule formation in the case of unavailable magnetic Feshbach resonances.

The fermionic isotope ^{87}Sr with nuclear spin is an especially interesting isotope. The nuclear spin opens an ultra narrow optical transition near 698 nm, which is used as frequency reference in the most precise atomic clocks in the world [250, 251]. The narrow-line MOT near 689 nm is an ideal source of cold Sr atoms, as temperatures below 1 μK can be reached directly by laser cooling and a single experimental run is quicker, which facilitates repeated precision measurements. The lack of electronic spin in ^{87}Sr leads to decoupling between

the nuclear and electronic degrees of freedom and gives rise to $SU(N)$ -symmetric two-body interaction between the N different spin components [252]. The cooling of the fermionic isotope and the detection and manipulation of the different spin states through optical Stern-Gerlach separation and optical pumping is a further achievement in the early days of the Sr-Rb experiment [253].

The many available isotopes, the convenient Doppler cooling to low temperatures, the presence of metastable states, and the rich experience that our group has with this element make strontium an optimal candidate for ultracold open-shell polar molecules.

4.2. Why Rb?

Rubidium is the ‘workhorse’ of the ultracold community. It is relatively easy to produce a Rb vapor, as the necessary vapor pressure for the oven is reached at temperatures below 100°C . The optical D2 transition near 780 nm is convenient for Doppler and sub-Doppler laser cooling. Laser light with sufficient power can be generated by Ti:Sapph lasers or diode lasers (with subsequent amplification using tapered amplifiers), or through frequency doubling from the infrared spectrum at 1560 nm. Most importantly, ^{87}Rb has excellent scattering properties with a background scattering length of about $100 a_0$ over a vast range of magnetic fields [254]. ^{87}Rb can be trapped and evaporatively cooled in magnetic or optical traps. The well-established technique to create BECs of ^{87}Rb lead to rubidium being successfully implemented as sympathetic coolant in many experiments [45, 255], even as a possible molecule coolant [256].

Next to ^{87}Rb , the other abundant and stable Rb isotope that is commonly used in ultracold gas experiments, is ^{85}Rb . The advantages of the vapor pressure and the availability of light sources for laser-cooling remain also for this isotope. The disadvantage of ^{85}Rb is the large and negative background scattering length of about $-400 a_0$. Nevertheless, with the application of a Feshbach resonance to tune the interactions, this isotope can also be successfully brought to quantum degeneracy [257]. The possibilities to tune the interactions of and between different spin states of ^{85}Rb are well-studied [258]. Therefore ^{85}Rb is a valuable alternative to the ‘user-friendly’ ^{87}Rb isotope.

RbSr is the straightforward choice for an alkali-metal/alkaline-earth molecule, not only because of the favorable cooling properties of each species separately. An important parameter for the choice of elements is the electric dipole moment that can be obtained in the ground state of the heteronuclear molecule. The electric dipole moments of the alkali-metal-atom-Sr molecules (ASr) molecules have been calculated in [259] and Figure 4.2 shows the potential energy curves for all those open-shell-molecules. Only CsSr with 1.9 D has a larger dipole moment than the 1.5 D of RbSr [260] (1 Debye $\simeq 3.335 \times 10^{-30}$ C m). An advantage of Rb over Cs is the availability of two bosonic isotopes, which gives a higher chance of finding good scattering properties in a mixture with Sr. Compared to more light-weighted molecules, e.g. LiSr, RbSr has a smaller energy splitting between rotational levels. The smaller energy splittings result in lower electric fields needed to fully polarize the molecules [29]. Note, that all ASr molecules are unstable against decay $2\text{ASr} \rightarrow \text{A}_2 + \text{Sr}_2$. The options for avoiding RbSr losses through such chemical reactions are to implement an optical lattice during the formation of the molecules (see Sec. 7.2) or to engineer repulsive intermolecular interactions Sec. 3.1.2.

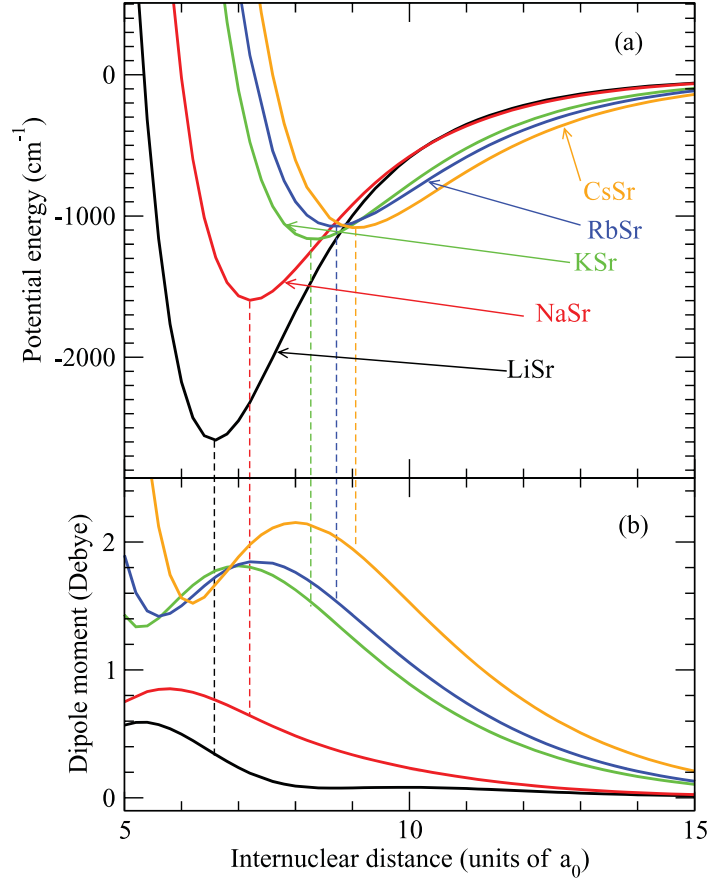


Figure 4.2.: Potential energy curves (a) and permanent electric dipole moments (b) for the ground state of alkali-metal-atom-strontium dimers. Vertical lines guide the eye to locate the value of the dipole moment at the equilibrium distance. From Ref. [259].

4.3. Sr-Rb interactions

In at least one isotopic combination of Sr and Rb we hope to see favorable inter-species interactions for cooling and further molecule creation. The presence and exploitation of Feshbach resonances in the Sr-Rb system is not self-evident. Bosonic Sr has a singlet ground state and no nuclear spin. The effective interaction operator between Rb and Sr does not contain any strong coupling between the atomic and molecular states. Some coupling is necessary for tuning of the scattering interactions with magnetic fields as in the case of two alkali atoms by Feshbach resonances (see Sec. 2.2). A weak coupling term comes from the Rb hyperfine coupling constant being modified by the presence of Sr [260]. Thereby Feshbach resonances with widths on the order of 1 mG to 10 mG at fields up to 2 kG have been predicted [260].

Recently, for the first time this type of Feshbach resonance was detected in the Sr-Rb experiment in a mixture of ^{88}Sr and ^{87}Rb [150]. The resonance is observed at 366 G through an atom loss feature with a width of about 50 mG. Also Feshbach resonances between the fermionic ^{87}Sr and ^{87}Rb were found. There, an additional coupling mechanism between the nuclear spin of fermionic Sr and the valence electron of Rb increases the density of Feshbach

resonances [150]. With the presence of Feshbach resonances magnetic fields could be used to tune molecular bound states across atomic thresholds. We wish to exploit that for the production of RbSr molecules.

Sr-Rb machine

The experimental setup for the Sr-Rb mixture is an upgrade of a machine that has proven highly efficient for the cooling of strontium alone. The vacuum apparatus in the Sr-Rb experiment is a copy of another ultracold mixture machine from our group, FeLiKx (Fermionic Lithium-Potassium-X). The FeLiKx machine was built for ${}^6\text{Li}$, ${}^{40}\text{K}$ and ${}^{87}\text{Sr}$ and is the first apparatus designed to combine alkali and alkaline-earth metals [261]. The experimental Sr-Rb apparatus is described in detail in the theses of E. Wille [261], S. Stellmer [190] and A. Bayerle [262]. Here, we will have a closer look on the special aspects of the vacuum setup and on the experimental procedure owing to the Sr-Rb mixture.

5.1. Vacuum setup and precooling

Every ultracold experiment starts very hot indeed. The single atoms come from the atomic vapor of solid or liquid samples of the metal, which are heated up in the oven part of the vacuum chamber. The operational oven temperature T is determined by the vapor pressure p , which is in a different range for alkali and non-alkali elements. This can be seen in the expression for the vapor pressure, called Antoine equation [263]:

$$\log_{10} p = A - \frac{B}{T}, \quad 5.1$$

where the coefficients A and B are about a factor of 2 higher for alkaline-earth elements than for alkali-metals [263].

The multispecies oven in the Sr-Rb vacuum apparatus is the same as in FeLiKx. The special design shown in Figure 5.1 is manufactured by the mechanical workshop of IQOQI Innsbruck. Each of the three possible elements has its own reservoir and its own microtube array, which gives a collimated beam in the direction of the Zeeman slower. This way the elements don't have the chance of mixing and undergoing chemical reactions already in the oven, where the densities are high. The segments are rotated by 120° and attached to each other with the coldest oven furthest and the hottest closest to the Zeeman slower. The strength of this oven design is that the collimation tubes are very close to each other, so that each element effuses along the Zeeman slower axis. Also the separate segments allow for vastly different operation temperatures of the oven. With this oven design, the use of an expensive enriched sample (of fermionic potassium for example) would not be wasteful. Nevertheless, as in older multispecies ovens for alkali-metal mixtures [264] or as in newer alkali-non-alkali ovens [265, 266] the limit in temperature is given by the copper gaskets that are sealing the vacuum and is approximately 550°C . In the Sr-Rb machine, the Rb oven section is at 200°C followed by the Sr oven section at 550°C .

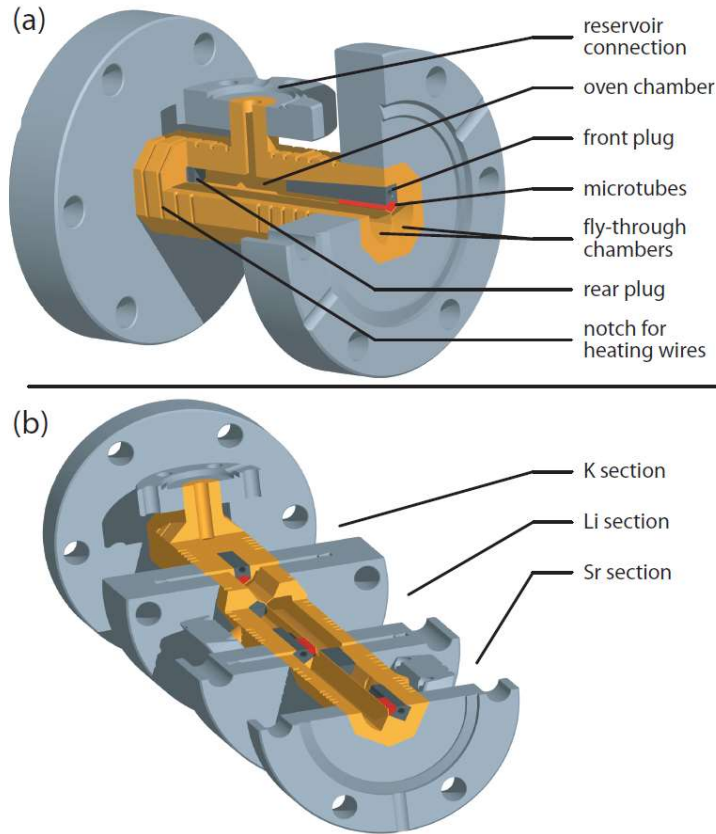


Figure 5.1.: Multispecies effusive oven. Figure (a) shows the details of a single oven section. Figure (b) shows three oven sections mounted together for the FeLiKx experiment. From Ref. [261].

The next important piece of the setup, where the species' properties come into play, is the Zeeman slower (ZS). The atoms leave the oven through a bundle of tubes, so that their velocity is mostly in the direction of the ZS. In the slower those atoms are decelerated by applying a strong light force from the opposite direction. In order for the single frequency laser to be constantly on resonance with the decelerating atoms, a magnetic field is used to compensate for the changing Doppler shift. The deceleration is approximately constant along the ZS and depends on the wavelength of the optical transition, its transition linewidth, the mass of the atom and on the laser intensity. For a constant deceleration the velocity will change like the square root of the position in the slower and also the magnetic field has to have a square root dependence on position [176]. The optimal ZS for a dual species experiment is always a compromise [265]. Since the Sr-Rb machine inherited the vacuum design from FeLiKx it was already fitting a mixture of alkali and alkaline-earth elements [261]. Rubidium has similar optical properties to potassium, but is twice as heavy, hence it requires a longer ZS [265]. The length of the Zeeman slower cannot be changed once constructed, but the strontium ZS has a 15 cm long zero-field region, where the glass cell is connected to the steel construction via bellows. In this region a coil delivering high fields, necessary for Sr or Li, isn't practical because of the large coil radius enforced by the size of the bellows. However, Rb requires only low fields and the ZS can be effectively prolonged by eliminating the zero field region, by adding a coil around the bellows. The resulting Sr-Rb ZS coil setup can be

seen in A. Bayerle's thesis [262]. Since the magnetic fields required to slow Sr and Rb differ significantly, the loading of the two species into a conservative trap is performed sequentially.

The ZS light enters the Sr-Rb machine through a special viewport. It has a broadband antireflection coating for 450 nm to 800 nm and is made of sapphire so it can be heated safely up to 250 °C. This viewport is kept at 150 °C to avoid the high flux atomic beam deposition onto the window, which would slowly turn into a reflective metal layer and degrade the Zeeman slower performance. S. Stellmer reports in Ref. [190] on the window being unintentionally left cold for a week, which led to a slight coating. Once a significant layer of strontium atoms deposits on the window, they cannot be removed at temperatures within the viewport specifications. A solution to this issue is to have a metal mirror inside the vacuum, as will be presented in part III, Chapter 9. The coating of the entrance window for the ZS light with atoms is one of the reasons why an atomic beam shutter is necessary in the setup. This shutter is a mechanical barrier that covers the opening of the oven. The atomic beam shutter is also a protection when producing quantum degenerate samples in the main chamber. Otherwise the very hot atoms will fly through the sample.

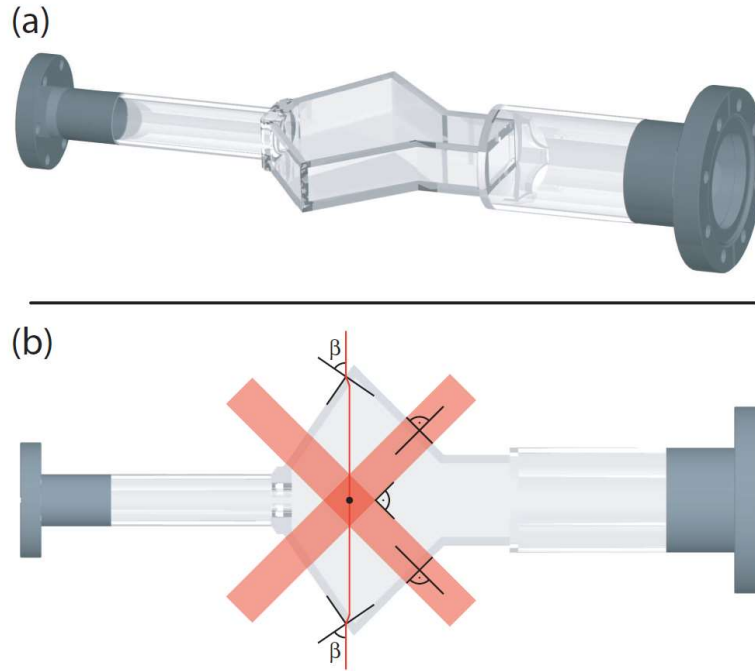


Figure 5.2.: Sr-Rb main chamber. Figure (a) shows the glass cell with vacuum connections. Figure (b) shows a top view of the glass cell with the perpendicular MOT beams and the optical dipole trap beam under Brewster angle β . From Ref. [261].

After the precooling in the ZS, the atoms are captured by a MOT in an ultra-high vacuum chamber. In the case of FeLiKx or Sr-Rb, all species come from one direction, so it is practical to use a glass cell as the main chamber. Figure. 5.2(a) shows the glass cell with the different vacuum flanges on both sides. The smaller one connects to the Zeeman slower by bellows, while the larger flange connects to the vacuum pumps for better pumping speeds. A glass cell is fragile under the pressure of keeping ultra-high vacuum, so to reduce stress on it in the Sr-Rb experiment it is fixed only on the pump side of the vacuum setup. The bellows on the other side of the glass cell is supported from the bottom by a spring. With

more than two vacuum connections, a glass cell setup requires a more complex suspension and still has a high risk of breaking.

It is crucial for ultracold experiments to have good optical access from many different directions. An obvious advantage of a glass cell is the nearly unlimited optical access. The number of laser beams for trapping, manipulating and imaging the atoms grows with the number of species involved and with the complexity of the experiment. Because of the many different wavelengths needed in FeLiKx and Sr-Rb, this particular glass cell is not antireflection-coated. However, as shown in Fig. 5.2(b), it has a specific shape, in order to allow near Brewster angle entrance for dipole trap lasers, so at least there the reflectance is smaller. Another advantage of a glass cell is that the lack of metal parts prevents eddy currents from limiting the switching speed of the magnetic field coils. Furthermore, around the compact glass cell from Fig. 5.2 it is possible to place coils or antennas closer to the atoms than around a massive steel vacuum chamber.

5.2. Magnetic field coils and control

The precise control of magnetic fields in the glass cell of the Sr-Rb apparatus has a twofold importance. First, the position of the narrow-line strontium MOT and therewith the loading efficiency into the optical dipole trap are very sensitive to magnetic fields. Therefore, the center of the quadrupole magnetic field is regularly adjusted in all three directions via so-called compensation coils [190]. These coils are wound around a rectangular frame, which is on the order of 1 m long in each direction and ensures homogeneity in the center of the glass cell.

The second reason why the control and stability of the homogeneous magnetic field are crucial in the Sr-Rb experiment is that the measured Feshbach resonances between Sr and Rb are mostly narrower than 10 mG at fields above 300 G [150]. Thus, for the association of Sr and Rb atoms into weakly bound RbSr molecules the control of the homogeneous field has to be exceptionally precise. The main coil system around the glass cell in the Sr-Rb apparatus is the same as in the FeLiKx setup. These coils are constructed out of square copper tubes, allowing for efficient water-cooling, since they are designed for homogeneous fields up to 4000 G with currents up to 1200 A [261]. The same coil pair is used for generating the magnetic gradient field for the MOT as well as the homogeneous magnetic field for Feshbach association by switching the current configuration through the coil pair with relays. The coil pair has roughly an inductance $L \approx 300 \mu\text{H}$ and a resistance $R \approx 27 \text{ m}\Omega$, which gives a lower limit for the magnetic field rise time with a time constant of $\tau_{\text{coil}} = L/R \approx 12 \text{ ms}$. The Sr-Rb team has developed a high-performance magnetic field stabilization scheme with 10ppm long-term stability, 5ppm accuracy and noise below 1ppm [267]. The power source for the setup is a stack of batteries, which reduces the noise from the mains electrical system. The setting of the current through the magnetic field coil is performed with a digital controller¹. The signal of a current transducer is processed by the digital feedback, which controls the gate voltage of a parallel stack of MOSFETs. The magnetic field system has multiple monitors and security switches.

¹ The digital controller was developed in the electronic workshop of the University of Amsterdam, Faculty of Sciences

5.3. Laser systems

The Sr-Rb experiment requires a multitude of wavelengths for cooling and trapping of both species. I present a short review of the used continuous-wave laser systems, which have been described in previous theses [190, 262, 268]. Further, I will introduce the frequency-shifted feedback (FSF) laser based on a tapered amplifier, which was developed in our group as possible spectroscopic tool and resulted in publication [243].

5.3.1. Rb lasers

Rubidium is commonly laser-cooled and suitable laser sources are readily available. In the Sr-Rb experiment, the Rb laser sources are external cavity diode lasers (ECDLs), both for cooling and repumper light near 780 nm. Both ECDLs are referenced to a Doppler-free saturated-absorption signal of ^{87}Rb using a single spectroscopy vapor cell. The cooling light on the D2 $F = 2 \rightarrow F' = 3$ transition is amplified by a tapered amplifier (TA) and is used for ZS, 3D MOT and imaging. The Rb laser system is presented in A. Bayerle's PhD thesis [262, Chapter 2.2].

5.3.2. Sr lasers

The laser-cooling of strontium was partly developed at this very same experiment (see Sec. 4.1) before rubidium was introduced. All laser setups for cooling of strontium are presented in S. Stellmer's PhD thesis [190, Chapter 3.5]. The light near 461 nm from an SHG-laser system is used for ZS, transverse cooling, MOT and imaging. Together with the 689 nm light for the narrow-line MOT, both are referenced to the respective atomic transition in a spectroscopy cell, operated at 340 °C. The line-width of the master ECDL, addressing the $\Gamma_{689} = 2\pi \times 7.4$ kHz transition, is reduced to about 2 kHz using the Pound-Drever-Hall lock [269] to a high-finesse cavity. The green laser light, which used to repump the dark atoms in the magnetic trap from the blue to the red 3D MOT, has a wavelength near 497 nm. The reference for its frequency stabilization is an ultra-low expansion cavity.

	^{88}Sr	^{87}Sr	^{86}Sr	^{84}Sr
$^1S_0 - ^1P_1$	0	-46.5 MHz	-124.8 MHz	-270.8 MHz
$^1S_0 - ^3P_1$	0	-62.15 MHz	-163.81 MHz	-351.49 MHz

Table 5.1.: Isotope shifts of the main optical transitions in strontium referenced to the most abundant isotope ^{88}Sr . The shift for the fermionic isotope ^{87}Sr is given here for an assumed $J = 0$ state, while the hyperfine structure spans over a few GHz. From Ref. [190].

A specialty of strontium is that the optical transitions have small isotope shifts. The values are presented in Table 5.1. In the blue, for example, all isotopes can be covered in a frequency range of 270 MHz. The small frequency differences allow for fast switching between isotopes in the experiment and most importantly for simultaneous work with two or more isotopes with a single laser system. The blue transition demands high laser power, so the small frequency shifts are advantageous for it. In the Sr-Rb setup the error signal for the laser stabilization of the 461 nm and 689 nm laser systems comes from the most abundant ^{88}Sr isotope and the respective operation laser frequency is shifted by acousto-optical modulators (AOM). These shifts by AOM can be controlled electronically and introduce a considerable tunability of the setup.

5.3.3. TA comb for spectroscopy

The path to RbSr molecule creation contains extensive spectroscopic investigations of the molecular potentials. A faster way of covering a broad spectroscopy range would be to implement a frequency comb. For this the laboratory doesn't have to be equipped with an actual expensive frequency comb, as we show in *SciPost Phys.* **1**, 002 (2016) (see Appendix A). We developed a simple and inexpensive frequency-shifted feedback (FSF) laser, based on a TA and an AOM, which spans a frequency range of hundreds of GHz.

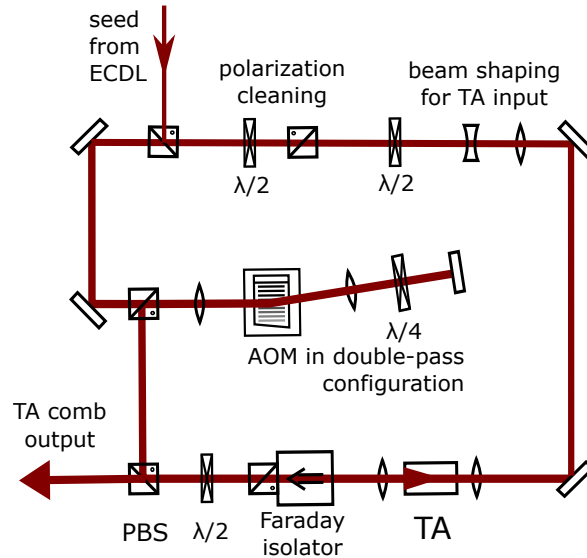


Figure 5.3.: Frequency-shifted feedback (FSF) laser based on a TA as a gain medium and an AOM as a frequency shifting element. With the AOM in a double-pass configuration, the spacing between the comb lines can be tuned in addition to the TA comb properties presented in Appendix A.

The basic idea of our TA comb is to implement a frequency shifting element in a ring cavity. Figure 5.3 shows the initial experimental setup of the FSF laser with tunable spacing of the comb frequency components. The seed laser, which can be frequency locked, is an ECDL with a carrier frequency f_{seed} and is sent into a TA chip. Part of the output of the amplifier is frequency-shifted with an AOM in a double-pass configuration to allow for changes in the frequency shift without a change in the beam path. The light propagating through the double-pass AOM is shifted in frequency by $2 \times f_{\text{AOM}}$ and sent back into the TA input together with the seed. We thus generate an output spectrum of the FSF laser with hundreds of sidebands with a controllable spacing via the AOM. The power distribution and the number of sidebands with frequency $f_n = f_{\text{seed}} + n \times 2f_{\text{AOM}}$ can be optimized by tuning the seed power and the AOM frequency. The spectral width of each sideband is given by the spectral width of the seed laser. The width and center frequency of the optical spectrum as well as the maximum available power of the FSF laser depend on the specifications of the chosen TA chip. The characterization of the FSF laser system in Appendix A compares the output of the FSF laser with and without an external seed laser for a fixed AOM frequency. The measurements demonstrate the comb character of the output of the seeded FSF laser in contrast to a modeless broadband emission of an unseeded FSF laser consisting of a TA chip and an AOM alone. An inexpensive comb such as the one from Fig. 5.3 is well-suited for spectroscopy of the molecular potentials of RbSr.

5.3.4. Infrared and green optical traps

The far-off-resonant lasers for optical trapping of the cold atoms have different requirements than the resonant lasers. They should have a high power output with a single spatial mode and a clean linear polarization, but do not need to be frequency stabilized. For a better control of ultracold atoms a stabilization of the laser power is of advantage. In the Sr-Rb experiment we use a 100 W fibre laser² at 1070 nm for the storage optical dipole trap (ODT) in a single beam configuration. Two 5 W fibre lasers³ operating at 1065 nm create the science dipole trap in a crossed beam configuration. The laser source for an optional green ODT is a solid state laser⁴ operating at 532 nm with a maximum output power of 8 W. A cubic optical lattice is created by another solid-state laser⁵ operating at 1064 nm with an output power of 48 W. The setups of the ODTs and lattice laser beams change in the course of the experimental investigations, since the production of RbSr molecules is tricky (see Sec. 7.2).

5.4. Loading into traps

Many dual-species experiments require a sequential cooling and loading scheme, since the optimal conditions for the two components are incompatible. In the Sr-Rb machine the incompatibility manifests in almost all cooling steps: Zeeman slower field strength and profile [262], magnetic field gradient for MOT and MOT shape for loading into the ODT (see Sec. 6.3). Even if the ZS fields of the two elements didn't differ, the combination of rubidium and strontium in a MOT would not deliver optimal performance because of the conflicting magnetic field gradients. The cooling of strontium starts with a rather high gradient of 55 G/cm in the blue MOT for 2 s to 10 s, mostly because the quadrupole field serves as a trap for the metastable 3P_2 state (see Fig. 4.1). After switching off the blue light and re-pumping the atoms to the ground state, the narrow-line red MOT is operated at a gradient of 1.8 G/cm. The cooling of rubidium, on the other hand, begins in a (collection) MOT with a magnetic field gradient of 12 G/cm, rising to 50 G/cm in the compressed MOT, which takes only hundreds of milliseconds. The main difference in the laser cooling of Rb and Sr is the linewidth of the corresponding cooling transition. It defines the shape of the MOT and thus influences the overlap with a dipole trap, which is essential for ODT loading. The initial temperatures of both species in the dipole trap are also different and demand correspondingly different trap depths. Thus an optimal scheme for the sequential loading of both species in the same dipole trap has to be developed.

² YLR-100-LP-AC-Y12 from IPG

³ YLD-5-LP from IPG with a specified linewidth of 0.5 nm

⁴ Verdi-V8 from Coherent

⁵ Mephisto MOPA from Coherent

Quantum degenerate mixtures of strontium and rubidium atoms

Published as Ref. [241]:

Benjamin Pasquiou, Alex Bayerle, Slava M. Tzanova, Simon Stellmer, Jacek Szczepkowski, Mark Parigger, Rudolf Grimm, and Florian Schreck

Phys. Rev. A **88**, 023601 (2013)

©[2013] American Physical Society

We report on the realization of quantum degenerate gas mixtures of the alkaline-earth element strontium with the alkali element rubidium. A key ingredient of our scheme is sympathetic cooling of Rb by Sr atoms that are continuously laser cooled on a narrow linewidth transition. This versatile technique allows us to produce ultracold gas mixtures with a phase-space density of up to 0.06 for both elements. By further evaporative cooling we create double Bose-Einstein condensates of ^{87}Rb with either ^{88}Sr or ^{84}Sr , reaching more than 10^5 condensed atoms per element for the ^{84}Sr - ^{87}Rb mixture. These quantum gas mixtures constitute an important step towards the production of a quantum gas of polar, open-shell RbSr molecules.

Author contribution

The author of the present thesis helped with data taking and analysis, and contributed to the writing of the article.

6.1. Introduction

Quantum degenerate gas mixtures of different chemical elements have opened up important new areas for the study of interacting quantum systems. The possibility to apply species-specific optical potentials [24] is a versatile tool and has for example been used to study the exchange of entropy between two gases [270] or mixed-dimensional systems [271]. The mass difference between the constituents of the mixture can lead to new few- and many-body phenomena [43, 272], such as novel trimer states [273, 274] or crystalline quantum phases [275]. Quantum gas mixtures of two elements have also attracted a great deal of attention because they are an ideal starting point for the coherent production of heteronuclear ground-state molecules, which can have large electric dipole moments [14, 111, 276]. The dipole interaction can dominate the behavior of a quantum gas of these molecules and lead to intriguing many-body phenomena [29–32]. Ultracold polar molecules also provide insights into chemistry at the quantum level and have the potential to be used as sensitive probes for variations of fundamental constants or as the basis of quantum computation schemes [14, 115].

Most experimentally investigated quantum gas mixtures of two elements consist of two alkali metals [47, 49, 86, 277–280]. Advances in producing quantum degenerate samples of Yb [281] and alkaline-earth elements [244, 282, 283] have led to efforts towards mixtures containing these elements and recently quantum degenerate Yb-Li mixtures were obtained [96, 284]. A driving force behind these efforts is the interest in quantum gases of polar molecules beyond alkali dimers, such as RbYb [98], LiYb [96, 284], or RbSr [94]. Contrary to alkali dimers, these open-shell molecules possess an unpaired electron, which provides them with a rich spin structure and a magnetic dipole moment. This property will enable new ways to design and control few- and many-body systems and could prove very useful to implement lattice-spin models [213], to suppress inelastic collisions [285], to imprint geometrical phases [286], or to study collective spin excitations [287].

In this Article, we present the realization of quantum gas mixtures composed of the alkali metal ^{87}Rb and the alkaline-earth metal ^{88}Sr or ^{84}Sr . An essential ingredient of our experimental strategy is the use of sympathetic laser cooling [46, 288, 289] on a narrow linewidth transition, which allows us to reach a high phase-space density (PSD) for both elements before evaporative cooling. Strontium atoms are laser cooled on the narrow $^1\text{S}_0 \rightarrow ^3\text{P}_1$ intercombination line and act as a refrigerant for Rb confined in an optical dipole trap. During this sympathetic laser cooling stage, the PSD of Rb increases by a factor of more than 200, with only a 20% reduction of the Rb atom number. In less than 400 ms the PSD of both elements can reach 0.06. These very favourable conditions allow us to efficiently reach quantum degeneracy for both species by evaporative cooling and to create BECs with more than 10^5 atoms per element. The ease of producing large quantum degenerate samples enabled by sympathetic narrow-line laser cooling, together with the large electric dipole moment of RbSr ground-state molecules of 1.5 Debye [259], make Sr-Rb quantum gas mixtures an ideal stepping stone towards the exploration of dipolar physics with open-shell molecules.

The organization of this paper is as follows. In Sec. 6.2, we present an overview of our scheme. Section 6.3 describes the loading of a cloud of Rb into an optical dipole trap, followed by the loading of Sr atoms into a narrow-line magneto-optical trap (MOT). Section 6.4 focuses on our sympathetic narrow-line laser cooling scheme. In Sec. 6.5 we describe the final evaporative cooling stage and the production of two different quantum degenerate mixtures, a ^{88}Sr - ^{87}Rb and a ^{84}Sr - ^{87}Rb double BEC.

6.2. Overview of the experimental strategy

To reach quantum degeneracy, most ultracold atom experiments rely on laser cooling followed by evaporative cooling. The latter process intrinsically leads to a loss of atoms. To minimize this loss, it is beneficial to develop laser cooling methods that are able to reach high PSDs. The main atomic transition for laser cooling of alkalis, such as Rb, is broad, on the order of several MHz. To achieve high PSDs by laser cooling of such species, one can apply sub-Doppler cooling techniques, such as polarization gradient cooling in optical molasses [165–169, 290], velocity selective coherent population trapping [291], Raman cooling [162], Raman sideband cooling [292], or narrow-line cooling on transitions to higher electronic states, which have linewidths down to the 100 kHz range [181, 293]. The best PSD achieved so far by laser cooling of an alkali is to our knowledge 0.03 [294]. As a member of the alkaline-earth family, Sr has a singlet/triplet electronic structure. Its $^1S_0 \rightarrow ^3P_1$ intercombination line has a width of only 7.4 kHz. It has been shown that simple Doppler cooling using this narrow line can reach temperatures as low as 250 nK [180]. A PSD of 0.1 has been reached by transferring Sr clouds from a narrow-line MOT into an optical dipole trap [247, 295]. Starting from such samples, evaporative cooling can produce BECs that contain 25% of the initial atoms, much more than the 1% typical for alkali BEC experiments. It is therefore tempting to transfer those excellent properties to other species, by using Sr as a cooling agent. Here we demonstrate the efficiency of sympathetic cooling of Rb with Sr atoms laser cooled on a narrow line and the formation of dual-species BECs by a consecutive evaporative cooling stage.

Our procedure to achieve quantum degeneracy can be divided into three main stages, see Fig. 6.1(a). During the first, “preparation” stage (Sec. 6.3) we use well-established cooling and trapping techniques to prepare ultracold samples of Rb and Sr. We accumulate Rb atoms in a magneto-optical trap and transfer them into a single beam optical dipole trap, henceforth referred to as the “storage” trap. After having stored Rb, we operate a “blue” Sr MOT, thereby accumulating metastable Sr atoms in a magnetic trap. We then optically pump Sr back to the ground state and capture the atoms in a “red”, narrow-line MOT, see Fig. 6.1(b). During the second, “sympathetic laser cooling” stage (Sec. 6.4) we sympathetically cool the Rb cloud by ^{88}Sr atoms that are continuously laser cooled to a few μK on a narrow linewidth transition. We then transfer Rb and either ^{88}Sr or ^{84}Sr into a second, “science” dipole trap, see Fig. 6.1(c). During the last, “evaporation” stage (Sec. 6.5) we perform evaporative cooling, where Sr sympathetically cools Rb until quantum degeneracy is reached for both elements.

6.3. Preparation of an ultracold sample of rubidium and strontium

In this Section, we describe our experimental setup and the preparation of an ultracold mixture consisting of Rb contained in the storage trap and Sr stored in a narrow-line MOT, see Fig. 6.1(b).

Our experimental setup is based on our Sr BEC apparatus, which has been described in detail in [190, 247]. The basic principle of the apparatus is to capture a Zeeman slowed atomic beam in a MOT and to cool the gas to quantum degeneracy by evaporation out of a dipole trap. Here we will focus on the upgrades carried out to also trap and cool Rb with the apparatus. Copropagating atomic beams of each element are produced by two independent ovens, heated to 550 °C for Sr and 200 °C for Rb [190, 261]. The same Zeeman slower (ZS) is used to slow both beams. Since the magnetic fields required to slow Rb and

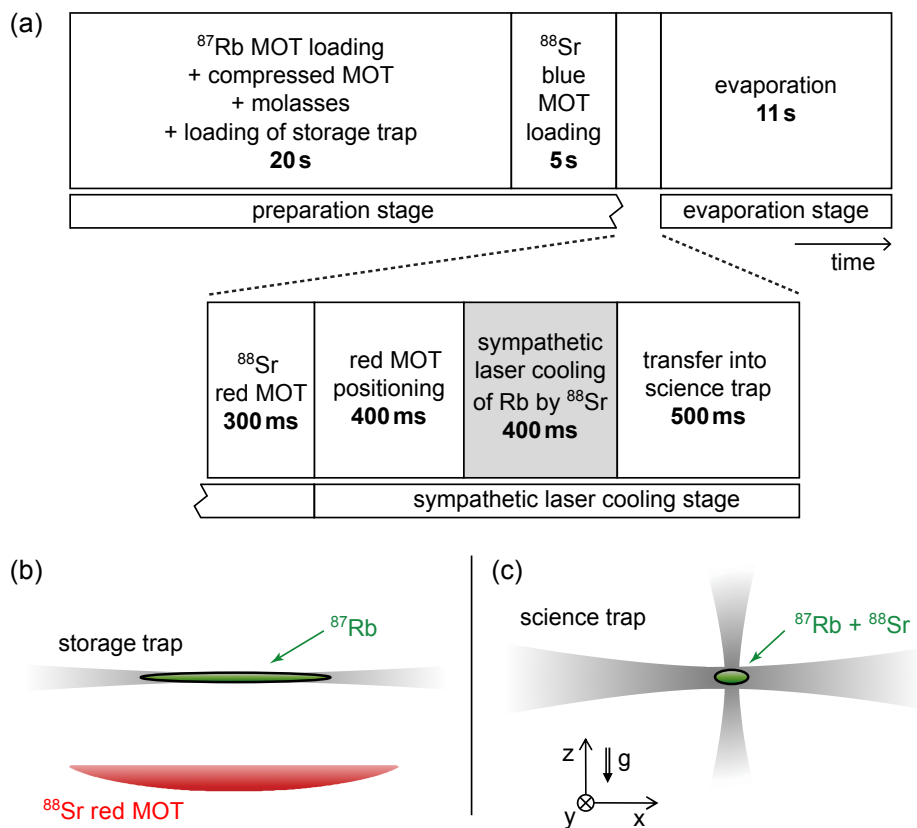


Figure 6.1.: Timing of the experimental sequence and trap configurations used to produce a ^{88}Sr - ^{87}Rb double BEC. (a) Timing sequence. The central sympathetic laser cooling of ^{87}Rb by ^{88}Sr shaded in gray is characterized in Fig. 6.2. (b,c) Dipole trap configurations and atomic clouds at the end of the preparation stage (b) and during the evaporation stage (c) (not to scale).

Sr differ significantly, we perform a time-sequential loading scheme. The Rb ZS laser beam is superposed with the Sr ZS beam by a dichroic mirror, and uses 14 mW of light detuned by -165 MHz from the $^2\text{S}_{1/2}$ - $^2\text{P}_{3/2}$, $|F = 2\rangle \rightarrow |F' = 3\rangle$ transition. A “repumping” beam with 4.5 mW of power, addressing the $|F = 1\rangle \rightarrow |F' = 1\rangle$ transition is overlapped with the ZS beam. All three laser beams have a waist of about 8 mm at the MOT position. Slowed atoms are captured by a 3D MOT. Producing an ultracold mixture of Rb and Sr requires the use of MOTs of three wavelengths, one for Rb and two for Sr. The Rb MOT uses 780-nm light, the blue Sr MOT is operated on the broad $^1\text{S}_0 \rightarrow ^1\text{P}_1$ transition at 461 nm, and the red MOT on the $^1\text{S}_0 \rightarrow ^3\text{P}_1$ intercombination line at 689 nm. MOT beams of the three wavelengths are overlapped by dichroic mirrors on each of the three retro-reflected MOT beam paths. The Rb MOT beams have a waist of 9.8 mm, a power of 18 mW (25 mW) in the horizontal (vertical) direction, and are detuned by -16 MHz from the $^2\text{S}_{1/2}$ - $^2\text{P}_{3/2}$, $|F = 2\rangle \rightarrow |F' = 3\rangle$ transition. A repumping beam with a waist of 6 mm and a peak intensity of $130 \mu\text{W}/\text{cm}^2$, on resonance with the $|F = 1\rangle \rightarrow |F' = 2\rangle$ transition, is shone onto the MOT. The quadrupole magnetic field of the Rb MOT has a gradient of 12 G/cm along the vertically oriented coil axis.

The experimental sequence starts by operating the Rb MOT during 20 s to accumulate a cloud of 2×10^7 atoms at a temperature of $175 \mu\text{K}$. We then compress the cloud in 140 ms by raising the gradient of the quadrupole field to 50 G/cm and increasing the MOT laser

detuning to -30 MHz. After compression the $1/e$ cloud radius is $\sim 250 \mu\text{m}$. To decrease the temperature we use polarization gradient cooling in an optical molasses. After switching off the magnetic field, the MOT laser detuning is set to -110 MHz and the beam power is halved. After 3 ms of molasses, we obtain 1.8×10^7 atoms cooled to $15 \mu\text{K}$ with a peak density of $3 \times 10^{10} \text{cm}^{-3}$.

We then transfer the Rb atoms into the storage trap. This trap consists of a horizontal beam with a waist of $40 \mu\text{m}$ propagating at a small angle to the x-direction, see Fig. 6.1(b). The beam is derived from a 100-W multimode fiber laser operating at a wavelength of 1070 nm (YLR-100-LP-AC-Y12 from IPG). It is linearly polarized in the vertical direction to minimize the light shift induced on the red Sr laser cooling transition [247]. Initially we use a power of 14 W for the storage trap, which results in a potential depth of $k_B \times 830 \mu\text{K}$ and trap frequencies of $f_{\text{rad}} = 2.2 \text{kHz}$ and $f_{\text{ax}} = 13 \text{Hz}$ in the radial and axial directions respectively. To improve loading of the storage trap, we toggle the repumping beam to a path where a wire is imaged onto the trap region, creating a dark spot. The repumping beam power is reduced to a peak intensity of $8 \mu\text{W}/\text{cm}^2$ and in 500 ms we transfer 10% of the molasses atoms into the trap, pumping them at the same time into the $F = 1$ manifold. Up to 1.7×10^6 atoms are stored in the storage trap at a density of $2 \times 10^{13} \text{cm}^{-3}$ and a temperature of $\sim 20 \mu\text{K}$.

Having stored Rb, we now capture Sr atoms. The loading and cooling of Sr is done in a manner similar to our previous work [244, 247]. We operate a blue MOT on the broad transition at 461 nm, which has a leak towards the metastable $^3\text{P}_2$ state. We accumulate $^3\text{P}_2$ atoms in the magnetic trap formed by the quadrupole field of the MOT. We typically load this reservoir in a few seconds with several million ^{88}Sr atoms. For the data presented in Sec. 6.3 and 6.4 we load for 0.5 s. The atoms are subsequently optically pumped back to the ground state using a flash of light on the $^3\text{P}_2 \rightarrow ^3\text{D}_2$ transition at 497 nm. The atoms are captured by a red MOT operating on the $^1\text{S}_0 \rightarrow ^3\text{P}_1$ intercombination transition and using a magnetic field gradient of 1.8 G/cm. The narrow, 7.4 kHz-linewidth intercombination transition allows us to cool Sr to less than $1 \mu\text{K}$ while keeping millions of atoms. The atoms settle in the lower part of an ellipsoid of constant magnetic field magnitude, see Fig. 6.1(b). The size and position of this cloud can be influenced by the magnetic field and the detuning of the MOT light. Varying these parameters facilitates the transfer of Sr into the optical dipole trap.

At the end of the preparation stage, we obtain 7×10^6 ^{88}Sr atoms at a temperature of $2.5 \mu\text{K}$ in a red MOT. The storage trap contains 1.6×10^6 Rb atoms at a temperature of $30 \mu\text{K}$ and a phase-space density of 2.5×10^{-4} , which is slightly worse than before loading the Sr atoms. The $1/e$ lifetime of the Rb cloud in the storage trap in presence of the blue ^{88}Sr MOT is 5.0(5) s. To detect the influence of Sr atoms on the Rb cloud in the storage trap, we perform the same experimental sequence, but shutter the atomic beam off after loading the Rb MOT. Under these conditions, the lifetime of the Rb sample in the storage trap is 30(1) s. This value does not change if also the Sr laser cooling beams are off.

6.4. Sympathetic narrow-line laser cooling

The following, sympathetic laser cooling stage is crucial in our approach to obtain a Sr-Rb double BEC. We make use of laser cooled Sr to further cool Rb and increase its PSD. To this aim, we overlap the cloud of ^{88}Sr atoms with the focus of the storage trap. This overlap is achieved by moving the magnetic field center upwards, while keeping the MOT laser frequency red detuned by 200 kHz from resonance. At this point, the Sr density is so

low that the influence on the Rb cloud is negligible on a timescale of 500 ms. To increase the density of the Sr cloud, the magnetic field together with the MOT detuning and intensity are changed over 200 ms such that the cloud is compressed while remaining at the same position.

The Sr atoms are loaded into the storage trap during this compression phase. The loading process is strongly influenced by the light shift induced on the red MOT transition by this trap. At the center of the trap, the light shift is $\sim +500$ kHz, which is almost 70 times the linewidth. In order to laser cool Sr atoms in the storage trap we tune the MOT laser frequency 350 kHz to the blue of the unshifted atomic transition in a 200 ms ramp, while reducing the peak beam intensity to $6 \mu\text{W}/\text{cm}^2$. The part of the Sr cloud that does not spatially overlap with the dipole trap is thereby expelled from the MOT, leading to a loss of 60% of the Sr atoms. This loss could be reduced by canceling the light shift of the transition, for example by inducing a light shift on the excited state of the laser cooling transition [174]. Since ^{88}Sr has a high natural abundance, leading to a high atom number in the MOT, we here simply tolerate the loss. The temperature of the Sr cloud in the storage trap increases to $15 \mu\text{K}$ before reducing to below $5 \mu\text{K}$ during the compression phase and a subsequent 200 ms hold phase. This temperature increase results from MOT dynamics in presence of the light shift induced by the dipole trap and would also occur in absence of Rb atoms. The Rb cloud thermalizes with laser cooled Sr by elastic collisions. During this process, the Rb PSD increases dramatically, by a factor of more than 200, reaching 0.062(6), while only 20(5)% of the Rb atoms are lost. From the thermalization behavior we can deduce a minimum absolute value of the interspecies scattering length of $30 a_0$ between ^{87}Rb and ^{88}Sr assuming pure s-wave scattering [296]¹. After the hold phase the Sr laser cooling beams are switched off. We observe that complete thermal equilibrium between Rb and Sr can only be reached in absence of the cooling light.

To prepare for the creation of a quantum degenerate sample, we transfer both elements into the science dipole trap, which has been described in detail in Ref. [247] and will be especially important for the creation of a large ^{84}Sr - ^{87}Rb double BEC (see Sec. 6.5.2). This crossed-beam dipole trap is composed of an elliptical beam propagating in the x-direction with waists of $w_z = 17 \mu\text{m}$ and $w_x = 300 \mu\text{m}$, crossed by a nearly vertical beam with a waist of $90 \mu\text{m}$, see Fig. 6.1(c). The center of this dipole trap is overlapped with the center of the storage trap, and the horizontal beams of the two traps intersect at an angle of 17° . Individual laser sources are used for each science trap beam (5-W, 1065-nm multimode fiber lasers, YLD-5-LP from IPG). At the wavelength of 1065 nm the polarizability of Rb is 2.9 times the polarizability of Sr [185, 298]. The ratio of trap depths is even higher because of gravitational sagging. Initially the science trap has a depth of $k_B \times 25 \mu\text{K}$ for Rb and $k_B \times 7 \mu\text{K}$ for Sr. The reduction of the Rb cloud volume and temperature by sympathetic laser cooling allows us to transfer Rb from the storage trap into this much shallower trap in 500 ms with a nearly perfect transfer efficiency (more than 95% of the atoms). The ^{88}Sr transfer efficiency is 30%. After transfer we typically obtain 1.25×10^6 Rb atoms and 1.6×10^6 Sr atoms at a temperature of $1.2 \mu\text{K}$. The Rb PSD is 0.5(2) and the Sr PSD is 0.10(3). We attribute the increase in PSD to evaporation of Sr during the transfer process.

¹ The p-wave centrifugal barrier has a height of $k_B \times 90 \mu\text{K}$ [297], rendering p-wave and higher order partial wave scattering negligible at our temperatures if shape resonances are absent [52].

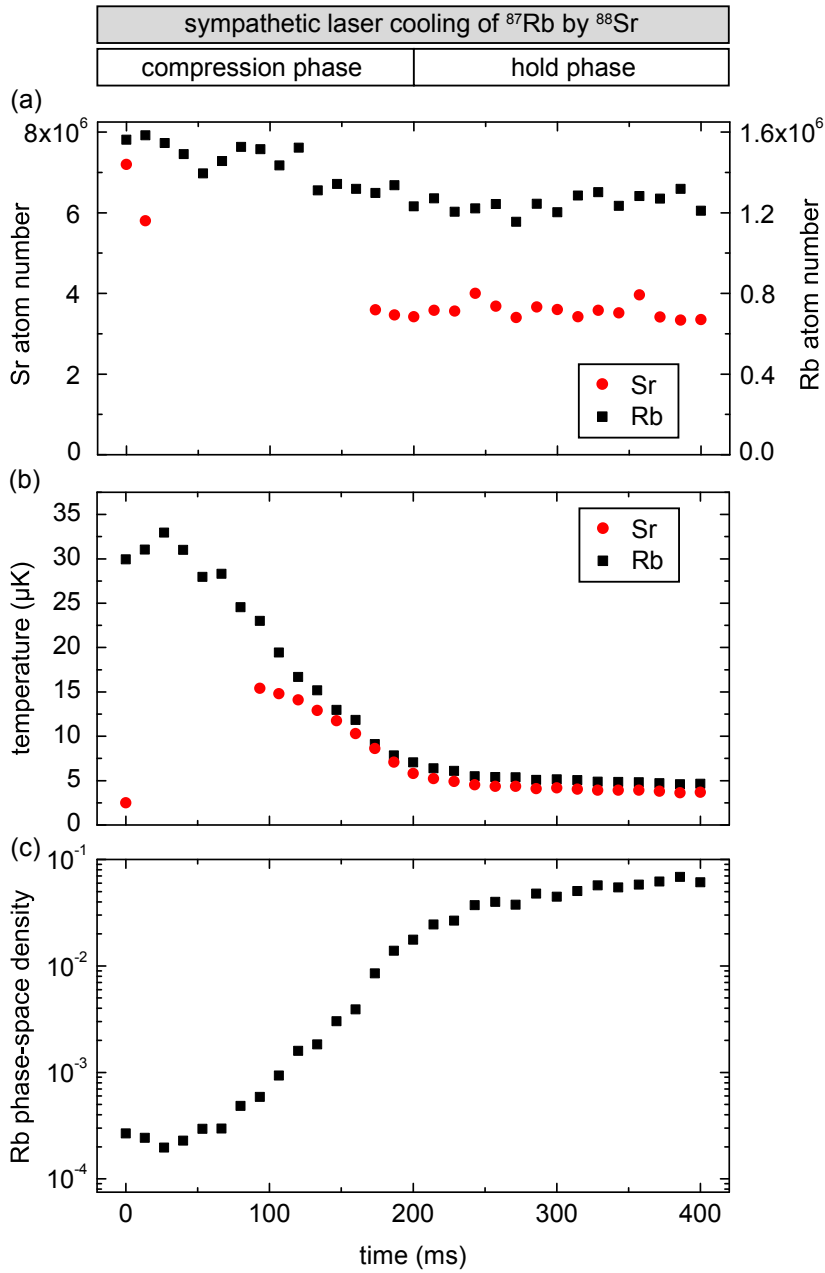


Figure 6.2.: Sympathetic laser cooling of ^{87}Rb by ^{88}Sr . During the compression phase the density of the red Sr MOT is increased and the Sr atoms are loaded into the storage dipole trap by changing magnetic field and both the MOT laser detuning and intensity. During the hold phase these parameters are held constant. (a,b) Evolution of the Rb and Sr atom numbers (a) and temperatures (b) as determined from time-of-flight absorption images. During a part of the compression phase the Sr cloud separates into two components, one being heated out of the system, the other remaining trapped and being transferred into the storage trap. We only show the number of trapped Sr atoms and the Sr temperature if we can determine them reliably from bimodal fits to the absorption images. (c) PSD of Rb, calculated from trap parameters and Rb atom number and temperature.

6.5. Evaporation to alkali/alkaline-earth double BECs

In this Section we present the creation of quantum degenerate mixtures of ^{87}Rb with either ^{88}Sr (Sec. 6.5.1) or ^{84}Sr (Sec. 6.5.2). These two Sr isotopes have markedly different properties, which we take into account in our experimental strategy. The ^{88}Sr isotope has a high natural abundance and provides us with an ideal coolant for sympathetic narrow-line laser cooling of ^{87}Rb . Since the ^{88}Sr scattering length is negative ($-2a_0$), the ^{88}Sr BEC atom number is limited to a few thousand atoms. By contrast, ^{84}Sr has a convenient scattering length of $+123a_0$, allowing us to create BECs with high atom number. Unfortunately this isotope has a low natural abundance (only 0.56%), which renders it less favourable for sympathetic laser cooling. To overcome this drawback, we employ both isotopes in the production of a ^{84}Sr - ^{87}Rb double BEC, using ^{88}Sr for sympathetic laser cooling of ^{87}Rb and ^{84}Sr for evaporative cooling to quantum degeneracy.

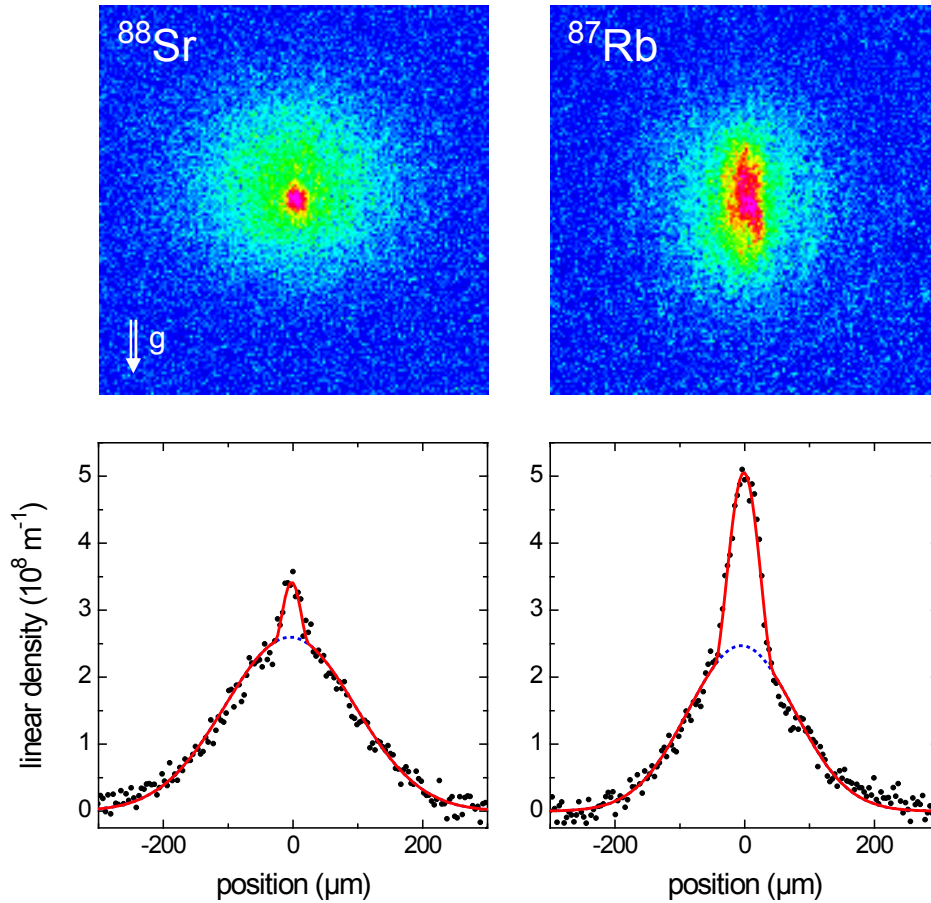


Figure 6.3.: ^{88}Sr - ^{87}Rb double BEC. The absorption images have been recorded after an expansion time of 26 ms. The lower panels show density profiles obtained by vertical integration of the absorption images. Bimodal fits consisting of a Gaussian and a Thomas-Fermi distribution are shown as red, solid lines. The Gaussian part of the fit corresponds to the thermal fraction of the cloud and is shown as blue, dotted line.

6.5.1. ^{88}Sr - ^{87}Rb double BEC

To obtain a ^{88}Sr - ^{87}Rb double BEC, we prepare as before a ^{88}Sr - ^{87}Rb mixture in the science trap. Compared to the previous sections, we here increase the number of ultracold ^{88}Sr atoms by increasing the Sr MOT loading time to 5 s. Then we perform forced evaporative cooling by lowering the trap depth exponentially over 11 s to $0.5\ \mu\text{K}$ for Sr. As demonstrated in Sec. 6.4, the interspecies scattering cross section is sufficient for interspecies thermalization. Note that by itself ^{88}Sr does barely thermalize because of its small scattering length of $-2a_0$ [299, 300] and only the presence of Rb ensures proper thermalization. Since the trap depth is more than three times deeper for Rb than for Sr, Rb is sympathetically cooled by evaporating Sr.

At the end of the evaporation stage, we obtain Rb and Sr BECs with low atom number immersed in thermal clouds (see Fig. 6.3). The Sr cloud contains 2.3×10^3 condensed atoms and 6.5×10^4 thermal atoms. The Rb cloud consists of a mixture of all three m_F states of the $F = 1$ manifold, as confirmed by Stern-Gerlach measurements. The spin state distribution can be influenced by applying a magnetic field offset and gradient during the evaporation stage [301]. The distribution for zero offset and gradient is 38%, 25%, and 37% for the $m_F = -1, 0,$ and $+1$ states after evaporation. In total the Rb cloud consists of 1.3×10^4 atoms in the spinor BEC and 5×10^4 thermal atoms. The temperature of both elements is 190(30) nK. The low ^{88}Sr BEC atom number is expected since the negative scattering length of ^{88}Sr leads to a collapse of the BEC for higher atom numbers [247, 302–305].

6.5.2. ^{84}Sr - ^{87}Rb double BEC

To obtain quantum degenerate samples with higher atom numbers, we now turn to the ^{84}Sr isotope. This isotope has a scattering length of $+123a_0$ [299, 300], which is well-suited for evaporative cooling. Despite the small ^{84}Sr natural abundance of only 0.56% the production of large ^{84}Sr BECs with 10^7 atoms has been demonstrated [247]. The low abundance can be compensated for by a longer blue MOT duration compared to the one used for the highly abundant ^{88}Sr isotope, leading to nearly the same atom number accumulated in the metastable state reservoir. By simply replacing ^{88}Sr with ^{84}Sr and operating the blue MOT for 20 s, we can prepare a ^{84}Sr - ^{87}Rb double BEC with essentially the same scheme as the one used for the production of a ^{88}Sr - ^{87}Rb double BEC. Nonetheless we have developed an improved strategy, which requires less time, makes optimal use of the precious ^{84}Sr atoms, and leads to much larger numbers of condensed atoms. Because of its high natural abundance, we use ^{88}Sr as the refrigerant for sympathetic laser cooling of Rb. We then use ^{84}Sr during the evaporation stage to obtain a ^{84}Sr - ^{87}Rb BEC.

We adapt the scheme of our experiment to this new strategy, see Fig. 6.4(a). During the Sr blue MOT stage we load both Sr isotopes, ^{88}Sr and ^{84}Sr . This double-isotope loading is achieved by accumulating one isotope after the other in the metastable state reservoir. In between, the frequency of the 461-nm cooling laser source is changed by the isotope shift [247, 306]. We first accumulate ^{88}Sr for 500 ms and then add ^{84}Sr during 10 s. The lifetime of Rb atoms in the storage trap in presence of the ^{84}Sr blue MOT is 23(1) s. Afterwards both isotopes are optically repumped into the electronic ground state. The two isotopic clouds are captured simultaneously by two narrow-line red MOTs, which contain 4×10^6 atoms of ^{88}Sr and 9×10^6 atoms of ^{84}Sr respectively, see Fig. 6.4(b) [247, 306]. The different isotopes are addressed independently by using two frequencies for the red MOT laser beams, separated by the isotope shift. Changing one of the MOT laser frequencies, vertically displaces the corresponding isotopic cloud and changes its radial size.

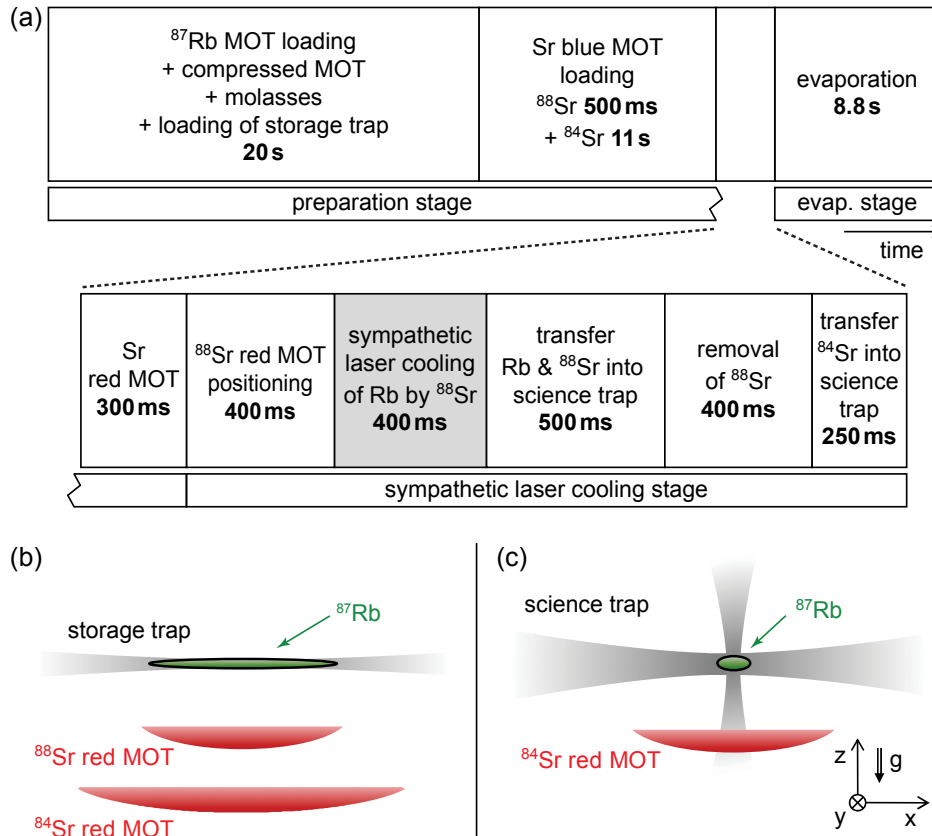


Figure 6.4.: Timing of the experimental sequence and trap configurations used to produce a ^{84}Sr - ^{87}Rb double BEC. (a) Timing sequence. ^{88}Sr is used for sympathetic laser cooling of Rb and discarded afterwards. ^{84}Sr , stored in a red MOT during sympathetic laser cooling, is transferred into the science dipole trap before evaporative cooling. (b,c) Dipole trap configurations and atomic clouds at the end of the preparation stage (b) and after removing ^{88}Sr (c) (not to scale).

We proceed as described in Sec. 6.4 with the sympathetic laser cooling of Rb by ^{88}Sr and the transfer of the ^{88}Sr - ^{87}Rb mixture into the science trap. In the meantime we keep the ^{84}Sr cloud about 0.7 mm below the center of the dipole traps. At this position the red MOT has a radius of about 1 mm and a low density, which reduces light-assisted collisions. The lifetime of the MOT is independent of the various operations on the other species and we lose only 10% of the ^{84}Sr atoms during the sympathetic laser cooling stage. Reciprocally, the presence of the ^{84}Sr red MOT does not affect the sympathetic laser cooling of Rb.

It is advantageous to expel the refrigerant ^{88}Sr after it has fulfilled its role. Without the removal of ^{88}Sr , the large scattering length between ^{84}Sr and ^{88}Sr of about $1700 a_0$ [299, 300] would lead to strong three-body loss as soon as ^{84}Sr is loaded into the science trap. We expel ^{88}Sr by adiabatically lowering the science trap depth in 300 ms. Including gravitational sagging the trap is about ten times shallower for Sr than for Rb at the end of the ramp, leading to a removal of all ^{88}Sr atoms without affecting the Rb atom number. We then raise the trap back to its former depth in 100 ms.

At this point we load ^{84}Sr into the science trap, see Fig. 6.4(c). We shift the red MOT upwards by changing the cooling laser frequency until the MOT overlaps with the science trap. Now 70% of the ^{84}Sr atoms are loaded into the dipole trap, compared to 40% when transferring into the storage trap as in Sec. 6.4. The reasons for this increased transfer

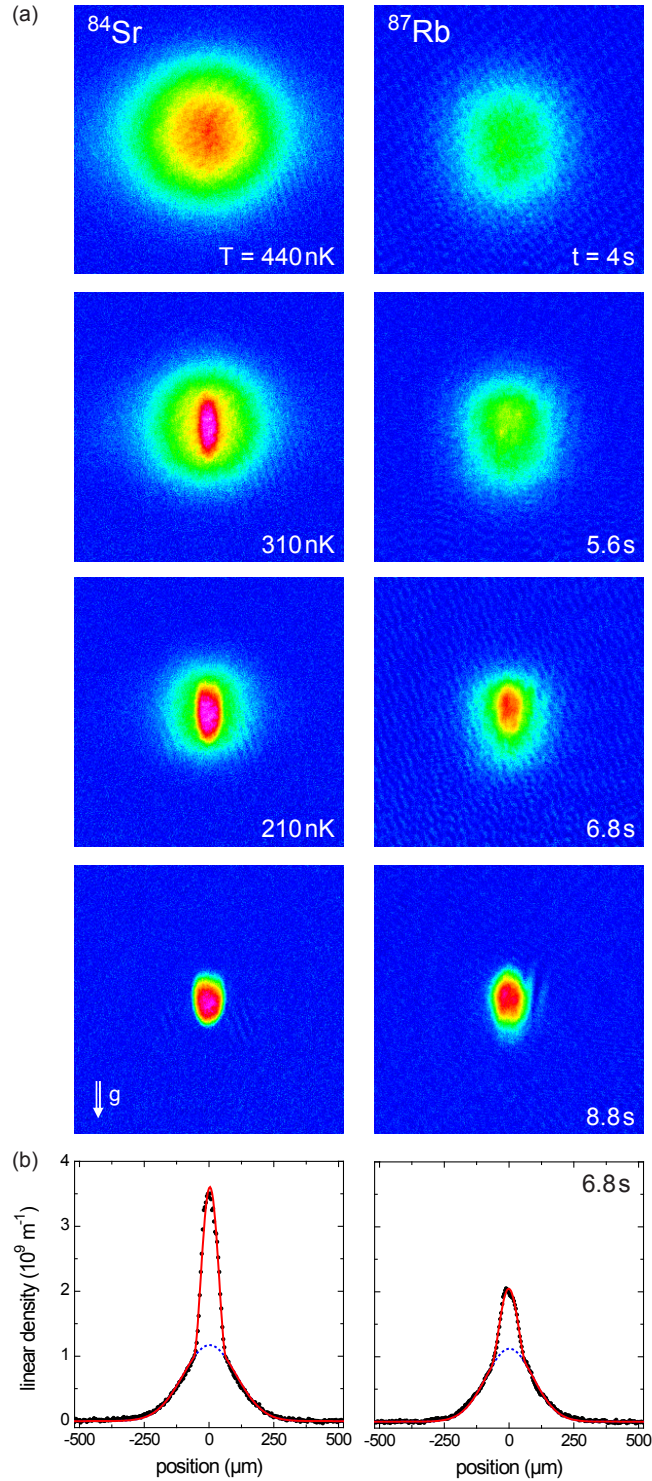


Figure 6.5.: Formation of a ^{84}Sr - ^{87}Rb double BEC while Sr is evaporated, sympathetically cooling Rb. (a) Absorption images of the Rb and Sr clouds at time t of the evaporative cooling ramp recorded after 24 ms of expansion. Strontium condenses at $t = 4.3\text{ s}$ and Rb at $t = 6\text{ s}$. The temperature T of Sr is given. (b) Density profiles obtained from the absorption images at $t = 6.8\text{ s}$ by integration along the vertical direction. The solid, red lines are bimodal fits to the data by a Gaussian plus a Thomas Fermi distribution. The blue, dotted line shows the Gaussian part of the fit corresponding to the thermal part of the cloud.

efficiency are that the much shallower science trap induces a negligible light shift on the red Sr laser cooling transition and that the horizontally extended science trap is well adapted to the pancake shape of the red MOT. The ^{84}Sr cloud is slightly colder than the Rb sample, which again leads to sympathetic laser cooling of Rb. When choosing the final red MOT parameters, we have to compromise between attainable temperature and remaining Rb and Sr atom numbers [180, 289]². We chose a temperature of $1\ \mu\text{K}$, for which we obtain $4.0(1) \times 10^6$ Sr atoms and $5.2(1) \times 10^5$ Rb atoms, both elements at a PSD of 0.4(1). At this point the cooling laser beams are switched off.

Starting with these excellent conditions, we perform evaporative cooling by lowering the science trap depth exponentially over 8.8 s to $k_B \times 150\ \text{nK}$ for Sr. Strontium is evaporated, sympathetically cooling Rb, and a double BEC is formed (see Fig. 6.5). At the end of evaporation we obtain a pure ^{84}Sr BEC of 2.3×10^5 atoms and 1.3×10^5 quantum degenerate Rb atoms accompanied by 6.5×10^4 thermal Rb atoms at a temperature of $\sim 70\ \text{nK}$. The Rb cloud again contains a nearly equal mixture of the three $F = 1\ m_F$ states. The trapping frequencies in the x-, y-, and z-direction are at this point 40 Hz, 37 Hz, and 190 Hz for Sr and 67 Hz, 63 Hz, and 400 Hz for Rb. For the lowest values of the science trap depth, the gravitational sagging of the Sr cloud is $\sim 3.5\ \mu\text{m}$ larger than the gravitational sagging of the Rb cloud. For comparison, the Thomas-Fermi radii, calculated neglecting the interspecies mean-field, is $2.5\ \mu\text{m}$ for the Sr BEC in the vertical direction and $2\ \mu\text{m}$ for the Rb BEC. The two elements are barely overlapping, which reduces interspecies thermalization. The differential gravitational sag between Sr and Rb could be compensated for the magnetic Rb $F = 1, m_F = +1$ or $m_F = -1$ state by using a magnetic field gradient in the vertical direction, which does not influence the non-magnetic Sr [307]. The peak density of the Sr BEC and of each m_F -state component of the Rb BEC is $1.5 \times 10^{14}\ \text{cm}^{-3}$. The $1/e$ lifetime of the BECs is about 10 s. The atom number of the Sr BEC can be increased at the expense of the Rb BEC atom number by reducing the MOT loading time of Rb. On absorption images of ^{84}Sr - ^{87}Rb double BECs taken after 24 ms of expansion, we observe that the position of the Sr BEC is shifting downwards for an increasing Rb BEC atom number. This observation hints at a positive mean-field interaction and therefore a positive interspecies scattering length between ^{87}Rb and ^{84}Sr .

6.6. Conclusion and outlook

We have presented the production of ^{88}Sr - ^{87}Rb and ^{84}Sr - ^{87}Rb double BECs. Crucial to our success are the favourable interaction properties of the two mixtures. For both mixtures we observe efficient thermalization. At the same time the mixtures do not suffer from large inelastic three-body losses. These interaction properties cannot be predicted by *ab-initio* calculation and were completely unknown prior to our work.

A central stage in our scheme is sympathetic narrow-line laser cooling of Rb by Sr. This powerful technique will also be useful to cool other species besides ^{87}Rb , including fermions, and should work if one of the four Sr isotopes has good interspecies scattering properties with the target species. It might even be possible to sympathetically laser cool the target species to quantum degeneracy without using evaporation [174]. This goal will be facilitated by selectively increasing the density of the target species with a species-specific dipole poten-

² The lifetime of Rb in the Rb-Sr mixture is reduced by the presence of Sr laser cooling light from $\sim 10\ \text{s}$ to $\sim 0.2\ \text{s}$. We attribute this reduction in lifetime to inelastic collisions between Rb and the $\sim 10\%$ of Sr atoms in the $^3\text{P}_1$ state.

tial [24] or by using a target species of low mass, which leads to a high critical temperature or Fermi temperature for a given density.

Our next goal is the creation of RbSr molecules. We plan to associate atoms to weakly-bound molecules by either magneto-association [260] or stimulated Raman adiabatic passage (STIRAP) [106, 249]. These molecules will then be transferred into the ro-vibrational ground-state by STIRAP [111, 308, 309]. We are currently performing photoassociation spectroscopy of the $^{84,88}\text{Sr}$ - ^{87}Rb mixtures, in order to precisely determine the interspecies scattering lengths of all Sr-Rb isotopic combinations, the magnetic field values of Sr-Rb magnetic Feshbach resonances, and STIRAP paths for molecule association and ground-state transfer. The optimal Sr-Rb isotopic mixture for our task will depend on these properties, especially the interspecies scattering length, which determines the miscibility of the Rb and Sr quantum gases.

Acknowledgments

We thank Piotr Żuchowski, Olivier Dulieu, Jeremy Hutson, John Bohn, Roman Krems, Kadan Hazzard, Paul Julienne, Mikhail Baranov, and Mikhail Lemeshko for fruitful discussions. We gratefully acknowledge support from the Austrian Ministry of Science and Research (BMWF) and the Austrian Science Fund (FWF) through a START grant under Project No. Y507-N20. As member of the project iSense, we also acknowledge the financial support of the Future and Emerging Technologies (FET) programme within the Seventh Framework Programme for Research of the European Commission, under FET-Open grant No. 250072.

Experimental steps towards ground-state RbSr molecules

In this chapter I will present the experimental steps towards the creation of RbSr molecules. The sympathetic optical cooling of Rb by Sr from last chapter is a key component in reaching quantum degeneracy in this mixture and is an example of an efficient new technique in mixing species with significantly different properties. The narrow transition of Sr will play an important role also for the photoassociation (PA) spectroscopy of the RbSr molecular potential, which is presented in the first half of this chapter. The PA investigation is used in Ref. [242] together with measurements on hot molecules to determine the ground state of RbSr. The resulting potential confirms the recent findings on narrow Feshbach resonances in the Sr-Rb mixture [150] and will allow to find the optimal wavelengths for an efficient STIRAP transition into a deeply bound molecular state [310]. The current experimental approach for molecule generation is briefly presented and the choice of RbSr isotopologue is discussed from experimental point of view as conclusion.

7.1. Photoassociation spectroscopy

For the coherent creation of RbSr molecules via magnetic or optical association the best possible understanding of the molecular potential energy curves (PECs) is required. The molecule transfer into specific quantum states and further manipulations are also based on a profound knowledge of the relevant energy levels and corresponding transition-dipole moments. In contrast to alkali dimers, little is known about the level structure of dimers made of a group-I and a group-II atom. We have seen a comparison of predicted permanent electric dipole moments for the ground state of alkali-metal-atom-strontium dimers in Fig. 4.2, Chapter 4. Ionization spectroscopy on RbSr in He droplets gives an insight into the energy levels over the entire visible spectrum [311], but its resolution is much too low (maximally tens of GHz) for ultracold applications. Similar results come from thermoluminescence (as in Ref. [242]) alone.

Our study of the long-range part of the RbSr molecular potential is performed via one- and two-color photoassociation spectroscopy in a mixture of ultracold Sr and Rb. Further, cross-thermalization measurements and detected Feshbach resonances are used together with studies on hot RbSr molecules for the determination of the PEC of the RbSr $^2\Sigma^+$ ground state. The work described in this section contributed to the publication [242] and direct quotes from [242] are surrounded by quotation marks.

‘The electronic states relevant to the present work are those dissociating into the two lowest atomic asymptotes Rb($5s\ ^2S$) + Sr($5s^2\ ^1S$) and Rb($5p\ ^2P$) + Sr($5s^2\ ^1S$), see Fig. 7.1. The

thermoluminescence spectra are dominated by transitions between levels belonging to the $X(1)^2\Sigma^+$ and $B(2)^2\Sigma^+$ states. Two-colour PA spectroscopy explores the $X(1)^2\Sigma^+$ ground-state potential, by using intermediate molecular levels supported by potentials dissociating into the $\text{Rb}(5s^2S) + \text{Sr}(5s5p^3P)$ asymptote, see Fig. 7.1. From our combined measurements we therefore derive quantitative information about the $X(1)^2\Sigma^+$ and $B(2)^2\Sigma^+$ states.’

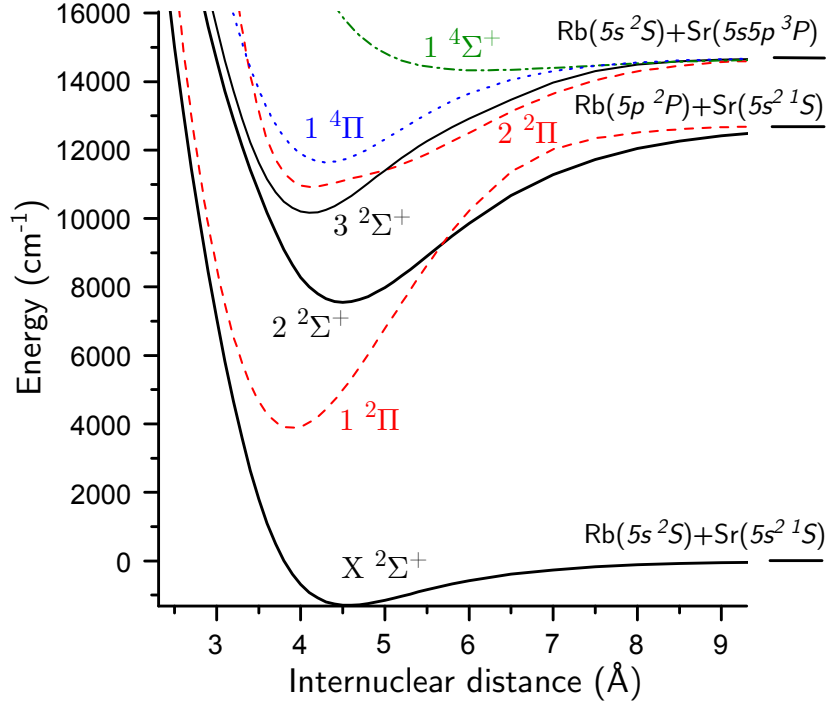


Figure 7.1.: The potential energy curves calculated using the MRCI method [312] for all states correlating to the $\text{Rb}(5s^2S) + \text{Sr}(5s^2^1S)$, $\text{Rb}(5p^2P) + \text{Sr}(5s^2^1S)$ and $\text{Rb}(5s^2S) + \text{Sr}(5s5p^3P)$ asymptotes. Our measurements derive information about the lowest two $^2\Sigma^+$ states (solid black lines). The dashed red lines are $^2\Pi$ states, the dotted blue line is a $^4\Pi$ state and the dash-dotted green line is a $^4\Sigma^+$ state. From Ref. [242]

We have performed PA spectroscopy close to the strontium intercombination line at 689 nm. PA excites vibrational levels close to the dissociation limit, thus probing the long-range properties of the molecular potentials [154]. Use of the narrow intercombination line for PA allows detection of least bound vibrational levels. Our probe light is derived from the Sr MOT laser with 2 kHz linewidth by frequency shifting using numerous AOMs and subsequent amplification using a TA¹. Photoassociation spectroscopy in the Sr-Rb experiment takes place in the ODT with thermal clouds and not with BECs. This way we avoid the the cloud size becoming smaller than the gravitational sagging due to differing potential depths for Rb and Sr. Thermal samples are typically inferior to quantum-degenerate samples for spectroscopy, because thermal motion broadens the spectroscopy signal. However, in the Sr-Rb case the thermal sample insures the overlap of the clouds. As shown in the previous chapter, sympathetic laser cooling on the red MOT line of Sr produces thermal samples of Rb and Sr at around 1 μK , corresponding to a Doppler broadening of the molecular line of about 25 kHz. This thermal broadening is negligible compared to the typical molecular binding energies of hundreds of MHz, measured in Ref. [242].

¹ In the final stages of the spectroscopy measurements at UvA the probe light comes from a separate ECDL referenced to the Sr MOT laser via beat-lock technique [268].

The key idea of photoassociation using a continuous-wave laser is to excite a colliding pair of atoms from the scattering state a into a bound level of an electronically excited state e [154]. When the frequency of the free-bound (FB) laser L_{FB} corresponds to a RbSr excitation frequency we observe atom loss in the one-color PA spectroscopy. A detailed description of the experimental and theoretical tools for the PA spectroscopy of RbSr in two different isotopic mixtures can be found in Ref. [262]. The two-color PA spectroscopy in RbSr investigates the bound-bound (BB) transition to a weakly-bound molecular state m with a second laser L_{BB} , while L_{FB} is on resonance with the $m - e$ transition. Figure 7.2 shows the increase of Rb atoms, when L_{BB} is tuned on resonance between e and m and the induced light-shift pushes e out of resonance with L_{FB} . The energy of the molecular level m referenced to the energy of the atom pair a is directly given by $h \times (f_{\text{BB}} - f_{\text{FB}})$, where h is the Planck constant and $f_{\text{BB}(\text{FB})}$ is the frequency of the $L_{\text{BB}(\text{FB})}$ laser respectively. In Figure 7.2 we see a typical molecular level energy of hundreds of MHz, with a transition linewidth on the order of 1 MHz.

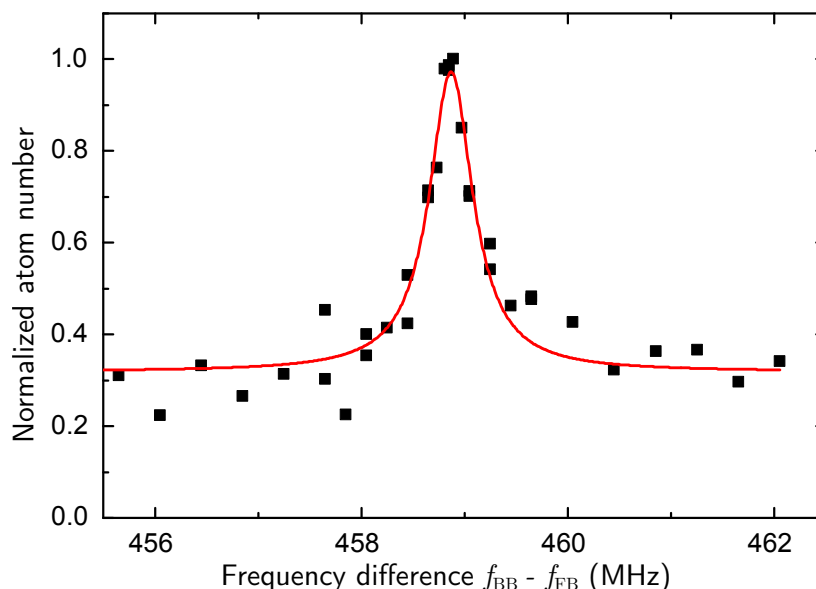


Figure 7.2.: Typical two-color photoassociation spectroscopy signal. The plot shows the number of Rb atoms in the $f^{\text{Rb}} = 1, m_f^{\text{Rb}} = 1$ level normalized to the atom number in the other two $f^{\text{Rb}} = 1, m_f^{\text{Rb}}$ levels, as function of the frequency difference between L_{BB} and L_{FB} , recorded during a scan of the L_{BB} frequency, while L_{FB} is on resonance with an a to e transition. This signal corresponds to the $\{\nu = 66, N = 0, F = 1\}$ level of the ^{87}Rb - ^{88}Sr ground-state potential, with the vibrational quantum number ν and molecular angular momenta N and F . From Ref. [242]

A crucial step to the successful analysis of the weakly-bound spectrum probed by two-color photoassociation is a line attribution, by which we mean the assignment of quantum numbers to both atomic and molecular levels used in the measurements of the bound energies. ‘We prepare ^{87}Rb in its hyperfine ground level ($^2S_{1/2}, f^{\text{Rb}} = 1$) with almost equal population of the Zeeman sub-levels $m_f^{\text{Rb}} = 0, \pm 1$. During PA spectroscopy, we measure each m_f^{Rb} population separately via time-of-flight expansion in a Stern-Gerlach magnetic field gradient. Bosonic Sr isotopes ^{84}Sr and ^{88}Sr have zero nuclear magnetic moment leading to a structureless 1S_0 ground state. Fermionic ^{87}Sr has a non-zero nuclear magnetic moment of $i^{\text{Sr}} = 9/2$ and is prepared in the stretched level $m_i^{\text{Sr}} = 9/2$ or $m_i^{\text{Sr}} = -9/2$ via optical pumping.’ Attributing quantum numbers to molecular levels is not trivial. ‘The possible

	^{84}Sr	^{86}Sr	^{87}Sr	^{88}Sr
^{85}Rb	689(20)	90.6(2)	44.3(3)	-35.8(1.0)
^{87}Rb	92.7(2)	-43.0(1.1)	1421(98)	170.3(6)

Table 7.1.: Inter-species s -wave scattering lengths in units of the Bohr radius a_0 . From Ref. [242].

molecular angular momenta can be restricted by considering the atomic angular momenta and the changes of angular momentum allowed by two-colour PA. All possible assignments of quantum numbers must then be tested by the fit in order to find the best one.’

In Ref. [242] ‘we present two-colour PA spectroscopy of three RbSr isotopologues performed on μK atomic mixtures. We use the PA spectroscopy results to fit a model from which we extract the long-range dispersion coefficients C_6 and C_8 along with the zero-energy semi-classical action. Based on this spectroscopy type alone, we calculate the s -wave scattering properties of all isotopic combinations of Rb and Sr [presented in Table 7.1] and explain the location of magnetic Feshbach resonances observed in previous work by some of the authors [150]. The Feshbach resonances are then included in the fit to provide a single comprehensive model. We corroborate this analysis by comparison with independent cross-thermalization experiments.’

An important ingredient for the determination of the RbSr PEC is the combination of the upper results with investigations of the short-range side of the potential. This is done by thermoluminescence and laser-induced fluorescence spectroscopy on hot RbSr molecules, which are created in a 1000 K gas mixture of Rb and Sr in a heat-pipe oven, and is also presented in Ref. [242]. ‘By combining the results from both experiments in a joint analysis and exploiting three previously reported state-of-the-art *ab-initio* calculations [313, 314], we can provide a PEC for RbSr ground-state molecules representing accurately all our experimental data and smoothly bridging the gap between the two spectral ranges investigated.[...] Thanks to this analysis, we can infer the molecular spectra with sufficient accuracy to guide future experiments (e.g. STIRAP path towards rovibronic ground state [315–317]).’

7.2. Molecule creation

Starting from a Sr-Rb double BEC and knowing the RbSr molecular potentials, we are in theory well prepared for the endeavor of deterministic production of ground-state molecules. In reality, the procedure for efficient molecule generation incorporates multiple delicate preparation steps, which will be briefly discussed in this section. The general idea for the formation of RbSr ground-state molecules is depicted in Fig. 7.3. A key component of the molecule production scheme is the Mott insulator (MI) phase in a three-dimensional (3D) optical lattice. The desired distribution of one atom of each species per lattice site would prevent three-body and atom-dimer inelastic collisions. The additional benefit of a 3D optical lattice is the tight confinement of a Sr-Rb precursor pair, which leads to higher efficiencies of atom-pair to molecule conversion for both, magnetic [105] and optical [58] molecule-formation means. Furthermore, the 3D optical lattice would protect the individual RbSr molecules from the detrimental chemical reaction $2\text{RbSr} \rightarrow \text{Rb}_2 + \text{Sr}_2$ and also from the formation of molecular complexes that would be prone to losses [112, 214, 215]. Finally, the low-entropy 3D lattice is the desired configuration for the investigation of lattice-spin models (see Sec. 3.1).

Loading the quantum degenerate mixture of Rb and Sr atoms into an optical lattice with

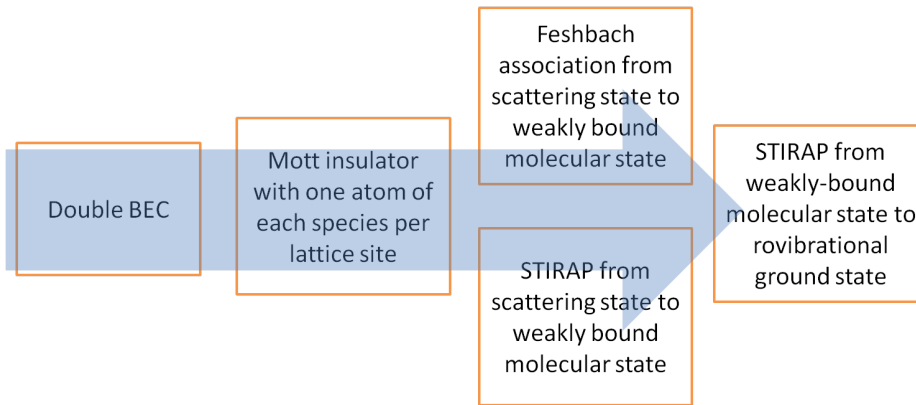


Figure 7.3.: Molecule formation scheme showing the option of magnetic or optical association of the atomic pairs into a molecule.

one atom of each species per lattice site is a finicky experimental step. Theoretically, the BECs are to be transferred from the ODT into an optical lattice and then the lattice depth is increased to the onset of the Mott insulator phase² for both species. The population of the Fock states in the MI state can be adjusted through the densities of the atomic clouds prior to lattice loading. Practically, the production of such low-entropy state requires exquisite control of the atom-light and atom-atom interactions, as shown for the bi-alkali mixtures of KRb [318] and RbCs [91]. The probability of having doubly occupied lattice sites increases with larger overlap between the Rb and Sr BECs as a starting condition for lattice loading. The Rb polarizability at 1064 nm is almost three times larger than the one of Sr. Therefore the BEC spatial overlap in the science trap is correspondingly small (see Chapter 6). Equilibration of the trap depths can be achieved by carefully mixing 532 nm light on top of the 1064 nm-trap. Such a green dipole trap is attractive for Sr and repulsive for Rb and thus it makes the overall trap depth higher for the alkaline-earth, while it decreases the trap depth for Rb. With careful adjustment of the focal positions and power ratios, an equal trapping potential for Rb and Sr has been achieved in the experiment [262]. (Here a reminder that the uncoated glass cell is advantageous as a main chamber, because it does not limit the experimentalist in the choice of wavelength.) Recently, the Sr-Rb team has optimized the deterministic production of ultralow-entropy Sr-Rb precursor pairs in the three-dimensional optical lattice for the bosonic ^{87}Rb - ^{84}Sr mixture [267].

The next experimental step from the scheme in Fig. 7.3 is the association of the free atoms to weakly-bound molecules. Creating heteronuclear molecules starting from an alkali atom and a nonmagnetic alkaline-earth atom is not straightforward. The predicted Feshbach resonances are with widths on the order of 1 mG to 10 mG [242, 260]. Thus very precise magnetic fields must be used to tune the molecular bound states across the atomic thresholds in the next step of the production of RbSr molecules. Should the Feshbach resonances be too narrow for useful experimental control, the atoms could be associated into molecules purely optically by STIRAP [310]. Efficient all-optical molecule formation from free atoms works best in a deep lattice [58, 310]. The harmonic trapping potential discretizes motionally the initial level of the colliding pair of atoms, which otherwise belongs to a dissociation continuum and hinders the creation of a perfect dark state needed for STIRAP. In addition, in a deep lattice the wavefunctions of the free atoms are localized and overlap better than

² In the case of identical fermions the phase in a deep optical lattice is a band insulator.

in a bulk of gas. With the Sr-Rb apparatus samples of weakly bound Sr_2 in the electronic ground state have already been produced via such a coherent optical transfer [249] starting from a MI phase. This nonmagnetic association has been optimized recently [208] and reveals the intricacies of STIRAP at the intercombination line. Such improvements helped us learn more about purely optical molecule production and provide promising paths for finding a suitable STIRAP for RbSr.

7.3. Conclusion on the Sr-Rb results

The aim of the Rb-Sr mixture is to create open-shell polar molecules to perform quantum simulation. The experimental path towards this goal is ambitious, therefore we have to identify the most promising tools and procedures available. The previous chapters showed the challenges but also the usefulness of mixing species with significantly different properties. Crucial for the hitherto developed procedures in the Sr-Rb experiment is the narrow transition of Sr, which provides low temperatures by simple Doppler cooling and sufficient precision in PA spectroscopy. Having multiple available isotopes proved helpful, since it increased the chances of finding a well-behaved mixture. The exquisite manipulation of the magnetic field for magnetoassociation via the narrow Feshbach resonances between Sr and Rb is the next important step towards the goal of open-shell polar molecules with tunable interactions.

From the estimated scattering lengths for all isotopic mixtures given in Table 7.1 we deduce which isotopic mixtures allow easy application of the planned procedures for molecule creation from Fig. 7.3. First, we need to consider the scattering properties for the cooling process, especially the sympathetic laser cooling followed by evaporation towards quantum degeneracy. All predicted and measured interspecies Feshbach resonances [150, 242] are too narrow to be used for precise tuning of the scattering length, hence we rely on the naturally given background scattering length. This means that the two isotopic mixtures with $a_{\text{RbSr}} > 500 a_0$ from Table 7.1 are not suited for RbSr molecule creation due to the resulting large 3-body losses. Furthermore, the isotopic mixtures with negative scattering length are inept for the reliable creation of a double BEC owing to the instability of a BEC with attractive interactions. Hence four of the eight available isotopic mixtures are basically ineligible for the planned molecule creation procedure.

The intraspecies scattering properties of each species also have to be considered for evaporation. While ^{87}Rb has an excellent background scattering length of about $100 a_0$, ^{85}Rb requires the use of an intraspecies Feshbach resonance near 155 G (or another Feshbach resonance [258]) to reach a good scattering length for efficient evaporation [257]. Since strontium is non-magnetic, it is experimentally possible to use a homogeneous magnetic field to adjust the intraspecies scattering length of ^{85}Rb during the double-species cooling, which was described in Chapter 6. In contrast, the strontium intraspecies scattering length is not adjustable. Although a BEC of ^{86}Sr with an intraspecies scattering length of about $830 a_0$ has been achieved in the Sr-Rb experiment [247, 319], the evaporative cooling takes place at low atom density in an ODT of large volume. With such a trap configuration the elastic scattering events between Rb and ^{86}Sr would be reduced to an insufficient level for sympathetic cooling. A possible workaround for the large scattering length of ^{86}Sr would be to use different ODTs for Rb and Sr to reach quantum degeneracy before mixing, as in the case for example for Rb and Cs [91]. However, we would then disable the sympathetic laser cooling of Rb by Sr, which brought a huge increase in PSD for Rb (see Fig. 6.2(c)). Furthermore, the experimental setup and procedure would need major modifications. So for the sake of

following the well-established advantageous procedures in the Sr-Rb experiment, we will at this stage discard ^{86}Sr from the list of candidates for efficient production of RbSr molecules.

Looking at the possible isotopic mixtures in Table 7.1 and considering the arguments from above, the experimentalist have three isotopologue options left: $^{85}\text{Rb}^{87}\text{Sr}$, $^{87}\text{Rb}^{84}\text{Sr}$ and $^{87}\text{Rb}^{88}\text{Sr}$. Although in Chapter 6, Sec. 6.5.1 we experimentally show the useful contribution of ^{87}Rb for the proper thermalization of ^{88}Sr in the evaporation process, the negative intraspecies scattering length of ^{88}Sr of about $-2 a_0$ hinders the reliable production of a stable BEC. Thus we can also discard the isotope ^{88}Sr from the list of candidates for efficient production of RbSr molecules. Finally, the bosonic $^{87}\text{Rb}^{84}\text{Sr}$ and the fermionic $^{85}\text{Rb}^{87}\text{Sr}$ are the two most promising isotopologues regarding the intra- and interspecies scattering properties. Since ^{85}Rb has so far never been used in the Sr-Rb experiment, currently the Sr-Rb team is working on the production of $^{87}\text{Rb}^{84}\text{Sr}$ Feshbach molecules. For the production of a ^{84}Sr - ^{87}Rb double BEC the experiment still involves a mixture of the ^{88}Sr and ^{84}Sr isotopes for more efficient sympathetic laser cooling (see Figure 6.4). After establishing a reliable scheme for the creation of Mott insulators in the three-dimensional optical lattice with one atom of each species per lattice site, the current experimental challenge is the control of the magnetic field for Feshbach association. The magnetoassociation using a Feshbach resonances of only 1 mG width near 1312 G is currently investigated thanks to the unrivalled magnetic field control of 5ppm and noise below 1ppm [267]. After mastering those important steps in the preparation of a quantum gas of bosonic $^{87}\text{Rb}^{84}\text{Sr}$ molecules, the Sr-Rb team can tackle the formation of fermionic $^{85}\text{Rb}^{87}\text{Sr}$ dipolar open-shell molecules.

Part III.

Dy-K mixtures

This part of the thesis presents my contribution to the realization and characterization of the Dy-K ultracold mixture. The combination of the rare-earth element dysprosium and the alkali-metal potassium is a promising platform for analog quantum simulation of novel types of superfluidity. The experimental apparatus for the Dy-K ultracold mixture has been set up from scratch within this thesis. In sight of the complex atomic mixture of elements with strongly differing properties the experimental architecture has to be stable as well as versatile. Next to the highly customized vacuum apparatus and magnetic field coils, the systems of resonant lasers are designed for efficient cooling and possible simultaneous manipulation of different isotopes. An important element in the design of the Dy-K setup is the possibility to implement an additional vacuum chamber for specialized experiments after characterizing the properties of the mixture. As a basis for every experimental procedure, we implement appropriate cooling and trapping techniques for the Dy-K mixture using bosonic and fermionic isotopes. A core component of the characterization of the mixture is the study of the interspecies scattering properties.

In Chapter 8 the selection of K and Dy for a novel ultracold atomic mixture is motivated. The abundance of stable isotopes in both species offers a wide choice of mixtures and the interaction between the species could be tuned with Feshbach resonances. The design of the experimental apparatus for the Dy-K ultracold mixture is presented in Chapter 9. I will emphasize specific features and details that make the Dy-K apparatus a technically sophisticated machine, which is robust and efficient. Then, in Chapter 10, I will present the first measurements with thermal samples of the new Dy-K mixture. After the main cooling and trap-loading steps are briefly characterized, I will outline the determination of the polarizability of Dy, which is published as Ref. [320]. Finally, I will present a study of the elastic and inelastic scattering properties between the bosonic isotope ^{162}Dy and the fermionic ^{40}K . The presence of interspecies Feshbach resonances and their characterization is a crucial step towards the investigation of strongly interacting mixtures of quantum gases.

Properties of Dy and K

The main motivation for the Dy-K experiment is to explore a strongly interacting mass-imbalanced Fermi-Fermi mixture. We wish to observe novel many-body states at ultra-low temperatures [27, 126–128, 227, 233]. From all available elements with fermionic isotopes, the combination of dysprosium and potassium has advantageous properties. The laser-cooling procedures for K and Dy are well-established and require accessible laser wavelengths, both elements exhibit Feshbach resonances, and dysprosium has two stable fermionic isotopes. Furthermore, the moderate mass ratio of four should allow for noticeable many-body effects [27, 126–128] in the fermionic mixture while the few-body losses remain suppressed at large scattering lengths [130, 132].

8.1. Why Dy?

Dysprosium is the non-alkali element of choice for the envisioned ultracold Fermi-Fermi mixture, after the success of the Erbium experiment in Innsbruck [140, 148, 321]. Dysprosium is a lanthanide element with favorable laser-cooling properties. Degeneracy has been reached by means of laser cooling and trapping [188] and the intraspecies interactions could be tuned with magnetic Feshbach resonances [147, 322]¹. The essential advantage of dysprosium over erbium is that dysprosium has two stable fermionic isotopes, ¹⁶¹Dy and ¹⁶³Dy, among its four isotopes with a natural abundance above 19% [323], while erbium has only one stable fermionic isotope, ¹⁶⁷Er. Thus, dysprosium offers a higher probability of finding an appropriate interspecies Feshbach resonance for the investigation of a strongly interacting (mass-imbalanced) fermionic mixture.

The energy-level scheme of dysprosium is shown in Figure 8.1. The electronic ground state of Dy is $[\text{Xe}]4f^{10}6s^2$. The 66 electrons are distributed first over the orbitals as in the noble gas xenon, then fill the 6s shell and the 4f is left with four electrons missing. This submerged-shell configuration gives rise to the exotic properties of dysprosium: complex energy-level scheme with multitude of optical transitions of different strength, high magnetic moment of almost $10 \mu_B$, and anisotropic scattering properties due to the magnetic dipole-dipole interaction (DDI). The filled 6s shell of dysprosium entails a ‘two-electron system’ excitation spectrum with a broad optical transition near 421 nm for precooling and a closed narrow intercombination transition near 626 nm for a narrow-line magneto-optical trap (MOT) [135]. Besides the low Doppler temperature, another practical property of a narrow-line MOT is that with the right detuning and polarization of the cooling light the atomic sample can

¹ These first motivational references are only up to year 2013, when the construction of the experiment began.

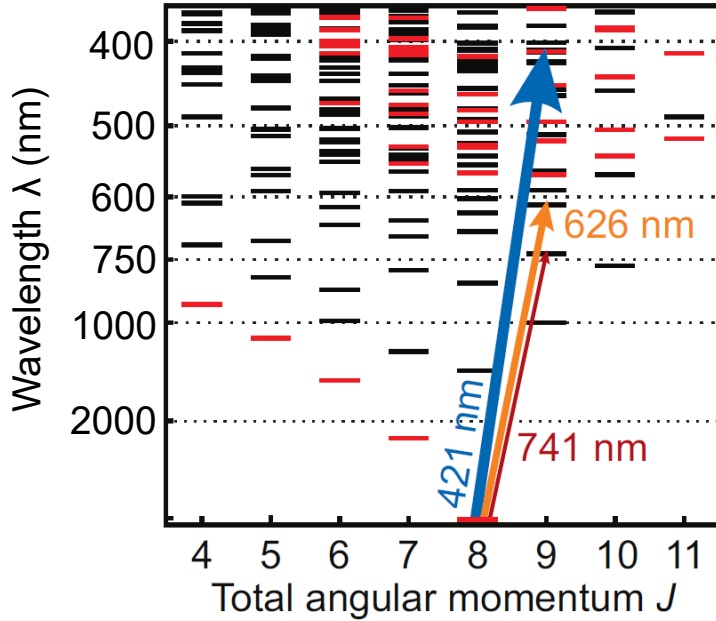


Figure 8.1.: Dysprosium energy-level scheme. The energy scale is given in wavelength λ of a possible optical transition from the ground state with a total angular momentum $J = 8$. Energy states with even (odd) parity are shown in red (black). The three typical optical transitions used for laser cooling are indicated by colored arrows. The thickness of the arrows indicates the different transition linewidths. Adjusted from Ref. [324]

be easily spin-polarized [189] (see Sec. 2.3.2). In addition, dysprosium possesses an even narrower optical transition near 741 nm. There, gravity is stronger than the optical force (see Sec. 2.3.2), so a blue-detuned MOT is necessary [186]. The laser cooling still happens with red-detuned light, of course, but the detuning of the laser-light from the transition at zero magnetic field is positive. The quadrupole magnetic field counteracts gravity and pushes the atoms above the zero of the quadrupole field, where the light is again red-detuned and the cooling happens. Using the transition near 741 nm laser cooling to very high phase-space density (PSD) should be possible as in the case for Sr [174].

Dysprosium is one of the most magnetic stable atoms in the periodic table. The large electronic orbital angular momentum $L = 6$ of the ground state of dysprosium is typical for the magnetic lanthanides in contrast to the missing orbital angular momentum of chromium, which is also magnetic. Having a large magnetic moment is not a necessity for the envisioned Fermi-Fermi experiments, but allows for alternative experimental directions. The DDI brings novelty to the typical contact interaction between ultracold atoms in being anisotropic and non-negligible at large distances. The interplay between contact and anisotropic dipole interactions leads to novel observations like the droplet formation in bosonic samples at high PSD [325] or the evaporation of single-spin fermions to degeneracy [140]. The anisotropy in the interatomic interactions further leads to a dense and chaotic Feshbach spectrum [149], in which, however, also broad Feshbach resonances can be found [326].

Other non-alkali elements were considered for this novel Fermi mixture and dismissed as candidates. For example, ^{52}Cr is rather difficult to laser-cool and requires a sophisticated scheme to be brought to quantum degeneracy [327], which is cumbersome for a species

mixture. ‘Two-electron systems’ like strontium and ytterbium, on the other hand, offer convenient laser-cooling schemes [134, 137] and ytterbium has even two stable fermionic isotopes. However, the closed-shell atoms Sr and Yb do not exhibit magnetic Feshbach resonances in their ground states. Even if interspecies Feshbach resonances between a closed-shell atom and an alkali-metal (like in Sr-Rb [150]) exist, they are very narrow. Interaction tunability with a sufficiently broad Feshbach resonance is a key property for the investigations of strongly interacting fermions [76, 132].

8.2. Why K?

Potassium is chosen as the second element with a fermionic isotope in the here presented mixture with dysprosium. As one of the pioneer elements in laser cooling, the alkali-metal potassium brings along well-established cooling and trapping procedures. In addition to the fermionic isotope ^{40}K , there are two stable bosonic isotopes, ^{39}K and ^{41}K . A particular reason to chose this element is the convenient mass ratio of four between dysprosium and potassium for the investigation of novel types of superfluidity with collisionally stable [130] strongly interacting fermionic mixtures (see Sec. 3.2.1).

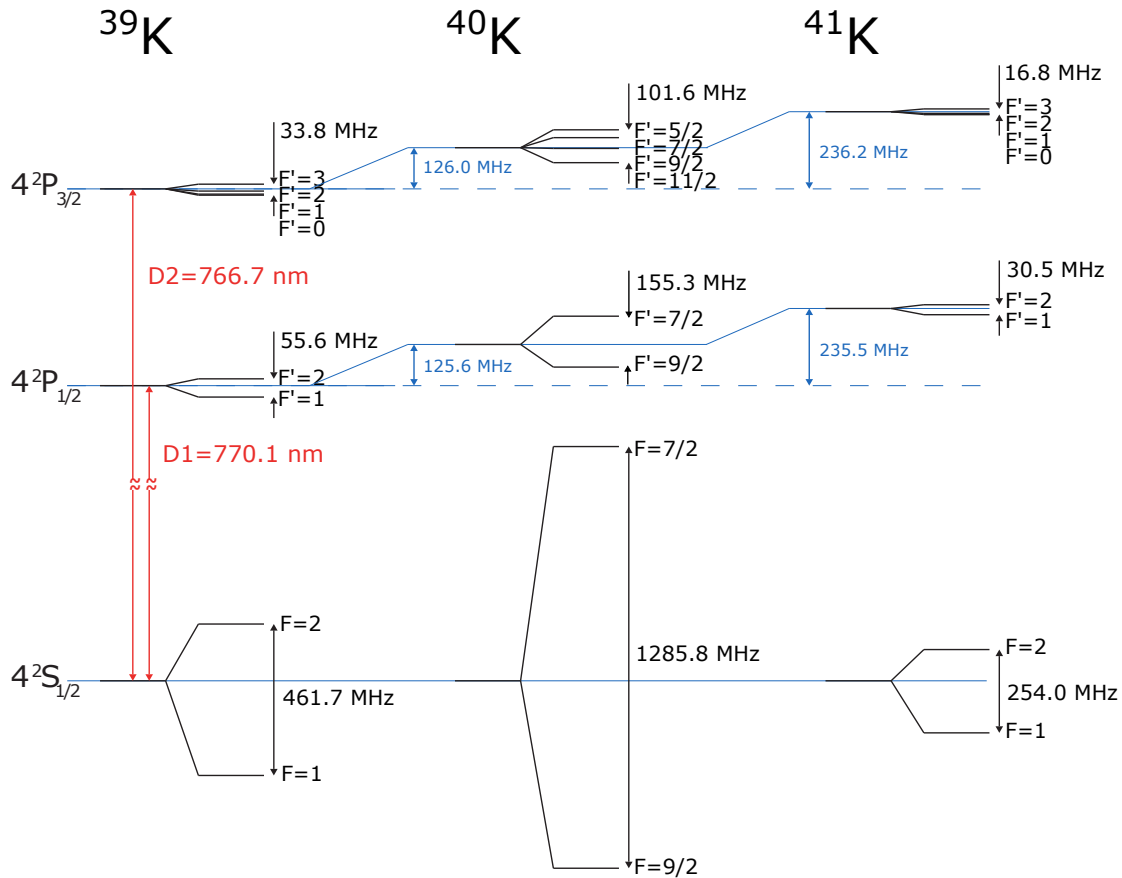


Figure 8.2.: Energy-level scheme of the three potassium isotopes. The red arrows show the D1 and the D2 transitions. The frequency values in blue are the isotope shifts in the fine structure. The frequency values in black give the difference between the lowest and the highest state in the corresponding hyperfine manifold. Note the inverted hyperfine structure of ^{40}K . Adjusted from Ref. [261].

Potassium has a hydrogen-like electronic structure, as shown for all its stable isotopes in

Figure 8.2. The light resonant with the D2 optical transition near 767 nm or with the D1 near 770 nm of potassium can be generated by many types of lasers: Ti:Sapph, diode lasers (amplified with tapered amplifiers (TA)), or through second-harmonic generation (SHG) from infrared (fiber) lasers. The isotope shifts are on the order of a few hundred MHz, so a single laser system could in principle be used for all isotopes. The hyperfine splitting of the $^2P_{3/2}$ state is well-resolved relative to the linewidth of the D2 transition $\Gamma_{767} \approx 2\pi \times 6$ MHz only for the fermionic isotope ^{40}K . This allows for sub-Doppler cooling with polarization gradients on the D2 line [290]. For the bosonic isotopes sub-Doppler cooling is achieved either with the well-resolved D1 line also with $\Gamma_{770} \approx 2\pi \times 6$ MHz [168] or by Raman sideband-cooling in a lattice [172, 328]. Another feature in the energy-level scheme of ^{40}K is the inversion of its hyperfine structure (see Fig. 8.2). This inversion of the ground and the excited-state hyperfine energies is caused by a large nuclear spin ($I=4$) that points in the opposite direction from the nuclear magnetic moment.

The possibilities to tune the interactions within an ultracold gas of potassium and its confinement are well-studied. Potassium exhibits magnetic Feshbach resonances, as do most alkali elements. The interactions between identical bosons, different spin-states of bosons and fermions and also in isotopic mixtures of potassium can be readily tuned by magnetic fields [279, 329–331]. Furthermore, the properties of potassium relevant for optical trapping are also well-known. The static and dynamic polarizabilities have been precisely calculated for a wide range of wavelengths and they have been benchmarked with experiments [332]. Also the so-called ‘magic’ wavelengths, for which the ground and excited states experience the same ac Stark shifts, are known and can be useful for attaining and manipulating a quantum gas of potassium at high PSD [332]. Experimentally, the isotope ^{40}K is the first fermion in an optical lattice [333], then in the Mott insulator phase [206], and it was further used in a special lattice to create Dirac points [334]. Those accumulated developments specifically with the fermionic isotope contribute to our decision to implement potassium in the mass-imbalanced Fermi-mixture.

The only drawback of ^{40}K is its low natural abundance of 0.02%. Work with ^{40}K demands isotopically enriched samples, as initially recognized in Ref. [53, 335]. The atomic samples in ampules or dispensers are usually enriched with ^{40}K to about 5% and can reach 10%. Both, the ampules for in-vacuum ovens and the dispensers with current activation, are not always available on the market. It is possible to construct the dispensers yourself, as described in a manual² [337].

The other alkali-metal option for a fermion would have been ^6Li . Many important experiments with fermionic spin mixtures have been successfully conducted with ^6Li . The molecular BEC [338] for example was achieved in an optical trap. The BEC-BCS crossover is well studied in ^6Li thanks to the very broad Feshbach resonance around 832 G, thus many of the universality measurements are with Li [339, 340]. However, lithium is a very light atom and in combination with most other fermions exceeds the mass ratio limit of 9, after which few-body effects dominate over many-body [130].

8.3. Dy-K interactions

In at least one isotopic combination of Dy and K we hope to find a favorable interspecies Feshbach resonance [76, 130, 132]. A great advantage of fermionic components for the investigation of strongly interacting many-body systems is the suppression of inelastic collisions

² The manual is part of an interesting wiki-page on ultracold atoms [336]

by the Pauli exclusion principle [75]. Therefore, we are interested in Fermi-Fermi and in Bose-Fermi Dy-K mixtures (see Sec. 3.2). Figure 8.3 depicts that in the mass-imbalanced Fermi-Fermi mixture unconventional pairing mechanisms should be observable in the strongly interacting regime. The mass ratio $m_{\text{Dy}}/m_{\text{K}} = 4$ lies above the predicted mass-imbalance limits for the appearance of many-body effects [128, 233]. Furthermore, this mass-ratio is still in the range where the atom-dimer and dimer-dimer inelastic collisions are strongly suppressed [130]. The only requirement for the achievement of the strongly interacting regime with suppressed collisional losses, besides low temperatures, is that the Feshbach resonance that is used to tune the scattering length is broad enough [76, 132].

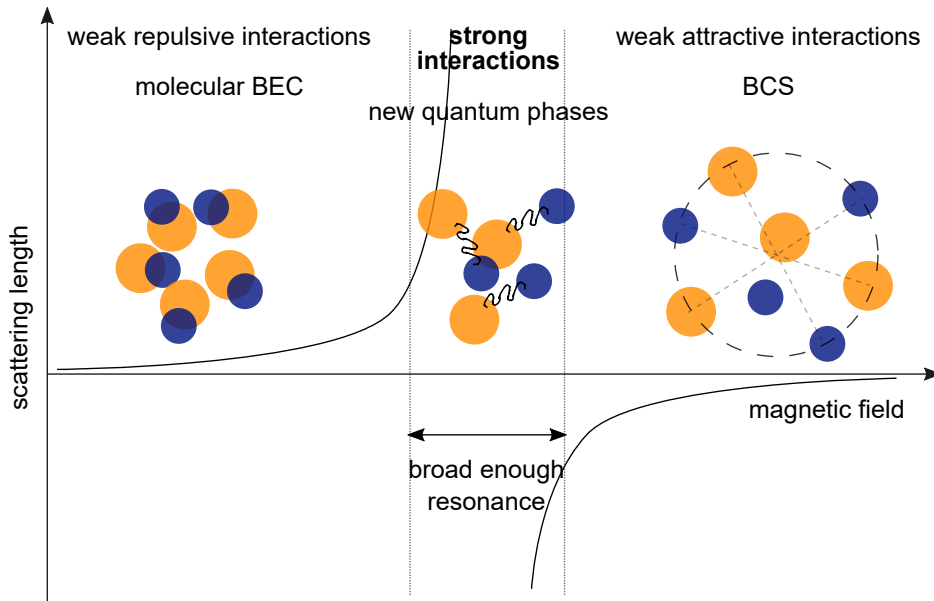


Figure 8.3.: Schematic of the interaction tuning through a BEC-BCS crossover with a fermionic Dy-K mixture. At sufficiently low temperatures, besides the unitarity regime, the mass-imbalanced ^{40}K - $^{161}\text{Dy}/^{163}\text{Dy}$ system should allow for exotic superfluid phases to emerge.

The complex electronic structure of dysprosium and the resulting anisotropy make predictions of intraspecies and interspecies Feshbach spectra based on scattering potentials difficult [147, 149, 151–153]. Due to the DDI in dysprosium all even/odd partial waves are involved in the scattering of bosons/fermions [147]. The density of intraspecies Feshbach resonances is very high with 4.3 G^{-1} for ^{164}Dy [149] and almost three times higher³ for a spin-mixture of the fermionic isotope ^{161}Dy [322]. In addition, the experimental observations with dysprosium show an increase in resonance density for increasing temperatures [149, 322], because more partial waves take part in a scattering event. The vast majority of the measured intraspecies Feshbach resonances in dysprosium are narrow. Nonetheless, a few broad Feshbach resonances with predominantly s -wave character in the Feshbach spectra of ^{164}Dy [326] and ^{162}Dy [341] also exist. Those resonances are found at easily achievable magnetic field values below 200 G and leave us optimistic that broad Feshbach resonances can also be found in our Dy-K ultracold system.

For the Dy-K mixture some rough estimations about the interspecies Feshbach spectrum

³ Here I do not give an exact number for the density of Feshbach resonances in ^{161}Dy , because it was determined for a total magnetic field range of only 6 G [322] compared to the magnetic field range of 70 G for ^{164}Dy [149].

can be attempted based on general considerations of two-body scattering and on theoretical predictions for other mixtures with lanthanide elements. The high density of intraspecies Feshbach resonances in dysprosium is due mainly to the DDI [147]. The strength of the DDI can be characterized by a universal dipolar scattering length $a_{\text{DD}} \propto \mu^2$ [237], where μ is the magnetic moment. For dysprosium $\mu_{\text{Dy}} \approx 10 \mu_{\text{B}}$ and for potassium $\mu_{\text{K}} \approx 1 \mu_{\text{B}}$ with the Bohr magneton μ_{B} . The two-body scattering cross section and therewith the elastic collision rate at low temperatures are proportional to the scattering length squared [138]. Considering that the total scattering length is the sum of the s -wave and the dipolar part, then the two-body scattering rate is proportional to the fourth power of the magnetic moment. Thus, for any isotopic mixture of Dy-K we expect a 100 times smaller scattering rate than in Dy-Dy. We therefore estimate a roughly 100 times less dense Feshbach spectrum for Dy-K than those measured for Dy-Dy. This rough estimation seems to hold for the mixture of Li and bosonic Er with $\mu_{\text{Er}} \approx 7 \mu_{\text{B}}$. There the predicted density of interspecies Feshbach resonances is 0.04 G^{-1} for ${}^6\text{Li-Er}$ and 0.07 G^{-1} for ${}^7\text{Li-Er}$ [153], while the intraspecies resonance density in erbium is around 3 G^{-1} [149]. The estimation approach through the magnetic moment breaks down for mixtures with nonmagnetic atoms, like Yb-Er [151] or Sr-Dy [152]. Nevertheless, we could use those theoretical works for a different estimation. With growing mass of the non-lanthanide element, the density of interspecies Feshbach resonances increases, because the spacing between molecular rotational levels decreases. The K-Dy mixture has a reduced mass in the middle between Li-Er and Yb-Er and thus also the resonance density should be rather in the middle of the range from 0.07 G^{-1} to 0.3 G^{-1} [151, 153]. The rough estimations from both approaches result in a density of Feshbach resonances in a Dy-K mixture to be on order of 0.1 G^{-1} .

The reasoning with the two-body scattering rate due to DDI can be also applied in the direction of the alkali element. Therewith we estimate a 100 times higher scattering rate for Dy-K than for K-K. We translate this into a higher probability to find a Feshbach resonance than in a bi-alkali mixture. So we do not need to look for a broad resonance up to field values of 3 kG as our colleagues did for the bi-alkali mixture, but a magnetic field up to 300 G should be enough. We expect to find a broad enough inter-species Feshbach resonance for at least one of the fermionic mixtures below 300 G.

Our main goal is to find a broad Feshbach resonance in a Fermi-Fermi mixture of ${}^{40}\text{K}$ and ${}^{161}\text{Dy}$ or ${}^{163}\text{Dy}$ in the respective lowest spin-state of the hyperfine manifold. The presence of two naturally abundant fermions in dysprosium doubles our chances for success. In addition, a broad resonance between a fermionic and a bosonic isotope of either species would be of interest for investigations of Fermi-Bose few-body effects. Also mass-imbalanced Fermi-Bose mixtures with tunable interactions in optical lattices are a possible research direction. For the Bose-Fermi mixture the number of isotopologues and therewith the chances to find a favorable Feshbach resonance are very high.

Dy-K machine

The prospect of the Dy-K machine is to be a modern experimental apparatus, which is stable as well as versatile. Excellent ultrahigh vacuum (UHV) and maximal optical access are the main requirements for any experimental apparatus with quantum degenerate gases. In this chapter I first present the design of the Dy-K experimental setup in Sec. 9.1 with emphasis on the required stability due to the mixture and the destructive detection method. The laser cooling of atoms from the oven to the three-dimensional magneto-optical trap (3D MOT) is referred to as ‘precooling’. An optimal precooling stage for fermionic potassium is a two-dimensional magneto-optical trap (2D MOT) and for dysprosium it is a Zeeman slower (ZS), as will be discussed in Sec. 9.2. The different cooling procedures for both species require a complex setup, where almost all parts of our vacuum system are custom. In addition to the desired stability, the setup has to offer flexibility because of the unknown inter-species properties. Our further approach to be flexible is presented in the middle of the chapter with the versatile main coil system in Sec. 9.3 and the high-power resonant laser sources in Sec. 9.4. Finally, in Sec. 9.5, I will present the outlook for the experimental setup, which is planned for from the start.

9.1. Design of the experimental setup

For this novel mixture of the lanthanide element dysprosium and the alkali element potassium the first goal is to identify the appropriate conditions for stability as well as for flexibility of the experimental setup. We looked into many PhD theses up to year 2013, which describe the design of a vacuum apparatus for atomic mixtures, magnetic atoms as dysprosium, erbium or chromium, and potassium alone in order to gain insight into practical and successful setups. Also the experience in Innsbruck with ultracold mixtures (RbCs, FeLiKx, Sr-Rb, KCs) and with erbium were of great influence to the new experiment. Figure 9.1 shows the progression of the vacuum design and helps identify the main constraints on the setup. First, Dy and K enter the main chamber from different sides, because of the differences in precooling (see Sec. 9.2). Second, the main chamber is the place for the 3D MOTs, but also for the investigation of the interactions in the preferably quantum-degenerate mixture. Thus, the main chamber requires high accessibility and imperative UHV. In the first planning stage in Fig. 9.1a) we can see ion-pumps (yellow) and vacuum gate valves (blue and red lines). The valves give, on the one hand, stability to the setup, since they can protect the ultrahigh vacuum in the main chamber during a refill of any of the ovens. On the other hand, the

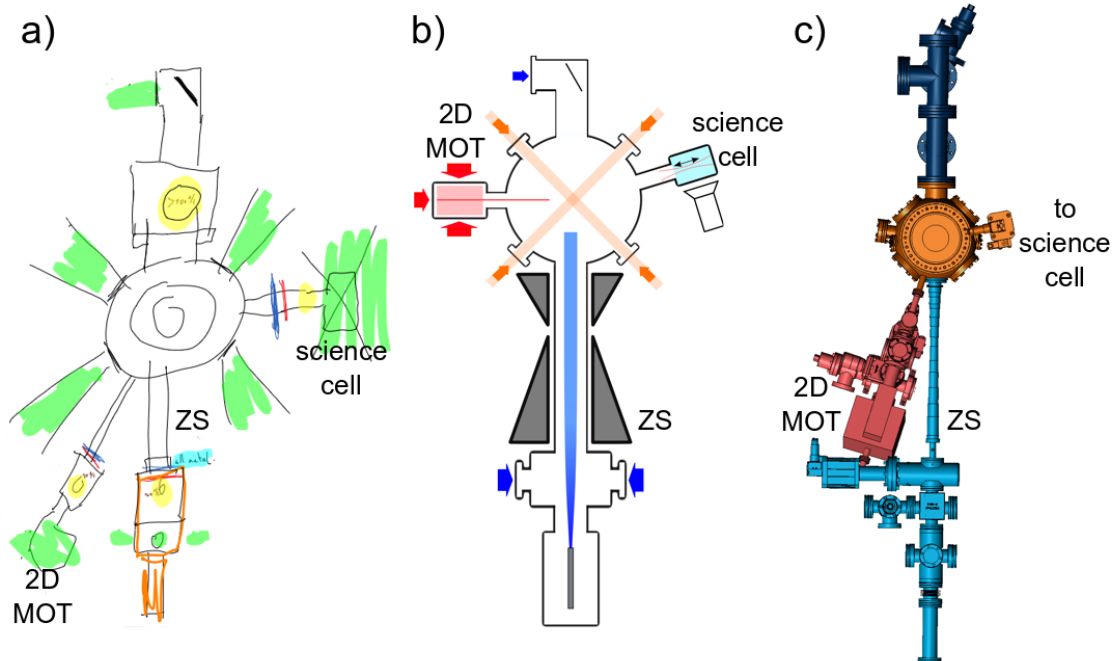


Figure 9.1.: Design steps in the development of the experimental setup. The sketch in a) underlines the main requirements on the vacuum setup: large optical access (laser light in green) and excellent vacuum (vacuum pumps in yellow and gate valves in blue and red lines). The schematic in b) depicts the optical spectrum for the cooling light, the different precooling stages for Dy and K, and the possible transport to the future science cell. The complex final setup in c) incorporates the concepts from a) and b) while being as compact and stable as possible.

valves offer flexibility, like the open end¹ to a future science cell, whose design will depend on the yet unknown properties of the Dy-K mixture (see Sec. 9.5). The valves at every entrance of the main chamber also allow to exchange existing parts in the setup, as we had to do with the dysprosium transverse cooling and also the potassium atomic source.

In the schematic in Fig. 9.1b) the vacuum pumps and valves are left out in favor of the main cooling laser beams: 421 nm (blue) for dysprosium precooling and imaging, 626 nm (orange) for dysprosium 3D MOT (overlapped with the potassium 3D MOT), 767 nm (red) for potassium 2D MOT, and an infrared dipole trap (black arrow indicating possible optical transport to the future science cell). These laser beams are marked in green in the sketch in Fig. 9.1a). From these two preliminary schematics we see already the many vacuum connections and the necessary optical access for the main chamber. In Fig. 9.1c) the design in SolidWorks is shown with the dysprosium slow-atoms-source in light blue, the potassium slow-atoms-source in red, and the main chamber in orange with its connections to vacuum pumps in dark blue. Our final vacuum setup for the mixture of those so different elements, Dy and K, attains a good level of compactness, stability and flexibility.

¹ In this chapter I refer to this closed gate valve as the link to the science cell, although the science cell is not yet installed.

9.1.1. Main chamber

The core of the Dy-K apparatus is a highly customized vacuum chamber. The view from the top of the chamber is shown in Fig. 9.2. Custom are the many versatile viewports, which offer high numerical aperture (NA), as well as the stainless steel vacuum piece. Top and bottom of the chamber contain the compact magnetic field coils (see Section 9.3) in re-entrant viewports that are for all beams in the direction of gravity. Radially we need to fit all the rest of the beams, the atom sources and the vacuum pumps. The main chamber is from Kimball Physics Inc., a modified MCF800 spherical cube made out of 316L grade stainless steel and a near-mirror surface polish (interior included). All flanges on the main chamber are in the Multi-CFTM (MCF) design [342], which is more compact but compatible with the usual ConFlatTM (CF) flange design. In addition, MCF flanges offer slightly larger bore sizes than CF and the outside diameter of one size can fit through the inside diameter of the next larger size. On that account, on multiple openings of the monolithic steel chamber a welded fitting ends in a MCF flange of the next larger size than the original opening. Therewith we effectively enlarge the area of the chamber. The custom made viewports are also in MCF design. The viewports are produced by the Special Techniques Group of the Culham Center for Fusion Energy. Their greatest advantage of those viewports is their high vacuum bake-out temperature. For us the bake-out temperature was limited by the optical coating on the viewports to 230 °C.

The primary constraints on the design of vacuum chamber come from the dysprosium MOT. First, the MOT is loaded from a high-temperature effusion cell followed by the long coil of the Zeeman slower (ZS). This hot and lengthy construction is placed in the horizontal plane for reasons of mechanical stability and water-cooling. The ZS-field ends at the wall of the main chamber and the slowed atomic beam fans out with a finite transverse velocity. In order to capture as many of the precooled atoms in the MOT in the middle of the main chamber, the path between end of ZS and edge of the MOT capture volume must be kept short. Thus, the diameter of the main chamber should be kept low for a good loading efficiency of the dysprosium MOT. Second, one of the narrow-line MOT beams is along gravity to ensure the spontaneous spin-polarization of the atomic sample (see Sec 2.3.2). Hence, the two other MOT axes are in the horizontal plane. Since we aim at large MOT-beam diameters for a large capture volume, four of the viewports in the horizontal plane are chosen to be MCF63.

The horizontal plane contains further the main optical dipole traps (ODTs), eventual transport beams, and the vacuum connection to a future science cell. A single-beam optical trap is open along the propagation direction of the trapping beam, so the transport and therewith the vacuum connection to a future science cell have to be in the horizontal plane. Furthermore, a deep optical trapping potential is achieved by a tight focus. For a given chamber diameter the tight focus requires a large beam diameter at the viewport and thus a large viewport size. In Fig. 9.2 we see the welded fitting for a MCF40 viewport that would allow a deep science dipole trap in the main chamber.

For the potassium source no space is left in the horizontal plane and none is available in the vertical, so the potassium source and precooling are tilted by 15° from the horizontal. The tilt of the entire potassium precooling setup can be clearly seen in the side view of the Dy-machine in Fig. 9.3. Also for the potassium precooling the transverse spread of the atoms limits the maximum allowed distance of the potassium cold-atoms-source from the main chamber.

In the main chamber a UHV is required. For a high pumping power the connection to

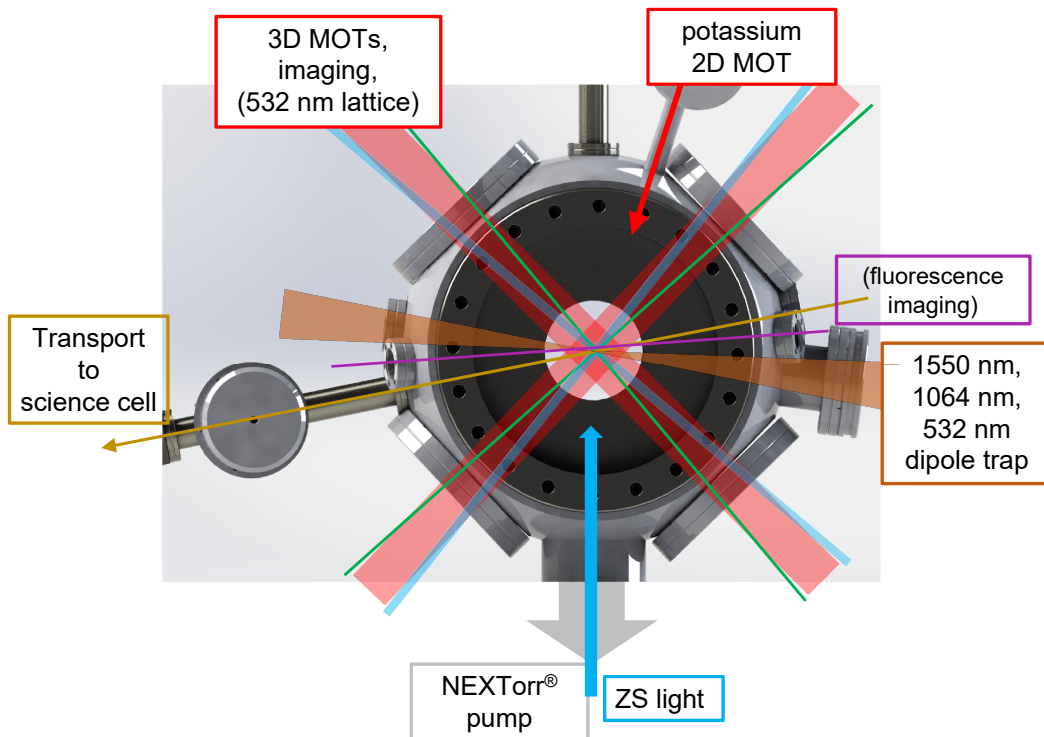


Figure 9.2.: View from the top of the main chamber with resonant and far-off resonant beams. The large MCF63 viewports are meant for the large 3D MOT beams, for imaging and eventually for an optical lattice at 532 nm. With the same antireflection coating for the visible range four MCF16 viewports are placed out of the horizontal plane and can be used for example for fluorescence imaging. The extended MCF40 viewport is meant for laser wavelengths for dipole trapping. The MCF16 viewports in the horizontal plane are also meant for far-off resonant beams. A large MCF60 fitting leads to the vacuum pump. We see in dark gray the top re-entrant viewport, which contains the main coils.

the vacuum pump has to be as large as possible. In our case it is a MCF63 flange, which is connected through a very short welded fitting to the chamber. The vacuum ion pump with a large non-evaporative getter (NEG) is located on the axis of the ZS-beam opposite to the Zeeman slower itself. The latter has a differential pumping section to the oven side, which provides four orders of magnitude pressure difference and protects the UHV in the main chamber [343]. On the potassium side there is also a four-orders-of-magnitude differential pumping stage. However, alkali atoms are known to be able to creep through such tubes [344]. On that account, in our design a NEG is implemented between the potassium differential pumping stage and the main chamber (see Fig. 9.4) to further ensure good vacuum at the core of the apparatus.

9.1.2. Stability

A double-species experiment requires a highly stable experimental setup to ensure the repeatability of measurements taken with destructive detection methods (see Sec. 2.3.4). The stability considerations involve the not easily controllable ambient magnetic field fluctuations, as well as thermal and mechanical stability.

An inevitable source of stray magnetic fields are the vacuum ion pumps. There, we opted for minimal possible ion pumps, where the pumping power is compensated by large NEG, which do not contain magnets. We use NEX Torr[®] pumps in the main chamber and in the dysprosium oven section, which can be seen as red cubes in Fig. 9.3. The alkali element requires a larger ion pump or it would clog the NEG very fast, so we have a pure ion getter pump (IGP) for the 2D MOT section. The IGP can be seen in the lower right end of Fig. 9.3. It is placed as far as possible from the main chamber and the dipole axis of its magnet is oriented for least impact on the magnetic field in the main chamber.

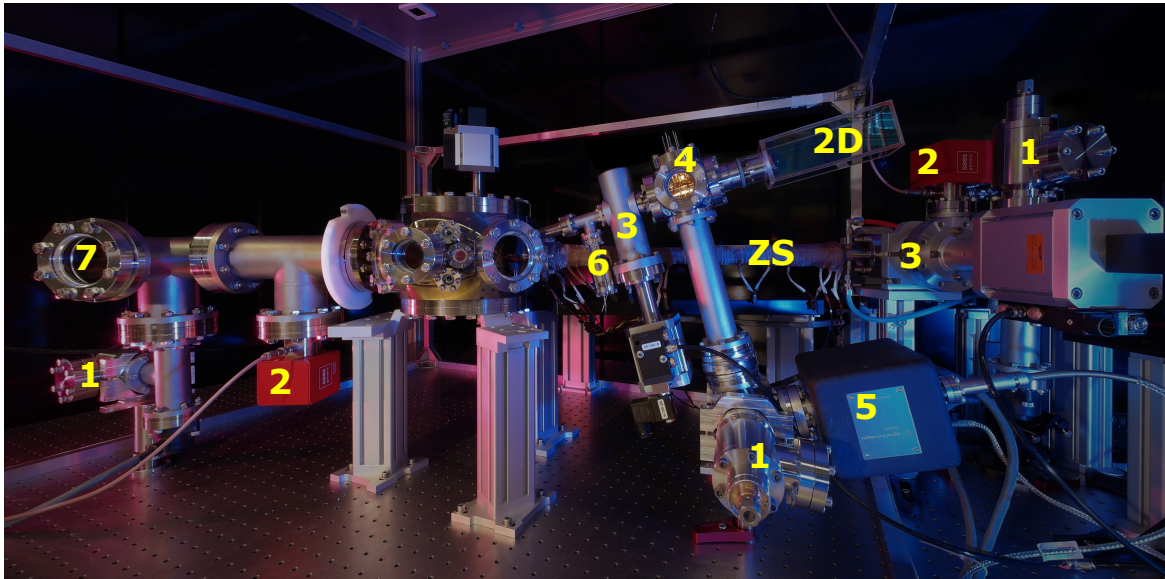


Figure 9.3.: Dy-K vacuum apparatus on the main optical table. On the right in the back we see the angle valve to a turbo vacuum pump (1) and the NEX Torr[®] pump (2) on the dysprosium oven side, followed by the gate valve (3) to the Zeeman slower (ZS). On the right in the front we see the large potassium 2D MOT cell (2D), the electrical feedthroughs for the dispensers (4), the ion-getter pump (5) and the angle valve to a turbo vacuum pump (1). Towards the main chamber there is another gate valve (3) and an additional NEG (6). On the left we see the entrance viewport for the ZS light (7), the third angle valve to a turbo vacuum pump (1) and the larger NEX Torr[®] pump (2) for the main chamber. The vacuum apparatus sits on aluminum feet filled with sand on the optical table, enclosed by black aluminum panels (here the black background). A large rectangular coil cage around the apparatus provides low homogeneous magnetic fields.

A further approach for preventing magnetic field fluctuations is to construct a preferably non-magnetic vacuum setup. For experiments with a magnetically sensitive element as dysprosium a magnetization of the vacuum apparatus can be fatal. Hence, all vacuum parts in the setup, including screws and washers, are made out of 316L or 316LN steel, which are the least responsive to magnetic fields [345]. Attention must be paid with welded parts made out of such steel, since processing can change the crystal structure of the alloy. We avoided welded parts where possible and otherwise checked their magnetic response before

implementing them in the setup. Also the optical setup around the vacuum apparatus is made of non-magnetic materials if possible. Furthermore, the power supplies for all magnetic fields except the 2D MOT gradient are placed outside of the laboratory. Therewith we aim to reduce thermal and magnetic fluctuations on the main optical table.

All parts of the setup on the main experimental table are meant to contribute to the overall stability of the experiment. The static background magnetic field, mostly Earth's magnetic field, at the position of the main chamber can be canceled by a large rectangular cage of coils (see Sec. 9.3). The aluminum frame for those Earth-field compensation coils appear in the background of Fig. 9.3. Inside the cage, large custom-fit aluminum breadboards are placed around the vacuum chamber, horizontally. The breadboards and the vacuum chamber are mounted on aluminum feet filled with sand, for possible vibration damping. The middle of the vacuum chamber and main horizontal plane for the optical paths are at 350 mm height above the main optical table. The breadboards have dense hole filling on any of their surfaces. On the side of the future science cell the breadboard consists of two parts. One part is a slice under the science cell, which can be removed in the future, but is indispensable for the initialization of the apparatus. The optics is mounted on 1-inch-diameter steel posts with well planned heights to avoid height-adjustable holders, which would bring instability to such a complex setup. All laser beams come from optical fibers from the neighboring laser table. The main experimental table is optically protected from the outside by black aluminum sliding panels (the black background of Fig. 9.3). Their core is made out of aluminum mesh, so the panels are light (6 kg a piece) and can withstand higher laser powers than plastic or fabric optical curtains². HEPA (high-efficiency particulate air) filtered air creates a slight overpressure at the main table, in order to keep dust away. The temperature on the main optical table is monitored, but not controlled further than with the laboratory air-conditioning settings.

9.1.3. Control

All changing experimental parameters are governed by the control system. In principle we could run the experiment with 4096 devices (digital, analog, or radio-frequency in- and outputs) with an update rate of 2 MHz. We use an updated version of the Control System software from [346] with a camera and data acquisition software developed in the Ultracold-Quantum-Matter and Dipolar-Quantum-Gases groups at the University of Innsbruck. The experimental parameters are set on the control computer and go from there through an National Instruments 32-bit digital output card NI6534 to the bussystem from [346]. The signal is referenced to a 10 MHz clock from a satellite signal and split into 5 galvanically isolated subbus systems. The time trigger can be synchronized with a mains electric power signal, in order to reduce the impact of 50 Hz noise on the experiment. Ground loops in the control system are avoided by galvanically isolated repeaters in the branching after each subbus. Each repeater controls preferably only one rack with outputs, which are powered by 5 V, ± 17.5 V and 24 V power supplies. Every clock cycle at 2 MHz we transmit eight bits to address an in- or output device and further 16 bits for the settings. A substantial role in the abilities of our experimental setup play the speed and resolution of the analog (and digital for shutters) output cards. They limit the complexity of an experimental run, since we cannot execute too many waveforms simultaneously. The home-made hardware system, based on circuits from [346], has also some bugs, mostly based on wrong power supply for the

² The black panels can be additionally used as blackboards.

electronics or false data repeaters. In total, the Control System is a reliable yet sometimes complex way to control all the experimental settings simultaneously.

The control program demands Windows as operating system for the Control computer. The computers for the imaging cameras, data analysis and backup run on Linux. Those computers communicate via TCP/IP and a router. Further, we have small single-board computers on the laser table, on which we operate the laser lock software (DiGiLock from Toptica) for multiple lasers via Remote Desktop Control. We use transportable Surface Pro's for flexible remote operation of the control computer or for measurement devices, such as a wavemeter, small Bluefox camera, polarimeter or beam-profiler.

9.2. Cold atomic beams: 2D MOT and Zeeman slower

As every experiment with ultracold atoms, the Dy-K mixture starts very hot indeed. The alkali and lanthanide elements have very different melting points, so they require different types of oven sources. One could implement two oven sections in series, separated by differential pumping sections, as in the erbium-lithium design described in the thesis of A. Frisch [321]. However, we chose to have a separate precooling stage per element. Thus the cold atomic beams of Dy and K atoms will enter the main chamber from different sides. The fermionic isotope of potassium has a notably small natural abundance and as typical for alkali elements a low melting point. Dysprosium, on the other hand, requires an effusion cell and coats any cold surfaces that are exposed to the oven orifice.

9.2.1. Potassium 2D MOT design

The precooling of potassium in the Dy-K experiment is done in a 2D MOT [177]. The main reason for this choice is to ensure the UHV in the main chamber. A Zeeman slower for fermionic potassium would allow for the more abundant bosonic isotopes to reach the main chamber as a thermal gas and contaminate the vacuum. Furthermore, a 2D MOT is more compact, produces less stray magnetic fields than a Zeeman slower, and delivers a transversely cold atomic sample. For fermionic potassium the highest loading rates from a 2D MOT up to 2013 have so far been achieved by the Li-K experiment in the group of Prof. Salomon in Paris [347]. So we adopted their vacuum design.

Our apparatus is presented in Figure 9.4 and consists of an elongated glass cell with a single flange connected to a CF40 cube (Kimball physics). The opposite side of the cube borders the gate valve to the main chamber and holds the differential pumping tube, that ends with a pierced mirror inside the glass cell. The mirror is for the axial molasses. The bottom cube surface connects to the vacuum pump (IGP) of the potassium 2D MOT and the angle valve for the turbo pump. The IGP is protected by a gate valve against possible damages to the capacitor plates due to the highly reactive potassium vapor. The top side of the CF40 cube contains a flange with five electrical feedthroughs. The current required for the potassium dispensers is relatively high with 3 A to 8 A. Two cube surfaces are closed by viewports (from Vacom) with broadband antireflection coating. They provide optical access into the dispenser area for eventual spectroscopy.

From previous experiments we learn that a ^{40}K 2D MOT is typically hungry for optical power [347]. Measurements from Ref. [347] show no saturation of the 3D MOT loading curve up to their maximal available total power. So we chose a doubly antireflection-coated glass cell to support our high power laser source (see Sec. 9.4.1). The coating on the inner and outer face of the glass cell means that the sides of the cell cannot be optically contacted, but

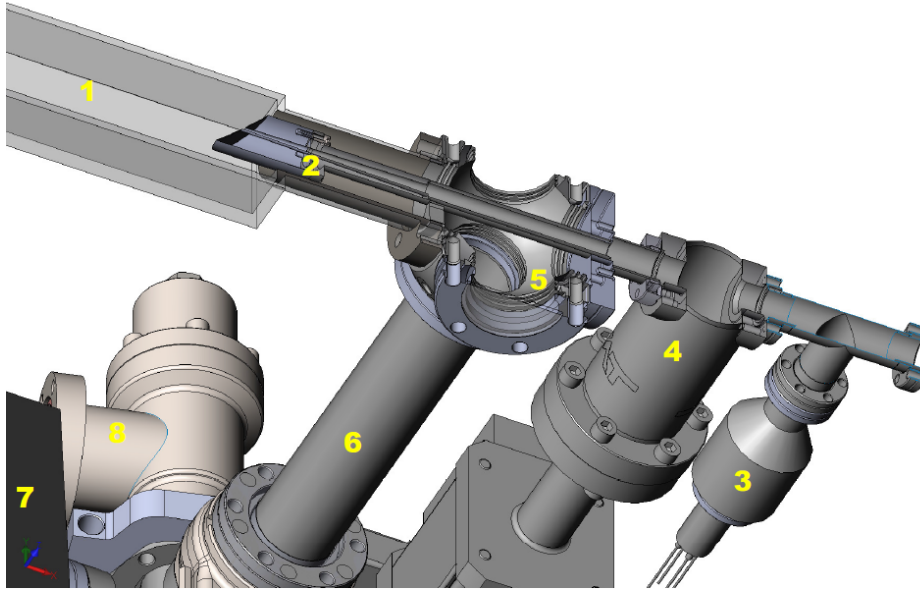


Figure 9.4.: Cut through the 2D MOT vacuum setup with view of the atomic path. The potassium dispensers are in the glass cell (1), where the atoms are cooled and sent to the main chamber through the conical tube in the in-vacuum-mirror (2), which is a four orders of magnitude differential pumping stage. In the bottom right we see the additional NEG (3) after the CF16 gate-valve (4). Support of the central CF40 cube (5) from the table comes along the long CF40 tube (6), attached to a fixed t-cross between IGP (ion getter pump) (7) and vacuum gate valve (8).

have to be glued to each other. This limits the maximal temperature for a vacuum bake-out to 120°C . Since the 2D MOT region does not require UHV, we decided that reducing reflection losses is more important than fast baking. The size of the cell seemed to be also important for the pre-cooling efficiency [347]. Unfortunately, we do not have data whether an elongated or a voluminous 2D MOT delivers a higher loading rate in the 3D MOT.

The transversely cold atomic beam is sent to the main chamber through a conical tube in the in-vacuum-mirror (see Fig. 9.4). Such a conical differential pumping design is modern and it is made with a wire electrical discharge machine at the IQOQI workshop. A sequential pumping stage is motivated by the 2D MOT in Paris [347]. The calculations according to Ref. [343] show that mainly the entrance face is important to ensure the necessary pressure difference. The conical design is equivalent to an infinite number of discrete steps between a small entrance face of 2 mm diameter and the MCF16 vacuum tube at the main chamber. Moreover, the conical design reduces loss of atoms because of diffusion due to the finite transverse velocity of the atoms from the 2D MOT. The typical pressure in the 2D MOT section is 1×10^{-9} mbar and the differential pumping stage gives four orders of magnitude pressure difference.

Our complete potassium precooling setup from Fig. 9.4 is tilted by 15° from the horizontal plane because of lack of space in the horizontal plane around the main chamber. The entire optomechanical setup of the 2D MOT is therefore tilted along with the optical breadboards. The stability and flexibility of this part of the DyK setup required very exact design of each optical, vacuum, or support element. The connection to the main chamber through the relatively small CF16 vacuum flange turned out to be delicate and susceptible to mechanical forces coming from an imperfect positioning of the entire 2D MOT setup. Nevertheless, the flexible optomechanical design around the glass cell allowed for multiple updates and changes

during the optimization of the 2D MOT.

Dispensers

The source of ^{40}K for ultracold gas experiments is a debated issue [53, 348], due to the low natural abundance of the fermionic isotope. We decided to use both types of commercial dispensers: enriched samples for investigations with ^{40}K and non-enriched samples for characterization work with ^{39}K . In the initial design the dispensers were attached directly to a vacuum flange with electrical feedthroughs (see Fig. 9.3). This position allows for an easy exchange of the dispensers without any disturbance of the optomechanical setup around the glass cell. We see in Fig. 9.4 the differential pumping tube holding the in-vacuum mirror. This long construction is stabilized by a cross-like holder in the port of the CF40 vacuum cube going to the glass cell. The dispensers hang from the top port of the cube around the differential pumping tube and their opening is oriented towards the glass cell. We assumed a diffusive atom output that would fill the entire volume with potassium vapor. Then, by having the glass cell as the coldest part in the vacuum setup, the potassium atoms would diffuse around the in-vacuum-mirror into the 2D MOT. However, as later fluorescence measurements suggest, the output from the dispensers is rather a strongly divergent, but directed atomic beam. So, in our case, most of the atoms were stuck on the cold surfaces of the differential pumping tube, its cross-like support and the back of the in-vacuum-mirror. This meant we had to operate at high dispenser current and emptied the initial atomic sources quickly.

A new design was made by E. Kirilov and was implemented in year 2017. It places the dispensers on long ceramic holders inside the glass cell oriented towards the zero-field axis of the 2D MOT. With this design, in order to exchange the dispensers the glass cell has to be removed from the CF40 cube. The difficulty is the limited space between the in-vacuum-mirror and the bottleneck of the glass cell. The dispensers have to fit through the bottleneck and also later not block the 2D MOT beams during operation. The strength and finesse of the new setup are the long ceramic holders for the dispensers. They hold the wires from the electrical feedthroughs to the dispensers. Their attachment to the cube allows for rotation and thus repositioning after entering the glass cell. With the dispenser inside the glass cell the operating current has to be adjusted carefully. At high dispenser current the in-vacuum mirror and the glass cell get coated with potassium.

Racetrack coils

The two-dimensionality of the atomic cloud in the 2D MOT is assured by the magnetic field coils in racetrack shape. For this precooling stage the magnetic field strength and the field gradient need to be zero along the main axis, which leads to the main chamber. Perpendicular to the main axis, at the long sides of the glass cell, we want to reach magnetic field gradients of up to 25 G/cm . We constructed a monolithic aluminum holder that holds all four racetrack coils together as close as possible to the glass cell. The schematic of the coil holder is shown in Figure 9.5. The glass cell is 58 mm wide outside, the holder is 64 mm inside and has 3 mm aluminum wall until the coil starts. The coils are made out of enameled round copper wire of 1 mm diameter. Each coil is wound on a lathe around the same master plate and then placed in the holder. The four identical coils of 40 windings are compact and are additionally glued with heat conducting epoxy to increase heat flow to the air-cooled mounting. Inside the coils we placed tiny NTC (negative temperature coefficient) thermistors to monitor the temperature. In addition, a thermistor with a limit temperature of 80°C is attached to the holder. The aluminum coil holder is mounted on specially made

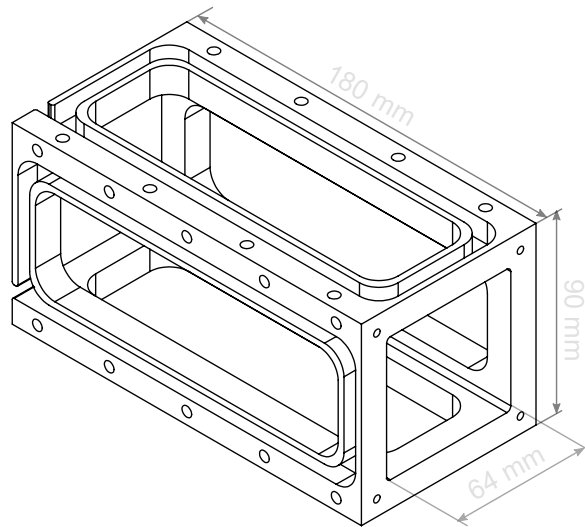


Figure 9.5.: Coil holder for the 2D MOT gradient coils. The monolithic aluminum design assures the stable coil geometry around the large glass cell for a clean long zero magnetic field along the 2D MOT axis. The tapped holes on the surface of the holder allow to mount optics in the vicinity of the glass cell.

aluminum feet to the 2D MOT breadboard. It additionally allows for attachment of optics close to the glass cell thanks to tapped holes along its surface.

The stability and the symmetry of the design with the monolithic holder and the identical coils assure zero field along the main axis in the 2D MOT and also high homogeneity of the magnetic field gradient across the glass cell. The simulation gives 2.7 G cm^{-1} per 1 A of current, while a fit of the measurement data delivers $2.6(1) \text{ G cm}^{-1} \text{ A}^{-1}$ (see M. Kreyer's master's thesis [349]). By using three individual power supplies, the zero line of the magnetic field can be shifted and aligned with the axis towards the main chamber, through the in-vacuum mirror and the differential pumping tube. One coil of each pair has its own power supply, whereas the two remaining coils are connected in series and driven by one power supply together.

To sum up, the potassium cold-atom-source is a large 2D MOT. It is loaded from enriched dispensers and operates at a comparatively low pressure. The entire 2D MOT setup is tilted by 15° from the horizontal plane.

9.2.2. Dy cold-atom-source

The precooling of dysprosium consists of a Zeeman slower with an effusion cell as a source of atoms. The high melting point of 1412°C requires careful design of the oven section. The strong blue transition of dysprosium near 421 nm allows for efficient collimation and precooling.

Effusion cell

For dysprosium we have a commercial effusion oven with an integrated atomic beam shutter from Dr. Eberl MBE-Komponenten GmbH. Such effusion cells are designed for sublimation or evaporation of elements with low partial pressure and are commonly used in molecular beam epitaxy. They are available on the market for different elements and temperatures.

In our cell a dysprosium sample³ is heated in the crucible by tantalum wire filaments. The heater is shielded and water cooled on the outside. A stability of 0.1 °C is specified for the commercial temperature controller delivered with the oven. The effusion cell has also a hot lip, which is always 100 °C warmer than the crucible in order to avoid clogging of the \varnothing 2.5 mm nozzle. The typical operation temperature of our dysprosium effusion oven is 1000 °C with a hot lip at 1100 °C. The effusion oven is connected to the vacuum setup via a port aligner, which allows for adjustment of the direction of the oven.

We anticipated that having a long nozzle would deliver a small output solid angle and thus a collimated beam of atoms. Unfortunately, plenty of hot dysprosium atoms leave the nozzle end in a solid angle of 2π and stick to the first cold surface they hit. We noticed this as our transverse cooling viewports began gradually to turn into mirrors from the inside. Also the gate valve on the way to the main chamber is susceptible to coating and eventually malfunctioned. The viewports and the gate valve were exchanged and the design was optimized for protection of those components: no direct line of sight between oven end and viewports, and additional apertures in front of the gate valve.

The design and positioning of the effusion cell are very important together with the protection of the additional vacuum setup through orifices. On top of the collimated atomic beam there is a thermal background exiting the end of the effusion cell, which is comparably low in atom number, but the apparatus needs to be protected from it in the long term. Nonetheless, the relatively high dysprosium MOT loading rate for low oven temperatures (see Sec. 10.1.2) confirms that we have a rather collimated atomic beam⁴, despite the spread of atoms from the nozzle end. The loading rate of the dysprosium 3D MOT is also insensitive to fine port aligner adjustments. This means that the nozzle length and size match nicely the Zeeman slower entrance position and size.

Transverse cooling

The transverse cooling is an important ingredient in dysprosium cooling. Since the 626 nm-MOT has a low capture velocity, the ZS must decelerate the dysprosium atoms to low enough longitudinal velocities. If the transverse velocity of the atoms leaving the ZS is comparable to their longitudinal velocity, then the atoms might escape the MOT capture volume sideways. To avoid this, the transverse velocity of the atoms should also be limited typically by transverse cooling with the broad optical transition near 421 nm. The transverse cooling beams should be as close as possible to the oven end, because the transverse cooling only collimates and doesn't refocus the effusive atomic beam. The atomic beam diameter allowed to enter the Zeeman slower is limited by the entrance cross section of the differential pumping, which ensures good vacuum in the main chamber (see Fig. 9.7).

The concept for the optical setup for the dysprosium transverse cooling is presented in Figure 9.6. The main optical component is a Powell lens. This laser-line generator-lens is a wedge with an aspherically curved roof top, which transforms a Gaussian beam entering the rounded roof into a uniformly illuminated line. The advantage compared to a telescopic setup with cylindrical lenses is that the Powell lens distributes the power uniformly along a line, contrary to the concentrated center and the fading edges of a Gaussian beam. Since the target of this beam is actually a line of atoms and not an ellipse, the limited laser power is used more efficiently. At the time we planned the setup the choice of Powell lenses was limited and the maximal entrance beam diameter was 0.8 mm. Because we wish to

³ We have used sheets, chunks or little bars of dysprosium with high purity.

⁴ We have even seen a tiny dysprosium MOT without the use of the Zeeman slower field.

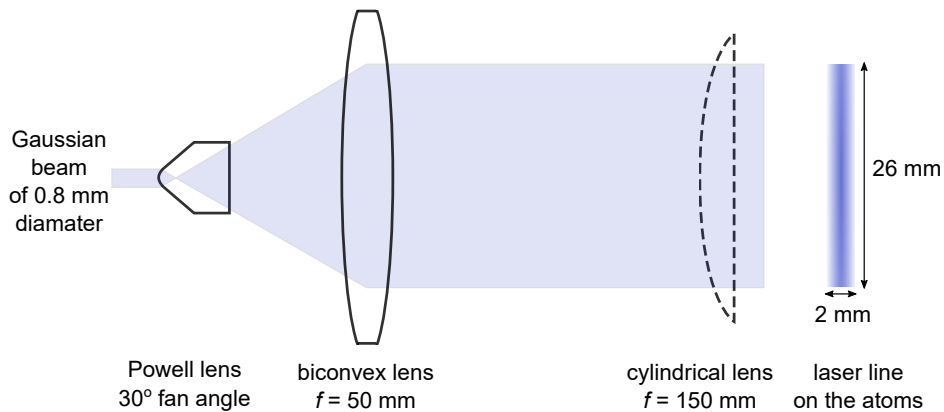


Figure 9.6.: For the dysprosium transverse cooling (TC) this optical setup produces a straight line of roughly equally distributed intensity out of a Gaussian laser beam. The Gaussian laser beam is sent through a Powell lens that stretches the beam into a uniformly illuminated line. This strongly divergent beam in one direction is collimated by a large biconvex lens and results in a roughly 26 mm long laser line. The biconvex lens forms an enlarging telescope together with a cylindrical convex lens in the unstretched direction (dashed outline) to match the size of the TC beam to the atomic beam of roughly 2 mm width.

transversely cool a 2 mm wide atomic beam and we have to collimate the fanning laser line, the setup in Fig. 9.6 contains additional lenses. The major loss with this setup are reflections at the Powell lens' surfaces. Nowadays, antireflection coated laser-line generators with larger entrance beam diameters are available. Such a Powell lens would reduce the intensity losses and simplify the optical setup.

We use two identical setups as the one in Fig. 9.6 for the horizontal and vertical direction of the TC. There is additionally a waveplate in the beam path to adjust the polarization of the 421 nm cooling light and in both directions the laser-line is retroreflected. The vertical TC-beam comes from the main optical table, underneath the vacuum apparatus. The vertical retroreflection setup is mounted on an optical cage system that is attached to the vacuum flange of the top TC-viewport. The setup for the horizontal TC-beam is built on breadboards, which are mounted on aluminum feet filled with sand, around the dysprosium oven vacuum-section. Next to the TC viewports in the horizontal plane, there is another set of viewports for possible spectroscopic measurements on the atomic beam. The strong effect of the transverse cooling to the loading of the dysprosium 3D MOT is shown in Fig. 10.5 in Sec. 10.1.2.

Zeeman slower

The design of the Zeeman slower (ZS) is inspired by the configuration used for the erbium experiment in Innsbruck [321] and is optimized thanks to newer machining tools. The Zeeman slower preparing atoms for a moderately narrow MOT has to end with a large cross section, because the longitudinal velocity of the atoms drops to the order of magnitude of the transverse velocity component and the decelerated atoms fan out. At the same time, the entrance cross section of the Zeeman slower should be small in order to serve as a differential pumping section between the oven and the main chamber. Our model, the erbium Zeeman slower [321], has a tube of 300 mm length and 8 mm diameter inside another tube of 460 mm length and 24 mm diameter. The larger tube ensures the wide ending of the Zeeman slower and at the same time enables evacuating the space around the thinner tube, which serves as a differential pumping section. However, the outer dimension of the Zeeman slower vacuum

tube has then a 40 mm diameter with the water cooling, which is relatively large as a the starting diameter for the ZS-coils. When the coils are far away from the center of the slower, larger currents or more massive coils are needed for the necessary magnetic fields and thus more heat is produced.

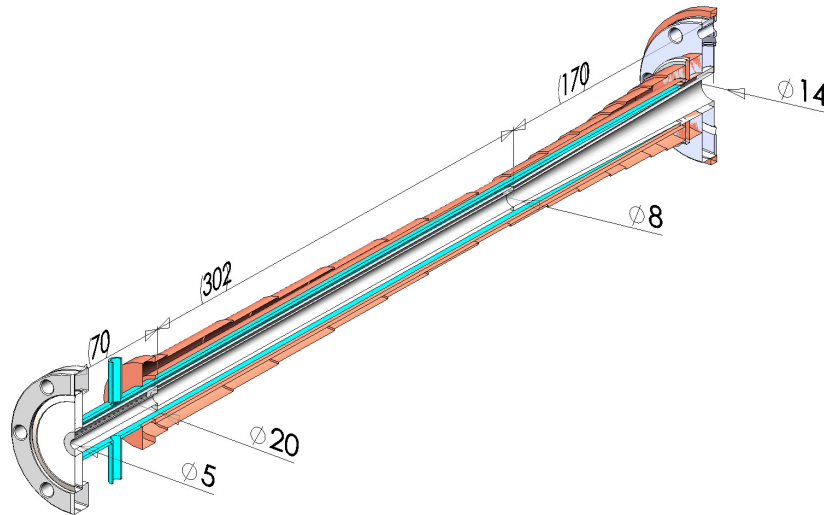


Figure 9.7.: Dysprosium Zeeman slower design. A compact set of coils around a water-cooling cylinder (in light blue) of only 20 mm diameter, ending with MCF40 vacuum flanges. Differential pumping on the oven side (70 mm long with 5 mm diameter), followed by the main ZS body of 302 mm with 8 mm diameter and the fancy conical end at 14 mm diameter. The magnetic field

The innovation in our design is to introduce a conical piece in the ZS tube, as shown in Fig. 9.7. The tube starts with a narrow 70 mm long differential pumping section of 5 mm diameter, goes over to a 300 mm long and 8 mm wide section and ends with a 170 mm long conical piece with an exit diameter of 14 mm. The differential pumping stage in the beginning of the Zeeman slower provides a pressure gradient of four orders of magnitude [343] and protects the UHV in the main chamber from the hot oven section. The entrance cross section of the ZS of only 5 mm strongly influences the resulting pressure gradient, but it also limits the volume of atoms that enter the Zeeman slower cooling stage. The conical part of the ZS is produced out of stainless steel with the wire electrical discharge machine at the IQOQI workshop and all parts were then welded together. The outer tube of the ZS is as narrow as the conical end allows and has a fin inside, which guides the water for the cooling of the coils. The water cooling inlets and outlets are both on the oven side, because the space close to the main chamber is precious. The conical end of the Zeeman slower allows for an outer diameter of the vacuum tube of only 24 mm and therewith a compact design of the coils.

The ZS coil construction is also inspired by the erbium ZS [321]. The ZS coil system consists of multiple coils, each powered by a separate power supply. All coils are made of the same type of enameled copper wire with 1 mm × 2.5 mm cross-section, which can withstand the vacuum bake-out temperature of 220 °C. The main coil has a variable number of windings along the tube (see Fig. 9.7) and provides the square root profile of the magnetic field. The start and end coils ensure the steep ends of the magnetic field profile and are crucial for setting the capture and end velocities of the ZS. One cylindrical coil around the entire tube can be used to shift the magnetic field profile up or down and in general provides fine tuning

of the capture range, but is currently not in use. And finally, there are two compensation coils on both sides of the main chamber (one of them is visible around the vacuum flange in Fig. 9.7), which eliminate any residual magnetic field and gradient at the position of the MOT due to the strong Zeeman slower field.

The magnetic field profile and coils are designed for a detuning of $-20\Gamma_{421}$ for the ZS light near 421 nm. It is important for this detuning to be large, because the transition is very broad ($\Gamma_{421} = 2\pi \times 32.2$ MHz) and the collected atoms in the middle of the MOT chamber still feel the light pressure from the ZS beam. The total frequency shift from resonance is about 650 MHz, which is a large frequency jump to be efficiently made with AOMs (see Sec. 9.4.2). The exact detuning of the ZS slower beam is not a critical parameter. For given ZS field and MOT beams configuration the dysprosium MOT loading stays the same for a range of about $-18.5\Gamma_{421}$ to $-22\Gamma_{421}$. The finicky part about the ZS beam is its geometry. The size in the MOT chamber and the position of the focal point around the Zeeman slower entrance are very sensitive parameters.

The Zeeman slower beam enters the vacuum chamber from the opposite side of the vacuum apparatus. The ZS beam enters along a direction perpendicular to the ZS axis before it is reflected by an aluminum in-vacuum mirror along the ZS axis. Thus, any hot dysprosium atoms flying through the entire apparatus would stick to the mirror and not to the viewport, as is the case in the Sr-Rb machine for comparison (see Sec. 5.1). Exactly the same vacuum mirror is also used in the erbium experiment [321]. The entrance viewport for the ZS beam is identical to the MCF63 viewports of the main chamber and allows high bake-out temperatures of the vacuum apparatus.

9.3. Main coils

Good control of the magnetic field allows for fine handling of the atomic ensembles. Stability and flexibility are here again highly desirable. In the main chamber of the DyK machine the magnetic fields are controlled by a set of (copper) coils assembled in a holder inside the recessed MCF180 vacuum flanges with 60 mm-wide viewports. We aim at a homogeneous field over a large volume up to a value of 300 G with possible fast jumps, a moderate constant field gradient up to 50 G cm^{-1} and a tunability in the curvature of the magnetic field. The important properties of the coils can be presented in two categories: static and dynamic. Static properties are size and maximum field or field-gradient attainable. The limit in speed of the magnetic field jumps and noise are dynamical properties. Both types of properties are strongly influenced by the power supply for the coil. The temperature change is also a dynamical property, but thanks to the watercooling we operate most coils at $18(1)^\circ\text{C}$.

Figure 9.8 shows a cut through the cylindrical coil assembly. The coil holder in gray and the enclosed water-cooling is specially designed to hold and cool all coils in the re-entrant viewports⁵. The holder is made out of a brass alloy that has a possibly low magnetization and a relatively high resistance. The coils are pressed in the holder via brackets, screwed to the flange of the top and bottom viewports. This ensures symmetry in the concentric positioning as well as in the distance from the middle of the chamber. The holder is electrically isolated from the main chamber by Kapton[®] tape on the sides and by custom-made Teflon[®] rings and caps at the tap holes. The coil holder consists of two parts. The bottom part contains

⁵ Three holders, consisting each of a main part for water-cooling with brazed lid and a top cylindrical coil holder, were produced at the mechanical workshop at the Institute of Experimental Physics at the University of Innsbruck for the Ultracold Quantum Matter group of Prof. Grimm.

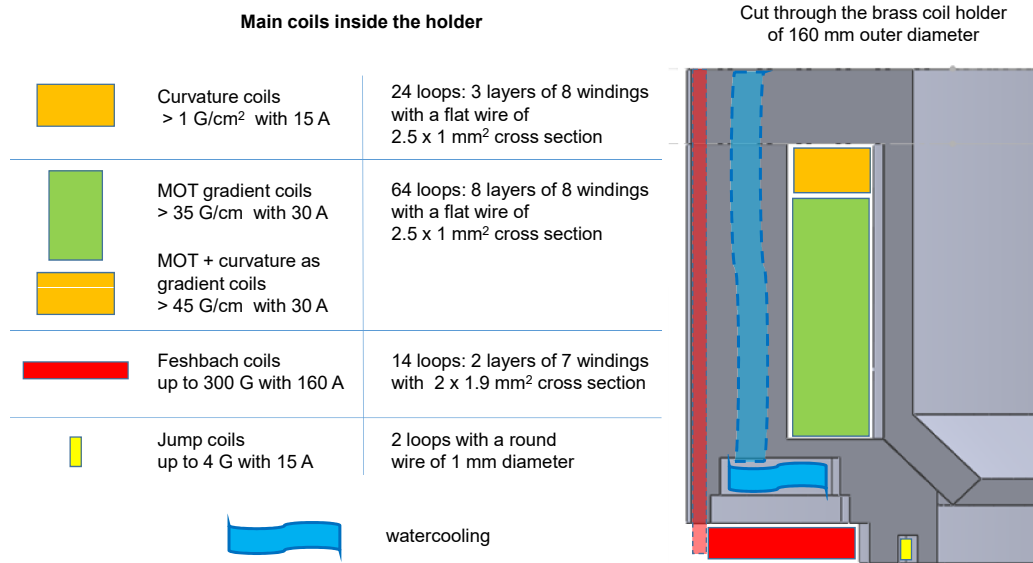


Figure 9.8.: Arrangement of the main coils in the coil holder. The curvature, gradient and homogeneous magnetic field coils are placed in a brass holder. In the radial cut-through one can also see the channel for the watercooling along the Feshbach coil. Underneath the ‘water’ a lid is brazed to the holder. The shaded red and blue horizontal symbols show the electrical and water connections for the Feshbach coil and water cooling, respectively. These connections limit the outer diameter of the gradient and curvature coils. Such a set of holder with coils is positioned inside the top and the bottom re-entrant MCF180 flanges of the main chamber.

the watercooling, the Feshbach and the jumps coils. The top part of the holder is like a lid, around which are wound the gradient and curvature coils. Both parts of the holder have a slit of 2 mm, in order to open the conducting circuit of the round holders and minimize eddy currents.

Figure 9.8 shows a sketch of all the main coils. In red is the Feshbach coil, which is the most special of our coils and will be described in detail in the following. Also for homogeneous fields we have the small ‘jump’ coil. Further away from the atoms are the MOT and curvature coils, which can be switched in any current configuration. The simulated magnetic field strength and gradient produced by each coil pair for 1 A are given in Figure 9.10.

Feshbach coil

For the coils which produce the offset field we aim for a Helmholtz configuration for optimal homogeneity of the magnetic field at the position of the atoms in the middle of the main chamber. With the homogeneous field we wish to tune the interactions between and/or within the atomic ensembles, so we name this coil pair the ‘Feshbach coil’. A Helmholtz configuration is when the radius of the coils equals the distance between the coil pair. Then, the gradient and the curvature of the field produced by such a coil pair are zero. The Feshbach coil is placed at the bottom of the inverted viewports, as close as possible to the atoms. This position inside the steel main chamber also insures lower eddy currents than a placement outside the metallic chamber. The distance between the recessed viewports is 63 mm and the maximum allowed outer radius for the coil is 76 mm. These spatial constraints given by the main chamber in addition to the physical requirements of a homogeneous field

up to 300 G with possible fast jumps, lead to the design of a very compact coil with low inductance.

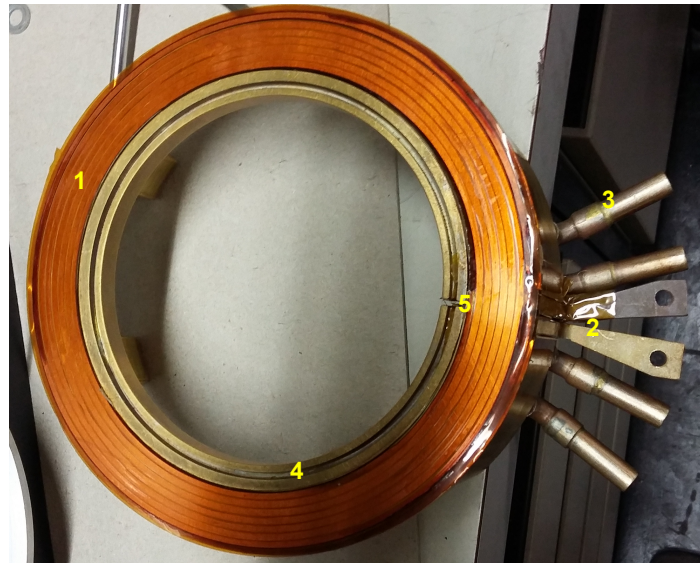


Figure 9.9.: Wire-cut Feshbach coil in holder with watercooling. The thin Feshbach coil (1) is isolated with Kapton[®] foil around the two layers (brown-orange foil) and with thin Teflon[®] band along the windings (faintly visible as white lines between some windings). The current connectors (2) are also isolated by Kapton[®] tape and have a possibly large cross-section for the connection of low-resistance cables. There are four connectors for watercooling (3) because the cross section on the side of the coil holder is smaller than the cross section along the water channel inside the coil holder. Further visible on that picture are the groove in the coil holder for the jump coil (4) and also the slit in the holder (5) for reducing eddy currents.

The necessary geometry for a Helmholtz configuration is a very flat coil. Another consideration is that the current carrying wires for the current through the coil should be adjacent, in order to avoid stray magnetic fields in the vicinity of the atoms. This means that the coil has to have an even number of layers. In addition, the number of windings enters quadratically in the calculation of the coil inductance, which we wish to keep as low as possible. A wire-wound coil cannot conform to all these criteria. Therefore, the Feshbach coils for the Dy-K experiment were manufactured out of 2 mm-thin sheets of copper in a spiral shape with a wire cutter machine at the mechanical workshop of IQOQI, Innsbruck. Two copper layers of 76 mm outer radius with seven windings to 52 mm inner radius are connected at the inner radius by a braze. A picture of the Feshbach coil is shown in Figure 9.9. The windings are isolated by a Teflon[®] wire, which is introduced by hand. The two layers are isolated from each other and from the chamber and cooling body by a Kapton[®] foil⁶. For comparison, the breakdown voltage through Kapton[®] of about 200 kV/mm is much larger than the 3 kV/mm in dry air. The isolating foil is very thin, only 75 μm , out of which 25 μm are Kapton[®] and the rest is adhesive that is activated by high temperatures or pressure. After positioning the Teflon[®] ribbon and the Kapton[®] foil between the windings and layers of the coil, the Feshbach coil is pressed to the holder and baked at 180 °C. After this bake-out the coil is well-isolated and glued to the coil holder. The rest of the electrical isolation, like the current connectors in Fig. 9.9 or the entire outer surface of coil holder is realized with Kapton[®] tape.

⁶ DuPont Pyralux bond ply LF0111

The compact design of the coil allows in theory for very fast changes in the magnetic field strength. The relatively low number of windings of only 14 per Feshbach coil results in a low coil inductance compared to typical (wire-wound) homogeneous field coils for ultracold experiments. The theoretical limit for the switching time of the coil is given by $\tau_{\text{coil}} = L/R$ and the current slope for switching on the coils is U_{max}/L . The inductance L of a single Feshbach coil is $30 \mu\text{H}$ (measured with an LRC meter), so in series the coil pair has a total inductance of $L_{\text{FB}} = 60 \mu\text{H}$, where FB stands for Feshbach. The estimated maximal necessary magnetic field in our experiments is achievable with the compact coils, however, with high currents. For the desired 300 G the design of the coils with 1.9 G/A (see Fig. 9.10 a)) demands more than 150 A. With such high currents, the resistance of the entire circuit has to be kept low to minimize Joule heating. The Feshbach coil pair alone has a resistance $\leq 0.05 \Omega$. Together with the cables to the power supply, which are 9 m long with a cross section of 100 mm^2 (a type of welding cable), and the imperfections of the connectors the total resistance is about $R_{\text{FB}} = 0.1 \Omega$. Hence, the switching time for the Feshbach coil should be $\tau_{\text{coil}} = 0.6 \text{ ms}$. Given the relatively high resistance of the circuit for the homogeneous field, the available voltage U_{max} from the power source is a crucial parameter. A stack of batteries is an optimal power source, since it can decouple the coil system from the 50 Hz-noise of the electrical grid and allows for high voltages. For the measurements presented in Sec. 10.3 we use a SM15-200D power supply from Delta Elektronika. For this power supply with $U_{\text{max}} = 15 \text{ V}$ and the measured circuit resistance, we get an initial slope for the switching of the Feshbach magnetic field of around 230 G/ms. For faster large jumps in magnetic field one needs a power supply with a higher voltage, whereas for fast small jumps, we have the jump coil.

Regarding the static magnetic field shown in Fig. 9.10 a), the Feshbach coils perform as planned. The centering of the coil pair and the distance in between is taken care of by the placement in the recessed vacuum flanges. We have measured the magnetic field along the symmetry axis of a single coil with a fluxgate magnetometer⁷ and the measurement is conform with the simulations, which are also used for Fig 9.10. In the Helmholtz configuration the magnetic field gradient is less than 3 mG/cm across a volume of 1 cm^3 around the center of the main chamber (see Fig. 9.10 b)). The corresponding field curvature is also very low. These are very good conditions for the use of relatively narrow Feshbach resonances for smooth interaction tuning throughout the entire atomic cloud.

‘Jump’ coil

The ‘jump’ coil is meant for small fast jumps in the homogeneous magnetic field around a Feshbach resonance. The ‘jump’ coil pair is almost in a Helmholtz configuration as can be seen from the calculations in Fig. 9.10 c) and d). The small size of each jump coil of only two windings should allow for very fast magnetic field changes when combined with appropriate current control. The jump coil is made out of enameled copper wire of 1 mm diameter and the coil pair has a resistance of $R_{\text{jump}} = 0.0237 \Omega$. The current configuration through the ‘jump’ coil pair could be switched for positive or negative magnetic field shifts.

Gradient coil (MOT coil)

The coil pair that delivers the magnetic field gradient mainly for the MOTs is called the gradient or MOT coil. For its design the physical requirements for the very different MOT

⁷ A single axis fluxgate magnetometer Mag-01 with a Mag G probe from Bartington[®] Instruments.

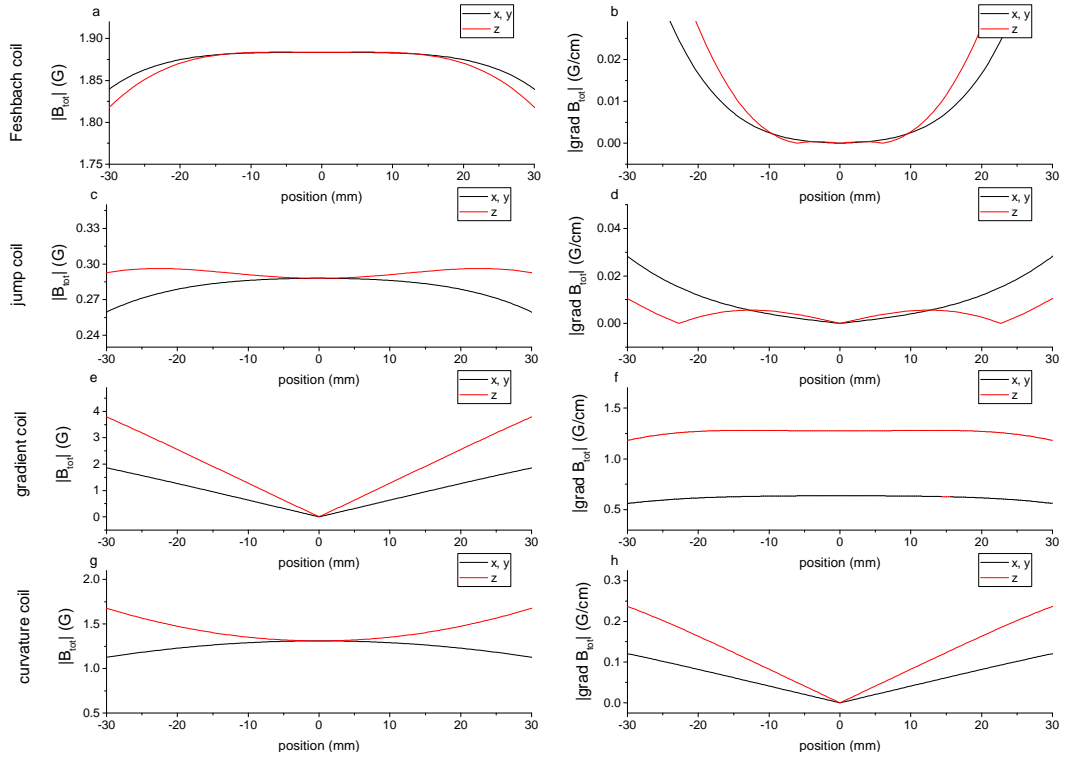


Figure 9.10.: Magnetic fields and their gradients generated by the main coil system. All values are for 1 A current through the respective coil. In red are given the field and it's gradient along the symmetry axis and gravity direction z . The radial directions x and y are given in black. The curvature of the magnetic field in the center of the chamber is negligible for all coils, except for the curvature coil that shows a notable linear change in the magnetic field gradient in h).

operation modes for dysprosium and potassium are important. Furthermore, some geometrical restrictions from the coil holder in the recessed viewports must be considered. On the one hand, the narrow line MOT of Dy requires low magnetic field gradients on the order of 1 G/cm, that can be smoothly controlled for the loading of the atomic cloud in the ODT. On the other hand, the alkali element potassium calls for a high field gradient for a compressed MOT on the order of 30 G/cm or even a magnetic trap with 60 G/cm for efficient loading into an ODT. One approach to incorporate a low tunable gradient with a very high gradient in the same coil system is to actually have a set of coils. This approach is depicted in Fig. 9.8, where we show how the curvature coil can be used as an addition to the MOT coil. The other approach would be to have a very sensitive and powerful power supply with a good current control, which can handle both modes of operation. We use a power supply⁸ with 80 V maximal output voltage, 60 A maximal output current, 1.5 kW power and an accuracy $< 0.2\%$. This setup does not allow for a magnetic trap, but the MOTs of both elements can be tuned freely.

The geometrical design of the MOT (and curvature) coils strongly depends on the coil holder inside the recessed viewports. Since the interaction tuning by magnetic Feshbach resonances is crucial for the experiment, the most value is set on the Feshbach coils and their cooling. The rest of the coils must fit in the remaining volume as shown in Fig. 9.8. The

⁸ EA-PS 8080-60 from Eletro-Automatik.

outer diameter of the MOT and curvature coils is limited by the in- and outlet channels for the watercooling of the coil-holder to 136 mm. A single gradient coil consists of 64 windings (8 layers of 8 windings) of the same wire as used for the Zeeman slower coil, namely enameled copper wire with $1\text{ mm} \times 2.5\text{ mm}$ cross-section. The MOT coils are designed to have minimal curvature, not maximum gradient, and deliver about $1.2\text{ G cm}^{-1}\text{ A}^{-1}$. Figure 9.10 f) shows that the gradient of the magnetic field is nearly constant in each direction throughout the entire volume of the large dysprosium MOT. The gradient field is also used for levitation of Dy to equilibrate the trap depths for both species in the ODT [95]. The MOT coils were designed with inductance of 0.8 mH per coil, we measured $L = 0.72(5)\text{ mH}$. We can switch the direction of the gradient field thanks to an H-bridge in the current circuit. The current carrying cable for the gradient and curvature coils is a four-core cable⁹, where the cores of 10 mm^2 copper cross-section are each isolated and twisted concentrically. The entire cable is wrapped with braided tinned-copper wires, which we connect to earth-ground on one side of the cable to screen from interference effects from other cables or power supplies. The large number of windings and the 6 m-long current carrying cables to the power supply result in a relatively high total resistance of $R_{\text{grad}} = 0.8\ \Omega$.

Curvature coil

Most experiments do not have a Helmholtz configuration for the homogeneous field coils, so they need a so called curvature coil to compensate for inhomogeneities. We put great effort into designing the magnetic field as homogeneous as possible and still we included curvature coils. A curvature magnetic trap can be used for axial confinement in addition to a single beam ODT, which provides mostly radial confinement, as in the case of the ^6Li experiment in Innsbruck [350]. For Dy a magnetic field curvature of 0.9 G/cm^2 results in an axial trapping frequency of about 20 Hz. Such a harmonic confinement with a magnetic trap is achieved when the current through both coils runs in the same direction (often misleadingly called ‘Helmholtz’ configuration in contrast to the again misleading ‘Anti-Helmholtz’ current configuration for the quadrupole field of the gradient coils). The magnetic field and gradient of the curvature coils are shown in Fig. 9.10 g) and h). The curvature in the middle of the chamber is almost constant with $0.08\text{ G cm}^{-2}\text{ A}^{-1}$.

Each curvature coil consists of 22 windings in the same geometry as the gradient coils. Both coils are highly symmetric, since they are wound around the lid of the coil holder and pressed against the water-cooled part. The electrical properties of the curvature coil can be deduced from the symmetry with the gradient coils. An H-bridge can be installed in the curvature coil circuit, such that the current direction in a single coil is changed. Then the curvature coil pair can be used as a prolongation of the MOT coils and thus produce a larger magnetic field gradient (see Fig. 9.8).

Imaging coil

The quantization along the horizontal imaging axis is ensured by a pair of coils wound around the MCF60 viewport flanges. They consist of 20 windings of the round copper wire also used for the ‘jump’ coil and the racetrack coils of the 2D MOT. The power supply for this coil pair limits the switching time and thus the coil must be switched on a few milliseconds before the camera trigger.

⁹ EMC-optimized (electromagnetic compatibility) motor cable ÖLFLEX® SERVO 2YSLCY-JB from Lapp Group. Unfortunately, we couldn’t find such highly protected cables with a large enough copper cross-section for the Feshbach coil and there we use a so-called welding cable.

Large compensation coil cube/ Earth coil

The static background magnetic field, mostly Earth's magnetic field, can be canceled by a large rectangular cage of coils centered at the main chamber. This cage is inspired by the design around the Sr-Rb apparatus [190]. In the vertical z direction the coil is 0.7 m high, in x direction (short side of the main optical table) the length is 1 m and in the third direction it is 1.2 m long. The cage is centered at the middle of the main chamber and due to its size it had to be installed before the assembly of the vacuum apparatus. The coils are wound from the enameled copper wire with $1\text{ mm} \times 2.5\text{ mm}$ cross-section, that is also used for ZS and gradient coils. The attainable magnetic fields are per design $B_z = 10\text{ G}$, $B_x = B_y = 5\text{ G}$. In the x directions the ambient magnetic field is very low and so the necessary current for the X-coil is close to zero and changes sign. For this we implemented bipolar power supplies for all three directions for consistency.

Coil control

Next to the coils and their power supplies, the quality of the magnetic fields as experimental tools for controlling the cold atoms is determined by the stabilization of the coil current. The static fields like in the Zeeman slower, in the 2D MOT, or in the large coil cage, rely on the stability given by the power supplies. The control of the gradient and homogeneous magnetic fields in the main chamber, however, is achieved by stabilizing the current by home-made electronics. Each coil circuit passes through a current transducer¹⁰, which measures accurately the current and feeds it into our device to produce an error-signal for the PID controller. The PID output controls the gate voltage of a line of MOSFETs, which act as the current switch and regulator. The high currents for the coils are distributed over the parallel MOSFETs, so it is crucial to use transistors that have similar performances and to build this electrical setup on a water-cooled plate. The analog PIDs, that we are using, can be optimized for a certain set value of the current and are never optimal for the entire current range of the power supply. This is because the PID is optimized for the response of the entire circuit. This changes depending on the wanted current value, the corresponding available voltage from the power supply, and also on the temperature of the building blocks (coil, connectors, MOSFET line). In addition to the control of the current stability, the coil circuits include some security measures. Every coil circuit comprises a varistor, which would protect the parts of a coil circuit from an inductive voltage spike. To every coil in the main coil holder we attached temperature sensors and thermistor switches to monitor the water-cooling. The thermistor switches and the flow-rate sensors that directly monitor the water-cooling can be connected to an interlock security switch¹¹. This interlock switch would turn off the power supplies for the coils in case of a temperature rise. This is especially important for the Feshbach coils, which are positioned directly inside the recessed viewports and the vacuum viewports support only a limited rate of temperature change.

All the power supplies for the coils on the main table (Zeeman Slower, main chamber, 2D MOT racetrack coils, compensation cage) are outside the laboratory, in order to reduce electrical and thermal noise close to the main chamber. This requires however longer cables between coils and power supplies, where the voltage drop has to be considered as well as possible antenna build-ups through bad cable positioning.

¹⁰ For the Feshbach coil we use the current transducer Ultrastab 867-200I from Danfysik. For the gradient coil we use the current transducer IT 200-S Ultrastab from LEM and the current carrying wire passes three times through the transducer.

¹¹ We use the commercial control system PNOZ mm0.1p from Pilz GmbH & Co. KG.

9.4. Resonant laser systems

The last ingredient for an experiment with ultracold atoms after the UHV apparatus and the magnetic field coils are the laser systems. For laser cooling we need frequency and amplitude stabilized lasers. In the Dy-K experiment we wish to achieve additional stability by having high-power laser sources. Furthermore, we aim at flexibility in the experiment by implementing the possibility to easily switch between the different isotopes of dysprosium and potassium. In the laboratory next to the 2 m long main table is a 6 m long optical table with all the necessary laser systems for laser cooling. We have many wavelengths from 421 nm to 1551 nm and we use different laser types: solid state (bulk and fiber) and semiconductor lasers. The light from the laser table is transported to the main table via power-suitable polarization maintaining fibers. The frequency stabilization of most resonant lasers uses the corresponding atomic transition as a reference. The stability of all laser systems simultaneously is required for conducting experiments with ultracold gases, especially due to the resonant imaging, which is a destructive type of detection and demands repeatability.

9.4.1. K lasers

The cooling of potassium in the Dy-K experiment relies on powerful laser sources mostly because of the use of large cooling beams. First, for a large capture range of the 2D MOT, we use the large glass cell presented in Section 9.2.1 and also large optical elements around it. Second, the 3D MOT beams for K and Dy at 767 nm and 626 nm, respectively, are overlapped already at the laser table and transmitted to the experiment using the same fiber. This saves space around the main chamber. However, the large MOT beam diameter for better capturing dysprosium is 35 mm and therewith unusually large for an alkali.

The potassium cooling wavelength is near 767 nm, which is available from diode lasers (amplified by tapered amplifiers (TAs)), Ti:Sapph directly or through frequency doubling from the infrared (IR) spectrum near 1534 nm. The typical laser setup for an alkali element consists of a master diode laser and an arrangement of tapered amplifiers (and/or slave lasers). Acousto-optical modulators (AOMs) are used for frequency shifts and fast, mechanics-free switching on and off of the laser light. The usual potassium reference point for frequency stabilization is the ^{39}K ground-state crossover resonance in saturation spectroscopy¹². Then AOMs shift the laser frequency to resonance and repumper frequency of a chosen isotope. The repumper frequency for the D2 line of the fermionic potassium isotope is 1.2 GHz away from the cooling frequency, while for the bosonic isotopes the shift is < 500 MHz (see Fig. 8.2). This makes an isotopically flexible diode laser setup with AOMs a power costly effort, because typical AOM frequencies are between 70 MHz and 400 MHz. In the Dy-K experiment the objective is to be able to switch isotopes from the control room (with a mouse click), even from shot to shot would be great. Therefore an electronic detuning control with a bandwidth covering all isotopes is needed.

IR fiber lasers

The laser system that should be able to fulfill our requirements for high output power and isotopic flexibility is a the fiber based system presented in Figure 9.11 and described in more

¹² The ground state crossover signal is relatively strong, because the hyperfine splitting of the excited state of the D2 line in the most abundant isotope ^{39}K is not resolved relative to Γ_{767} (see Fig. 8.2). In addition, the hyperfine splitting of the ground-state of ^{39}K is small enough, so that the velocity classes responsible for the crossover are well populated.

detail in the master's thesis [349]. A seed fiber laser at 1533 nm and 50 kHz linewidth feeds two identical fiber amplifiers for 10 W output each. Before the amplifiers the light passes through fiber-coupled phase modulators, which imprint frequency sidebands that act as the repumper. The frequency and amplitude of the sidebands can be varied depending on the isotope and on the application in the 2D or 3D MOT. The large bandwidth of the electro-optical modulator (EOM) of 20 GHz (due to its small size) allows for a remote control of the frequency, without changes in the optical setup. Flexibility between isotopes is not the only advantage of the fiber-laser-scheme. The IR light is frequency doubled (and mixed) in a free-space PPLN crystal (single pass periodically poled nonlinear crystal) after each fiber amplifier. This results in about 1.2 W at 767 nm for the 2D and 3D MOT each. Thus, the fiber based laser systems gives enough power and independent tunability of the 2D and 3D MOTs.

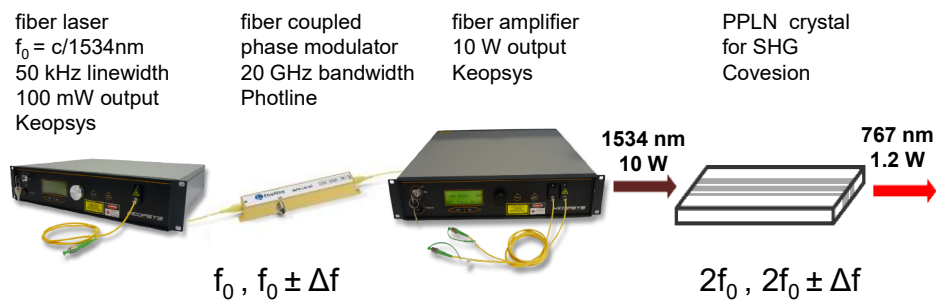


Figure 9.11.: Potassium resonant light generation in the fiber-based setup. The output of the fiber laser at f_0 with a narrow linewidth goes through a fiber-coupled EOM and seeds a fiber amplifier with $f_0 \pm \Delta f$. The amplified output is then frequency doubled (mixed) in a free space PPLN crystal and the main output frequencies are $2f_0$ and $2f_0 \pm \Delta f$. Except for the seed laser, all components are in double versions and allow independent control of the 2D MOT the 3D MOT light settings.

The reference for the frequency stabilization of this fiber laser setup is the usual potassium ground state crossover of ^{39}K from modulation transfer spectroscopy in a potassium spectroscopy cell. One of the advantages of the fiber laser with the EOM was supposed to be the easy and quick swap of isotopes. An issue with our setup appears for ^{39}K since the lock point is distorted by the almost resonant repumper sidebands in the spectroscopy cell (see Ref [349] for a detailed explanation and more possible solutions). An elegant solution for the many sidebands in the spectroscopy is to implement a fiber-coupled EOM at 767 nm that undoes what the first EOM at 1550 nm did. Notice this scheme works with the second-harmonic generation (SHG) in between the modulating and demodulating EOM.

Although this fiber-laser-based system seems to have many advantages for the laser cooling of the alkali metal potassium, the technical specifications of the fiber amplifiers appear to be unreliable for high output power. Due to repeated and unresolvable technical issues with the fiber amplifiers from Keopsys, in 2017 the potassium laser system was switched to a Ti:Sapph laser.

Ti:Sapph laser

The solid state laser from M^2 with around 6 W output power at 767 nm is the current laser source for the D2 line of potassium. The linewidth of the laser is only around 1 kHz. The repumper is still produced using an EOM, only this time it is in free space. The resonance frequency of this device with a much larger crystal cannot be changed, contrary to the small

fiber-coupled EOM. One advantage of the EOM still is power efficiency. The laser is locked to the ground state crossover of ^{39}K . The laser frequency is very close to a transition in gaseous O_2 , so that the cavity of the solid state laser has to be regularly purged with nitrogen.

D1 laser systems

For additional cooling of potassium, a laser system on the D1-line of ^{40}K was implemented. At first we operated a diode laser with a cat-eye design from Moglabs near 770 nm with a linewidth of about 100 kHz and output power up to 180 mW. The laser is locked to a separate potassium spectroscopy cell than the D2 lasers, since the setups are physically far apart, but it also makes them independent. The necessary frequency shifts from and to the lock-point are performed using AOMs. The major issue of this setup is the limited available power or the short laser-diode lifetime of around three months at the highest output power. So a fibre laser setup similar to the one from Fig. 9.11 was later on built for the D1-line. This time a fibre amplifier from Quantel operating at 1140 nm with about 8 W output power is used.

9.4.2. Dy lasers

The multitude of laser types and wavelengths in the dysprosium laser setups is the evidence of a major transformation in the research with ultracold atoms. For some time the ultracold experiments were rather restricted to alkali atoms because the wavelengths of the optical transitions were easily accessible. For the cooling of non-alkali elements a broader spectrum of wavelengths must be generated. Moreover, the narrow optical transitions require a higher stability of the lasers and their linewidths. In contrast to cold ions, where UV and narrow lines are usual, the laser cooling and trapping of neutral atoms requires higher optical power. Luckily, as fundamental research advances also do the applied sciences¹³, such that the laser range of products can cover most of our needs. For the Dy-K experiment we use laser diodes and tapered amplifiers, also blue laser diodes, fiber lasers and fiber amplifiers and different frequency mixing techniques to produce the light necessary for dysprosium cooling. The lasers are stabilized with the appropriate technique to an atomic, optical or cavity reference. The frequency shifts to the precise experimental values are achieved by AOMs, EOMs and/or beat-lock electronics. In the blue laser system we can switch isotopes remotely.

Blue laser system

For the blue transition in dysprosium near 421 nm (see Fig. 8.1) there are a couple of options for the laser source. Either a system with a high power source in the IR near 842 nm, which is then frequency doubled into the blue, or directly using blue diode lasers. In our experiment actually both systems are used, one as a high power source and one as reference. Therewith it is possible to easily switch between dysprosium isotopes (see Fig 9.13). Besides the resonant frequency, the requirements for our experiment are strict on the minimal available power, while the linewidth of the laser is not crucial because of the broad optical transition. The laser source at 421 nm should have a linewidth smaller than 3 MHz ($\approx \Gamma_{421}/10$) and an output power greater than 500 mW. Since the blue cooling transition is broad, the saturation intensity is high, thus the initial cooling is hungry for power. Options for blue laser light sources and details on the 421 nm laser system of the Dy-K experiment can be found in Appendix B.

¹³ A good example of the importance of advancing laser technology is the 2014 Nobel Prize in physics for the development of blue light emitting diodes [351], which lead to a new class of ECDLs in the blue spectrum.

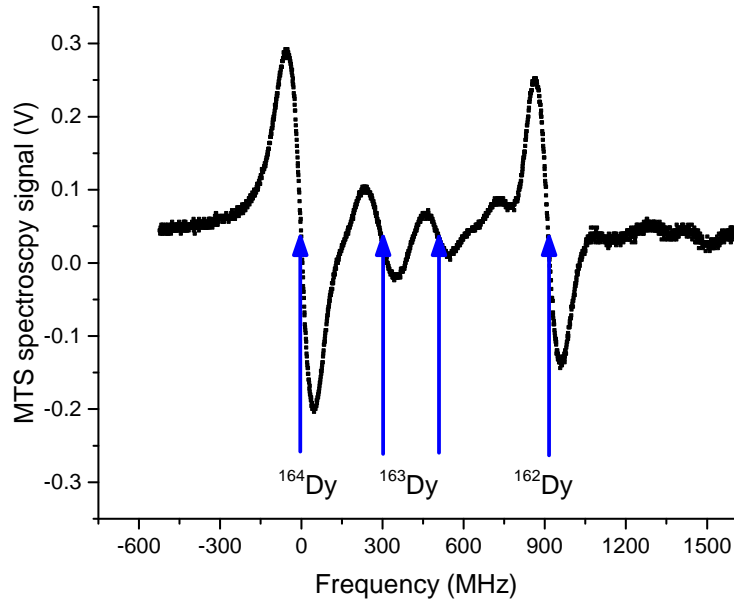


Figure 9.12.: Modulation transfer spectroscopy (MTS) signal at the hollow cathode lamp (HCL) of dysprosium. The arrows indicate zero crossings coming from the ^{164}Dy isotope at 0 MHz, a crossover between the two highest hyperfine states of ^{163}Dy at 297 MHz, a clear signal from the $F = 8.5$ hyperfine manifold of ^{163}Dy at 506 MHz and again a large signal for the second most abundant boson, the ^{162}Dy isotope at 913 MHz. The blue diode laser runs in a single mode only for a limited frequency range, so the ^{161}Dy and ^{160}Dy isotopes are not detected here.

The precooling of dysprosium demands high power for both, the nearly resonant transverse cooling (TC) and the highly detuned Zeeman slowing (ZS) beam of about $-20\Gamma_{421}$. The main laser source near 421 nm is a TA SHG pro laser from Toptica (the laser scheme is shown in Fig. B.1, Appendix B) with 600 mW output power. An external cavity diode laser at 842 nm with a linewidth of less than 300 kHz seeds a high power TA chip for an output of 1.5 W IR. After beam shaping, the light is frequency doubled in a bow-tie ring cavity with a nonlinear crystal¹⁴. The typically available output power in the blue is 600 mW. The laser can be referenced directly to the atomic transition of one of the dysprosium bosons. For more tunability though, a beat-lock (or frequency offset stabilization) is implemented to a second blue light source that is referenced to the ^{164}Dy isotope. The high-power commercial laser is in general stable in frequency and output power, only the SHG alignment must be optimized every couple of months. One issue with the blue laser setup was assuring efficient and stable fiber coupling. On the one hand, the optical elements for the blue visual spectrum are not always reliable¹⁵ and on the other hand, the highest diffraction efficiencies of the AOMs do not yield Gaussian beams. So an iterative optimization of AOM and fiber coupling efficiency was necessary. For the case, that the optical power of the blue setup was limited by the transport from one optical table to the other, the entire setup is built on a relatively compact breadboard. This way, one could place the blue high-power setup on the main optical table.

¹⁴ The type of the crystal is a corporate secret of Toptica.

¹⁵ We had bad experience with Schaefer and Kirchhoff fiber couplers, confirmed by the company as defective lens batch.

Atomic reference and frequency settings For referencing the laser to the atoms we perform spectroscopy on the 421 nm transition in dysprosium in a hollow cathode lamp (HCL) with a buffer gas of argon. Details on the HCL and the modulation transfer spectroscopy can be found in Appendix B. In Figure 9.12 the modulation transfer signal with the most abundant bosonic isotopes is shown and also the hyperfine structure of the ^{163}Dy fermion is visible. The relative amplitudes of the observed signals reflect the natural isotope abundances. Noticeable in Fig. 9.12 is the frequency separation of almost 1 GHz between ^{164}Dy and ^{162}Dy . The isotope shift between ^{164}Dy and the fermionic ^{161}Dy is even > 2 GHz. Those shifts are not efficiently bridgeable with AOMs, in contrast to the case of strontium (see Table 5.1). To overcome this, we lock a blue diode laser (DLpro from Toptica) with about 15 mW total output power to the ^{164}Dy isotope and use it as an optical reference at a 7 GHz fast photodiode¹⁶ for frequency offset locking of the high-power blue laser. This so-called ‘beat-lock’ allows for fast and GHz-long jumps of the main laser, such that cooling and imaging of dysprosium isotopic mixtures in the experiment should be possible (see Fig 9.13). For the spectroscopy at the HCL and the frequency shift to the beat-lock, the blue diode laser is used at the high end of the specified output power of 15 mW. A typical issue then is that the DLpro runs in a single mode only for a narrow range of current and temperature settings, which drift on the timescale of several weeks. Other than that, the entire blue laser system is generally stable. The used frequencies for laser cooling and imaging near 421 nm for all isotopes are shown in Figure 9.13. The frequency of the main laser (called SHG laser in the figure) lies between the ZS frequency and resonance (or TC), which are $20\Gamma_{421}$ apart. This large distance of 740 MHz is bridged by single pass AOMs for TC and ZS of ± 320 MHz respectively, in order to avoid increased power loss through a double pass. With only single passes we cannot freely tune the ZS and TC frequencies, but we save power. The initial frequency tuning is done by the lock and then fixed at the optimum. The beat-lock frequency referencing technique and the stability of the SHG laser allow for fast electronic switching between dysprosium isotopes. The set value of the beat-lock frequency can be only in a given range and with a fixed sign. Details on the beat-lock are given in Appendix B.

Narrow-lines laser systems

After the precooling on the broad blue line of dysprosium follows a narrow-line 3D MOT near 626 nm (see Fig. 8.1 or Sec. 2.3.2). This narrow transition sets the spectral linewidth as the most significant criterion for the laser system. The source of 626 nm can be a dye laser, a SHG system as for the blue, or a sum frequency generation (SFG) system. Dye lasers are cumbersome to work with. The SHG system works well, however it gives a linewidth in the order of 100 kHz. The sum frequency generation scheme for 626 nm stems from work with Beryllium ions at 313 nm [352] and in 2013 was already successfully implemented for dysprosium in the group of Prof. Pfau in Stuttgart [324]. It is based on fiber lasers and amplifiers at standard wavelengths, which makes this system cheaper than an SHG setup. We built the exact same laser system as in Ref. [324] with fiber lasers and amplifiers from NKT and a PPLN crystal for the SFG from Covision. For the SFG in the PPLN crystal a stable optical setup has to be designed, where the crucial parameter is the matching size of both beams in the crystal.

The seed fibre lasers have narrow linewidths themselves (< 1 kHz the 1550 nm and < 10 kHz the 1051 nm according to the specifications) and deliver appropriate SFG results. We end up with 1.5 W of 626 nm light. The transport of the high laser power to the main table via

¹⁶ Ultrafast Si photodetector UPD-50-SP from ALPHALAS GmbH

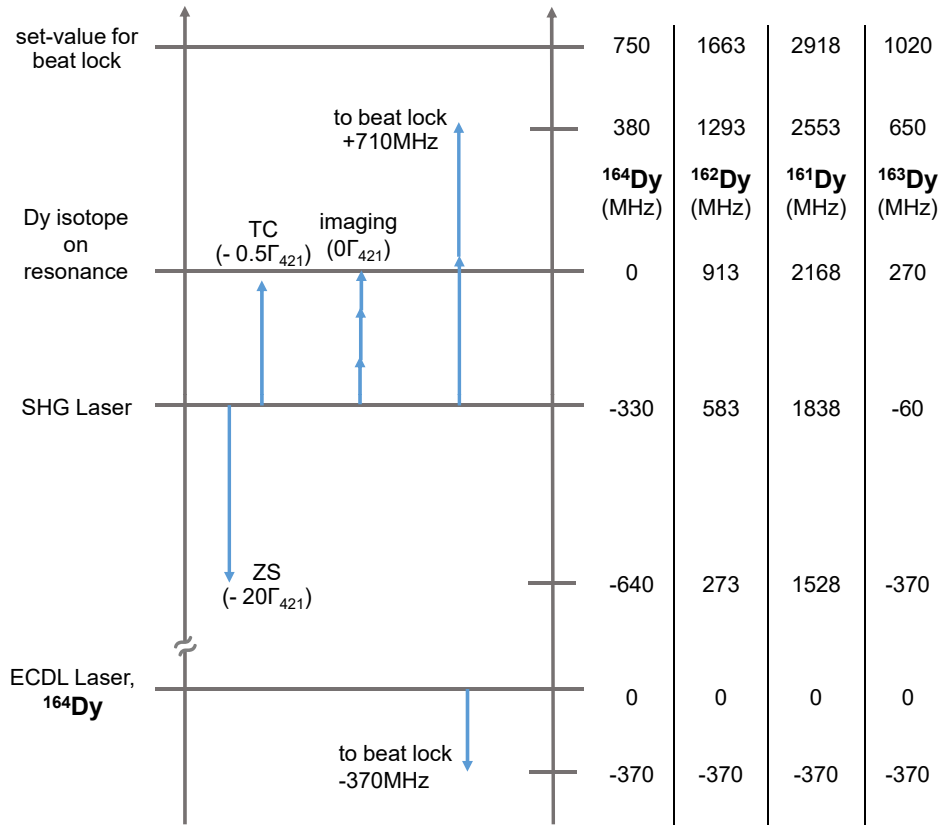


Figure 9.13.: Frequency shifts between different laser beams in the 421 nm setup. Each blue arrow is a single pass through an AOM. The blue ECDL is always on resonance with ^{164}Dy . A beam shifted by -370MHz from the ECDL is overlapped with a beam shifted by 720MHz from the SHG laser for the beat-lock signal. With the setting of the beat-lock frequency the high-power laser can switch between Dy isotopes. The frequencies for ZS and TC are fixed, only the frequency for imaging is tunable with a double-pass AOM.

high-power polarization-maintaining fibres is not especially stable. However, for the stages of the dysprosium MOT the light intensity is changed by a few orders of magnitude. Therefore, an AOM on the laser table and a photo-diode on the main table are implemented to control the power level of the 626nm light. In addition, a free-space EOM on the laser table is used to introduce many frequency sidebands spaced by 104kHz to the 626nm laser light and thus artificially ‘broaden’ the dysprosium cooling transition, by addressing atoms from different velocity classes.

The 626nm system is not stabilized on a spectroscopy signal from the HCL because of the pressure broadening coming from the buffer gas. The HCL lamp was used once with red light to reference the ultra-low expansion (ULE) cavity, to which the 626nm system is stabilized. The specified linewidth of the reference cavity of about 30kHz for 626nm should be larger than the linewidth of the laser light coming from the laser sources with a narrow spectral linewidth in the IR. The actual linewidth of the 626nm light has not been explicitly measured. We are not yet able to switch isotopes with the 626nm light as fast as with the beat-lock system for the 421nm light.

The 741nm laser system is in planning. It is based on a cat-eye laser from Moglabs with

total power of 100 mW. In the future if linewidths of the laser below 1 kHz have to be reached, then also fiber noise cancellation in the laboratory needs to be implemented.

The ULE cavity in the Dy-K experiment is designed to be used as a reference for the narrow optical transitions in dysprosium, which are at 626 nm and 741 nm (see Fig. 8.1 or Table 2.1). In addition, the 842 nm source light for the 421 nm transition could also be locked to the same cavity. The finesse of the reference cavity is highest for 741 nm. The ULE cavity is bought from Stable Laser Systems with the special demand for zero crossing of the expansion coefficient at temperatures above 25 °C. The reason is that the housing contains only heating and no cooling elements. The zero crossing of our ULE cavity is at 27.74(3) °C.

9.5. Experimental outlook

The mixture of Dy and K has unknown properties, so the experimental setup has to offer flexibility. The resonant laser systems are built for easy change between isotopes, fermionic or bosonic. The main chamber, its antireflection coated viewports, and the optomechanics around the main chamber are designed for maximal possible optical access. This includes resonant beams for cooling as well as off-resonant beams for trapping. Also two possible imaging directions are planned. The first one is along the horizontal plane for large clouds and is the one used in the measurements within this these. The second direction for imaging is along gravity. The the recessed viewports along the z -axis allow for the imaging optics to be as close as possible to the atoms. Furthermore, the vacuum design includes a connection to a future science cell. With a stable operation in the main chamber and possible optical transport, the science cell can be designed for any experimental update.

9.5.1. Trapping beams and geometry

The modification of the atomic confinement is a valuable experimental tool. It offers multiple research possibilities, once the atomic gases have reached the ultracold regime. Moreover, the possibility to separate the atomic species from each-other can be of use during the preparation of a quantum system. In addition, loading dysprosium in a shallow optical lattice would reduce the density of an ultracold dysprosium cloud. Therewith, the atomic sample can be protected from few-body losses while ramping the magnetic field through the numerous narrow Feshbach resonances of fermionic dysprosium, for example. The trapping potential depends on the geometry of the off-resonant laser beams, but also on the polarizability of the atoms at a given the wavelength (see Sec. 2.3.3). That is why it is important to have a vacuum setup that allows to use different wavelengths for trapping.

The trapping potentials of the mixture can be modified optically and with the curvature coils. The main chamber allows for optical trapping wavelengths such as 1064 nm or 532 nm along the gravity axis z and in the horizontal plane (see Fig. 9.2). The four sapphire viewports in the horizontal plane have an antireflection coating for 532 nm, 1064 nm and 1550 nm. The dipole potential of a focused 532 nm beam is attractive for dysprosium and repulsive for potassium. Such a beam can be overlapped with an attractive 1064 nm potential and thus regulate the trap depth species-selectively. Furthermore, the large MCF63 viewports, which are used for the MOT beams, also allow for a 532 nm lattice or trapping beams. With a type of ‘magic’ wavelength one could also arrange species selective lattices [24].

As examples of the benefits of having versatile far-detuned high-power beams in the main chamber of the Dy-K experiment, two specific applications are presented. First, it would be advantageous to be able to apply the sympathetic laser cooling mechanism on a narrow line,

as is done in the Sr-Rb mixture (see Chapter 6). Preliminary measurements and calculations from our group show that the excited state of the 741 nm-transition of Dy is not trapped in the 1064 nm ODT. Thus, the envisioned simple cooling in the ODT on this narrow ($\Gamma_{741} = 2\pi \times 1.7$ kHz) transition requires a gimmick. Either some ‘anti-magic’ wavelength is found that can counteract the antitrapping effect of the 1064 nm for the the excited state of the 741 nm-transition, or a blue-detuned doughnut-shaped trapping beam is used, where the atoms are trapped at the intensity minimum in the center of the doughnut beam. Both possibilities require the use of a high-power beam at a wavelength far away from 1064 nm. The second application of an unusual trapping wavelength in the Dy-K experiment is a ‘magic’ trap for the mass-imbalanced Fermi-Fermi mixture. For a wavelength close to 970 nm the trapping frequencies of K and Dy are reciprocal to their masses $\omega_K/\omega_{Dy} = m_{Dy}/m_K$. In this scenario, the Fermi surfaces of both species would match in momentum space even if the chemical potentials of both elements are different [353].

9.5.2. High-resolution imaging

The more complex the quantum system, the more precise must be the detection. For the Dy-K experiment this would probably mean, that in order to reach very low temperatures, most of the atoms will be lost during forced evaporation. The final atomic samples would be relatively small with a few thousand atoms and very compact, in order to have a high phase-space density. Moreover, the signatures of many exotic superfluid phases are detectable in noise correlations or in fine changes of the momentum distribution. Therefore, the imaging setup should have a high resolution. For high-resolution imaging we need to be as close as possible to the atoms. In the main chamber, this is granted by the recessed viewports along the z -axis. Around the future glass cell, maybe even a high-resolution microscope objective [19, 201] can be installed. The next parameter that helps to increase the resolution is a shorter imaging wavelength. For Dy the imaging light is naturally 421 nm. In addition, also potassium has an almost closed optical transition around 405 nm [181]). Thus, both species can be imaged with a common optical system in the blue visible spectrum. The challenge for a high-resolution imaging system along the z -axis of the main chamber is that the optics with high numerical aperture would cover the entire viewport and thus all other resonant and off-resonant beams along the z -axis must also pass through the same optics. A design by E. Kirilov of a microscope objective that fulfills all necessary requirements for shape and polarization of the beams was installed recently around the main chamber of the Dy-K experiment.

9.5.3. Future Science Cell

The Dy-K apparatus offers the possibility of a purposeful extension from the main chamber. Depending on the interaction properties of the dysprosium and potassium isotopic mixtures and the achievable temperatures, multiple quantum simulation directions should be realizable (see Sec. 3.2). The total setup on the main table and the available space considers a possible small glass cell connected to the main chamber. This so-called science-cell will have its own small vacuum pump, own appropriate magnetic field coils, high optical access and a stable input of cold atoms from the main chamber. A high-resolution imaging microscope will most probably be in place.

Experimental results

In this chapter I will present a characterization of Dy-K laser cooling and first measurements with thermal samples in the optical dipole trap (ODT). Because of the very different properties of dysprosium and potassium the cooling and loading into traps of the atomic clouds from both species is better carried out sequentially. With both species in the ODT, we measure the precise dynamical polarizability of Dy relative to K. Further, I present the first measurements of the interaction between bosonic ^{162}Dy and fermionic ^{40}K in the presence of a homogeneous magnetic field.

10.1. MOTs

After precooling, both species can be trapped simultaneously in a 3D MOT. This is shown in the two-color absorption image in Fig. 10.1. We do not observe any effects from the other atom's resonant light, not even from the Zeeman slower (ZS) light. Because of the different optimal magnetic field gradients for Dy and K, an experimental sequence for simultaneous 3D MOT is not favorable for high atom numbers and low temperatures. In the following I will present the MOT parameters for the sequential loading of the alkali and the lanthanide elements.

In all measurements the atom numbers are obtained using absorption imaging in the horizontal direction. The scattering cross-section of the imaging light is assumed to be the resonant one for a two-level system for the relevant polarization of the probe beam. We image potassium with 767 nm and dysprosium with 421 nm laser light. For all MOT measurements, the clouds are compressed before imaging in order to fit the image on the camera. The camera is a Neo 5.5 sCMOS and it is used for both species.

To analyze the loading and hold behavior of both species we use the following differential equation for the rate of change of atom number N in the MOT [138]:

$$\frac{dN}{dt} = L_0 - \gamma N - \beta \int n^2 dV. \quad 10.1$$

Here L_0 is the initial loading rate, γ describes the one-body decay rate and β is the density dependent two-body loss rate. The equation is used for dysprosium and potassium dynamics separately in our investigations. For low densities we can set $\beta = 0$ and then describe the MOT loading to a steady state $N_{ss} = L_0/\gamma$ with:

$$N(t) = N_{ss}[1 - \exp^{-\gamma t}]. \quad 10.2$$

When the MOT saturates and the loading is switched off ($L_0 = 0$ from Eq. 10.1) the atom

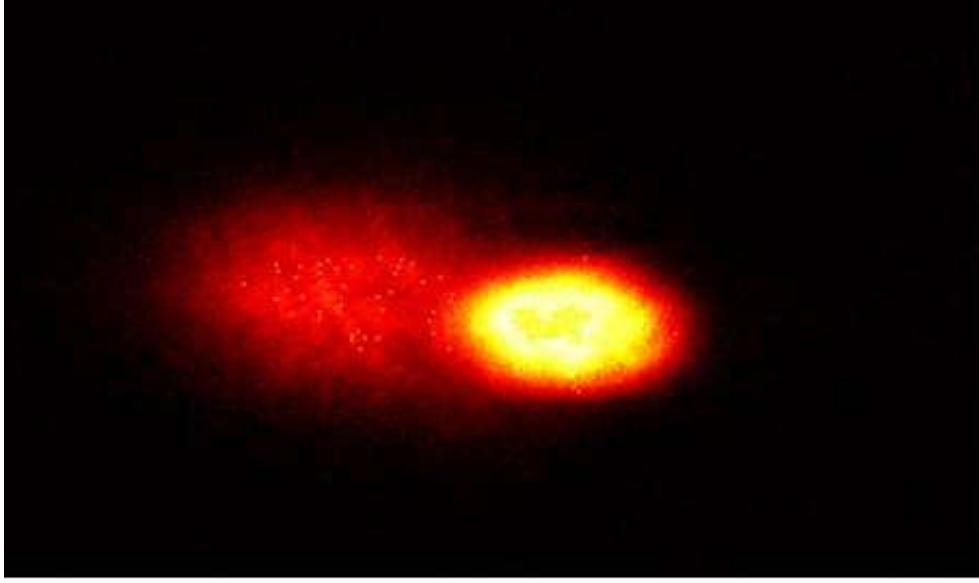


Figure 10.1.: A two-color absorption image of a double fermionic Dy-K MOT. The strongly compressed cloud on the right is ^{161}Dy and the dilute one on the left is ^{40}K at 3 G/cm field gradient. The MOTs do not overlap in this picture because of a power imbalance in the MOT beams.

number decay is given by :

$$N(t) = \frac{N_0 \exp^{-\gamma t}}{1 + \frac{N_0 \beta}{V \gamma} [1 - \exp^{-\gamma t}]} \quad 10.3$$

We collect information about both timescales of the decay. Initially, at high densities the losses are dominated by two-atom collisions and we can extract β . The longer timescale of $1/\gamma$ can be a measure of the quality of the vacuum in the main chamber. The value of γ should be the same for loading and decay.

10.1.1. Potassium MOT

In the Dy-K experiment the source of cold potassium atoms delivers moderate loading rates for all isotopes, while keeping the vacuum high. The 2D MOT as well as the 3D MOT of potassium operate on the D2 line near 766.7 nm. The 2D MOT, which is presented in the master's thesis [349], is loaded from the background pressure created by the activation of dispensers of enriched potassium (around 5.5 % of ^{40}K) placed inside the glass cell presented in Sec. 9.2.1. We use red-detuned beams on all three axes of the 2D MOT and the magnetic confinement is two-dimensional.



Figure 10.2.: Fluorescence image of the 2D MOT, which is about 50 mm \times 4 mm large. It shows the size of the cell, but also the flaws in polarization. From Ref. [349].

The large 2D MOT is created by two perpendicular retro-reflected elliptical laser beams ($1/e^2$ waist of $50\text{ mm} \times 13\text{ mm}$) and by the 2D quadrupole magnetic field realized by the coils presented in Sec. 9.2.1. The gradient of the magnetic field is about 22 G/cm , which is relatively high compared to other potassium 2D MOT-setups and increases the velocity spectrum captured by the MOT in exchange for high densities along the middle of the trap. The transversely cooled atoms are trapped around the line of zero magnetic field, forming a cloud as on the fluorescence image shown in Fig. 10.2. The deviations from a perfect cigar-shape in this figure stem from inhomogeneities in the laser light polarization. The retro-reflection was initially achieved by coated prisms, see Ref [349]. These optical elements are not optimal for the polarization of the 2D MOT beams, so they were later on replaced by mutually perpendicular mirrors.

We have never reached the loading rates from Ref. [347] that we aimed at. We have larger beams, but also higher laser power, so the intensities are comparable. The major difference between both experiments is the vapor pressure of potassium, which is kept relatively low in our setup. The 2D MOT vacuum part is under $1 \times 10^{-9}\text{ mbar}$. Otherwise we see a direct degradation of the vacuum in the potassium section as well as in the main chamber. For some measurements, high dispenser currents were used, which lead to a coating of the glass cell and the in-vacuum mirror. In Fig. 10.2, the mirror inside the glass cell still provides a third pair of laser beams for optical molasses along the axis of the trap. After coating of this mirror with potassium at high dispenser currents, its low reflectivity means we cannot cool axially anymore. I do not have an explicit characterization of the 2D MOT with the new dispenser design from Sec. 9.2.1. Here I will present only the loading and decay of the 3D MOT. The characterization of the initial 2D MOT design can be found in the Ref. [349].

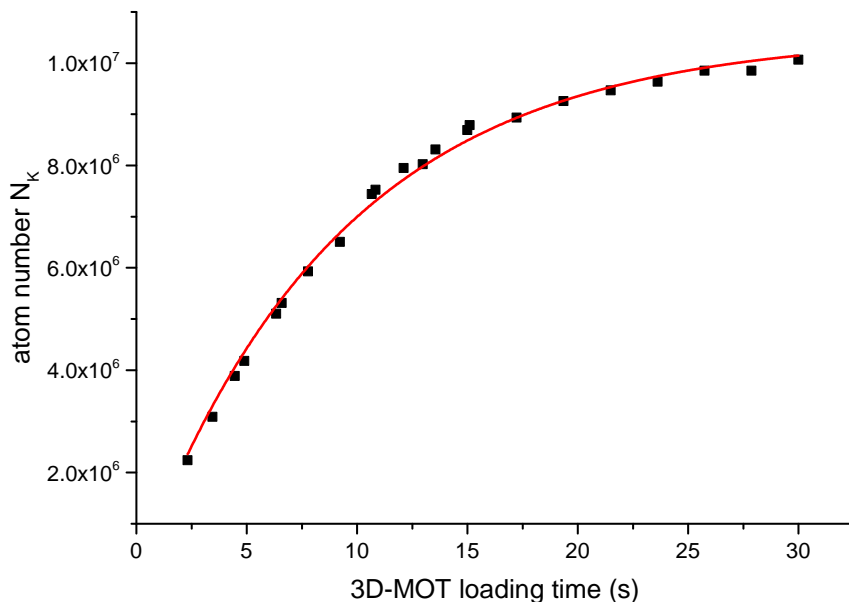


Figure 10.3.: 3D MOT loading of ^{40}K for fixed 2D MOT settings. Every data point represents one experimental realization. The red curve is the fit with Eq. 10.2. It delivers moderate loading rates.

From the 2D MOT a near resonant beam pushes the axially cold atoms through the differential pumping tube into the vacuum chamber, where the atoms are collected in the 3D MOT. The MOT geometry is realized by two orthogonal sets of retro-reflected beams propagating in the horizontal plane and by one pair of counterpropagating beams along the

vertical axis. The 3D MOT gradient in vertical direction is 9 G/cm. The detuning of the cooling light is $-4\Gamma_{767}$ relative to the $F = 9/2 \rightarrow F' = 11/2$ transition. The intensity of the cooling laser field is $I_{\text{cool}} = 6 I_{\text{sat},767}$ and the intensity of the repump laser field is $I_{\text{rep}} = 0.3 I_{\text{sat},767}$, where $I_{\text{sat},767} = 1.75 \text{ mW/cm}^2$ is the saturation intensity of the D2 line of K and Γ_{767} its natural linewidth. The K MOT beams combine the cooler and repumper frequencies. The latter is created by a free space EOM and is detuned by $\delta_{\text{rep}} = -2.7\Gamma_{767}$ from the $F = 7/2 \rightarrow F' = 9/2$ transition. The MOT atom number is constant as δ_{rep} is varied over few Γ_{767} , probably because of the relatively low repumper intensity. We use comparable 3D MOT parameters to other ^{40}K experiments, except for the relatively large beams for an alkali MOT, because the MOT laser beams for both elements are brought to the vacuum chamber using the same optical fibers.

In the Dy-K apparatus the potassium MOT has a typical loading rate of 1×10^6 atoms/s at 3.3 A dispenser current. Fig. 10.3 shows a typical potassium MOT loading curve fitted with Eq. 10.2. The MOT atom number saturates at 1×10^7 atoms with a time constant of $1/\gamma = 10$ s. For a higher dispenser current of 3.8 A, the loading rate goes up to 5×10^6 atoms/s and saturates at 3×10^7 atoms with a time constant of $1/\gamma = 5$ s. With this higher dispenser current the glass cell is coated with potassium atoms from the inside within a day. So we use the lower and safe dispenser current of 3.3 A. We typically load for 3 s, which is far from the saturation value of the loading curve. The measured fluctuations of the particle number of 3.4×10^6 atoms in the MOT stage (after compression for imaging) are $< 5\%$.

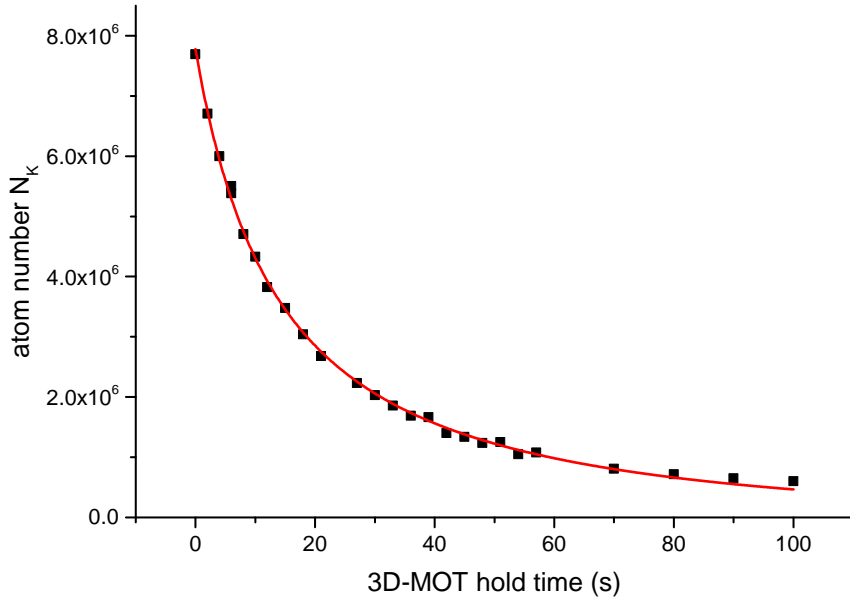


Figure 10.4.: Atom number decay in a 3D MOT of ^{40}K . Every data point represents one experimental realization. The red curve is the fit with Eq. 10.3. The fast decay gives $\beta = 8.0(4) \times 10^{-11} \text{ cm}^3/\text{s}$ and the slow decay scale shows good vacuum with a lifetime of around 80 s.

A decay measurements of the potassium 3D MOT fitted with Eq. 10.3 is shown in Fig. 10.4. The decay rate of $\gamma = 0.013(1) \text{ s}^{-1}$ gives the decay due to scattering with the background gas. This indicates that the vacuum in the main chamber is very good with an atomic lifetime of about 80 s. A MOT with background pressure of 10^{-10} mbar will typically have a lifetime of about 100 s, when collisions with the background gas are the dominating loss mechanism. The one-body decay for loading and decay (or hold time) should be identical,

but we measure a relatively high value of γ for the potassium 3D MOT loading in Fig. 10.3. This difference between the loss coefficients for loading and hold of the MOT are probably due to the push beam from the 2D MOT. The push light is very close to resonance and cuts through the large potassium MOT, which can increase the value of γ during MOT loading.

From the fit of the data in Fig. 10.4 we also extract the two-body loss coefficient β from Eqs.(10.1, 10.3). The determined value of $\beta = 8.0(4) \times 10^{-11} \text{ cm}^3/\text{s}$ is comparable to carefully measured two-body loss coefficients in a ^{40}K MOT [354]. A common experimental technique to reduce such light assisted two-body losses in the potassium MOT is a dark SPOT (dark spontaneous optical trap) configuration [344], where there is almost no repumper light in the center of the 3D MOT. In the Dy-K experiment the repumper frequency for potassium is a sideband produced by an EOM and cannot be separated from the cooling frequency. In addition, a double species experiment typically has an already a complex optomechanical setup around the main chamber. Thus we do not target a dark SPOT and just use a low repumper intensity in total for the 3D MOT.

Before transfer into a non-dissipative optical trap the K MOT is compressed. This compression is achieved by simultaneously ramping up the gradient of the magnetic field to 25 G/cm in 4 ms and ramping down the detunings to $\delta_{\text{cool}} = -1.1\Gamma_{767}$ and $\delta_{\text{rep}} = 0$ and the intensities down to $I_{\text{cool}} = 0.5 I_{\text{sat},767}$ and $I_{\text{rep}} = 0.01 I_{\text{sat},767}$. At the end of the compressed MOT phase the temperature of the potassium cloud is 110(30) μK , the gradient of the magnetic field is set to zero, and the homogeneous magnetic field is canceled¹.

10.1.2. Dysprosium MOT

In this section the parameters influencing the dysprosium MOT loading rate will be discussed. A rather qualitative evaluation will be presented starting from the hot atoms source, through the precooling with the 32 MHz-strong transition near 421 nm to the 3D MOT, which operates on the narrow ($\Gamma_{626} = 2\pi \times 135 \text{ kHz}$) intercombination line near 626 nm. We aim at high loading rates for the Dy MOT, because in our double-species experiments the potassium atoms are loaded first and they have a relatively short lifetime in the reservoir-ODT (see Sec. 10.2). The shape of the Dy MOT is shell like and its position depends on the magnetic field gradient and on the detuning from resonance (see Sec. 2.3.2). Apart from the oven temperature and the resonance frequencies, the settings for the bosons ^{162}Dy and ^{164}Dy and the fermion ^{161}Dy are generally the same. The MOT operates with a gradient of 2 G/cm (along the vertical axis) and with an intensity of $170 I_{\text{sat},626}$ per beam in the horizontal plane and twice that intensity along the vertical axis, with $I_{\text{sat},626} = 72 \mu\text{W}/\text{cm}^2$. The atomic cloud is compressed before imaging, in order to capture it fully on the camera. The loading curves of the dysprosium MOT presented in this section are taken in different months with different total power of most beams. Also the oven temperatures differ slightly and some of the measurements were taken the week before the Dy oven was depleted. So I will restrict myself in this section to orders of magnitude and a qualitative description of the parameters that influence the MOT loading.

The first important and fixed parameter is the $1/e^2$ -diameter d of the MOT beams, since the capture velocity of the narrow-line MOT depends on it. In addition, large MOT beams should allow us to separate the narrow-line MOT from the close to resonant ZS laser beam. The optical path of the 3D MOT beams is shared for Dy and K light coming through the same optical fiber from the laser table. The potassium MOT requires high intensities, so

¹ The homogeneous magnetic field is canceled within the precision of our passive control. We measure 50 Hz noise of about 5 mG

we limit our wish for large Dy MOT beams to only $d = 35$ mm through the 60 mm large viewports. Therewith, we get a relatively low capture velocity of the narrow-line MOT for Dy of $v_c = \sqrt{2da_{\max,626}/3} \approx 6$ m/s, with the maximal deceleration $a_{\max,626} = \Gamma_{626}\hbar k/(2m_{\text{Dy}})$, where k is the wave number and m_{Dy} is the mass of dysprosium. With the given beam size, we can further enhance the loading rate by efficient precooling and by frequency broadening of the 626 nm light, as discussed in the following.

The capture rate of the 3D MOT strongly depends on the temperature of the effusion oven. With bosons we typically work at oven temperature of 1000 °C and with fermions at 1100 °C. These are relatively low temperatures, compared to other dysprosium experiments. The Dy experiment in Stuttgart operates at 1200 °C to 1250 °C [324], the one in Paris at 1100 °C [189] and the Er-Dy experiment in Innsbruck also at 1100 °C [355]. Nevertheless, reasonable loading rates are reached, while the vacuum in the main chamber is high. In addition, the operation at low oven temperatures increases the lifetime of the dysprosium sample in the oven and reduces the need of a refill, which is always a risk for the vacuum apparatus.

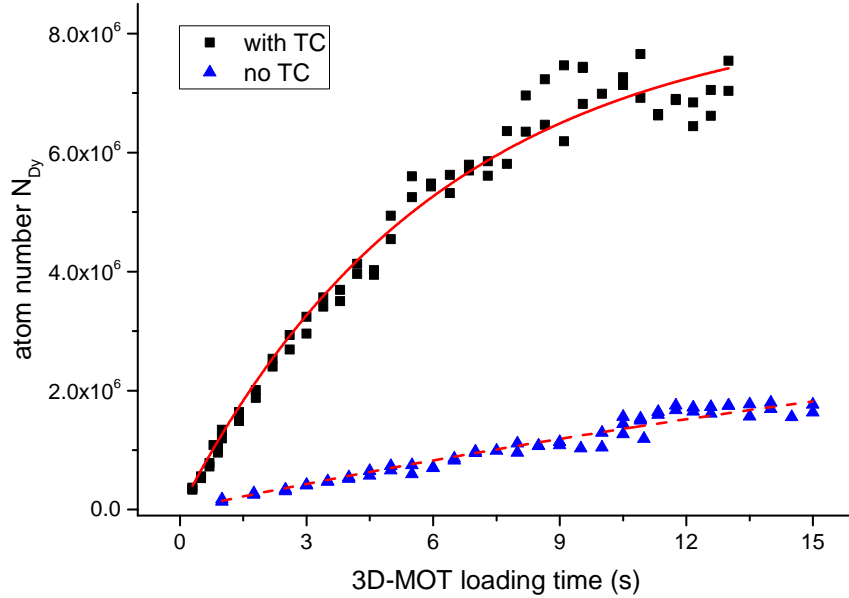


Figure 10.5.: Effect of the transverse cooling (TC) on the dysprosium 3D MOT loading. Each data point represents a single experimental run with ^{162}Dy . The red curves are the fits to the data with Eq. 10.2: the solid line with TC and the dashed red line without TC. The resulting loading rate L_0 is an order of magnitude higher with TC. This measurement is taken the week before the Dy oven was depleted, so the atom numbers and loading rates are lower than typical for the Dy-K experiment.

The next important ingredient in optimizing the Dy MOT loading is the transverse cooling (TC) with the laser line design (see Fig. 9.6). Figure 10.5 shows a comparison of the ^{162}Dy MOT loading with and without TC. The transverse cooling increases the MOT capture rate by one order of magnitude. Most experiments aim at high laser intensities for TC. For the measurements from DyK presented in Figure 10.5 the power on the 421 nm transition is only 25 mW per beam, which corresponds to an intensity of $\approx 1 I_{\text{sat},421}$, with $I_{\text{sat},421} = 56$ mW/cm². At optimal settings for output power of the blue laser and fibers we can reach $4 I_{\text{sat},421}$ per beam. The detuning of the TC light is $-0.5 \Gamma_{421}$. The data from Figure 10.5 delivers better information about the loading rate than about the saturation atom number.

It seems the saturation atom number is increased by a factor of three by the TC.

The optically collimated atomic beam enters the Zeeman slower (ZS) with an average velocity of 450 m/s and is slowed down to <10 m/s by the $-20\Gamma_{421}$ detuned 421 nm light. For such a large velocity change the beginning and end coils of the ZS must deliver high fields for the optimal magnetic field profile. For a given ZS magnetic field and MOT beams configuration the MOT loading stays the same as we vary the detuning of the ZS beam from $-18.5\Gamma_{421}$ to $-21\Gamma_{421}$. Compared to other Dy experiments [189, 324, 355], we use the largest detuning for ZS. This is only possible thanks to the frequency generation scheme presented in Fig. 9.13, because the power of the ZS beam has to be as high as possible. The finicky part about the ZS beam is its geometry. The size in the MOT chamber and the position of the focal point around the Zeeman slower entrance are very sensitive parameters.

The typical dysprosium MOT loading rates in the range from 1×10^7 atoms/s to 1×10^8 atoms/s for an oven temperatures from 1000°C to 1100°C are relatively high and demonstrate an efficient design and implementation of the dysprosium precooling. The commercial effusion cell with the custom nozzle delivers a fairly collimated atomic beam and can be operated at moderate temperatures. Then, the TC contributes significantly to the loading rate even at low optical power. And finally, the radially compact Zeeman slower design permits the use of high magnetic fields and grants high capture velocities.

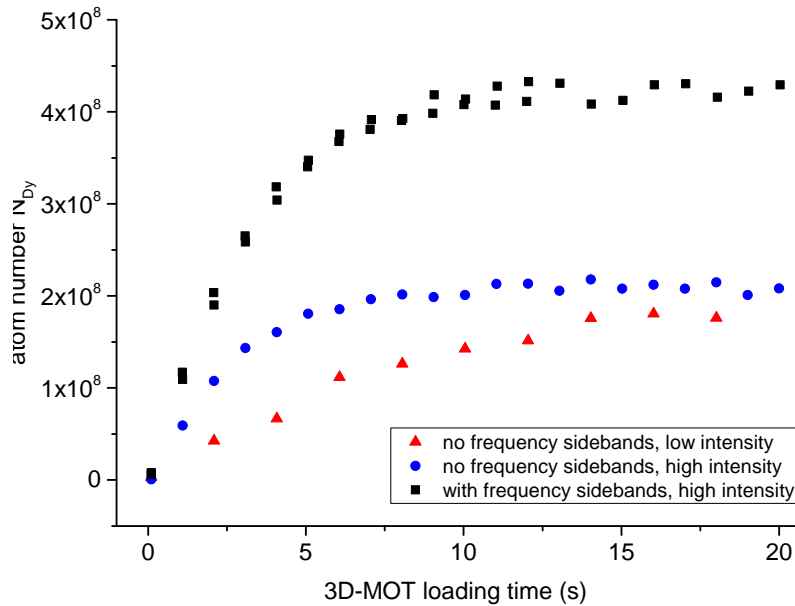


Figure 10.6.: Narrow-line 3D MOT loading behavior. Each data point represents a single experimental run with ^{164}Dy . We determine the loading rate and the one-body loss rate with Eq. 10.2. We can only discuss these results qualitatively, because the intensity for these experimental runs is unknown.

The qualitative loading behavior of the dysprosium MOT is further discussed on the basis of the measurements in Figure 10.6. The plot shows the MOT loading of bosonic ^{164}Dy MOT at an oven temperature of 1050°C for different settings of the 626 nm light. The absolute intensity values for these experimental runs is unknown and thus the following discussion will be mainly qualitative. The most striking result from the loading curves shown in Fig. 10.6 is that the capture range of the MOT and thus the loading rate can be notably increased by modulating the MOT frequency. The red-detuned 626 nm laser

is spectrally broadened by an EOM driven at 104 kHz. The EOM adds sidebands up to the 15th order to the main cooling beam and thus distributes the optical power among the spectral components. A fit of Eq. 10.2 to the data from Fig. 10.6 gives a loading rate of $L_0 = 7 \times 10^7$ atoms/s without broadening and an almost doubled $L_0 = 13 \times 10^7$ atoms/s with broadening. The two-fold increase in loading rate and atom number, when frequency modulation is applied to the MOT light, is a typical experimental observation for a Dy 626 nm-MOT [189, 324, 355]. The next observation from Fig. 10.6 is that the saturated atom number in the MOT for different 626 nm intensity stays the same at about 2×10^8 atoms. However, the change in intensity influences the loading rate: $L_0^{\text{high intensity}} = 7 \times 10^7$ atoms/s and $L_0^{\text{low intensity}} = 2 \times 10^7$ atoms/s. According to Ref. [180], the damping coefficient of the MOT and therewith the capture velocity are different depending on the regime of the MOT: In the narrow-line regime, the capture velocity is supposed to decrease with intensity. In the normal case, as for alkali metals, the capture velocity increases with intensity. Figure 10.6, shows an increase in loading rate with increased intensity. Hence, during loading we are in the normal and not narrow-line regime [180]. The last statement from the measurements in Fig. 10.6 and the fits with Eq. 10.3 is about the one-body loss parameter γ . This decay rate of the atom number depends on the overlap of the MOT with the ZS beam, on the collisions with the background gas, and on the intensity of the 626 nm light. The decay rate $\gamma_{\text{high intensity}} = 0.4 \text{ s}^{-1}$ is indeed much higher than $\gamma_{\text{low intensity}} = 0.1 \text{ s}^{-1}$ due to the higher intensity settings without sidebands. Although the frequency sidebands redistribute the intensity among the frequency components $\gamma_{\text{sidebands}} = 0.3 \text{ s}^{-1}$ stays rather high. A possible explanation is that the capture volume of the MOT is larger for cooling light with sidebands and therefore the overlap with the ZS beam is affecting the decay. The typical decay rate of $\gamma = 0.3 \text{ s}^{-1}$ for the loading with sidebands of the dysprosium MOT in the Dy-K experiment is relatively low compared to other dysprosium MOTs [189, 324, 355]. We attribute this good parameter value to the quality of our vacuum and an effective spatial separation from the ZS laser beam thanks to the large MOT beams².

The fermionic ^{161}Dy MOT shows similar qualitative behavior. We typically load about 5×10^7 atoms in 3 s. The fermions have a lower loading rate than the bosons despite the higher effusion cell temperature due to the thermal distribution among hyperfine states in the oven together with the slightly lower natural abundance of the ^{161}Dy isotope. The hyperfine splitting also leads to a higher decay rate $\gamma = 0.4 \text{ s}^{-1}$ than for the bosons, because now spin-changing collisions are allowed [189].

We load the 3D MOT only for a couple of seconds and the atom number stays relatively stable, although we do not load until saturation, which is reached at about 10 s in Fig. 10.6. The spectral broadening is then abruptly switched off and within 170 ms the MOT is compressed by shifting the detuning closer to resonance while reducing the power down to $I = 0.5 I_{\text{sat},626}$ and the gradient of the magnetic field to 1.4 G/cm. The atoms are then held in the compressed MOT for 80 ms. During this hold time the dysprosium cloud is polarized by the bottom MOT beam in the absolute ground state (see Sec. 2.3.2 or Ref. [189]), which is $|J = 8, m_J = -8\rangle$ for the bosonic Dy isotopes and $|F = 21/2, m_F = -21/2\rangle$ for the fermionic ^{161}Dy . The temperature after the compression of the MOT is approximately 8 μK .

To summarize, in the beginning of every experimental run we apply a sequential MOT

² Unfortunately, the decay/hold measurements of the dysprosium MOT do not deliver meaningful results, because we had an issue with the digital control of the dysprosium oven shutter and we could not stop the atomic flow. Such a measurement with ZS light on and off would be a robust evidence of a good spatial separation between MOT and ZS.

loading of the alkali element potassium and then the lanthanide element dysprosium. We reach typical loading rates and temperatures compared to single species experiments and we have very good vacuum conditions in the main chamber of the setup.

10.2. Optical dipole traps

In the Dy-K experiment the strategy for cooling after the MOT relies on a combination of evaporative and sympathetic cooling in an optical dipole trap (ODT). The transfer of atoms from a MOT or a molasses directly into the optical trap needs special care. The different MOT shapes and magnetic field gradients for potassium and dysprosium require sequential ODT loading, similar to the sequential MOTs in the Sr-Rb-procedure (see Sec. 6). Here I present the ODT-system that was designed to meet the requirements for efficient loading of cold K and Dy. It consists of two laser sources for a reservoir (RDT) and science (sODT) optical dipole traps. After a short discussion of the double species loading in the RDT, the first important measurements in the sODT with thermal atomic samples are briefly presented. The dynamical polarizability of dysprosium is determined relative to the well known potassium value. These results are published in as *Accurate Determination of the Dynamical Polarizability of Dysprosium*, *Phys. Rev. Lett.* **120**, 223001 (2018) (Ref. [320]).

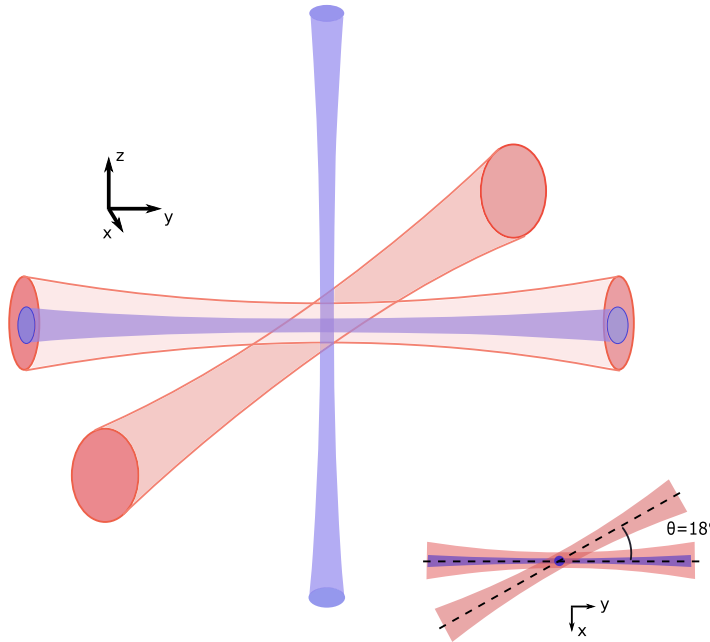


Figure 10.7.: Optical dipole trap setup in the Dy-K main chamber. The RDT in red has $85\ \mu\text{m}$ waist. The sODT in blue has $30\ \mu\text{m}$ waist in the horizontal beam. The vertical beam has $60\ \mu\text{m}$ waist, but is not used in any of the experiments presented here. The lower scheme shows a view from the top. From Ref. [95].

The optical dipole trap system in the Dy-K main chamber is illustrated in Figure 10.7. The reservoir-ODT (RDT) in red consists of two beams coming from one fibre laser (IPG 100 W) at 1070 nm and crossing in the horizontal plane under an angle of 18° . The two beams have equal power, perpendicular polarizations and are focused on identical waists of approximately $85\ \mu\text{m}$. The second ODT, in which experiments take place, is depicted in blue

in Fig. 10.7. The laser source for this second trap is a Nd:YAG laser at 1064 nm with 17 W total power. This trap is tighter, has a waist of 30 μm approximately, and is referred to as the science dipole trap (sODT). One beam of the sODT overlaps in the horizontal plane with one beam of the RDT. For the measurements presented in this thesis the horizontal sODT trap was used without additional confinement from the vertical beam in Fig. 10.7, which has a waist around 60 μm .

10.2.1. Loading of ODTs

For efficient loading of the ODTs the circumstances of collecting (MOTs) and also further cooling (forced evaporation) the double-species atomic sample must be considered. First potassium is loaded in the RDT and then dysprosium because of the high magnetic field gradient used in the potassium cooling (see Sec. 10.1.1). The second consideration is that the evaporative cooling stage is more efficient for similar (possibly low) starting temperatures for the two species.

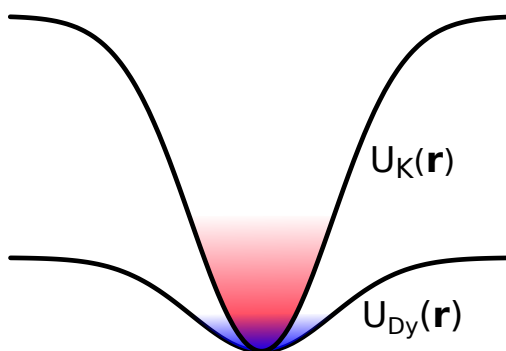


Figure 10.8.: The science dipole trap (sODT) for the Dy-K mixture. The trap consists of a single horizontal beam of 30 μm waist and is deeper for K.

After the MOT stage the temperatures of K and Dy components differ by an order of magnitude. This is due to the different linewidths of the cooling transitions for the alkali and lanthanide elements. In order to approach the temperature of potassium to the one of dysprosium, we perform sub-Doppler cooling of the K atoms in the form of gray molasses on the D1 line [168] in the presence of the large volume RDT. The laser beams creating the gray molasses are overlapped on polarizing beam splitters (PBSs) with the MOT beams, which fixes their polarization to circular with opposite helicity compared to the MOT beams. The cooler and repumper beams are detuned in the blue of the $F = 9/2 \rightarrow F' = 7/2$ and $F = 7/2 \rightarrow F' = 7/2$ transitions respectively. A detailed description of the D1 cooling of potassium in the Dy-K experiment can be found in the supplemental material of Ref. [95].

We typically load 5×10^5 ^{40}K atoms at a temperature of around 30 μK in the RDT. The loading efficiency is larger than 20%. A short optical pumping pulse of 0.8 ms with σ^- polarization and with frequency components resonant with the D1 transitions $F = 7/2 \rightarrow F' = 9/2$ and $F = 9/2 \rightarrow F' = 7/2$ transfers most of the atoms to the stretched $|F = 9/2, m_F = -9/2\rangle$ state. During the pulse the gradient of the magnetic field is canceled and a small homogeneous field is applied along the direction of the beam. This optical pumping has a very slight effect on the temperature of the cloud on the order of 1 μK . The potassium cloud fully polarizes later on together with dysprosium, when the DDI allows for spin-changing

collisions. The ^{40}K atomic sample waits in the RDT with a relatively short lifetime of 4 s, while the Dy MOT is loaded.

The Dy MOT forms below the zero of the quadrupole magnetic field and is thus spatially separated from the potassium cloud. Neither the dysprosium atoms, nor the ZS or MOT light affect the lifetime of the potassium atoms in the dipole trap. The spin-polarized cMOT of dysprosium is brought to the RDT by shifting the magnetic field zero. We typically load 10^7 bosonic Dy or about 3×10^6 fermionic Dy atoms in the crossed region of the RDT. This gives a loading efficiency $> 10\%$. The temperature of the dysprosium cloud increases during the transfer into the RDT to about $15\ \mu\text{K}$. At the end of the Dy MOT, all resonant light is switched off and the gradient of the magnetic field is zero. A homogeneous magnetic field of $\approx 430\ \text{mG}$ is applied along the vertical direction to maintain the polarization of the atoms. From the crossed RDT both species are transferred into a single (or later on crossed) beam of the sODT. Figure 10.8 shows a schematic of the single beam sODT for both elements. Forced evaporation is performed on Dy, since the trap is shallower for the lanthanide element. We perform measurements with thermal clouds [320] or we can reach double degeneracy [95].

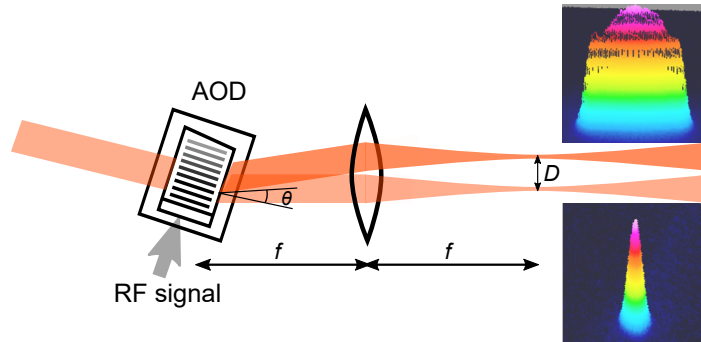


Figure 10.9.: Schematic of the dipole trap elongation setup. A lens in the path of an acousto-optical deflector (AOD) shifts sideways the position of the focus of the RDT for different diffraction angles θ . For a broad bandwidth of the AOD and appropriate modulation of the RF input signal a time-averaged elongated optical potential is produced. The images from a beam profiler on the right show the unmodulated beam at the bottom and the elongated beam of the RDT to an effective width of D on the top.

Given the different MOT shapes of potassium and dysprosium, the possibility of an elongation of the ODT is built in the beam path of the RDT. The loading of a dipole trap is a complex process and its efficiency strongly depends on the spatial overlap with the MOT. Figure 10.9 shows the setup that allows to switch between a circular ODT and a time-averaged elongated dipole potential. The main idea is that the lens after the acousto-optical deflector (AOD) converts the diffraction angle θ into a sideways shift D of the position of the focus. The images taken with a beam profiler show the beam profile for a constant RF signal to the AOD and the elongated beam profile for an arccosine modulation through the entire bandwidth of the AOD. In an optimal setup, one can easily elongate a circular beam to an ellipse ratio of 10. Experiments with alkali [356] and lanthanides [321] show higher loading rate for elongated dipole traps. We do not see a clear advantage of the trap elongation for the loading rate with the AOD in the laser path of the 100 W-IPG fiber laser. It seems that the spatial profile of the rather old IPG laser is corrupted. In addition, the IPG has a 3kHz amplitude noise below 40 W and strong power oscillations above 70 W. Probably a trap elongation with the Nd:YAG laser would work better.

10.2.2. Determination of Dy polarizability (Publication)

This section presents briefly the main result from the publication *Accurate Determination of the Dynamical Polarizability of Dysprosium*, *Phys. Rev. Lett.* **120**, 223001 (2018). For optical manipulation of our mixture we need an accurate determination of the dipole polarizability of Dy. We use thermal clouds of Dy and K in the single beam sODT at 1064 nm. Potassium is the reference species, for which the dynamical polarizability is known on the permille level [332] (as for most alkali atoms). We measure a trap frequency ratio between both species and get an accurate measurement of the polarizability ratio. Therewith we obtain the scalar polarizability of dysprosium in atomic units at the wavelength of 1064 nm to be $\alpha_{\text{Dy}} = 184(2)$ a.u..

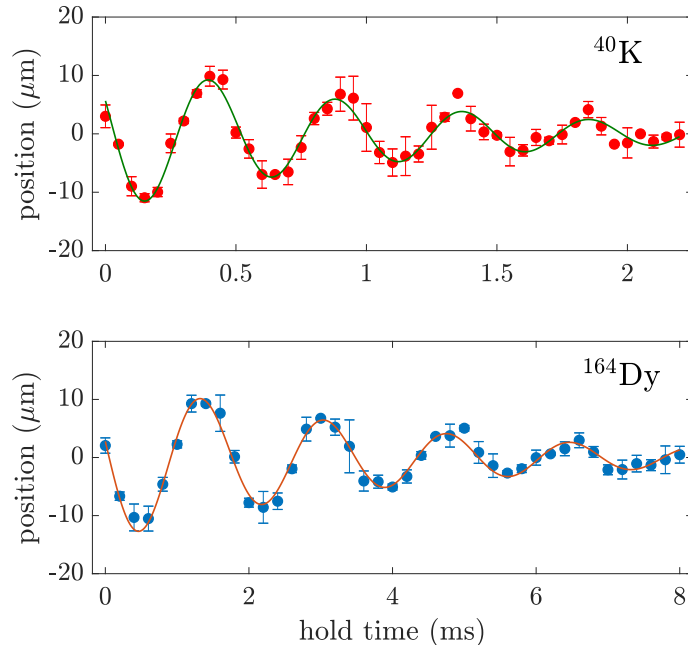


Figure 10.10.: Determination of trapping frequency ratio between Dy and K. Shown is the position of the clouds after TOF versus the hold time in the dipole trap after a short displacement. We obtain a frequency ratio $\alpha = 3.6$. From [320]

The radial trap frequency of the dipole trap ω_r , as defined in Eq. 2.8, depends on laser parameters and on atomic properties. The laser parameters are the wavelength ω_L , the power of the laser beam P and its waist w_0 . The atomic properties are the mass m and the polarizability $\alpha(\omega_L)$. Usually experimentalists determine the polarizability in a trap by measuring the trap frequency ω_r from collective oscillations for a given laser beam waist w_0 . The size and quality of the trapping beam at the focus are experimentally uncertain and w_0 contributes to the fourth power in Eq. 2.8. This typically leads to large uncertainties in the measured polarizability. Those limitations do not disturb the accuracy of our measurement of the polarizability, because we have a reference species in the same imperfect trap. The main type of measurements for this experiment are presented in Fig. 10.10. We determine the oscillation frequencies of both species after the same excitation of the ODT and examine the frequency ratio $\alpha = \omega_{\text{K}}/\omega_{\text{Dy}}$. The quantity α is independent of major experimental

systematics and imperfections. Our measurements deliver $\alpha = 3.63(2)$. We then use

$$\alpha_{\text{Dy}} = \alpha_{\text{K}} \frac{m_{\text{Dy}}}{m_{\text{K}}} \left(\frac{\omega_{\text{Dy}}}{\omega_{\text{K}}} \right)^2 \quad 10.4$$

to determine the scalar and tensor polarizability of Dy at the wavelength of 1064 nm. This is a particularly interesting wavelength for cooling and trapping experiments. The uncertainties from previous Dy polarizability values as from Ref. [188, 324, 357] are circumvented since we perform a measurement relative to a reference with a precisely known value. The extensive polarizability measurement presented in Ref. [320] is not only valuable to experimentalists working with Dy. Thanks to its clarity and accuracy, the reported method could be implemented in precision measurements of atom-light interaction for atoms with complex electronic structure or even molecules.

With the polarizability measurement we determine an important parameter for the intended Dy-K Fermi-Fermi mixture. A ‘magic’ wavelength is expected to exist where the polarizability ratio for the two species corresponds to their inverse mass ratio. An optical dipole trap operating at this particular wavelength would automatically match the Fermi surfaces of both species at ultra-low temperatures [353]. Next, we wish to investigate the interactions between the species.

10.3. ^{162}Dy - ^{40}K interactions

In this section the first results on the characterization of elastic and inelastic interactions between ^{40}K and the bosonic isotope ^{162}Dy in a thermal sample are presented. In a single beam sODT a homogeneous magnetic field with variable strength is applied for a certain hold time t_{hold} and the changes in atom number and cloud size (temperature) are measured. We identify multiple positions of Feshbach resonances and investigate the thermalization and loss rates for selected resonances around 70 G. We will mainly analyze the potassium data, which has a sufficient signal to noise ratio, rather than the measurements of dysprosium with large atom-number fluctuations. I will introduce models for extracting the two-body scattering cross section and the three-body loss rate coefficient.

10.3.1. Feshbach scans

All measurements in this section have the same preparation steps in common as already presented in Sec. 10.2.1. Both elements are in their absolute ground states. We load ^{40}K after optical pumping in the RODT in the stretched $|F = 9/2, m_F = -9/2\rangle$ state and then spin-polarized bosonic ^{162}Dy in the $|J = 8, m_J = -8\rangle$ state. After transfer of both species into the single beam sODT of about $30\ \mu\text{m}$ waist, we exponentially decrease the laser power. Dysprosium is evaporated and sympathetically cools potassium. We apply a fast evaporation ramp and thermalization between the species is not reached. The temperature of Dy is between $1\ \mu\text{K}$ and $5\ \mu\text{K}$ and the temperature of K is between $2.5\ \mu\text{K}$ and $9\ \mu\text{K}$ (depending on the day). We have roughly 10^5 potassium atoms and 2 to 4 times more dysprosium. The mean trap frequency is between $2\pi \times 50\ \text{Hz} < \bar{\omega} < 2\pi \times 75\ \text{Hz}$ for dysprosium and is 3.6 times larger for potassium (see Section 10.2.2). The homogeneous magnetic field is switched on in less than 1 ms and is applied to the atomic mixture in the sODT for a time t_{hold} . The magnetic field is calibrated via RF-spectroscopy on dysprosium. We measure the atom numbers and the size of the clouds after shutting off the coils and ODTs in a time-of-flight

measurement.

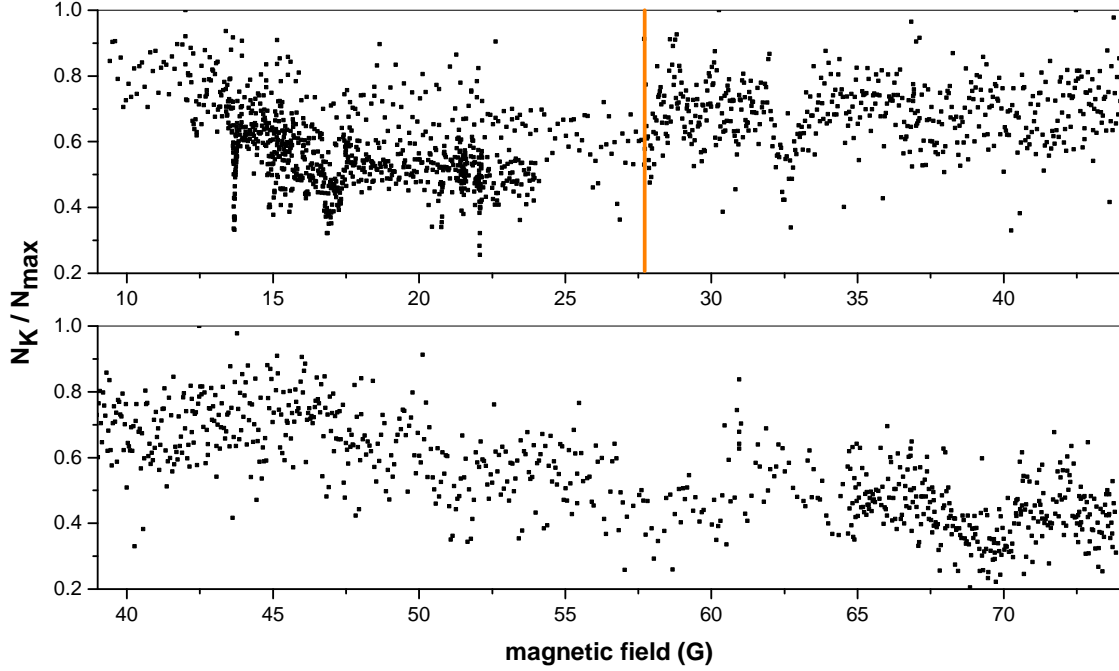


Figure 10.11.: Atom loss spectroscopy. The atom number of potassium is normalized to the maximum value of the day. The same data from 38 G to 44 G is shown in the upper and lower graphs for a better scale match of the magnetic field axes. The vertical orange line separates the data from 2 different days with slightly different settings (see text). Each data point represents a single experimental run.

Figure 10.11 shows an overview of a Feshbach loss spectrum from 10 G to 74 G. The goal of this set of measurements is to identify possible broad inter-species resonances. Hence, we did not perform single species scans for the entire magnetic field region. The loss spectroscopy in the magnetic field range between 1 G and 10 G shows no Feshbach resonances in the potassium numbers. The measurements were carried out with a different magnetic field coil, which was not well calibrated and thus the range between 1 G and 10 G is not shown in Fig. 10.11. For the range between 10 G and 27.7 G the initial atom numbers are $N_K = 10^5$ atoms and $N_K = 3 \times 10^5$ atoms. The initial temperatures are $T_{\text{Dy}} = 1 \mu\text{K}$ and $T_K = 3 \mu\text{K}$. The mean trap frequency of the sODT beam is $2\pi \times 50$ Hz and $t_{\text{hold}} = 1$ s in the homogeneous magnetic field. We can see effects on the potassium numbers at around 13.5 G, 17 G and 20 G in the top part of Fig. 10.11. Around 22 G, as observed before in Ref. [324, 341], we could confirm a broad ^{162}Dy resonance in the noisy dysprosium data, which is shown in Fig 10.12.

In the magnetic field range between 27.7 G and 74 G the experimental parameters are somehow different and only the hold time is identical to the low fields' scan, $t_{\text{hold}} = 1$ s. Due to daily experimental fluctuations the sample is hotter with less atoms: $T_{\text{Dy}} = 4 \mu\text{K}$ and $T_K = 7 \mu\text{K}$, while the ^{40}K atom number is 0.7×10^5 and 2.5×10^5 is the number of ^{162}Dy atoms. The mean trap frequency in the sODT beam for dysprosium is $2\pi \times 63$ Hz. We can identify some broad-looking inter-species Feshbach resonances from the effects on the potassium numbers at around 32 G and 70 G. The region around 70 G will be examined closer in the following sections.

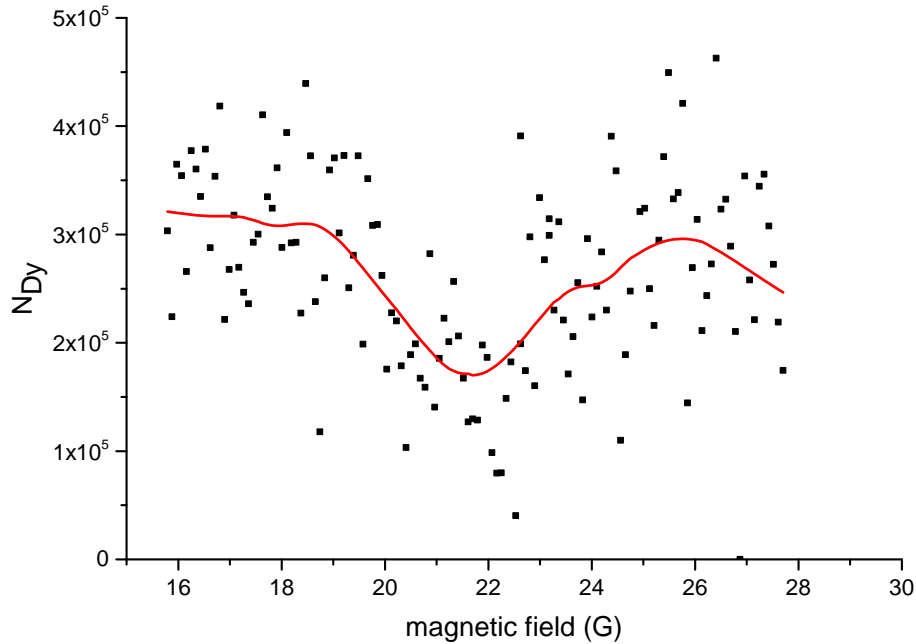


Figure 10.12.: Dysprosium atom loss spectroscopy. The black squares are data points and the red curve is a smoothed guide to the eye. Each data point represents a single experimental run. Despite strong atom number fluctuations, we confirm the broad dysprosium intraspecies resonance around 22 G.

In the Feshbach scans displayed in Fig. 10.11 we notice a possible imaging issue. Between 10 G and 27 G the total atom number of potassium decreases with magnetic field. The same behavior is present in the noisy dysprosium atom numbers. In the next set of measurements for fields higher than 27 G, a delay of 10 ms between switching off the magnetic field coils and imaging was introduced. At around 47 G the potassium atom number starts to decrease again. In a later measurement, we detect more atoms with increasing time delay between switching off the magnetic field coils and imaging. The presence of a residual magnetic field from the Feshbach coils during imaging was ruled out by scanning the imaging frequency of potassium. Another plausible explanation for the reduced detected atom number is a depolarization of the atomic clouds. While turning off the Feshbach coil and turning on the coils along the imaging axis, the B-field at the position of the atoms might be crossing zero. After roughly 50 ms delay between switching off the Feshbach coils and imaging, the DDI of dysprosium seems to polarize both species back to the spin ground-states that we image. The maximum Dy atom number is reached faster than the maximum potassium atom number. In all measurements presented in this section we observe stronger fluctuations in the dysprosium data than in potassium. By the time we caught on the imaging problem, the Dy oven was empty and we lack a thorough investigation of the issue. The imaging has been later on corrected in the experiment, however, the ^{162}Dy - ^{40}K interaction measurements were not retaken.

The further study will concentrate at the region around 70 G, which in Fig. 10.11 seems to indicate a larger inter-species resonance. A closer look shows a region of multiple resonances, namely at least four shown in Fig. 10.13. Additional reference scans with only K or only Dy in this magnetic field region exhibit no features, so all we see around 70 G can be attributed to

inter-species resonances. The depolarization imaging issue is present, so in the measurements presented in this section we only image a part of the atoms (1/3 of the potassium atoms and about 1/2 of the dysprosium atoms) and the dysprosium numbers fluctuate heavily. Again, we will analyze only the potassium data, where we see clear features in the potassium atom numbers and temperature.

10.3.2. ^{162}Dy - ^{40}K two-body collisions and thermalization

All measurements in this section have the same preparation steps in common as already presented in Sec. 10.3.1. We load ^{40}K and ^{162}Dy in their absolute ground states. In the single beam sODT of $30\ \mu\text{m}$ waist Dy is evaporated and sympathetically cools potassium. We apply a fast exponential evaporation ramp with a time constant of typically 5 s and full thermalization between the species is not reached. At different magnetic fields for a given hold time we measure the thermalization rate between the species. In the magnetic field region between 68 G and 72 G we took one measurement per field value on three different days. The experimental parameters of day 1, 2, 3 are presented in Tab. 10.1 and the corresponding uncertainties are discussed at the end of the analysis.

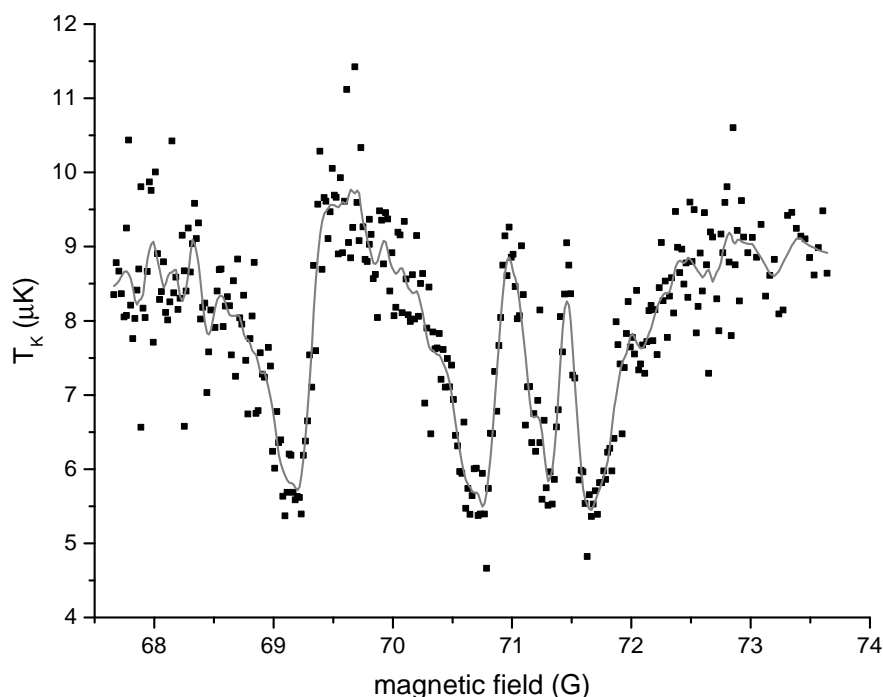


Figure 10.13.: Change in the potassium temperature T_K after a fixed hold time in the sODT with the colder Dy at a homogeneous magnetic field B around 70 G. The experimental parameters of day 3 are given in Tab. 10.1. Each data point represents a single experimental run. The gray curve represents the same data after smoothing and serves as a guide to the eye.

Figure 10.13 represents an example of our thermalization measurements. The shown data from day 3 have the highest resolution in magnetic field. We can identify 4 resonances for which we see a clear change in the potassium temperature. The lowest temperatures in K are reached at the poles of the resonances where maximum cooling by Dy occurs. Close to the zero-crossings, where elastic scattering vanishes, we observe the highest temperature of K. We use the size of the potassium cloud σ_{TOF} in the radial trap direction from the

data	day 1	day 2	day 3
t_{hold}	1 s	0.3 s	0.4 s
$\bar{\omega}_{\text{Dy}}/2\pi$	63 Hz	68 Hz	68 Hz
N_{Dy}	3.2×10^5	2.6×10^5	3.6×10^5
N_{K}	1×10^5	1.8×10^5	1.8×10^5
T_{Dy}	4 μK	6 μK	6 μK
T_{K}	7 μK	8 μK	9 μK
\bar{v}	6.5 cm/s	7.1 cm/s	7.4 cm/s
$\langle n_{\text{Dy}} \rangle_{\text{K}}$	$2.2 \times 10^{11} \text{ cm}^{-3}$	$1.5 \times 10^{11} \text{ cm}^{-3}$	$2.0 \times 10^{11} \text{ cm}^{-3}$
S^2	$5.1 \times 10^{16} \text{ m}^{-2}$	$1.4 \times 10^{16} \text{ m}^{-2}$	$2.3 \times 10^{16} \text{ m}^{-2}$

Table 10.1.: Experimental parameters for the thermalization measurements on day 1-3. The mean trap frequency $\bar{\omega}$ is given for dysprosium and it is 3.6 times larger for potassium (see Section 10.2.2).

time-of-flight absorption imaging as a measure of temperature with

$$T_{\text{K}} = \frac{\sigma_{\text{TOF}}^2 m_{\text{K}}}{k_B} \left(\frac{1}{\omega_r^2} + t_{\text{TOF}}^2 \right)^{-1}. \quad 10.5$$

The measurements from day 1, 2, 3 are analyzed separately and the combined results are discussed later together, since the sampling step of the magnetic field and most settings from Tab. 10.1 vary in the scans from day to day.

The three data sets are analyzed with the same models investigating the dependence of the two-body scattering cross section on the magnetic field in the ^{162}Dy - ^{40}K -mixture. The change in potassium temperature in Fig. 10.13 is determined by the thermalization rate with the colder dysprosium. We measure thus the dependence of the thermalization rate $\tau(B) = \left(\frac{1}{\Delta T} \frac{d\Delta T}{dt} \right)^{-1}$ on the magnetic field B for a fixed hold time t_{hold} . The initial temperature difference between the species after evaporation is $T_1 - T_0 = \Delta T(t_{\text{hold}} = 0 \text{ s})$ with $T_0 = T_{\text{Dy}}(t_{\text{hold}} = 0 \text{ s})$ and $T_1 = T_{\text{K}}(t_{\text{hold}} = 0 \text{ s})$. The temperature change with magnetic field and hold time is then

$$\Delta T(t_{\text{hold}}, B) = (T_1 - T_0) \exp \left(-\frac{t_{\text{hold}}}{\tau(B)} \right). \quad 10.6$$

We extract the thermalization time $\tau(B)$ from the experimental data and convert it into a Dy-K collision rate γ_{el} using [288]

$$\frac{1}{\tau(B)} = \frac{\xi}{3} \frac{N_{\text{Dy}} + N_{\text{K}}}{N_{\text{Dy}}} \gamma_{\text{el}}, \quad 10.7$$

with a reduction factor $\xi_{\text{DyK}} = 0.635$ for the mass ratio in the Dy-K mixture. The collision rate γ_{el} depends on the scattering cross section $\sigma_{\text{DyK}} = 4\pi a_{\text{DyK}}^2$, the mean thermal relative velocity \bar{v} and the overlap density between the species $\langle n_{\text{Dy}} \rangle_{\text{K}} = \frac{1}{N_{\text{K}}} \int n_{\text{K}} n_{\text{Dy}} dV$ (see calculation in Appendix C):

$$\gamma_{\text{el}} = 4\pi a_{\text{DyK}}^2 \bar{v} \langle n_{\text{Dy}} \rangle_{\text{K}}. \quad 10.8$$

We define S as the factor that absorbs all experimental parameters present in Eqs. 10.7

and 10.8

$$S = \sqrt{\bar{v}\langle n_{\text{Dy}} \rangle_{\text{K}} \frac{4\pi\xi}{3} \frac{N_{\text{Dy}} + N_{\text{K}}}{N_{\text{Dy}}} t_{\text{hold}}} \quad 10.9$$

and thus

$$\frac{t_{\text{hold}}}{\tau(B)} = a_{\text{DyK}}^2 S^2. \quad 10.10$$

The observed temperature change in potassium is then

$$T_{\text{K}}(t_{\text{hold}}) = T_0 + (T_1 - T_0) \exp\left(-a_{\text{DyK}}^2 S^2\right), \quad 10.11$$

where we set $T_{\text{Dy}}(t_{\text{hold}}) = T_0$, since we regard the dysprosium particles as a thermal bath.

The next step of the analysis is to implement a model for the dependence of the scattering length on the magnetic field $a_{\text{DyK}}(B)$ into Eq. 10.11. In this way we can extract positions and resonance widths from the data. We observe multiple resonances, which partly overlap, therefore they might influence one another. In the following, two parametrizations for the scattering length in a scenario of overlapping resonances are introduced. The two formulas are based on an analytical model [358] and complement each-other.

In one of the models we start with the explicit formula from Ref. [358]

$$a_{\text{DyK}} = a_{\text{bg}} \left(1 - \sum_{i=1}^4 \frac{\Delta_i}{B - B_i} \right), \quad 10.12$$

to which we apply a resonance approximation

$$a_{\text{DyK}} = - \sum_{i=1}^4 \frac{a_{\text{bg}} \Delta_i}{B - B_i}. \quad 10.13$$

Here we neglected the a_{bg} offset term and only keep the resonance contributions. The pole positions are given by B_i while the background scattering length a_{bg} and the resonance width Δ_i are merged into a single parameter, the resonance pole strength $a_{\text{bg}}\Delta_i$. With this ansatz for the scattering length, we fit the observed temperature change in potassium from Eq. 10.11 with

$$T_{\text{K}} = T_0 + (T_1 - T_0) \exp\left(- \sum_{i=1}^4 \left(\frac{a_{\text{bg}} \Delta_i S}{B - B_i} \right)^2\right). \quad 10.14$$

Note that $a_{\text{bg}}\Delta_i S$ is a single fit parameter, hence we cannot extract a background scattering length from this fit model. In the following, I will refer to this fit function as the ‘sum fit’, since we use a sum expression for the scattering length in the resonance approximation. The fit results are listed in Table 10.2 and the corresponding fit functions are plotted in Fig. 10.14.

In the second model we apply the scattering length expression for multiple resonances from Ref. [359]

$$a_{\text{DyK}} = a_{\text{bg}} \prod_{i=1}^4 \left(1 - \frac{\tilde{\Delta}_i}{B - B_i} \right). \quad 10.15$$

data	day 1	day 2	day 3
$a_{\text{bg}}\Delta_1 S$	0.24(3)	0.10(1)	0.17(1)
B_1	69.08(3)	69.17(3)	69.16(2)
$a_{\text{bg}}\Delta_2 S$	0.32(4)	0.17(2)	0.21(1)
B_2	70.73(4)	70.73(2)	70.72(2)
$a_{\text{bg}}\Delta_3 S$	0.23(3)	0.11(1)	0.17(1)
B_3	71.31(4)	71.32(3)	71.27(2)
$a_{\text{bg}}\Delta_4 S$	0.18(2)	0.14(1)	0.14(1)
B_4	71.59(4)	71.62(2)	71.59(2)
T_0 (μK)	4.4(1)	6.4(1)	5.9(1)
T_1 (μK)	7.6(2)	8.4(1)	9.1(1)

Table 10.2.: Thermalization fit results with ‘sum fit’ function Eq. 10.14 of the data from day 1-3. All values for width and position of the four resonances are in Gauss. The uncertainty of the parameters is the respective standard error given by the fit.

The two scattering length expressions, Eqs. 10.12 and 10.15, are equivalent [358]. The practical advantage of the product formula is that a_{bg} remains a separate fit parameter and cannot be eliminated in a resonance approximation. The parameters $\tilde{\Delta}_i$ should give the distance between the pole of the resonance and the nearest zero crossing of the scattering length. However, in a product expression we cannot definitely assign the $\tilde{\Delta}_i$ parameter to the i -th resonance. The parameters $\tilde{\Delta}_i$ thus cannot be determined uniquely in a fit and we cannot view them as resonance widths [358]. Nonetheless, the product $\tilde{a}_{\text{DyK},i}\tilde{\Delta}_i$ is well-determined and can be regarded as the pole strength of the resonance, identical to $a_{\text{bg}}\Delta_i$ from Eq. 10.13, with

$$\tilde{a}_{\text{DyK},i} = a_{\text{bg}} \prod_{j \neq i}^4 \left(1 - \frac{\tilde{\Delta}_j}{B_i - B_j} \right) \quad 10.16$$

being the local background scattering length and $\tilde{\Delta}_i$ the local resonance width [358]. Implementing Eq. 10.15 into Eq. 10.11 gives us the second fit function for the temperature change of potassium

$$T_{\text{K}} = T_0 + (T_1 - T_0) \exp \left(-(a_{\text{bg}} S)^2 \prod_{i=1}^4 \left(1 - \frac{\tilde{\Delta}_i}{B - B_i} \right)^2 \right). \quad 10.17$$

In the following, I will refer to this fit function as the ‘product fit’, as it has a product expression for the scattering length. The fit results are listed in Table 10.3 and the corresponding fit functions are plotted in Fig. 10.14.

We have two fit functions with different outcomes. The ‘sum fit’ delivers magnetic field resonance poles and resonance strengths, but hides the background scattering length. The ‘product fit’ gives information about the local background scattering length, but does not have a unique solution due to the additional fit parameter. Since our data are noisy, we will use both fit functions Eq. 10.14 and Eq. 10.17 to the data of each day and compare the results at the end.

Crucial for convergence of the fits are the initial values of the temperatures and the resonance pole positions. The ‘sum fit’ is applied to the data starting with initial values for T_1 and T_0 as in Table 10.1 and the initial B_i values are set by eye. The ‘sum fit’ is robust and

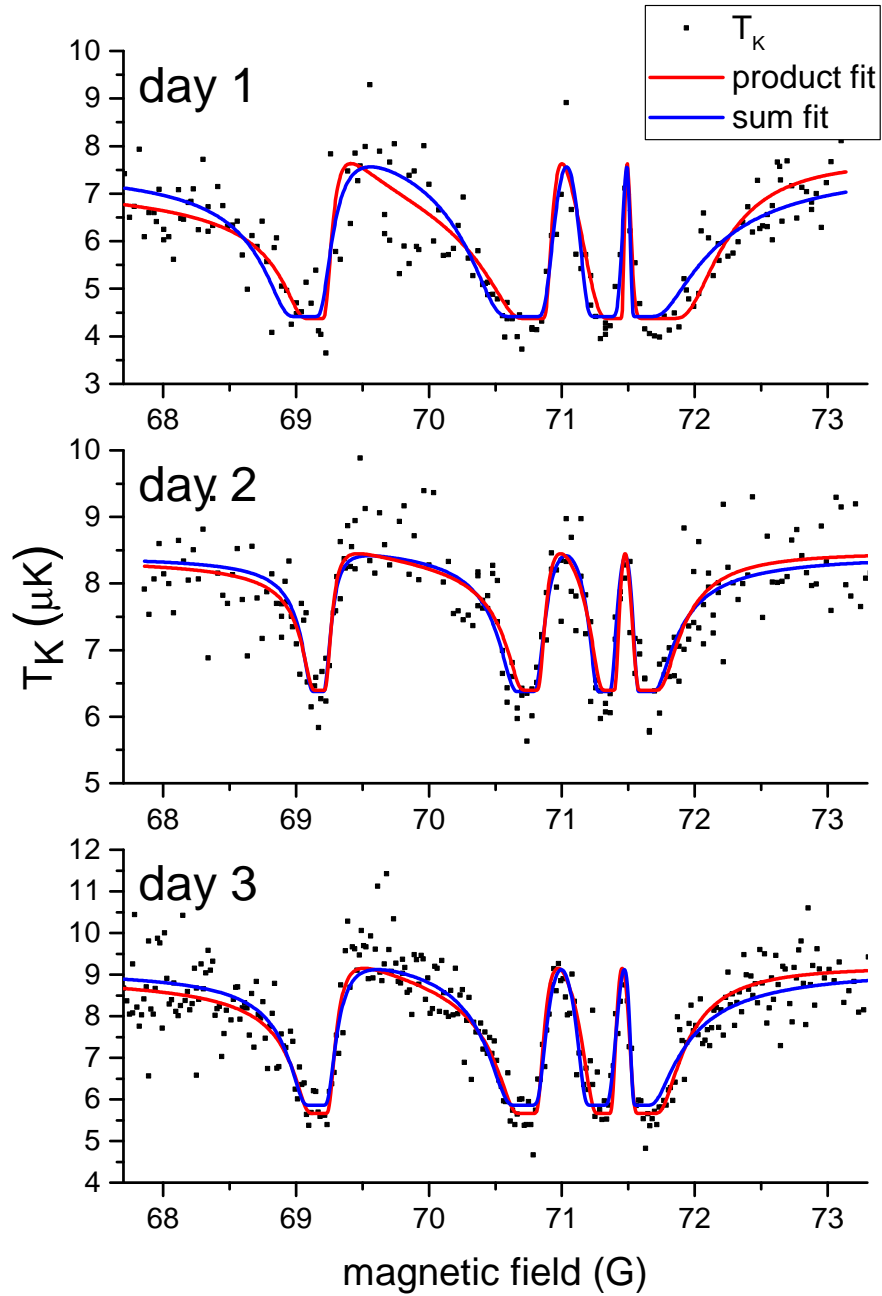


Figure 10.14.: Analysis of the thermalization between Dy-K around 70 G using the potassium temperature T_K after a fixed hold time in magnetic field B . The best fits with functions Eq. 10.14 and Eq. 10.17 are presented in blue and red, respectively. The experimental parameters of day 1, 2, 3 are given in Table 10.1.

data	day 1	day 2	day 3
$a_{\text{bg}}S$	0.24(4)	0.11(4)	0.15(2)
$\tilde{\Delta}_1$ (G)	0.26(3)	0.29(4)	0.33(2)
B_1 (G)	69.15(3)	69.18(3)	69.18(2)
$\tilde{\Delta}_2$ (G)	0.20(2)	0.22(2)	0.23(1)
B_2 (G)	70.79(4)	70.77(2)	70.75(2)
$\tilde{\Delta}_3$ (G)	0.082(7)	0.12(1)	0.14(1)
B_3 (G)	71.40(6)	71.36(4)	71.32(2)
$\tilde{\Delta}_4$ (G)	3.1(7)	4(2)	3.6(7)
B_4 (G)	71.70(4)	71.64(3)	71.63(2)
T_0 (μK)	4.4(1)	6.4(1)	5.7(1)
T_1 (μK)	7.6(2)	8.5(1)	9.2(1)

Table 10.3.: Thermalization fit results with ‘product fit’ function Eq. 10.17 for the data from day 1-3.

the results with minimal χ^2 are presented in Table 10.3 and plotted in blue in Fig. 10.14. The fit function Eq. 10.17 (‘product fit’) is also applied to the data with initial values of T_1 and T_0 from Table 10.1 and the initial B_i values are the results from the ‘sum fit’. The ‘product fit’ function has one additional parameter compared to the ‘sum fit’ and converges for a vast range of the temperatures and $a_{\text{bg}}S$. Furthermore, the fit results strongly depend on the chosen initial values of all parameters. That is why the reliability of the parameters must be tested. The values of B_i are each limited by upper and lower bounds to a region of about 200 mG width. This is necessary mainly for the clear separation of the last two resonances and allows fixing other parameters to extreme values. Fixing either T_1 or T_0 up to $\pm 10\%$ of the T_0 values in Table 10.3 (or to the most extreme value for which the fit converges) shows strong fluctuations in $a_{\text{bg}}S$ and $\tilde{\Delta}_i$, but the B_i values stay robust within their respective errors (which are smaller than the bounds). For fixed B_i values as in Table 10.3 and with $a_{\text{bg}}S$ fixed to $\pm 50\%$ of the values in Table 10.3, the parameters T_0 , T_1 and $\tilde{\Delta}_{1,2,3}$ are rather robust within their respective errors but $\tilde{\Delta}_4$ changes drastically. The ‘product fit’ is uncertain due to the number of free parameters, but after many iterations with some of the parameters fixed, we find satisfying initial conditions for fit results with lowest χ^2 . The final fit results are presented in Table 10.3 and are plotted in Fig. 10.14.

We start the discussion of the results with the fit parameters, which do not depend on the specific experimental settings: the resonance poles, the temperatures and the parameters $\tilde{\Delta}_i$. A significant outcome of both fit models is that the extracted resonance poles B_i in Tables 10.2 and 10.3 agree within one or two standard errors with each other. The uncertainties in B_i are highest for day 1, probably because the increment of the magnetic field in this data set is large with about 35 mG. All B_i values fluctuate more than the experimental uncertainty of the magnetic field of about 10 mG. Nevertheless, the two independent fits of day 1,2,3 deliver convincing values for the resonance positions. It is also affirmative that both fits deliver T_0 and T_1 values which are identical within their errors. Those fitted values are not far from the temperatures presented in Table 10.1, which are measured in a TOF measurement with an error of about 0.7 μK . The relative uncertainties in $\tilde{\Delta}_i$ from the ‘product fit’ are high with more than 10%. And as the fitting procedure already showed, the uncertainty in $\tilde{\Delta}_4$ is the largest. But here again, the results from the three data sets are consistent.

For the discussion of the remaining results from the fit functions we will implement the

parameter	day 1	day 2	day 3
$a_{\text{bg}} (a_0)$	20	18	19
$\tilde{a}_{\text{DyK},1} (a_0)$	52	56	56
$\tilde{a}_{\text{DyK},2} (a_0)$	85	97	93
$\tilde{a}_{\text{DyK},3} (a_0)$	136	147	118
$\tilde{a}_{\text{DyK},4} (a_0)$	10	7	7
$a_{\text{bg}}\Delta_1 (a_0\text{G})$	20	16	21
$\tilde{a}_{\text{DyK},1}\tilde{\Delta}_1 (a_0\text{G})$	14	16	19
$a_{\text{bg}}\Delta_2 (a_0\text{G})$	27	27	27
$\tilde{a}_{\text{DyK},2}\tilde{\Delta}_2 (a_0\text{G})$	17	21	21
$a_{\text{bg}}\Delta_3 (a_0\text{G})$	19	18	21
$\tilde{a}_{\text{DyK},3}\tilde{\Delta}_3 (a_0\text{G})$	11	18	17
$a_{\text{bg}}\Delta_4 (a_0\text{G})$	15	22	17
$\tilde{a}_{\text{DyK},4}\tilde{\Delta}_4 (a_0\text{G})$	32	27	23

Table 10.4.: Derived parameters for background scattering length and resonance strength from both thermalization fits of the data from day 1-3.

experimental settings through the factor S for each day (see Table 10.1 and Eq. 10.9) and also consider the derived parameters $\tilde{a}_{\text{DyK},i}$, which are presented in Table 10.4. An important property of our system and the reason to introduce the ‘product fit’ in the analysis is the background scattering length. Since the fits of the three data sets are of unequal quality, we use the weighted mean and get $a_{\text{bg}} = 19(1)a_0$. Therewith, the background scattering cross section is $\sigma_{\text{DyK}}^{\text{bg}} = 1.3(2) \times 10^{-17} \text{ m}^2$.

In addition to the fit uncertainties, the factor S introduces a relatively large error coming from the uncertainties in the experimental settings from Table 10.1. Looking at Eq. 10.9 we have to consider the error propagation of the temperature uncertainty of about $0.7 \mu\text{K}$ for both species and the atom number uncertainty. The atom numbers of both species fluctuate heavily with about 20 % due to the imaging issue that was discussed in the beginning of the chapter. This introduces a very high relative error in the peak and overlap densities of dysprosium of 28 % and 46 %, respectively. The error in the overlap density is the main error contribution to S , in contrast to the low relative uncertainty of 4 % in the relative velocity \bar{v} coming from the temperature uncertainty. An error in the sODT beam waist of only $1 \mu\text{m}$ would give an error of $2a_0$ in a_{bg} . This is, however, a systematic error to all measurements and is not added in the Gaussian error propagation for S . Furthermore, the total relative error in S is so large with 26 %, that it would cover the uncertainty in beam waist. Therewith, our result for the background scattering length obtains the relative error from S and becomes $a_{\text{bg}} = 19(5)a_0$. The derived background scattering cross section is then $\sigma_{\text{DyK}}^{\text{bg}} = 1.3(4) \times 10^{-17} \text{ m}^2$.

The large uncertainty in the experimental parameters could also explain the deviations between $a_{\text{bg}}\Delta_i$ and $\tilde{a}_{\text{DyK},i}\tilde{\Delta}_i$ presented in Table 10.4. Those resonance strengths from the ‘sum’ and ‘product’ fit should be identical for a given resonance. While we can calculate the relative error in $a_{\text{bg}}\Delta_i$ from fit and experimental uncertainties to about 30 %, the accurate uncertainty of $\tilde{a}_{\text{DyK},i}$ is difficult to determine, since the errors of the parameters it depends on are most likely correlated (see Eq. 10.16). Overall, both fits yield somehow consistent results for the resonance pole strengths.

To characterize those Feshbach resonances in terms of open- or closed-channel dominated

resonances the range parameter R^* is introduced. R^* is a characteristic length typically used to describe if a resonance between fermions has a broad enough universal range for Pauli suppression of few-body losses [76, 132]. The universal range is reached for $|a| \gg R^*$ and the range parameter is defined by

$$R^* = \frac{\hbar^2}{2m_r \delta\mu a_{\text{bg}} \Delta} \quad 10.18$$

with the reduced mass m_r of ^{162}Dy and ^{40}K , the resonance pole strength $a_{\text{bg}}\Delta$ and the differential magnetic moment $\delta\mu$ between the scattering and the molecular state involved in the resonance. Actually $\delta\mu$ is unknown for our system, so we will take a conservative guess of $\delta\mu = 0.1\mu_B$ with the Bohr magneton $m\mu_B$. The resonance with $i = 2$ around 70.75 G has the largest resonance pole strength of about $24 a_0\text{G}$ from the four fitted resonances and will be used as an example. We obtain $R \approx 1.7 \times 10^4 a_0$ and therefore a very narrow magnetic field range for which $|a| \gg R^*$. Therefore, we can conclude that all four resonances are very narrow.

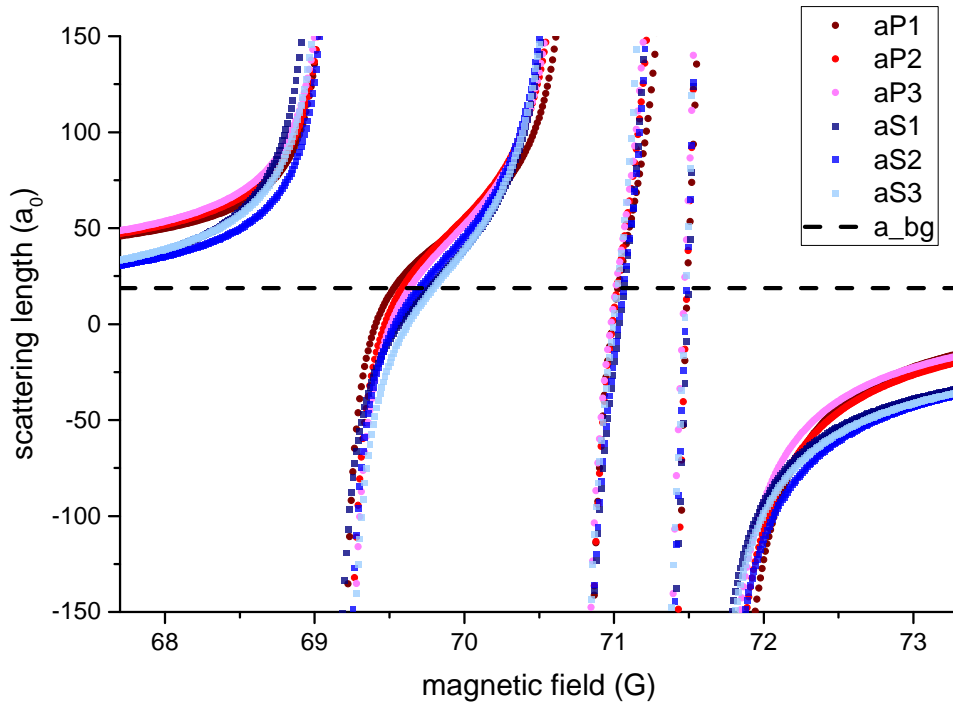


Figure 10.15.: Scattering length calculation from the extracted fit parameters from Tables 10.3 and 10.2. We see four narrow resonances within 3G. The abbreviations S and P stand for ‘sum’ and ‘product’ fit, respectively. The plotted a_{bg} is the weighted average of the ‘product fit’ results.

Figure 10.15 shows the simulated scattering length $a(B)$ for the three data sets using Eq. 10.13 and Eq. 10.15 and the experimental settings from Table 10.1. We see again that the results from both fits agree very well with each other. The difference between the two models is very clear in Fig. 10.15: the product formula delivers an overall offset to the scattering length, namely a_{bg} , compared to the sum formula, where we omitted the

background contribution.

The experimental accuracy and the lack of statistics aside, one major issue with our fit models is that we choose to see only four resonances in the B-field region in Fig. 10.14. In our further measurements, we see smaller resonances overlapping as in Fig. 10.16. We did not increase the number of resonances in the models used so far, since the splitting of overlapping resonances would have been arbitrary. Nevertheless, we have a first estimate of the scattering length behavior using rather simple models based on kinematics and s-wave scattering theory. The first important assumption in our model is that we neglect any losses during thermalization, see Eq. 10.7. The measurement timescale is short for background losses and we do not have evidence for strong intra-species 3-body-losses, hence this part of our assumption is valid. We do measure inter-species 3-body-loss in the following section, but since the trap is tighter for potassium and $N_K \ll N_{Dy}$, the presumption of a constant overlap density is $\langle n_{Dy} \rangle_K$ is effective for the thermalization analysis. On the other hand, we do not recompress the sODT after evaporation and thus plain evaporation of dysprosium is still present. However, we measure on short timescales and there is no evidence of any significant atom loss or temperature change in dysprosium. Hence our approach to analyze only the potassium temperature dependence in a dysprosium bath is credible.

Another important assumption in the model is the use of s-wave theory in Eq. 10.15. Which partial waves contributed to the coupling that is responsible for a resonance is hard to know. Nonetheless, the temperatures are relatively low, hence the scattering events themselves are s-wave scattering. Without the knowledge of the exact inter-atomic potentials, the origin and position of the Feshbach resonances cannot be predicted. By the time of writing this thesis, there are no theoretical predictions for the magnetic Feshbach spectra in the Dy-K mixture. In the theoretical predictions for Li-Er systems from Ref. [153] for example, the scattering events are also in s-wave. Similarly to the work in Ref. [153], our elements are in their ground state.

The thermalization measurements between ^{40}K and ^{162}Dy presented in this section reveal two important interaction properties. First, we demonstrate that the background scattering length in this Bose-Fermi mixture is small and second, we detect multiple possibilities to tune the inter-species interactions already at low ($< 100\text{ G}$) magnetic fields, even if the resonances are too narrow for investigations with strong interactions.

10.3.3. Three-body loss in ^{162}Dy - ^{40}K

In a second type of measurement we look into the resonance with $i = 1$ near 69 G. In Fig. 10.13 this resonance seems to be broad and well isolated compared to the following three. We record the atom loss for different values of t_{hold} in the homogeneous magnetic field. We estimate a lower bound for the three-body loss coefficient L_3 for Bose-Bose-Fermi decay across the resonance and at the pole of the resonance.

In this set of experiments, the evaporation is about twice slower than for the thermalization measurements from Sec. 10.3.2 and both species almost thermalize at about 4 μK . The sODT is slightly re-compressed before applying the homogeneous magnetic field and $\bar{\omega}_{Dy} = 2\pi \times 74\text{ Hz}$. All other experimental steps are identical to the thermalization measurements from the previous section. The atom number of Dy fluctuates by up to 40% and no clear interaction features can be obtained from the detected dysprosium cloud. Here again, the recorded atom numbers are altered by the imaging issue with the depolarized clouds for zero magnetic field. For this set of experiments, however, we have a good estimate of the real atom numbers from stability measurements without homogeneous Feshbach field, where the

magnetic field zero is not crossed and the clouds stay polarized for imaging. The initial atom numbers are $N_K = 8 \times 10^4$ and $N_{Dy} = 4.2 \times 10^5$. The size of the potassium cloud does not change much and is not shown. We know from preparation measurements the temperature of dysprosium to be $T_{Dy} = 3.7 \mu\text{K}$ and potassium is at $T_K = 4.4 \mu\text{K}$. For the analysis of the data we will assume thermal equilibrium at $T_{Dy} = T_K = 4 \mu\text{K}$.

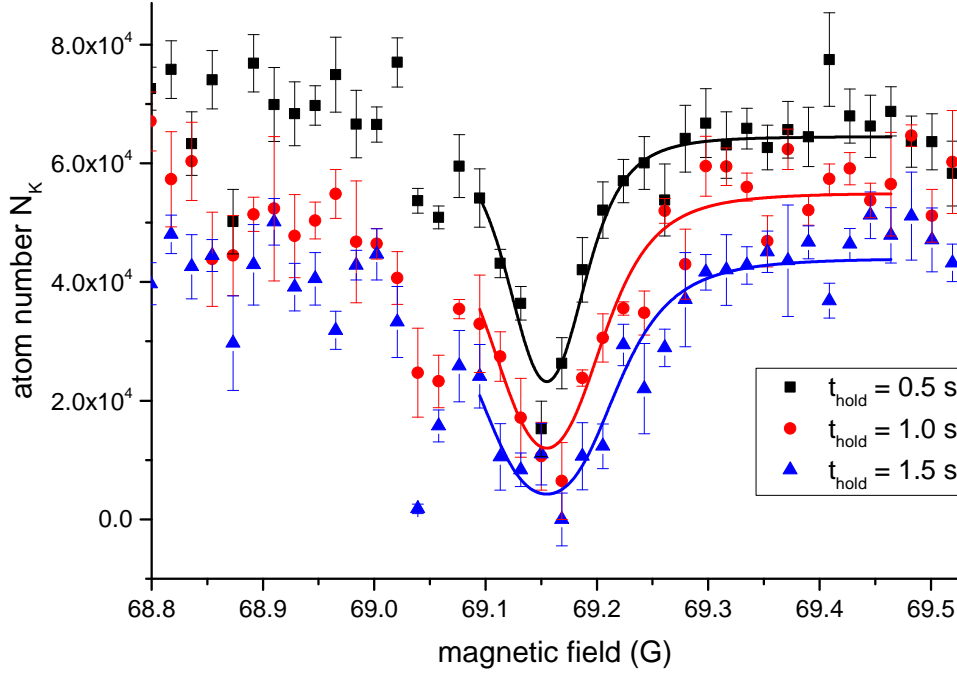


Figure 10.16.: Atom loss measurements for different hold times $t_{\text{hold}} = 0.5\text{ s}$, 1 s and 1.5 s near 69.15 G . The error bars show the standard error of the mean atom number for a small amount of measurements. The lines are the fits with Eq. 10.24, which is used for determination of the L_3 coefficient.

In this boson-fermion mixture three-body processes involving two bosons and one fermion are the dominant loss mechanism. Two-body loss is fully suppressed, because both atomic species are in their lowest internal states. Decay processes of three identical bosons (^{162}Dy) are allowed, but will occur at a low rate [65]. The reason is that the intraspecies background scattering length of ^{162}Dy is about $150 a_0$ [341] and thus will be much smaller than the interspecies scattering in the magnetic field region across the Dy-K Feshbach resonance. Any recombination processes involving more than one fermion are Pauli suppressed [360]. Figure 10.16 presents the loss features in the potassium atom numbers for three different values of the hold time t_{hold} . We have three to five measurements per magnetic field value at a different value of the hold time. We investigate the dependence of the three-body loss coefficient L_3 on the two-body scattering length a_{DyK} across the Feshbach resonance. The maximum atom loss occurs at the resonance pole B_1 , which is at about 69.15 G . Our loss measurement reveals that on the low-field side of this first resonance from Fig. 10.14 we actually have an overlapping resonance scenario around 69.03 G . With increasing t_{hold} the width of the loss features increases, which is a saturation effect.

We analyze again only the potassium data. The dominant three-body loss mechanism in

the thermal sample involves one ^{40}K (fermion) and two ^{162}Dy (bosons). Since we have more dysprosium and the trap is deeper for potassium, we make the approximation that Dy forms a large reservoir. The time evolution of the atom number at a certain field then is given by

$$\dot{N}_{\text{K}} = -L_3 \langle n_{\text{Dy}}^2 \rangle_{\text{K}} N_{\text{K}}. \quad 10.19$$

The squared density of dysprosium in the overlap region with potassium at interspecies thermal equilibrium is

$$\langle n_{\text{Dy}}^2 \rangle_{\text{K}} = n_0^2 \left(1 + 2 \frac{\alpha_{\text{Dy}}}{\alpha_{\text{K}}} \right)^{-3/2}, \quad 10.20$$

where n_0 is the peak dysprosium density and α_{Dy} and α_{K} are the polarizabilities of dysprosium and potassium respectively (see Appendix C for the derivation of $\langle n_{\text{Dy}}^2 \rangle_{\text{K}}$). The solution of the atom loss equation 10.19 is an exponential decay:

$$N_{\text{K}}(t_{\text{hold}}) = N_0 \exp\left(-L_3 \langle n_{\text{Dy}}^2 \rangle_{\text{K}} t_{\text{hold}}\right). \quad 10.21$$

For a given value of the magnetic field we measure the atom number only at three different values of t_{hold} . The fit of Eq. 10.21 through the few measured points is shown in Fig. 10.17 as an example for the two magnetic field values, for which we obtain the largest L_3 . All values of L_3 , which are obtained in this way across the Feshbach resonance, are presented in Fig. 10.18. We observe the resonance behavior around B_1 and we measure a maximal value of the three-body-loss coefficient $L_c = 8(1) \times 10^{-24} \text{ cm}^6/\text{s}$. L_c is the cutoff value of the three-body-loss coefficient at unitarity [361].

We will use an additional approach in order to introduce the magnetic field dependence in the model. We are looking for a reasonable model that connects L_3 to a_{DyK} . It should reproduce the $L_3 \propto a_{\text{DyK}}^4$ dependence for not too large values of $|a_{\text{DyK}}|$ [362] and it should show the unitarity cutoff [361]. We chose thereafter the following phenomenological ansatz

$$L_3(B) = \left(\frac{1}{\sqrt{L_a(B)}} + \frac{1}{\sqrt{L_c}} \right)^{-2}, \quad 10.22$$

where L_c is the cutoff value of the three-body loss parameter in the unitarity regime and

$$L_a(B) = C \frac{\hbar}{2m_r} a_{\text{DyK}}^4 = C \frac{\hbar}{2m_r} \left(\frac{a_{\text{bg}} \Delta_1}{B - B_1} \right)^4 \quad 10.23$$

reflects the dependence of the three-body loss coefficient on the two-body scattering length a_{DyK} . The coefficient C can take values between zero and 68 [363], $2m_r$ is the chosen mass for the three body process, with m_r being the reduced mass between ^{162}Dy and ^{40}K [361]. The parameters $a_{\text{bg}} \Delta_1$ and B_1 describe a_{DyK} across the resonance and should be the same as the results from the two-body analysis from the previous section 10.3.2. Later in the analysis we will discuss the accuracy of these parameters. Since the major three-body loss mechanism involves one ^{40}K and two ^{162}Dy and we analyze the potassium number, the atom-loss rate L_3 is the same as the loss-event rate \dot{K}_3 .

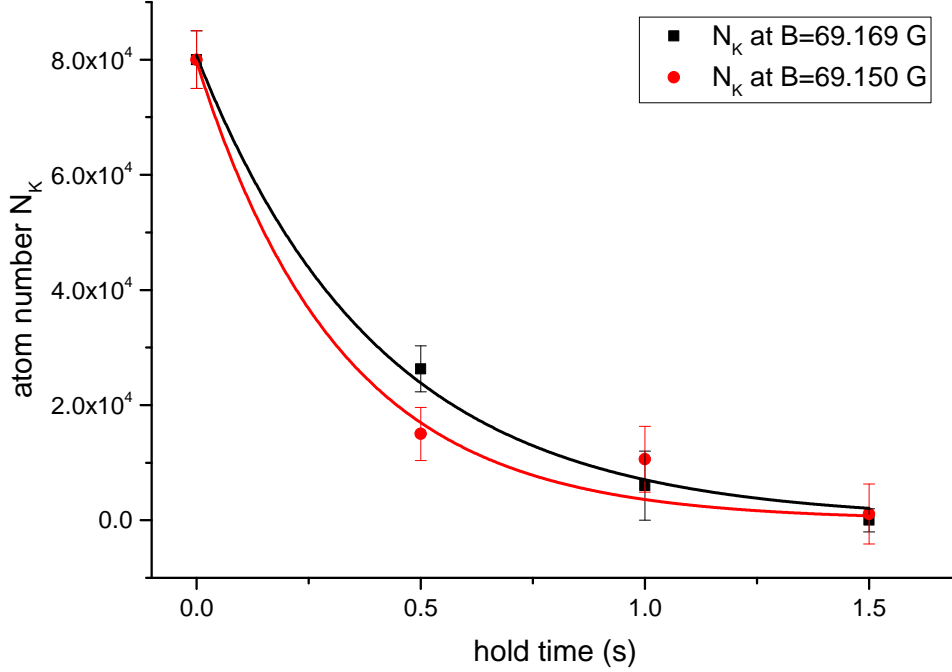


Figure 10.17.: Determination of L_3 coefficient at $B = 69.169$ G and $B = 69.150$ G with the atom loss Eq. 10.21. The error bars show the standard error of the mean atom number for a small amount of measurements. We obtain $L_3(B = 69.169 \text{ G}) = 6.2(7) \times 10^{-24} \text{ cm}^6/\text{s}$ and $L_3(B = 69.150 \text{ G}) = 8(1) \times 10^{-24} \text{ cm}^6/\text{s}$.

Inserting Eqs. 10.23 and 10.22 into the atom loss equation 10.21 gives our L_3 -fit function

$$N_K(B) = \tilde{N}_0 \exp \left(- \frac{\langle n_{\text{Dy}}^2 \rangle_K t_{\text{hold}}}{\left(\sqrt{\frac{2m_r}{C\hbar}} \left(\frac{B-B_1}{a_{\text{bg}}\Delta_1} \right)^2 + L_c^{-1/2} \right)^2} \right). \quad 10.24$$

The fit parameters that we are mostly interested in are the saturation value of the three-body loss coefficient L_c and the combined parameter $W = \sqrt{C} (a_{\text{bg}}\Delta_1)^2$, which is proportional to the resonance pole strength. The initial atom number \tilde{N}_0 is also a free fit parameter here, while the overlap squared density is kept constant at $\langle n_{\text{Dy}}^2 \rangle_K = 4 \times 10^{23} \text{ cm}^{-6}$ (see Eq. 10.20). The fit function from Eq. 10.24 is applied separately to the data-sets for each value of t_{hold} and the results are merged afterward.

As depicted in Fig. 10.16 we fit only one side of the Feshbach resonance above 69.1 G. On the one hand, the small resonance(s) at the low field side corrupts the fitting. On the other hand, the background level \tilde{N}_0 at higher and lower fields is not identical, due to the many neighboring resonances. The different background level of \tilde{N}_0 is also confirmed by the differing $\tilde{a}_{\text{DyK},1}$ and $\tilde{a}_{\text{DyK},2}$ values from the two-body analysis (see Table 10.4). We consider only the resonance contribution to L_3 (see Eq. 10.23), so our model cannot reproduce the change in reference level \tilde{N}_0 . The fit outcomes $\tilde{N}_0(t_{\text{hold}})$ together with $\tilde{N}_0(t_{\text{hold}} = 0) = N_0$ are used in the simple decay Eq. 10.21, in order to find a background value L_{bg} of the three-body-loss coefficient to supplement our resonance model.

t_{hold}	$a_{\text{bg}}\Delta_1/a_0$	L_c	\tilde{N}_0
0.5 s	91(12) G	$5.2 \times 10^{-24} \text{ cm}^6/\text{s}$	$6.5(2) \times 10^4$
1.0 s	98(9) G	$3.9 \times 10^{-24} \text{ cm}^6/\text{s}$	$5.5(2) \times 10^4$
1.5 s	115(23) G	$4.0 \times 10^{-24} \text{ cm}^6/\text{s}$	$4.4(2) \times 10^4$

Table 10.5.: Atom loss fit results for fixed $B_0 = 69.155 \text{ G}$. For extracting $a_{\text{bg}}\Delta_1/a_0$ from K we use the maximal value of $C = 68$. The standard error of L_c from the fit is a few orders of magnitude larger than the L_c value and is not given here (see text for discussion). The results for $\tilde{N}_0(t_{\text{hold}})$ are used to find a background value L_{bg} of the three-body-loss coefficient with Eq. 10.21.

The fitting process starts with some iterations with upper and lower bounds for the resonance center $69.11 \text{ G} \leq B_1 \leq 69.19 \text{ G}$. In order to reduce the number of free fit parameters we will fix $B_1 = 69.155 \text{ G}$, which agrees very well with all data and has more significant digits than our experimental resolution. The width or strength of the resonance $a_{\text{bg}}\Delta_1$ is also supposed to be identical for all hold times. The fit results with minimum χ^2 are presented in Table 10.5 and deliver a somehow growing value of $a_{\text{bg}}\Delta_1$ with t_{hold} . Nevertheless, the results agree within the fit standard error and the mean is $a_{\text{bg}}\Delta_1/a_0 = 100(20) \text{ G}$ for the maximum $C = 68$. The resonance strength obtained with this model is more than five times higher than the resonance strength from the two-body analysis in Table 10.4, even for the maximum value of the coefficient C . A possible explanation of this discrepancy is that in Fig. 10.14 we use a model for a single resonance at B_1 , while in Fig. 10.16 we see overlapping resonances around B_1 . Intuitively, the width of two overlapping resonances should be larger than for a single one. However, we evaluate the resonance strength that includes a_{bg} , which cannot be clearly determined in the region of overlapping Feshbach resonances. It could be that the local background scattering length is much higher due to the small resonance around 69.05 G and that is why the fitted resonance strength is also higher. So, the value of $a_{\text{bg}}\Delta_1$ from the two-body analysis was a good starting point for the fitting procedure and is not invalidated by the differing result in this section.

The fitted value of L_c is also presented in Table 10.5. The cutoff value of the three-body-loss coefficient has a fit standard error that is about five orders of magnitude larger than L_c itself, which might be due to the small absolute value of this fit parameter. Otherwise for every converging fit, the outcome for L_c is within one order of magnitude of the final results. In Fig. 10.16 we see the fitted curves with minimal χ^2 for each t_{hold} . We notice that none of the curves crosses the respective data point with lowest atom number at the resonance center. This is also not the case for $B_1 \neq 69.155 \text{ G}$. A higher value of L_c lowers the peak of the respective fit curve, but it also slightly influences \tilde{N}_0 and therewith increases the χ^2 of the fit. A narrower fit range reduces the weight of the background level, but it also makes the fit unreliable, since we fit only one side of the resonance and we need the wings of the peak function. The average value from the three fits is $L_c = 4.4(7) \times 10^{-24} \text{ cm}^6/\text{s}$. With an additional evaluation of the background level \tilde{N}_0 , we will obtain a lower bound for the unitarity limit of the three-body-loss coefficient.

The behavior of L_3 across the Feshbach resonance at $B_1 = 69.155 \text{ G}$ evaluated with both approaches from this section is presented in Figure 10.18. The black squares are the results from the direct fit of the atom loss equation 10.21. The dashed blue line in Fig 10.18 is the calculation of L_3 using the resonance model in Eq. 10.22 with the averaged results from Table 10.5. The black solid curve is the same resonance model, only with an additional offset L_{bg} . The offset value $L_{\text{bg}} = 9.8(5) \times 10^{-25} \text{ cm}^6/\text{s}$ is obtained by fitting Eq. 10.21 to the results for $\tilde{N}_0(t_{\text{hold}})$ from Table 10.5. The results for the three-body-loss coefficient

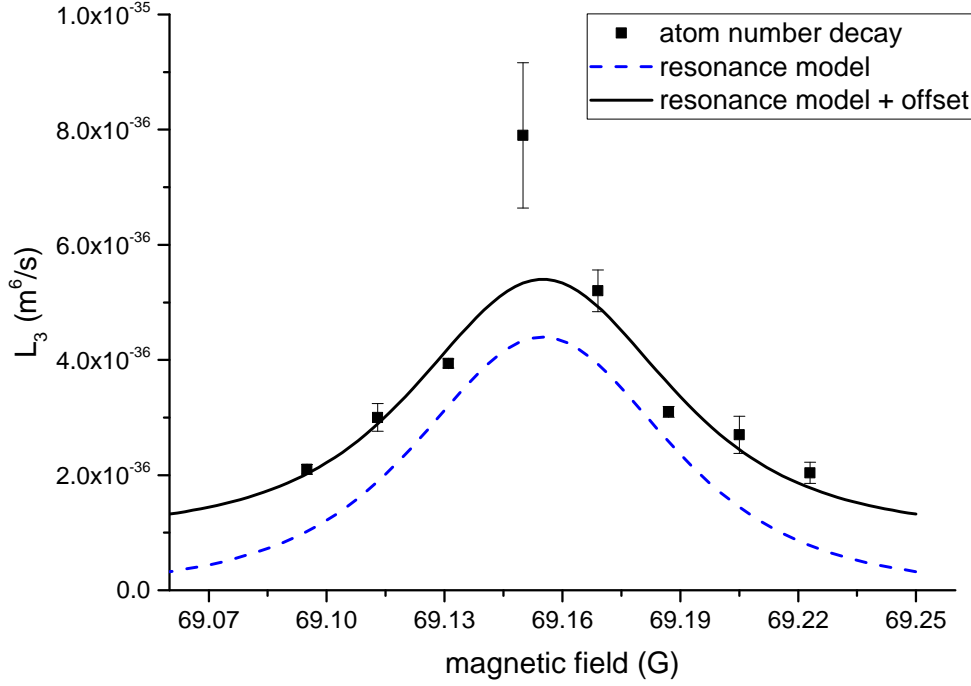


Figure 10.18.: Comparison of L_3 coefficient around $B = 69.15$ G from both approaches, with Eqs. 10.21 and 10.24. The error bars show the standard error of the fits as in Fig. 10.17 and for some of the data points are smaller than the symbol. The uncertainties in the resonance model are discussed in the text.

L_3 from both approaches presented in Fig. 10.18 agree well with each-other. Only at the resonance pole there is a mismatch between the maximum L_3 value evaluated with Eq. 10.21 and the fitted $L_c + L_{\text{bg}}$ value. As already discussed in the description of the fitting process, the result for $L_c + L_{\text{bg}} = 5.4(9) \times 10^{-24} \text{ cm}^6/\text{s}$ gives then a lower limit for the cutoff value of the three-body-loss coefficient at the resonance pole.

Up to now we have only considered the standard errors from the fits. The error propagation of the experimental uncertainties is similar to the two-body analysis in the previous section. The overlap density plays a more important role here and the error in dysprosium atom number of 10% contributes massively to the error of about 38% of the final L_3 value. The uncertainty in temperature is $0.3 \mu\text{K}$ for both species and has negligible effect on the total error. The experimental uncertainty in the magnetic field of 10 mG has also an impact on the precision for a narrow resonance. We do not explicitly consider the experimental uncertainty in the magnetic field, we assume it is covered by the error in the fit. The large relative error from the overlap density $\langle n_{\text{Dy}}^2 \rangle_{\text{K}}$ is present in both approaches that are used to evaluate L_3 in this section. Therefore, for the comparison of both approaches it can be considered as a systematic error. We can thus take an average value of L_c from the atom-loss and the B-field dependent calculations and then include the large error. Therewith we get an estimate for the limit of the three-body loss coefficient at infinite scattering length for $^{162}\text{Dy}-^{40}\text{K}$ of about $L_c = 7(3) \times 10^{-24} \text{ cm}^6/\text{s}$.

The loss measurements in this $^{162}\text{Dy}-^{40}\text{K}$ Bose-Fermi system are an important step in the characterization of the Dy-K system. The results obtained here are a first reference

for the loss-rate in this mass-imbalanced mixture of a lanthanide and an alkali element. Although the atomic sample is thermal and by far not quantum-degenerate, the result of this section gives a guide value for the three-body loss coefficient at infinite scattering length of $L_c = 7(3) \times 10^{-24} \text{ cm}^6/\text{s}$ in the Bose-Fermi Dy-K mixture. For the realization of exotic superfluid phases in a Fermi-Fermi mixture the inelastic loss at large scattering lengths must be reduced by the Pauli principle [76, 130, 132]. The newest measurements from the Dy-K experiment report on a Fermi-Fermi loss-rate of $L_c(\text{K-Dy-Dy}) = 4 \times 10^{-25} \text{ cm}^6/\text{s}$ and $L_c(\text{K-K-Dy}) = 3 \times 10^{-25} \text{ cm}^6/\text{s}$ [364]. Those values for the ^{161}Dy - ^{40}K mixture are at least an order of magnitude lower than the one measured here and attest a reduction of inelastic losses in the fermionic system. In addition, the Feshbach resonance in ^{161}Dy - ^{40}K near 217 G is measured to have a broad enough universal range [364] to tackle investigations towards superfluid phases in the mass-imbalanced fermionic mixture.



Tapered amplifier laser with frequency-shifted feedback

Published as Ref. [243]:

A. Bayerle, S. M. Tzanova,
P. Vlaar, B. Pasquiou and F. Schreck
SciPost Phys. **1**, 002 (2016)

We present a frequency-shifted feedback (FSF) laser based on a tapered amplifier. The laser operates as a coherent broadband source with up to 370 GHz spectral width and 2.3 μ s coherence time. If the FSF laser is seeded by a continuous-wave laser a frequency comb spanning the output spectrum appears in addition to the broadband emission. The laser has an output power of 280 mW and a center wavelength of 780 nm. The ease and flexibility of use of tapered amplifiers makes our FSF laser attractive for a wide range of applications, especially in metrology.

Author contribution

The author of the present thesis built the setup of the FSF laser up to proof of principle before it moved in 2014 to the University of Amsterdam (UvA) from IQOQI Innsbruck and further contributed to the writing of the article.

A.1. Introduction

An FSF laser consists of a pumped gain medium inside a cavity that also contains a frequency shifting element such as an acousto-optic modulator (AOM). After each round trip the photons experience an increment in frequency through the AOM. Consequently exponential amplification of single frequency modes will not occur, since the fields of different round trips through the cavity cannot interfere constructively. Instead, spontaneously emitted photons from the gain medium are frequency shifted and amplified, resulting in a coherent modeless broadband emission spectrum. Seeding the FSF laser with a continuous-wave (cw) laser adds a second spectral component to the laser output, a comb of equidistantly spaced frequency components [365]. If parameters are chosen correctly, the FSF laser can generate Fourier-limited laser pulses with tunable repetition rate [366–368].

FSF lasers have many applications. Their coherent broadband emission is used for optical domain ranging, as in [369], where a distance of 18.5 km was measured with parts-per-million accuracy. The broad spectrum of FSF lasers allows one to cover a larger velocity class in Doppler broadened atomic transitions, improving optical pumping of room temperature He* gases [370] or increasing the fluorescence in Na vapors, which could improve astronomy guide star techniques [371]. The frequency comb like feature of an externally seeded FSF laser can be applied to spectroscopy, wavelength division multiplexed coherent communications [372] and optical frequency referencing [373].

Several implementations of FSF lasers with different gain media were reported. Early versions were based on HeNe [374], dye [375, 376], Ti:sapphire [367], and Nd:YLF lasers [368]. Modern implementations make use of a Yb³⁺ doped fiber amplifiers [377] as well as semiconductor lasers [378–381].

In this article we demonstrate an FSF laser that uses a tapered amplifier (TA) as gain medium. TAs are electrically pumped semiconductor laser amplifiers, which are capable of emitting single-mode laser radiation at Watt levels. TA chips are commonplace in many laboratories and can be built into miniaturized setups [382]. The relatively cheap devices are available at a wide range of emission wavelengths. Our work leverages these advantages, making FSF lasers easily accessible to more researchers, thereby widening the range of applications of these light sources. In mutually independent work, a similar system was developed for broadband laser cooling, as indicated by conference abstract [383]. In the following, we present first our experimental setup and then the spectral properties of the FSF laser.

A.2. Experimental setup

The experimental setup consists of four electro-optical sub-systems shown in Fig. A.1a-d, namely the FSF laser (a), the seed source (b), and the characterization tools (c,d). Each sub-system will now be described in detail. Our FSF laser consists of a TA and an AOM inside a four-mirror ring-cavity of 1440 mm optical length. The total loss through the mirrors is 1.4%. The gain medium of the laser is realized by a tapered amplifier (Toptica TA-0780-2000-4). Its gain profile is centered at 780 nm with a full width at half maximum (FWHM) of 10 nm. The TA chip is temperature stabilized to 20 °C and operated at a current of 1 A yielding an output power of 300 mW. The divergent output beam of the TA is collimated by the lens L_{TA2} . The Faraday isolator (FI) prevents laser light from traveling in the backwards direction, which would damage the input facet of the TA. The emission of the TA is split into two orthogonally polarized parts by a half-wave plate and a polarizing beam splitter (PBS). The vertically polarized reflection off the PBS serves as the output port of the

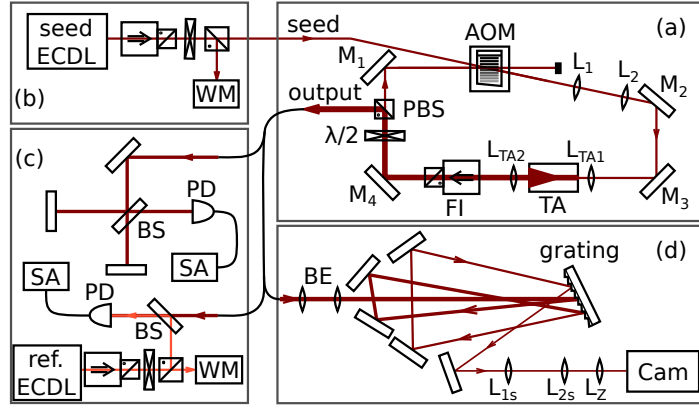


Figure A.1.: Schematic of the FSF laser and characterization tools. (a) cavity of the FSF laser, (b) seed laser, (c), radio frequency characterization setup, (d) grating spectrometer.

FSF laser which is sent to the diagnostic tools via optical fiber. The horizontally polarized transmission of the PBS continues into the feedback loop. The power in the feedback loop is deduced from the power of the leakage light through mirror M_1 . The half-wave plate is adjusted such that the power at the TA input facet remains below 30 mW in order to avoid damaging the TA chip. The feedback light propagating through the acousto-optic modulator (AOM, Gooch & Housego 3080-120 or Crystal Technology 3350-190) is shifted in frequency by $f_{\text{AOM}} = 60 \text{ MHz}$ to 380 MHz with efficiencies of up to 87%. Lenses L_1 and L_2 adapt the beam waist for optimal injection of the TA through focusing lens L_{TA1} . The focal distance of L_{TA1} and the orientation of mirrors M_2 , M_3 is adjusted to achieve maximal output power of the TA.

The seed laser light (Fig. A.1b) is provided by an external cavity diode laser (ECDL, Toptica DL Pro). The ECDL single-mode emission is tunable around 384.25 THz (780.2 nm) with a linewidth below 1 MHz on a timescale of $5 \mu\text{s}$. The ECDL optical frequency is measured by a Burleigh 1500 wavemeter (WM) with 0.5 GHz precision. The seed laser beam is introduced into the FSF ring cavity through the back of the AOM coaligned with the first order diffraction of the feedback.

The spectral properties of the output of the FSF laser are analysed in the optical and the RF domain. For phase noise measurements in the radio frequency (RF) domain the output of the FSF laser is sent through a Michelson interferometer shown in the upper half of Fig. A.1c. The light from the output port of the interferometer is detected by a 2 GHz bandwidth photodiode (PD) connected to a spectrum analyzer (SA, Rohde-Schwarz FSH8). A second interferometer setup, used to resolve the mode structure of the FSF laser, is shown in the lower part of Fig. A.1c. The output is coaligned with the equally polarized beam of a second ECDL laser on a PD, producing a beat signal between the two lasers. The beat signal is measured by the SA and the optical frequency of the reference ECDL is measured by the Burleigh 1500 wavemeter (WM).

The optical spectrum of the FSF laser output is recorded by a spectrometer (Fig. A.1d). The dispersive element of the spectrometer is a holographic grating with 1800 grooves per mm and a size of $50 \text{ mm} \times 50 \text{ mm}$. In order to illuminate a large number of grooves and increase the resolution of the spectrometer, the input beam is widened by a beam expander (BE) to roughly 20 mm. The first order diffraction is guided back onto the same grating at a different angle by a pair of mirrors. The same arrangement is repeated so that the resolution is enhanced threefold. The third diffraction off the grating is sent through a telescope (L_{1s} ,

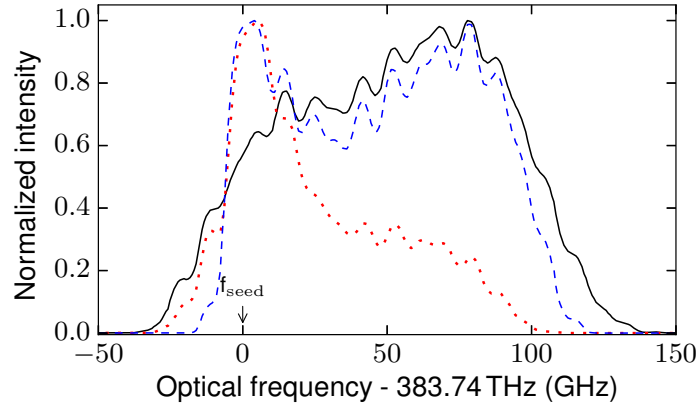


Figure A.2.: Optical spectrum of the FSF laser measured with the grating spectrometer without external seed (solid black) and an external seed power of $460 \mu\text{W}$ (dashed blue) and $720 \mu\text{W}$ (dotted red).

L_{2s}) to decrease the beam waist to 1 mm. Subsequently the diffracted beam is projected onto a CMOS camera (Cam) by a cylindrical lens of 150 mm focal length. The spectrometer is calibrated using the seed laser set to different optical frequencies. The measured resolution of the spectrometer is 4 GHz.

A.3. Properties of the laser

Two modes of operation of the frequency-shifted feedback laser are realized. Firstly, the laser is internally seeded by spontaneous emission from the tapered amplifier, resulting in the emission of modeless broadband light. Secondly, the cw-laser seed light is introduced into the cavity resulting in a comb of narrow, equidistant frequency components in addition to the modeless emission.

A.3.1. Broadband modeless laser

We first discuss the operation of the laser without external seed. We use $f_{\text{AOM}} = 80 \text{ MHz}$ and chose the +1-order diffracted beam of the AOM for feedback. The diffraction efficiency is 75%. After the feedback is injected into the TA the output power of the FSF laser reaches 280 mW, which matches the specified output power of the TA.

The optical spectrum of the FSF laser is shown in Fig. A.2. The center of the profile is tunable over 1 THz (2 nm) by changing the angle of the injection mirror M_2 in the horizontal plane and here is set to 383.0 THz (782.75 nm). The full width half maximum of the spectrum is 120 GHz, independent of the center frequency. The spectrum can be broadened by increasing the AOM frequency, as shown in Sec. A.3.2.

To prove that the broadband laser emission is modeless we use the beat setup (Fig. A.1c). The reference ECDL frequency is set close to the center of the FSF output spectrum and scanned over 200 GHz. The measurement reveals an RF spectrum without beat signals as expected for a modeless spectrum.

The RF spectrum obtained through the Michelson interferometer (see Fig. A.3 a) also shows the characteristic features of a modeless broadband laser. The spectrum exhibits a comb structure with lines separated by integer multiples of the cavity free spectral range

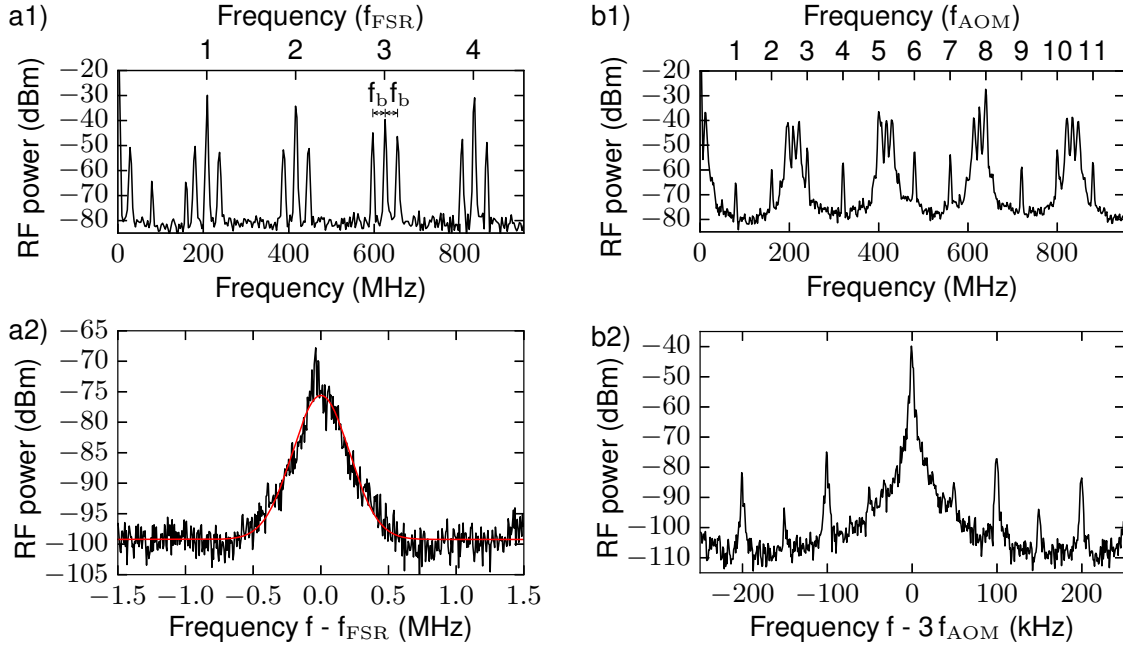


Figure A.3.: RF noise spectrum of the Michelson interferometer output. **(a)** Output of the modeless broadband laser. **(a2)** Zoom on the peak at f_{FSR} and Gaussian fit. The width of the Gaussian is 430(7) kHz. **(b)** Output of the FSF laser seeded with 450 μW cw narrow-band light. **(b2)** Zoom on the peak at $3f_{\text{AOM}}$. The half-width at half-maximum is (30 ± 2) Hz.

$(n \times f_{\text{FSR}})$, where each comb line is accompanied symmetrically by a pair of lines at $n \times f_{\text{FSR}} \pm f_b$. The comb structure stems from the fact that the initial spontaneous emission of the TA reoccurs after each round trip [365] and has a spacing of $f_{\text{FSR}} = 208.54(6)$ MHz. The frequency difference between the comb lines and the side peaks, f_b , is related to the arm length difference ΔL of the Michelson interferometer and $f_b = \gamma 2\Delta L/c$, where $\gamma = f_{\text{AOM}}f_{\text{FSR}} = 1.6683(3) \times 10^{16}$ Hz/s is called the chirp rate of the FSF laser [384]. The measured value $f_b = 28.95(6)$ MHz corresponds to an arm length difference of 260.12(5) mm. This value is consistent with a direct length measurement using a ruler, demonstrating the use of our FSF laser as range finder [384]. It was shown in [365] that the peaks in the RF noise spectrum are of Gaussian shape with a width related to the effective photon lifetime inside the cavity. Figure A.3a2 shows the peak at f_{FSR} with higher resolution. The FWHM of the peak is 430(7) kHz and hence the lifetime of a photon in the cavity is $t_{\text{coh}} = 2.33(4)$ μs .

A.3.2. Externally seeded laser

In the experiments described so far spontaneous emission is the only source of seed for the FSF laser. Now the laser is seeded with a small amount of narrow-band cw radiation. The cw seed introduces a mode with fixed frequency into the ring cavity from which the amplification and frequency shifting process starts. A sequence of comb lines alongside the modeless broadband emission of the FSF laser is expected to appear [365], which we demonstrate experimentally in the following. Since the AOM shifts light to higher frequencies, the seed laser frequency is set to a value close to the low-frequency edge of the output spectrum of

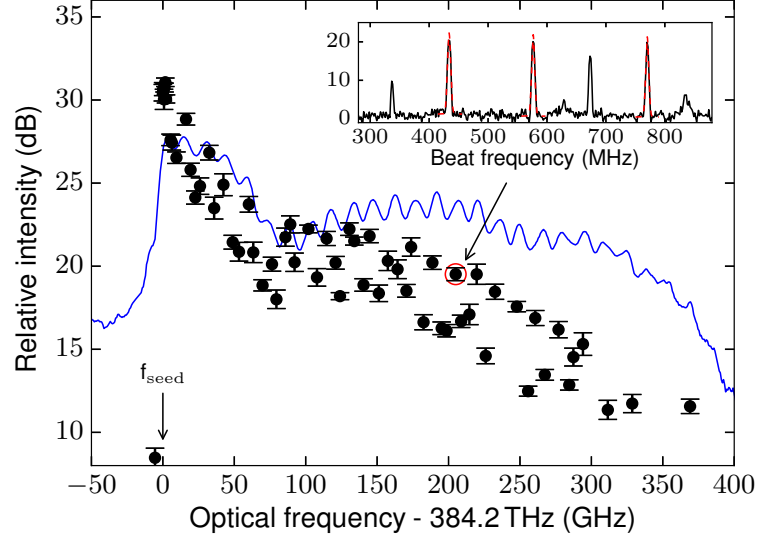


Figure A.4.: Spectrum of the seeded FSF laser. The intensity within a few GHz bandwidth is given relative to an arbitrary reference value. The blue trace stems from the grating spectrometer. Black circles show the height of the beat signal between the reference laser and FSF output, relative to the background. The inset shows the RF spectrum corresponding to the data point marked by an arrow and being encircled.

the FSF laser without external seed. The spectrum changes compared to the case without external seed, as shown in Fig. A.2 for two seed powers. For $460 \mu\text{W}$ seed power a sharp increase in intensity appears at the frequency of the seed laser and extending 50 GHz to higher frequencies. For even higher frequencies the spectrum is similar to the spectrum of the modeless FSF laser. If the laser is seeded with higher power ($720 \mu\text{W}$, red curve), the feature near the seed frequency decays faster, and the lobe at higher frequencies shrinks substantially and the overall width decreases.

Compared to the situation without external seed, the RF spectrum at the output port of the Michelson interferometer (Fig. A.3 b) contains additional sharp lines at integer multiples of f_{AOM} . Figure A.3 b2 shows a high-bandwidth measurement of such a line at $3f_{\text{AOM}}$. The FWHM width is less than 100 Hz and therefore narrower than the broadband emission peaks shown in Fig. A.3 a2 by four orders of magnitude.

Figure A.4 shows the spectrum of a frequency comb spanning 370 GHz. To obtain a frequency comb over this larger spectral width compared to before we find it necessary to increase the AOM frequency and diffraction efficiency. In the following we worked with $f_{\text{AOM}} = 370 \text{ MHz}$ and optimized the diffraction efficiency to 87%. The power of the seed laser at the TA input facet is set to $80 \mu\text{W}$. The mode structure of the cw seeded FSF laser is resolved by means of the beat measurement with the reference ECDL. The inset shows an example RF spectrum of the beat photodiode signal. Every comb line at $f_n = f_{\text{seed}} + n \times f_{\text{AOM}}$ of the FSF laser beats with the reference laser at frequency f_{ref} , leading to peaks (dashed red) at $|f_n - f_{\text{ref}}|$. The other features in the inset are beat signals between comb lines at $m \times f_{\text{AOM}}$ and more noisy peaks at multiples of f_{FSR} . The reference laser frequency f_{ref} is now incremented in 5 GHz steps. The height of the strongest beat signal between the reference laser and the FSF output in a range from DC to 2 GHz is plotted against the optical frequency of the reference laser in Fig. A.4. We observe that the spectral weight of the frequency comb decreases roughly exponentially with frequency. For comparison we also show the spectrum

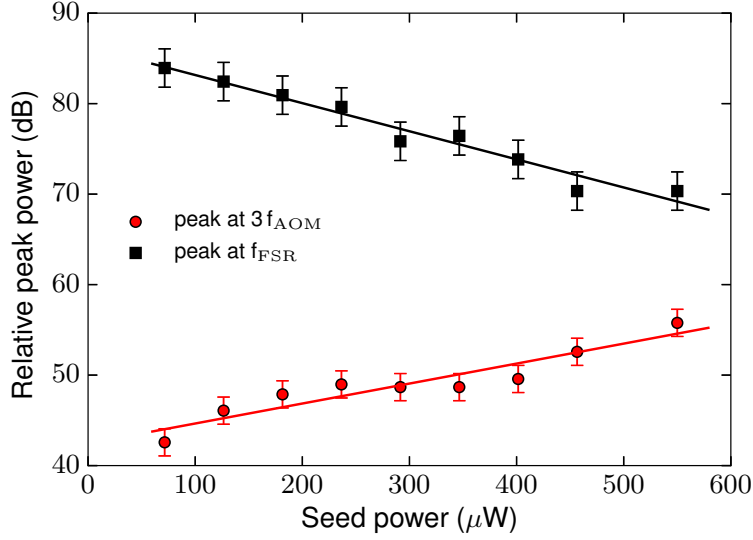


Figure A.5.: Dependence of the broadband signal at the frequency f_{FSF} (black squares) and comb feature at $3f_{\text{AOM}}$ (red circles) on seeding laser power and linear fits to the data. The relative peak power is obtained by integrating peaks such as the ones shown in Fig. A.3 a2 and A.3 b2 over frequency and comparing them to the noise floor.

obtained by the grating spectrometer in Fig. A.4 (solid blue). Since this spectrum shows the sum of the modeless broadband spectrum and the frequency comb, we observe that the ratio of broadband intensity to comb intensity increases with higher frequency. This behavior is a consequence of the accumulation of amplified spontaneous emission for higher frequencies.

Although the presence of a narrow-band cw seed adds a sequence of equidistant modes to the spectrum, the signature of broadband emission is present in the spectrum for all seed intensities explored here. In contrast to a conventional laser where a single mode can dominate the spectrum due to exponential amplification [385], in an FSF laser single modes cannot be favoured. The frequency shift in each round trip does not allow for constructive interference. Instead spontaneous emission as well as a cw seed is amplified in the FSF laser. Therefore the discussed spectral features, the frequency comb and the broadband emission, coexist in the laser when seeded with a cw source [365]. To characterize the relative importance of the two spectral features, we measure the intensity of the corresponding RF peaks (see Fig. A.3 a2 and A.3 b2), in dependence of the seed power. For each seed power the power of the light circulating in the cavity is adjusted to a safe, fixed value using the intracavity half-wave plate. We record the height of the RF peaks relative to the background at $n \times f_{\text{FSF}}$ and $m \times f_{\text{AOM}}$. The averaged values of each type of frequency component for $m, n = 1$ to 5 are shown in Fig. A.5. Within the range of parameters examined the comb intensity increases exponentially with seed power, whereas the broadband emission is exponentially suppressed.

The comb can be stabilized in frequency by locking the seed laser to a desired frequency, e.g. a Rb spectroscopy line. In previous work such stabilization required an additional lock of a comb line to a reference laser, see [377, 386] and references therein.

A.4. Conclusion and outlook

We have demonstrated an FSF ring laser based on a tapered amplifier. The FSF laser emits coherent modeless broadband radiation with 120 GHz bandwidth and a coherence time of $2.3 \mu\text{s}$. The center frequency of the broadband source is tunable over 1 THz. A frequency comb spanning up to 370 GHz was realized by seeding the FSF laser with a narrow-band cw source. Both spectral components existed simultaneously in the FSF laser and we measured their relative strength depending on seed power.

Since TAs are relatively cheap devices, available for many wavelengths, we expect that our work makes FSF lasers easily accessible to more researchers, leading to more applications of these devices. In contrast to other frequency combs [372, 387] our comb has a narrower spectrum. The comb covers 0.7 nm, which is a fraction of the 3dB gain bandwidth of our TA (11 nm). We observe that the spectrum can be broadened by increasing the AOM frequency, although less than proportional to that frequency. Broadening the comb width would be valuable to increase the range of applications of our scheme and could be a topic for further research. Still, a comb spanning hundreds of GHz is relevant to many applications and we plan to use the frequency comb of our FSF laser as frequency reference for photoassociation spectroscopy of RbSr molecules [241].



421 nm laser system for Dy

The laser system for the strong optical transition of dysprosium in the blue visible spectrum (see Fig. 8.1 or Table 2.1) offers stability and flexibility. The major requirements for the laser system are high output power > 500 mW and the possibility to remotely switch frequencies between the dysprosium isotopes. In the following the options for a laser source, frequency reference, and frequency stabilization techniques are presented in more detail as addition to Sec. 9.4.2.

B.1. Laser source

The available laser sources at 421 nm are either blue diode lasers or a laser system with a high-power source in the infrared (IR) at 842 nm, which is then frequency doubled into the blue spectrum. In our experiment we have both.

Direct sources of blue light are blue laser diodes (e.g. from [NICHIA Corp.](#)). They cover the desired wavelength of 421 nm and are specified for an output power of up to 120 mW. However, experience in our group has shown that they do not run in a single mode above an output power of 30 mW. A high-power blue diode laser that is specified to 70 mW is available from [Toptica](#). In order to reach this relatively high power and still run at a single frequency, the blue diode mounting is additionally temperature controlled and the control electronics correlates temperature and current stabilization. As a consequence of the complex design, the exchange of the laser diode is only possible in factory and not by the customer, which is not convenient for a complex experiment. For a total power > 500 mW the blue laser system would consist of too many blue diode lasers. Thus only diode lasers are ineligible for our experiment. Nevertheless, we use a blue diode laser DLpro from Toptica in our setup as a reference for frequency offset locking of the high power blue laser. The diode laser is specified up to 15 mW. It can reach higher output power and still emit in a single mode, but not on the timescale of months.

Since high power for a single frequency in the blue is not directly accessible, it can originate from the IR followed by efficient frequency doubling. Second harmonic generation (SHG) is possible in a single pass periodically poled nonlinear crystal (PPLN), which assures the phase matching between pump and output frequencies. Although such crystals in general simplify a SHG setup, they are (were) limited approximately down to 460 nm in the blue. The reason is that their doubling efficiency and damage thresholds decrease with output wavelength due to multiphoton excitations. The most efficient SHG of 421 nm light for now to our knowledge is in a bow-tie ring cavity with a nonlinear crystal. Tunable and stable cavities with high doubling efficiencies are commercially available (e.g. [SHGpro](#) or [SolsTiS ECD-X](#)) and provide a good alternative to the mostly not so stable homemade option.

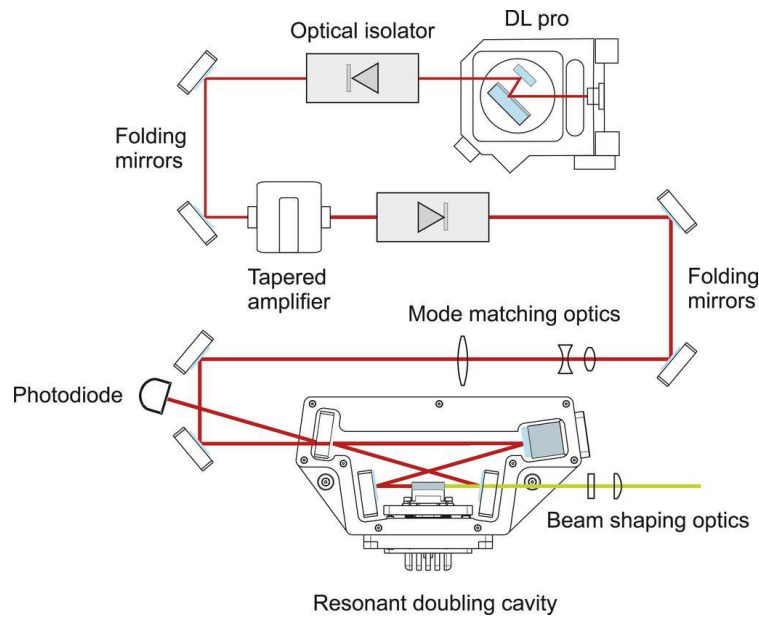


Figure B.1.: Stable and efficient SHG setup in the laser system TA-SHG pro. The seed at 842 nm (red) is amplified and sent to a stabilized SHG cavity. The output at 421 nm (green) typically delivers 600 mW. Scheme from Toptica.

For the high power (> 1 W) IR source one can choose between a Ti:Saph and a system of a diode laser followed by a tapered amplifier (TA). In general, the greatest advantage of a continuous-wave Ti:Saph laser is its tunability over hundreds of nanometers, while keeping a low linewidth (< 100 kHz). But for us the wavelength is fixed and we would be left with the inconvenient sides of a Ti:Saph. It is bulky, since it also requires a high power pump laser in the green, and it is a more complex system than the diode plus TA option, which makes it more expensive and also more complicated to debug. For the sake of completeness I must add that new generation continuous-wave Ti:Saph lasers (e.g. from M^2) can deliver more than 4 W of power at 842 nm. That would result in more than 1.5 W of 421 nm-light after efficient SHG. In contrast, the TA output power goes to 2.5 W and a TA never has an optimal spatial mode. Hence, if an experiment demands 1 W or more of blue resonant light, then a Ti:Saph plus SHG is the only option.

For our experiment 600 mW of 421 nm-light are enough and we opted for a TA SHG pro laser from Toptica. The laser scheme is shown in Fig. B.1. An external cavity diode laser at 842 nm with a linewidth of less than 300 kHz seeds a high power TA chip. The TA chip has maximum output power of 2 W, but its lifetime would be very short if operated constantly at maximum. In addition, at high driving currents the TA chip acts increasingly as a cavity itself and then internal modes start competing with the seed. Thus, for optimal stability of the TA output, maximum seed power and moderate driving current are required. In our experiment the TA typically runs at 2.2 A (maximum is 3 A), outputs 1.5 W IR and we can then work with 600 mW in the blue.

B.2. Laser stabilization

For referencing a laser frequency to an atomic transition of alkali elements typically a heated glass cell is used for spectroscopy. Considering the high melting point of Dy, such a conventional spectroscopy cell is inapplicable. One could use a wave-meter for pinning the wavelength, since the transition is very broad and does not require a high resolution of the device, but our wave-meter covers the mid-IR and not the blue spectrum. Moreover, it is always favorable to have the actual atom as a reference. This can be achieved by spectroscopy in the main experimental setup of the hot atomic beam or by using a hollow cathode lamp. The vacuum setup gives the necessary optical access for spectroscopy on the atomic beam after the transverse cooling. However, we chose to avoid the spectroscopy of the hot atomic beam in order to minimize optical and electronic load on the main experimental table. The choice for the Dy-K experiment is inspired by the spectroscopy method in a hollow cathode lamp (HCL) that is used to investigate the hyperfine structure of Erbium [388]. Furthermore, the reference cavity from ultra-low expansion (ULE) glass that we use as a reference for the 626 nm-transition can be also used as reference for 842 nm. This is our backup plan, in case there is an issue with the HCL.

The spectroscopy of the 421 nm transition in dysprosium is performed in a see-through HCL from Hereaus with buffer gas of argon. In a HCL the atoms are not emitted by direct heating of the cell, but by sputtering. The hollow cathode is coated with dysprosium, which is ejected from the surface when a highly accelerated argon ion hits it. The buffer gas plasma discharge is controlled by the adjustable current from the lamp power supply¹. This power supply also provides an ignition voltage of 500 V to start the plasma discharge. The applied spectroscopy method is modulation transfer spectroscopy (MTS). MTS is a heterodyne technique based on four-wave-mixing in the nonlinear atomic vapour, which provides well-defined zero crossings sitting on a flat background. For the modulation we use a tunable electro-optic modulator² (EOM) and we find the optimal modulation frequency to be $27 \text{ MHz} = 0.84 \Gamma_{421}$. A critical parameter for a good signal to noise ratio is the current through the HCL. We need at least 8 mW for the MTS.

The type of HCL is decisive for the successful implementation for frequency referencing. The HCL should be of the see-through type and must have as low as possible buffer gas pressure. We first tried a HCL (from Photron) with neon buffer gas and a buffer gas pressure of tens of mbar. The high buffer gas pressure leads to broadening of the natural transition linewidth. In the case of our first HCL the pressure broadening was more than 1 GHz and the different isotopes were not separable. In addition, the absorption signal was very weak, probably due to the low mass of neon and therewith limited kinetic energy for the sputtering. With the HCL from Hereaus with buffer gas of argon and only 4 mbar pressure we achieved a very good signal from our MTS, shown in Fig. B.2. Note that the HCL is convenient only for frequency referencing of the broad 421 nm transition in dysprosium. For the narrow transition near 626 nm, the pressure broadening is larger than the transition linewidth. The HCL was used for spectroscopy on the 626 nm transition only once to initially reference the ULE cavity.

The relatively large frequency distance between isotopes in Fig. B.2 is the reason why the MTS is not directly performed on the high-power laser. It would be difficult and power costly to switch electronically between isotopes, so we would have to relock the laser by hand for an isotope change. To allow for mixtures of isotopes in the experiment we have installed a

¹ The HCL power supply is model HC2024-R from EMCO High Voltage Corporation.

² Model EO-T28M3 from QUBIG.

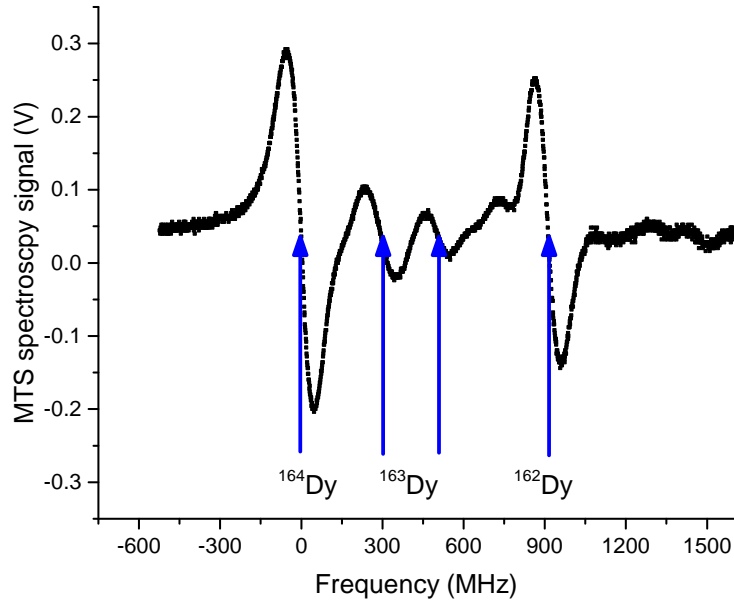


Figure B.2.: Modulation transfer spectroscopy (MTS) signal at the hollow cathode lamp (HCL) of dysprosium. The arrows indicate zero crossings coming from the ^{164}Dy isotope at 0 MHz, a crossover between the two highest hyperfine states of ^{163}Dy at 297 MHz, a clear signal from the $F = 8.5$ hyperfine manifold of ^{163}Dy at 506 MHz and again a large signal for the second most abundant boson, the ^{162}Dy isotope at 913 MHz. The blue diode laser runs in a single mode only for a limited frequency range, so the ^{161}Dy and ^{160}Dy isotopes are not detected here.

reference laser for the MTS spectroscopy and a so-called beat-lock for the high-power laser. The blue ECDL is always locked to the ^{164}Dy isotope and the frequency of the high-power laser is shifted electronically to the desired dysprosium isotope, as shown in Fig. 9.13.

The DL pro is always locked to the ^{164}Dy isotope using most of its output power for the MTS at the HCL. The DL output is elliptical in shape and we do not correct for it, except shortly before coupling into the fiber for the frequency offset stabilization (beat-lock). The overlap and coupling of the beams from both lasers into a single mode polarization-maintaining fiber is very important for the stability of the interference signal. The fiber output is focused on a 7 GHz-fast photodiode³, which delivers the beat-note used for referencing. The beat signal is amplified and fed into an offset phase lock servo⁴ (OPLS). The OPLS can precisely control the frequency detuning between the two lasers in a given range of frequencies, depending on its configuration. Given the isotopic shifts of dysprosium, the OPLS divides the input signal by $N = 16$ and mixes it with the set-frequency coming from a 500 MHz-DDS [346]. The set-values given in Fig. 9.13 must be therefore divided by $N = 16$. We use only the phase-frequency detector of the OPLS, not the integrated PID, because its minimal frequency is higher than the bandwidth of the piezo crystal that controls the wavelength of the 842 nm ECDL. With this system we can electronically tune the frequency over a few GHz and remotely change the settings of the high-power laser between different isotopes.

³ Ultrafast Si photodetector UPD-50-SP from ALPHALAS GmbH

⁴ Model D2-135 from Vescent.



Overlap density

For the interaction measurements in Section 10.3, we have $N_{\text{Dy}} \gg N_{\text{K}}$ and the ODT is 3.6 times deeper for K than for Dy. We thus assume that the dysprosium density as seen by the potassium atoms is constant and replace it by the peak density. The overlap density between the species is defined by the integral of the density distributions of the two species

$$\langle n_{\text{Dy}} \rangle_{\text{K}} = \frac{1}{N_{\text{K}}} \int n_{\text{K}} n_{\text{Dy}} dV. \quad \text{C.1}$$

The thermal clouds are described by the Boltzmann distribution

$$n = n_0 \exp\left(-\frac{x_i^2}{2\sigma_i^2}\right) \quad \text{with} \quad \sigma_i^2 = \frac{k_B T}{m\omega_i^2}, \quad \text{C.2}$$

where n_0 is the peak density of the particles with mass m and temperature T in a trap with trap frequency ω_i . For each species then, knowing that $\omega_{\text{K}}/\omega_{\text{Dy}} = \alpha = 3.6$, we have

$$n_{0,\text{Dy}} = \left(\frac{m_{\text{Dy}}}{2\pi k_B T_{\text{Dy}}}\right)^{3/2} \bar{\omega}_{\text{Dy}}^3 N_{\text{Dy}} \quad \text{and} \quad n_{0,\text{K}} = \left(\frac{m_{\text{K}}\alpha^2}{2\pi k_B T_{\text{K}}}\right)^{3/2} \bar{\omega}_{\text{Dy}}^3 N_{\text{K}} \quad \text{C.3}$$

So we get

$$\langle n_{\text{Dy}} \rangle_{\text{K}} = \frac{1}{N_{\text{K}}} \int n_{0,\text{K}} \exp\left(-\frac{x_i^2}{2\sigma_{\text{K},i}^2}\right) n_{0,\text{Dy}} \exp\left(-\frac{x_i^2}{2\sigma_{\text{Dy},i}^2}\right) dV \quad \text{C.4}$$

$$= \frac{n_{0,\text{K}} n_{0,\text{Dy}}}{N_{\text{K}}} \int \exp\left(-\frac{x_i^2}{2} \left(\frac{1}{\sigma_{\text{K},i}^2} + \frac{1}{\sigma_{\text{Dy},i}^2}\right)\right) dV \quad \text{C.5}$$

$$= \frac{n_{0,\text{K}} n_{0,\text{Dy}}}{N_{\text{K}}} \int \exp\left(-\frac{x_i^2 \omega_{\text{Dy},i}^2}{2k_B} \left(\frac{\alpha^2 m_{\text{K}}}{T_{\text{K}}} + \frac{m_{\text{Dy}}}{T_{\text{Dy}}}\right)\right) dV. \quad \text{C.6}$$

The solution of this Gauss integral in x, y, z directions with $dV = d^3x_i$ is then

$$\langle n_{\text{Dy}} \rangle_{\text{K}} = \frac{n_{0,\text{K}} n_{0,\text{Dy}} (2\pi k_B)^{3/2}}{N_{\text{K}} \omega_x \omega_y \omega_z} \left(\frac{\alpha^2 m_{\text{K}}}{T_{\text{K}}} + \frac{m_{\text{Dy}}}{T_{\text{Dy}}}\right)^{-3/2}. \quad \text{C.7}$$

Using C.3, the equation simplifies to

$$\langle n_{\text{Dy}} \rangle_{\text{K}} = n_{0,\text{Dy}} \left(\frac{\alpha^2 m_{\text{K}}}{T_{\text{K}}}\right)^{3/2} \left(\frac{\alpha^2 m_{\text{K}}}{T_{\text{K}}} + \frac{m_{\text{Dy}}}{T_{\text{Dy}}}\right)^{-3/2} = n_{0,\text{Dy}} \left(1 + \alpha^{-2} \frac{m_{\text{Dy}} T_{\text{K}}}{m_{\text{K}} T_{\text{Dy}}}\right)^{-3/2}. \quad \text{C.8}$$

In a similar way we derive the squared density of dysprosium in the overlap region with potassium for the three-body analysis:

$$\langle n_{\text{Dy}}^2 \rangle_{\text{K}} = \frac{1}{N_{\text{K}}} \int n_{\text{K}} n_{\text{Dy}}^2 dV \quad \text{C.9}$$

$$= \frac{1}{N_{\text{K}}} \int n_{0,\text{K}} \exp\left(-\frac{x_i^2}{2\sigma_{\text{K},i}^2}\right) n_{0,\text{Dy}}^2 \exp\left(-\frac{x_i^2}{\sigma_{\text{Dy},i}^2}\right) dV \quad \text{C.10}$$

$$= \frac{n_{0,\text{K}} n_{0,\text{Dy}}^2}{N_{\text{K}}} \int \exp\left(-\frac{x_i^2}{2} \left(\frac{1}{\sigma_{\text{K},i}^2} + \frac{2}{\sigma_{\text{Dy},i}^2}\right)\right) dV \quad \text{C.11}$$

$$= \frac{n_{0,\text{K}} n_{0,\text{Dy}}^2}{N_{\text{K}}} \int \exp\left(-\frac{x_i^2 \omega_{\text{Dy},i}^2}{2k_B} \left(\frac{\alpha^2 m_{\text{K}}}{T_{\text{K}}} + \frac{2m_{\text{Dy}}}{T_{\text{Dy}}}\right)\right) dV \quad \text{C.12}$$

$$= \frac{n_{0,\text{K}} n_{0,\text{Dy}}^2 (2\pi k_B)^{3/2}}{N_{\text{K}} \omega_x \omega_y \omega_z} \left(\frac{\alpha^2 m_{\text{K}}}{T_{\text{K}}} + \frac{2m_{\text{Dy}}}{T_{\text{Dy}}}\right)^{-3/2}. \quad \text{C.13}$$

And again with C.3, we get:

$$\langle n_{\text{Dy}}^2 \rangle_{\text{K}} = n_0^2 \left(1 + 2\alpha^{-2} \frac{m_{\text{Dy}} T_{\text{K}}}{m_{\text{K}} T_{\text{Dy}}}\right)^{-3/2}. \quad \text{C.14}$$

Bibliography

- [1] R. Feynman. “Simulating physics with computers”, *Int. J. Theor. Phys.* **21**, 467 (1982) (cit. on p. 8).
- [2] I. Buluta and F. Nori. “Quantum simulators”, *Science* **326**, 108–111 (2009) (cit. on pp. 8, 9).
- [3] I. M. Georgescu et al. “Quantum simulation”, *Rev. Mod. Phys.* **86**, 153–185 (2014) (cit. on pp. 8, 9).
- [4] E. Altman et al. “Quantum simulators: Architectures and opportunities”, *arxiv e-prints*, [1912.06938](https://arxiv.org/abs/1912.06938) (2019) (cit. on pp. 8, 9).
- [5] I. Bloch et al. “Quantum simulations with ultracold quantum gases”, *Nat. Phys.* **8**, 267 (2012) (cit. on pp. 8, 9).
- [6] A. Adams et al. “Strongly correlated quantum fluids: ultracold quantum gases, quantum chromodynamic plasmas and holographic duality”, *New J. Phys.* **14**, 115009 (2012) (cit. on pp. 8, 9, 15).
- [7] A. Celi et al. “Quantum optics and frontiers of physics: the third quantum revolution”, *Physica Scripta* **92**, 013003 (2016) (cit. on pp. 8, 9).
- [8] J. I. Cirac and P. Zoller. “Goals and opportunities in quantum simulation”, *Nat. Phys.* **8**, 264–266 (2012) (cit. on pp. 8, 9).
- [9] G. Wendin. “Quantum information processing with superconducting circuits: a review”, *Rep. Prog. Phys.* **80**, 106001 (2017) (cit. on p. 9).
- [10] R. Blatt and C. F. Roos. “Quantum simulations with trapped ions”, *Nat. Phys.* **8**, 277 (2012) (cit. on p. 9).
- [11] J. Preskill. “Quantum computing in the NISQ era and beyond”, *arxiv e-prints*, [1801.00862](https://arxiv.org/abs/1801.00862) (2018) (cit. on p. 9).
- [12] A. Browaeys and T. Lahaye. “Many-body physics with individually controlled Rydberg atoms”, *Nature Physics* (2020) (cit. on p. 9).
- [13] L. D. Carr et al. “Cold and ultracold molecules: science, technology and applications”, *New J. Phys.* **11**, 055049 (2009) (cit. on pp. 9, 10, 13, 14, 34).
- [14] R. V. Krems et al., eds. *Cold Molecules: Theory, Experiment, Applications*. Taylor & Francis (2009) (cit. on pp. 9, 13, 54).
- [15] L. M. Vandersypen and M. A. Eriksson. “Quantum computing with semiconductor spins”, *Phys. Today* **72**, 38 (2019) (cit. on p. 9).
- [16] H. Bernien et al. “Probing many-body dynamics on a 51-atom quantum simulator”, *Nature* **551**, 579–584 (2017) (cit. on p. 9).
- [17] J. Zhang et al. “Observation of a many-body dynamical phase transition with a 53-qubit quantum simulator”, *Nature* **551**, 601–604 (2017) (cit. on p. 9).
- [18] F. Arute et al. “Quantum supremacy using a programmable superconducting processor”, *Nature* **574**, 505–510 (2019) (cit. on p. 9).
- [19] C. Gross and I. Bloch. “Quantum simulations with ultracold atoms in optical lattices”, *Science* **357**, 995–1001 (2017) (cit. on pp. 9, 29, 30, 38, 108).
- [20] D. Blume. “Few-body physics with ultracold atomic and molecular systems in traps”, *Rep. Prog. Phys.* **75**, 046401 (2012) (cit. on p. 9).

- [21] M. Bartenstein et al. “Crossover from a molecular Bose-Einstein condensate to a degenerate Fermi gas”, *Phys. Rev. Lett.* **92**, 120401 (2004) (cit. on pp. 9, 11, 15).
- [22] M. Greiner et al. “Quantum phase transition from a superfluid to a Mott insulator in a gas of ultracold atoms”, *Nature* **415**, 39–44 (2002) (cit. on pp. 9, 30).
- [23] P. Massignan et al. “Polarons, dressed molecules and itinerant ferromagnetism in ultracold Fermi gases”, *Rep. Prog. Phys.* **77**, 034401 (2014) (cit. on p. 9).
- [24] L. J. LeBlanc and J. H. Thywissen. “Species-specific optical lattices”, *Phys. Rev. A* **75**, 053612 (2007) (cit. on pp. 9, 30, 54, 65, 107).
- [25] M. Lewenstein et al. “Atomic Bose-Fermi mixtures in an optical lattice”, *Phys. Rev. Lett.* **92**, 050401 (2004) (cit. on pp. 9, 11, 38).
- [26] J. Ulmanis et al. “Heteronuclear Efimov scenario with positive intraspecies scattering length”, *Phys. Rev. Lett.* **117**, 153201 (2016) (cit. on pp. 9, 12).
- [27] J. E. Baarsma et al. “Population and mass imbalance in atomic Fermi gases”, *Phys. Rev. A* **82**, 013624 (2010) (cit. on pp. 9, 16, 36, 75).
- [28] M. Ortner et al. “Quantum information processing in self-assembled crystals of cold polar molecules”, *Quantum Inf. Process.* **10**, 793 (2011) (cit. on p. 10).
- [29] M. A. Baranov et al. “Condensed matter theory of dipolar quantum gases”, *Chem. Rev.* **112**, 5012–5061 (2012) (cit. on pp. 10, 38, 43, 54).
- [30] A. V. Gorshkov et al. “Tunable superfluidity and quantum magnetism with ultracold polar molecules”, *Phys. Rev. Lett.* **107**, 115301 (2011) (cit. on pp. 10, 54).
- [31] Y. L. Zhou et al. “Long-range and frustrated spin-spin interactions in crystals of cold polar molecules”, *Phys. Rev. A* **84**, 052332 (2011) (cit. on pp. 10, 54).
- [32] S. R. Manmana et al. “Topological phases in ultracold polar-molecule quantum magnets”, *Phys. Rev. B* **87**, 081106 (2013) (cit. on pp. 10, 54).
- [33] R. V. Krems. “Cold controlled chemistry”, *Phys. Chem. Chem. Phys.* **10**, 4079–4092 (2008) (cit. on p. 10).
- [34] C. Chin et al. “Feshbach resonances in ultracold gases”, *Rev. Mod. Phys.* **82**, 1225 (2010) (cit. on pp. 10, 18, 20, 21, 29).
- [35] I. Bloch. “Ultracold quantum gases in optical lattices”, *Nat. Phys.* **1**, 23–30 (2005) (cit. on pp. 10, 11).
- [36] B. Yan et al. “Observation of dipolar spin-exchange interactions with lattice-confined polar molecules”, *Nature* **501** (2013) (cit. on pp. 10, 33).
- [37] A. Patscheider et al. “Controlling dipolar exchange interactions in a dense three-dimensional array of large-spin fermions”, *Phys. Rev. Research* **2**, 023050 (2020) (cit. on p. 10).
- [38] M. H. Anderson et al. “Observation of Bose-Einstein condensation in dilute atomic vapor”, *Science* **269**, 198–201 (1995) (cit. on p. 10).
- [39] K. B. Davis et al. “Bose-Einstein condensation in a gas of sodium atoms”, *Phys. Rev. Lett.* **75**, 3969–3973 (1995) (cit. on p. 10).
- [40] C. C. Bradley et al. “Evidence of Bose-Einstein condensation in an atomic gas with attractive interactions”, *Phys. Rev. Lett.* **75**, 1687–1690 (1995) (cit. on p. 10).
- [41] B. DeMarco and D. S. Jin. “Onset of Fermi degeneracy in a trapped atomic gas”, *Science* **285**, 1703–1706 (1999) (cit. on p. 10).
- [42] R. Grimm et al. “Optical dipole traps for neutral atoms”, *Adv. At. Mol. Opt. Phys.* **42**, 95 (2000) (cit. on pp. 10, 11, 27, 28).
- [43] I. Bloch et al. “Many-body physics with ultracold gases”, *Rev. Mod. Phys.* **80**, 885 (2008) (cit. on pp. 10, 54).

- [44] C. J. Myatt et al. “Production of two overlapping Bose-Einstein condensates by sympathetic cooling”, *Phys. Rev. Lett.* **78**, 586–589 (1997) (cit. on p. 11).
- [45] G. Modugno et al. “Bose-Einstein condensation of potassium atoms by sympathetic cooling”, *Science* **294**, 1320–1322 (2001) (cit. on pp. 11, 43).
- [46] F. Schreck et al. “Sympathetic cooling of bosonic and fermionic lithium gases towards quantum degeneracy”, *Phys. Rev. A* **64**, 011402 (2001) (cit. on pp. 11, 29, 54).
- [47] Z. Hadzibabic et al. “Two-species mixture of quantum degenerate Bose and Fermi gases”, *Phys. Rev. Lett.* **88**, 160401 (2002) (cit. on pp. 11, 54).
- [48] C. Silber et al. “Quantum-degenerate mixture of fermionic lithium and bosonic rubidium gases”, *Phys. Rev. Lett.* **95**, 170408 (2005) (cit. on p. 11).
- [49] M. Taglieber et al. “Quantum degenerate two-species Fermi-Fermi mixture coexisting with a Bose-Einstein condensate”, *Phys. Rev. Lett.* **100**, 010401 (2008) (cit. on pp. 11, 54).
- [50] D. Greif et al. “Short-range quantum magnetism of ultracold fermions in an optical lattice”, *Science* **340**, 1307–1310 (2013) (cit. on p. 11).
- [51] L. W. Cheuk et al. “Quantum-gas microscope for fermionic atoms”, *Phys. Rev. Lett.* **114**, 193001 (2015) (cit. on p. 11).
- [52] B. DeMarco et al. “Measurement of p -Wave Threshold Law Using Evaporatively Cooled Fermionic Atoms”, *Phys. Rev. Lett.* **82**, 4208–4211 (1999) (cit. on pp. 11, 29, 58).
- [53] B. DeMarco. “Quantum behavior of an atomic Fermi gas”. PhD thesis. University of Colorado (2001) (cit. on pp. 11, 78, 89).
- [54] K. M. O’Hara et al. “Observation of a strongly interacting degenerate Fermi gas”, *Science* **298**, 2179–2182 (2002) (cit. on p. 11).
- [55] M. W. Zwierlein et al. “Condensation of pairs of fermionic atoms near a Feshbach resonance”, *Phys. Rev. Lett.* **92**, 120403 (2004) (cit. on pp. 11, 15).
- [56] N. Navon et al. “The equation of state of a low-temperature Fermi gas with tunable interactions”, *Science* **328**, 729–732 (2010) (cit. on pp. 11, 15).
- [57] A. Mosk et al. “Mixture of ultracold lithium and cesium atoms in an optical dipole trap”, *Appl. Phys. B* **73**, 791 (2001) (cit. on p. 11).
- [58] B. Damski et al. “Creation of a dipolar superfluid in optical lattices”, *Phys. Rev. Lett.* **90**, 110401 (2003) (cit. on pp. 11, 69, 70).
- [59] L. Mathey et al. “Luttinger liquid of polarons in one-dimensional boson-fermion mixtures”, *Phys. Rev. Lett.* **93**, 120404 (2004) (cit. on p. 11).
- [60] K. Günter et al. “Bose-Fermi mixtures in a three-dimensional optical lattice”, *Phys. Rev. Lett.* **96**, 180402 (2006) (cit. on p. 12).
- [61] S. Ospelkaus et al. “Localization of bosonic atoms by fermionic impurities in a three-dimensional optical lattice”, *Phys. Rev. Lett.* **96**, 180403 (2006) (cit. on pp. 12, 13).
- [62] C. Kohstall et al. “Metastability and coherence of repulsive polarons in a strongly interacting Fermi mixture”, *Nature* **485**, 615–618 (2012) (cit. on pp. 12, 16).
- [63] M. Cetina et al. “Decoherence of impurities in a Fermi sea of ultracold atoms”, *Phys. Rev. Lett.* **115**, 135302 (2015) (cit. on pp. 12, 16).
- [64] M. Cetina et al. “Ultrafast many-body interferometry of impurities coupled to a Fermi sea”, *Science* **354**, 96–99 (2016) (cit. on pp. 12, 13, 16).
- [65] R. S. Lous et al. “Probing the interface of a phase-separated state in a repulsive Bose-Fermi mixture”, *Phys. Rev. Lett.* **120**, 243403 (2018) (cit. on pp. 12, 133).
- [66] T. Rentrop et al. “Observation of the phononic Lamb shift with a synthetic vacuum”, *Phys. Rev. X* **6**, 041041 (2016) (cit. on pp. 12, 13).

- [67] V. Efimov. “Energy levels of three resonantly interacting particles”, *Nucl. Phys. A* **210**, 157–188 (1973) (cit. on p. 12).
- [68] F. Ferlaino et al. “Efimov resonances in ultracold quantum gases”, *Few-Body Syst.* **51**, 113–133 (2011) (cit. on pp. 12, 21).
- [69] T. Kraemer et al. “Evidence for Efimov quantum states in an ultracold gas of caesium atoms”, *Nature* **440**, 315–318 (2006) (cit. on p. 12).
- [70] J. R. Williams et al. “Evidence for an excited-state Efimov trimer in a three-component Fermi gas”, *Phys. Rev. Lett.* **103**, 130404 (2009) (cit. on p. 12).
- [71] B. Huang et al. “Observation of the second triatomic resonance in Efimov’s scenario”, *Phys. Rev. Lett.* **112**, 190401 (2014) (cit. on p. 12).
- [72] S.-K. Tung et al. “Geometric scaling of Efimov states in a ${}^6\text{Li}$ – ${}^{133}\text{Cs}$ mixture”, *Phys. Rev. Lett.* **113**, 240402 (2014) (cit. on pp. 12, 13).
- [73] J. P. D’Incao and B. D. Esry. “Enhancing the observability of the Efimov effect in ultracold atomic gas mixtures”, *Phys. Rev. A* **73**, 030703(R) (2006) (cit. on p. 12).
- [74] B. Marcelis et al. “Collisional properties of weakly bound heteronuclear dimers”, *Phys. Rev. A* **77**, 032707 (2008) (cit. on pp. 12, 16).
- [75] D. S. Petrov et al. “Weakly bound dimers of fermionic atoms”, *Phys. Rev. Lett.* **93**, 090404 (2004) (cit. on pp. 12, 15, 21, 37, 79).
- [76] D. S. Petrov et al. “Scattering properties of weakly bound dimers of fermionic atoms”, *Phys. Rev. A* **71**, 012708 (2005) (cit. on pp. 12, 15, 16, 21, 36, 37, 77–79, 131, 138).
- [77] T. M. Rvachov et al. “Long-lived ultracold molecules with electric and magnetic dipole moments”, *Phys. Rev. Lett.* **119**, 143001 (2017) (cit. on pp. 13, 14).
- [78] F. Sievers et al. “Simultaneous sub-Doppler laser cooling of fermionic ${}^6\text{Li}$ and ${}^{40}\text{K}$ on the D_1 line: Theory and experiment”, *Phys. Rev. A* **91**, 023426 (2015) (cit. on pp. 13, 24).
- [79] T. G. Tiecke et al. “Broad Feshbach resonance in the ${}^6\text{Li}$ – ${}^{40}\text{K}$ mixture”, *Phys. Rev. Lett.* **104**, 053202 (2010) (cit. on p. 13).
- [80] J. W. Park et al. “Ultracold dipolar gas of fermionic ${}^{23}\text{Na}$ – ${}^{40}\text{K}$ molecules in their absolute ground state”, *Phys. Rev. Lett.* **114**, 205302 (2015) (cit. on pp. 13, 14).
- [81] M. W. Gempel et al. “Versatile electric fields for the manipulation of ultracold NaK molecules”, *New J. Phys.* **18**, 045017 (2016) (cit. on p. 13).
- [82] F. Seeßelberg et al. “Extending rotational coherence of interacting polar molecules in a spin-decoupled magic trap”, *Phys. Rev. Lett.* **121**, 253401 (2018) (cit. on p. 13).
- [83] B. Deh et al. “Giant Feshbach resonances in ${}^6\text{Li}$ – ${}^{85}\text{Rb}$ mixtures”, *Phys. Rev. A* **82**, 020701 (2010) (cit. on p. 13).
- [84] S. Dutta et al. “Two-photon photoassociation spectroscopy of an ultracold heteronuclear molecule”, *Phys. Rev. A* **95**, 013405 (2017) (cit. on p. 13).
- [85] X. Ye et al. “Collisions of ultracold ${}^{23}\text{Na}$ – ${}^{87}\text{Rb}$ molecules with controlled chemical reactivities”, *Sci. Adv.* **4** (2018) (cit. on pp. 13, 14).
- [86] G. Roati et al. “Fermi-Bose quantum degenerate K-Rb mixture with attractive interaction”, *Phys. Rev. Lett.* **89**, 150403 (2002) (cit. on pp. 13, 14, 29, 54).
- [87] L. De Marco et al. “A degenerate Fermi gas of polar molecules”, *Science* **363**, 853–856 (2019) (cit. on pp. 13, 14, 34).
- [88] C. Haimberger et al. “Formation of ultracold, highly polar $X^1\Sigma^+$ NaCs molecules”, *New J. Phys.* **11**, 055042 (2009) (cit. on p. 13).
- [89] M. Gröbner et al. “Observation of interspecies Feshbach resonances in an ultracold ${}^{39}\text{K}$ – ${}^{133}\text{Cs}$ mixture and refinement of interaction potentials”, *Phys. Rev. A* **95**, 022715 (2017) (cit. on p. 13).

- [90] P. K. Molony et al. “Creation of ultracold $^{87}\text{Rb}^{133}\text{Cs}$ molecules in the rovibrational ground state”, *Phys. Rev. Lett.* **113**, 255301 (2014) (cit. on pp. 13, 14).
- [91] L. Reichsöllner et al. “Quantum engineering of a low-entropy gas of heteronuclear bosonic molecules in an optical lattice”, *Phys. Rev. Lett.* **118**, 073201 (2017) (cit. on pp. 13, 14, 30, 70, 71).
- [92] E. Neri et al. “Realization of a cold mixture of fermionic chromium and lithium atoms”, *arXiv e-prints*, 2001.11616 (2020) (cit. on p. 13).
- [93] X. Ma et al. “A dual-species magneto-optical trap for lithium and strontium atoms”, *arXiv e-prints*, 1904.05230 (2019) (cit. on p. 13).
- [94] T. Aoki et al. “Photoionization loss in simultaneous magneto-optical trapping of Rb and Sr”, *Phys. Rev. A* **87**, 063426 (2013) (cit. on pp. 13, 54).
- [95] C. Ravensbergen et al. “Production of a degenerate Fermi-Fermi mixture of dysprosium and potassium atoms”, *Phys. Rev. A* **98**, 063624 (2018) (cit. on pp. 13, 99, 117–119).
- [96] H. Hara et al. “Quantum degenerate mixtures of alkali and alkaline-earth-like atoms”, *Phys. Rev. Lett.* **106**, 205304 (2011) (cit. on pp. 13, 54).
- [97] A. Green et al. “Two-photon photoassociation spectroscopy of the $^2\Sigma^+$ YbLi molecular ground state”, *Phys. Rev. A* **99**, 063416 (2019) (cit. on p. 13).
- [98] F. Münchow et al. “Two-photon photoassociation spectroscopy of heteronuclear YbRb”, *Phys. Chem. Chem. Phys.* **13**, 18734–18737 (2011) (cit. on pp. 13, 54).
- [99] A. Guttridge et al. “Production of ultracold Cs*Yb molecules by photoassociation”, *Phys. Rev. A* **97**, 063414 (2018) (cit. on p. 13).
- [100] A. Trautmann et al. “Dipolar quantum mixtures of erbium and dysprosium atoms”, *Phys. Rev. Lett.* **121**, 213601 (2018) (cit. on p. 13).
- [101] M. Witkowski et al. “Dual Hg-Rb magneto-optical trap”, *Opt. Express* **25**, 3165–3179 (2017) (cit. on p. 13).
- [102] J. D. Weinstein et al. “Magnetic trapping of calcium monohydride molecules at millikelvin temperatures”, *Nature* **395**, 148 (1998) (cit. on p. 13).
- [103] E. S. Shuman et al. “Laser cooling of a diatomic molecule”, *Nature* **467**, 820–823 (2010) (cit. on p. 13).
- [104] L. Anderegg et al. “Laser cooling of optically trapped molecules”, *Nat. Phys.* **14**, 890–893 (2018) (cit. on p. 13).
- [105] T. Köhler et al. “Production of cold molecules via magnetically tunable Feshbach resonances”, *Rev. Mod. Phys.* **78**, 1311 (2006) (cit. on pp. 14, 20, 69).
- [106] N. V. Vitanov et al. “Laser-induced population transfer by adiabatic passage techniques”, *Annu. Rev. Phys. Chem.* **52**, 763 (2001) (cit. on pp. 14, 65).
- [107] S. Inouye et al. “Observation of heteronuclear Feshbach resonances in a mixture of bosons and fermions”, *Phys. Rev. Lett.* **93**, 183201 (2004) (cit. on p. 14).
- [108] S. Ospelkaus et al. “Tuning of heteronuclear interactions in a degenerate Fermi-Bose mixture”, *Phys. Rev. Lett.* **97**, 120403 () (cit. on p. 14).
- [109] C. Ospelkaus et al. “Ultracold heteronuclear molecules in a 3D optical lattice”, *Phys. Rev. Lett.* **97**, 120402 (2006) (cit. on p. 14).
- [110] J. M. Sage et al. “Optical production of ultracold polar molecules”, *Phys. Rev. Lett.* **94**, 203001 (2005) (cit. on p. 14).
- [111] K.-K. Ni et al. “A high phase-space-density gas of polar molecules”, *Science* **322**, 231–235 (2008) (cit. on pp. 14, 54, 65).
- [112] A. Christianen et al. “Photoinduced two-body loss of ultracold molecules”, *Phys. Rev. Lett.* **123**, 123402 (2019) (cit. on pp. 14, 34, 69).

- [113] M. Aymar and O. Dulieu. “Calculation of accurate permanent dipole moments of the lowest $1,3\Sigma^+$ states of heteronuclear alkali dimers using extended basis sets”, *J. Chem. Phys.* **122**, 204302 (2005) (cit. on p. 14).
- [114] P. S. Żuchowski and J. M. Hutson. “Reactions of ultracold alkali-metal dimers”, *Phys. Rev. A* **81**, 060703 (2010) (cit. on p. 14).
- [115] S. Ospelkaus et al. “Quantum-state controlled chemical reactions of ultracold potassium-rubidium molecules”, *Science* **327**, 853–857 (2010) (cit. on pp. 14, 54).
- [116] M. Tomza et al. “Chemical reactions of ultracold alkali-metal dimers in the lowest-energy 3Σ state”, *Phys. Rev. A* **88**, 050701 (2013) (cit. on p. 14).
- [117] S. Giorgini et al. “Theory of ultracold atomic Fermi gases”, *Rev. Mod. Phys.* **80**, 1215–1273 (2008) (cit. on pp. 15, 35).
- [118] M. R. Norman. “The challenge of unconventional superconductivity”, *Science* **332**, 196–200 (2011) (cit. on pp. 15, 35, 36).
- [119] A. Sedrakian and J. W. Clark. “Superfluidity in nuclear systems and neutron stars”, *Eur. Phys. J. A* **55**, 167 (2019) (cit. on pp. 15, 36).
- [120] G. C. Strinati et al. “The BCS–BEC crossover: From ultra-cold Fermi gases to nuclear systems”, *Physics Reports* **738**, 1–76 (2018) (cit. on pp. 15, 36).
- [121] T.-L. Ho. “Universal thermodynamics of degenerate quantum gases in the unitarity limit”, *Phys. Rev. Lett.* **92**, 090402 (2004) (cit. on p. 15).
- [122] W. Zwerger, ed. *The BCS-BEC Crossover and the Unitary Fermi Gas*. Springer, Berlin Heidelberg (2012) (cit. on p. 15).
- [123] S. Nascimbène et al. “Exploring the thermodynamics of a universal Fermi gas”, *Nature* **463**, 1057–1061 (2010) (cit. on p. 15).
- [124] M. J. H. Ku et al. “Revealing the superfluid lambda transition in the universal thermodynamics of a unitary Fermi gas”, *Science* **335**, 563–567 (2012) (cit. on p. 15).
- [125] M. W. Zwierlein et al. “Fermionic superfluidity with imbalanced spin populations”, *Science* **311**, 492–496 (2006) (cit. on p. 16).
- [126] L. Radzihovsky and D. E. Sheehy. “Imbalanced Feshbach-resonant Fermi gases”, *Rep. Prog. Phys.* **73**, 076501 (2010) (cit. on pp. 16, 36, 75).
- [127] K. Gubbels and H. Stoof. “Imbalanced Fermi gases at unitarity”, *Phys. Rep.* **525**, 255–313 (2013) (cit. on pp. 16, 36, 75).
- [128] D. Roscher et al. “Phase structure of mass- and spin-imbalanced unitary Fermi gases”, *Phys. Rev. A* **91**, 053611 (2015) (cit. on pp. 16, 36, 37, 75, 79).
- [129] M. Jag et al. “Observation of a strong atom-dimer attraction in a mass-imbalanced Fermi-Fermi mixture”, *Phys. Rev. Lett.* **112**, 075302 (2014) (cit. on pp. 16, 37).
- [130] D. S. Petrov et al. “Diatomic molecules in ultracold Fermi gases - novel composite bosons”, *J. Phys. B: At. Mol. Opt. Phys.* **38**, S645–S660 (2005) (cit. on pp. 16, 36, 37, 75, 77–79, 138).
- [131] D. Naik et al. “Feshbach resonances in the ${}^6\text{Li}$ - ${}^{40}\text{K}$ Fermi-Fermi mixture: Elastic versus inelastic interactions”, *Eur. Phys. J. D* **65**, 55–65 (2011) (cit. on p. 16).
- [132] M. Jag et al. “Lifetime of Feshbach dimers in a Fermi-Fermi mixture of ${}^6\text{Li}$ and ${}^{40}\text{K}$ ”, *Phys. Rev. A* **94**, 062706 (2016) (cit. on pp. 16, 36, 75, 77–79, 131, 138).
- [133] L. Pitaevskii and S. Stringari. *Bose-Einstein Condensation and Superfluidity*. Oxford University Press (2016) (cit. on p. 17).
- [134] H. Katori et al. “Magneto-optical trapping and cooling of strontium atoms down to the photon recoil temperature”, *Phys. Rev. Lett.* **82**, 1116–1119 (1999) (cit. on pp. 18, 25, 27, 77).
- [135] T. Maier et al. “Narrow-line magneto-optical trap for dysprosium atoms”, *Opt. Lett.* **39**, 3138–3141 (2014) (cit. on pp. 18, 27, 75).

- [136] A. Frisch et al. “Narrow-line magneto-optical trap for erbium”, *Phys. Rev. A* **85**, 051401 (2012) (cit. on p. 18).
- [137] T. Kuwamoto et al. “Magneto-optical trapping of Yb atoms using an intercombination transition”, *Phys. Rev. A* **60**, R745–R748 (1999) (cit. on pp. 18, 77).
- [138] J. Weiner et al. “Experiments and theory in cold and ultracold collisions”, *Rev. Mod. Phys.* **71**, 1–85 (1999) (cit. on pp. 19, 21, 24, 80, 109).
- [139] T. Lahaye et al. “The physics of dipolar bosonic quantum gases”, *Rep. Prog. Phys.* **72**, 126401 (2009) (cit. on p. 19).
- [140] K. Aikawa et al. “Reaching Fermi degeneracy via universal dipolar scattering”, *Phys. Rev. Lett.* **112**, 010404 (2014) (cit. on pp. 19, 75, 76).
- [141] S. Kotochigova and A. Petrov. “Anisotropy in the interaction of ultracold dysprosium”, *Phys. Chem. Chem. Phys.* **13**, 19165 (2011) (cit. on p. 19).
- [142] T. Lahaye et al. “Strong dipolar effects in a quantum ferrofluid”, *Nature* **448** (2007) (cit. on p. 20).
- [143] M. Schmitt et al. “Self-bound droplets of a dilute magnetic quantum liquid”, *Nature* **539**, 259–262 (2016) (cit. on p. 20).
- [144] D. Petter et al. “Probing the roton excitation spectrum of a stable dipolar Bose gas”, *Phys. Rev. Lett.* **122**, 183401 (2019) (cit. on p. 20).
- [145] G. Pagano et al. “Strongly interacting gas of two-electron fermions at an orbital Feshbach resonance”, *Phys. Rev. Lett.* **115**, 265301 (2015) (cit. on p. 20).
- [146] M. Höfer et al. “Observation of an orbital interaction-induced Feshbach resonance in ^{173}Yb ”, *Phys. Rev. Lett.* **115**, 265302 (2015) (cit. on p. 20).
- [147] S. Kotochigova. “Controlling interactions between highly magnetic atoms with Feshbach resonances”, *Rep. Prog. Phys.* **77**, 093901 (2014) (cit. on pp. 21, 75, 79, 80).
- [148] A. Frisch et al. “Quantum chaos in ultracold collisions of gas-phase erbium atoms”, *Nature* **507**, 475–479 (2014) (cit. on pp. 21, 75).
- [149] T. Maier et al. “Emergence of chaotic scattering in ultracold Er and Dy”, *Phys. Rev. X* **5**, 041029 (2015) (cit. on pp. 21, 76, 79, 80).
- [150] V. Barbé et al. “Observation of Feshbach resonances between alkali and closed-shell atoms”, *Nat. Phys.* **14**, 881–884 (2018) (cit. on pp. 21, 44, 45, 49, 66, 69, 71, 77).
- [151] M. B. Kosicki et al. “Quantum chaos in Feshbach resonances of the ErYb system”, *New Journal of Physics* **22**, 023024 (2020) (cit. on pp. 21, 79, 80).
- [152] M. D. Frye et al. “Prospects of forming high-spin polar molecules from ultracold atoms”, *arXiv e-prints*, 1910.09641 (2019) (cit. on pp. 21, 79, 80).
- [153] M. L. González-Martínez and P. S. Żuchowski. “Magnetically tunable Feshbach resonances in Li+Er”, *Phys. Rev. A* **92**, 022708 (2015) (cit. on pp. 21, 79, 80, 132).
- [154] K. M. Jones et al. “Ultracold photoassociation spectroscopy: Long-range molecules and atomic scattering”, *Rev. Mod. Phys.* **78**, 483, 483 (2006) (cit. on pp. 21, 67, 68).
- [155] P. van der Straten and H. Metcalf. *Atoms and Molecules Interacting with Light: Atomic Physics for the Laser Era*. Cambridge University Press (2016) (cit. on p. 22).
- [156] S. Chu. “Nobel Lecture: The manipulation of neutral particles”, *Rev. Mod. Phys.* **70**, 685–706 (1998) (cit. on pp. 22, 24).
- [157] C. N. Cohen-Tannoudji. “Nobel Lecture: Manipulating atoms with photons”, *Rev. Mod. Phys.* **70**, 707–719 (1998) (cit. on pp. 22, 24).
- [158] W. D. Phillips. “Nobel Lecture: Laser cooling and trapping of neutral atoms”, *Rev. Mod. Phys.* **70**, 721–741 (1998) (cit. on pp. 22, 24).

- [159] H. J. Metcalf and P. van der Straten. *Laser Cooling and Trapping*. Springer, New York (1999) (cit. on p. 22).
- [160] V. S. Letokhov et al. “Laser cooling of atoms: a review”, *J. Opt. B: Quantum Semiclass. Opt.* **7**, 5–40 (1995) (cit. on p. 22).
- [161] D. Jervis and J. H. Thywissen. “Making an ultracold gas”. In: *Quantum Gas Experiments* (2014). Chap. 2, 5–32 (cit. on p. 22).
- [162] M. Kasevich and S. Chu. “Laser cooling below a photon recoil with three-level atoms”, *Phys. Rev. Lett.* **69**, 1741–1744 (1992) (cit. on pp. 22, 55).
- [163] J. Dalibard et al. “Artificial gauge potentials for neutral atoms”, *Rev. Mod. Phys.* **83**, 1523–1543 (2011) (cit. on p. 22).
- [164] R. Chang et al. “Three-dimensional laser cooling at the Doppler limit”, *Phys. Rev. A* **90**, 063407 (2014) (cit. on p. 23).
- [165] P. D. Lett et al. “Observation of atoms laser cooled below the Doppler limit”, *Phys. Rev. Lett.* **61**, 169–172 (1988) (cit. on pp. 24, 55).
- [166] J. Dalibard and C. Cohen-Tannoudji. “Laser cooling below the Doppler limit by polarization gradients: simple theoretical models”, *J. Opt. Soc. Am. B* **6**, 2023–2045 (1989) (cit. on pp. 24, 55).
- [167] M. Landini et al. “Sub-Doppler laser cooling of potassium atoms”, *Phys. Rev. A* **84**, 043432 (2011) (cit. on pp. 24, 55).
- [168] D. R. Fernandes et al. “Sub-Doppler laser cooling of fermionic ^{40}K atoms in three-dimensional gray optical molasses”, *Europhys. Lett.* **100**, 63001 (2012) (cit. on pp. 24, 55, 78, 118).
- [169] A. T. Grier et al. “ Λ -enhanced sub-Doppler cooling of lithium atoms in D_1 gray molasses”, *Phys. Rev. A* **87**, 063411 (2013) (cit. on pp. 24, 55).
- [170] G. Colzi et al. “Sub-Doppler cooling of sodium atoms in gray molasses”, *Phys. Rev. A* **93**, 023421 (2016) (cit. on p. 24).
- [171] V. Vuletić et al. “Degenerate Raman sideband cooling of trapped cesium atoms at very high atomic densities”, *Phys. Rev. Lett.* **81**, 5768–5771 (1998) (cit. on p. 24).
- [172] M. Gröbner et al. “Degenerate Raman sideband cooling of ^{39}K ”, *Phys. Rev. A* **95**, 033412 (2017) (cit. on pp. 24, 78).
- [173] J. Eschner et al. “Laser cooling of trapped ions”, *J. Opt. Soc. Am. B* **20**, 1003–1015 (2003) (cit. on p. 24).
- [174] S. Stellmer et al. “Laser cooling to quantum degeneracy”, *Phys. Rev. Lett.* **110**, 263003 (2013) (cit. on pp. 24, 42, 58, 64, 76).
- [175] A. Urvoy et al. “Direct laser cooling to Bose-Einstein condensation in a dipole trap”, *Phys. Rev. Lett.* **122**, 203202 (2019) (cit. on p. 24).
- [176] W. D. Phillips and H. Metcalf. “Laser deceleration of an atomic beam”, *Phys. Rev. Lett.* **48**, 596–599 (1982) (cit. on pp. 24, 47).
- [177] K. Dieckmann et al. “Two-dimensional magneto-optical trap as a source of slow atoms”, *Phys. Rev. A* **58**, 3891–3895 (1998) (cit. on pp. 24, 87).
- [178] A. L. Migdall et al. “First observation of magnetically trapped neutral atoms”, *Phys. Rev. Lett.* **54**, 2596–2599 (1985) (cit. on p. 24).
- [179] V. Bolpasi et al. “A gradient and offset compensated Ioffe–Pritchard trap for Bose–Einstein condensation experiments”, *J. Phys. B: At. Mol. Opt. Phys.* **45**, 235301 (2012) (cit. on p. 24).
- [180] T. H. Loftus et al. “Narrow line cooling and momentum-space crystals”, *Phys. Rev. A* **70**, 063413 (2004) (cit. on pp. 25, 55, 64, 116).

- [181] D. C. McKay et al. “Low-temperature high-density magneto-optical trapping of potassium using the open $4S \rightarrow 5P$ transition at 405 nm”, *Phys. Rev. A* **84**, 063420 (2011) (cit. on pp. 25, 26, 55, 108).
- [182] T. Tiecke. *Properties of Potassium* (2010). URL: www.tobiastiecke.nl/archive/PotassiumProperties.pdf (cit. on p. 26).
- [183] D. A. Steck. *Rubidium 87 D Line Data* (2015). URL: <http://steck.us/alkalidata> (cit. on p. 26).
- [184] M. Yasuda et al. “Photoassociation spectroscopy of ^{88}Sr : Reconstruction of the wave function near the last node”, *Phys. Rev. A* **73**, 011403 (2006) (cit. on p. 26).
- [185] M. M. Boyd. “High precision spectroscopy of strontium in an optical lattice: Towards a new standard for frequency and time”. PhD thesis. University of Colorado (2007) (cit. on pp. 26, 58).
- [186] M. Lu et al. “Spectroscopy of a narrow-line laser-cooling transition in atomic dysprosium”, *Phys. Rev. A* **83**, 012510 (2011) (cit. on pp. 26, 27, 76).
- [187] M. Gustavsson et al. “Lifetime measurements for excited states of rare-earth atoms using pulse modulation of a cw dye-laser beam”, *J. Opt. Soc. Am.* **69**, 984–992 (1979) (cit. on p. 26).
- [188] M. Lu et al. “Strongly dipolar Bose-Einstein condensate of dysprosium”, *Phys. Rev. Lett.* **107**, 190401 (2011) (cit. on pp. 26, 75, 121).
- [189] D. Dreon et al. “Optical cooling and trapping of highly magnetic atoms: the benefits of a spontaneous spin polarization”, *J. Phys. B: At. Mol. Opt. Phys.* **50**, 065005 (2017) (cit. on pp. 26, 76, 114–116).
- [190] S. Stellmer. “Degenerate quantum gases of strontium”. PhD thesis. University of Innsbruck (2013) (cit. on pp. 26, 28, 41, 46, 48–50, 55, 100).
- [191] S. Dörscher et al. “Creation of quantum-degenerate gases of ytterbium in a compact 2D-/3D-magneto-optical trap setup”, *Rev. Sci. Instrum.* **84**, 043109 (2013) (cit. on p. 27).
- [192] A. Ashkin. *Nobel lecture: Optical Tweezers and their Application to Biological Systems*. Ed. by Nobel Media AB (2019). URL: <https://www.nobelprize.org/prizes/physics/2018/ashkin/lecture/> (cit. on p. 27).
- [193] J. L. Roberts et al. “Magnetic field dependence of ultracold inelastic collisions near a Feshbach resonance”, *Phys. Rev. Lett.* **85**, 728–731 (2000) (cit. on p. 29).
- [194] W. Ketterle and N. J. van Druten. “Evaporative cooling of trapped atoms”, *Adv. At. Mol. Opt. Phys.* **37**, 181 (1996) (cit. on p. 29).
- [195] T. Weber et al. “Bose-Einstein condensation of cesium”, *Science* **299**, 232–235 (2003) (cit. on p. 29).
- [196] C.-C. Chien et al. “Quantum transport in ultracold atoms”, *Nat. Phys.* **11**, 998 (2015) (cit. on p. 29).
- [197] J. Billy et al. “Direct observation of Anderson localization of matter waves in a controlled disorder”, *Nature* **453**, 891 (2008) (cit. on p. 29).
- [198] C. Muldoon et al. “Control and manipulation of cold atoms in optical tweezers”, *New J. Phys.* **14**, 073051 (2012) (cit. on p. 29).
- [199] B. Zimmermann et al. “High-resolution imaging of ultracold fermions in microscopically tailored optical potentials”, *New J. Phys.* **13**, 043007 (2011) (cit. on p. 30).
- [200] W. S. Bakr et al. “A quantum gas microscope for detecting single atoms in a Hubbard-regime optical lattice”, *Nature* **462**, 74 (2009) (cit. on p. 30).
- [201] G. J. A. Edge et al. “Imaging and addressing of individual fermionic atoms in an optical lattice”, *Phys. Rev. A* **92**, 063406 (2015) (cit. on pp. 30, 108).
- [202] D. Stadler et al. “Observing the drop of resistance in the flow of a superfluid Fermi gas”, *Nature* **491**, 736–739 (2012) (cit. on p. 30).

- [203] D. Jaksch and P. Zoller. “The cold atom Hubbard toolbox”, *Ann. Phys.* **315**, Special Issue, 52–79 (2005) (cit. on p. 30).
- [204] T. Esslinger. “Fermi-Hubbard physics with atoms in an optical lattice”, *Annu. Rev. Condens. Matter Phys.* **1**, 129–152 (2010) (cit. on p. 30).
- [205] O. Dutta et al. “Non-standard Hubbard models in optical lattices: a review”, *Rep. Prog. Phys.* **78**, 066001 (2015) (cit. on p. 30).
- [206] R. Jördens et al. “A Mott insulator of fermionic atoms in an optical lattice”, *Nature* **455**, 204 (2008) (cit. on pp. 30, 78).
- [207] S. Schmid et al. “Long distance transport of ultracold atoms using a 1D optical lattice”, *New J. Phys.* **8**, 159–159 (2006) (cit. on p. 30).
- [208] A. Ciamei et al. “Efficient production of long-lived ultracold Sr₂ molecules”, *Phys. Rev. A* **96**, 013406 (2017) (cit. on pp. 30, 42, 71).
- [209] J. F. Sherson et al. “Single-atom-resolved fluorescence imaging of an atomic Mott insulator”, *Nature* **467**, 68 (2010) (cit. on p. 30).
- [210] W. Ketterle et al. “Making, probing and understanding Bose-Einstein condensates”. In: *Bose-Einstein condensation in atomic gases*. Ed. by M. Inguscio et al. Proceedings of the International School of Physics “Enrico Fermi”, Course CXL, Varenna, July 1998. IOS Press (1998), 67 (cit. on p. 31).
- [211] W. Ketterle and M. Zwierlein. “Making, probing and understanding Fermi gases”. In: *Ultracold Fermi Gases*. Ed. by M. Inguscio et al. Proceedings of the International School of Physics “Enrico Fermi”, Course CLXIV, Varenna, June 2006. IOS Press (2008), 95–287 (cit. on p. 31).
- [212] M. R. Andrews et al. “Direct, nondestructive observation of a Bose Condensate”, *Science* **273**, 84–87 (1996) (cit. on p. 32).
- [213] A. Micheli et al. “A toolbox for lattice-spin models with polar molecules”, *Nat. Phys.* **2**, 341 (2006) (cit. on pp. 33, 34, 54).
- [214] M. Mayle et al. “Scattering of ultracold molecules in the highly resonant regime”, *Phys. Rev. A* **87**, 012709 (2013) (cit. on pp. 34, 69).
- [215] P. D. Gregory et al. “Loss of ultracold ⁸⁷Rb¹³³Cs molecules via optical excitation of long-lived two-body collision complexes”, *Phys. Rev. Lett.* **124**, 163402 (2020) (cit. on pp. 34, 69).
- [216] A. V. Avdeenkov et al. “Suppression of inelastic collisions of polar ¹Σ state molecules in an electrostatic field”, *Phys. Rev. A* **73**, 022707 (2006) (cit. on p. 34).
- [217] G. Wang and G. Quémener. “Tuning ultracold collisions of excited rotational dipolar molecules”, *New J. Phys.* **17**, 035015 (2015) (cit. on p. 35).
- [218] S. A. Moses. “A quantum gas of polar molecules in an optical lattice”. PhD thesis. University of Colorado (2016) (cit. on p. 35).
- [219] G. Quémener and J. L. Bohn. “Shielding ²Σ ultracold dipolar molecular collisions with electric fields”, *Phys. Rev. A* **93**, 012704 (2016) (cit. on p. 35).
- [220] P. F. Bedaque et al. “Phase separation in asymmetrical fermion superfluids”, *Phys. Rev. Lett.* **91**, 247002 (2003) (cit. on pp. 36, 37).
- [221] D. T. Son and M. A. Stephanov. “Phase diagram of a cold polarized Fermi gas”, *Phys. Rev. A* **74**, 013614 (2006) (cit. on p. 36).
- [222] A. I. Larkin and Y. N. Ovchinnikov. “Inhomogeneous state of superconductors”, *Sov. Phys. JETP* **20**, 762 (1965) (cit. on p. 36).
- [223] P. Fulde and R. A. Ferrell. “Superconductivity in a strong spin-exchange field”, *Phys. Rev.* **135**, A550–A563 (1964) (cit. on p. 36).
- [224] A. Bulgac and M. M. Forbes. “Unitary Fermi supersolid: The Larkin-Ovchinnikov phase”, *Phys. Rev. Lett.* **101**, 215301 (2008) (cit. on pp. 36, 37).

- [225] R. Casalbuoni and G. Nardulli. “Inhomogeneous superconductivity in condensed matter and QCD”, *Rev. Mod. Phys.* **76**, 263–320 (2004) (cit. on p. 36).
- [226] Y. Shin et al. “Phase diagram of a two-component Fermi gas with resonant interactions”, *Nature* **451**, 689–694 (2008) (cit. on p. 36).
- [227] J. Wang et al. “Enhancement effect of mass imbalance on Fulde-Ferrell-Larkin-Ovchinnikov type of pairing in Fermi-Fermi mixtures of ultracold quantum gases”, *Sci. Rep.* **7**, 39783 (2017) (cit. on pp. 36, 37, 75).
- [228] C. A. Regal et al. “Observation of resonance condensation of fermionic atom pairs”, *Phys. Rev. Lett.* **92**, 040403 (2004) (cit. on p. 37).
- [229] S.-T. Wu and S. Yip. “Superfluidity in the interior-gap states”, *Phys. Rev. A* **67**, 053603 (2003) (cit. on p. 37).
- [230] K. B. Gubbels et al. “Sarma phase in trapped unbalanced Fermi gases”, *Phys. Rev. Lett.* **97**, 210402 (2006) (cit. on p. 37).
- [231] M. Iskin and C. A. R. Sá de Melo. “Two-species fermion mixtures with population imbalance”, *Phys. Rev. Lett.* **97**, 100404 (2006) (cit. on p. 37).
- [232] Q. Chen et al. “Stability conditions and phase diagrams for two-component Fermi gases with population imbalance”, *Phys. Rev. A* **74**, 063603 (2006) (cit. on p. 37).
- [233] M. M. Parish et al. “Polarized Fermi condensates with unequal masses: Tuning the tricritical point”, *Phys. Rev. Lett.* **98**, 160402 (2007) (cit. on pp. 37, 75, 79).
- [234] K. Aikawa et al. “Observation of Fermi surface deformation in a dipolar quantum gas”, *Science* **345**, 1484–1487 (2014) (cit. on p. 37).
- [235] V. Veljić et al. “Ground state of an ultracold Fermi gas of tilted dipoles in elongated traps”, *New J. Phys.* **20**, 093016 (2018) (cit. on p. 37).
- [236] J. Herbig et al. “Preparation of a pure molecular quantum gas”, *Science* **301**, 1510 (2003) (cit. on p. 38).
- [237] M. A. Baranov. “Theoretical progress in many-body physics with ultracold dipolar gases”, *Phys. Rep.* **464**, 71–111 (2008) (cit. on pp. 38, 80).
- [238] T. Shi et al. “Singlet and triplet Bardeen-Cooper-Schrieffer pairs in a gas of two-species fermionic polar molecules”, *Phys. Rev. A* **82**, 033623 (2010) (cit. on p. 38).
- [239] S. Baier et al. “Realization of a strongly interacting Fermi gas of dipolar atoms”, *Phys. Rev. Lett.* **121**, 093602 (2018) (cit. on p. 38).
- [240] A. Sotnikov et al. “Advantages of mass-imbalanced ultracold fermionic mixtures for approaching quantum magnetism in optical lattices”, *Phys. Rev. Lett.* **109**, 065301 (2012) (cit. on p. 38).
- [241] B. Pasquiou et al. “Quantum degenerate mixtures of strontium and rubidium atoms”, *Phys. Rev. A* **88**, 023601 (2013) (cit. on pp. 40, 53, 146).
- [242] A. Ciamei et al. “The RbSr $^2\Sigma^+$ ground state investigated via spectroscopy of hot and ultracold molecules”, *Phys. Chem. Chem. Phys.* (2018) (cit. on pp. 40, 66–71).
- [243] A. Bayerle et al. “Tapered amplifier laser with frequency-shifted feedback”, *SciPost Phys.* **1**, 002 (2016) (cit. on pp. 40, 50, 139).
- [244] S. Stellmer et al. “Bose-Einstein condensation of strontium”, *Phys. Rev. Lett.* **103**, 200401 (2009) (cit. on pp. 42, 54, 57).
- [245] S. Stellmer et al. “Degenerate quantum gases of strontium”. In: *Annual Review of Cold Atoms and Molecules*. World Scientific Publishing Co. Pte. Ltd. (2014). Chap. 1, 1–80 (cit. on p. 41).
- [246] D. Das and V. Natarajan. “Absolute frequency measurement of the lithium D lines: Precise determination of isotope shifts and fine-structure intervals”, *Phys. Rev. A* **75**, 052508 (2007) (cit. on p. 41).

- [247] S. Stellmer et al. “Production of quantum-degenerate strontium gases”, *Phys. Rev. A* **87**, 013611 (2013) (cit. on pp. 41, 55, 57, 58, 61, 71).
- [248] S. Stellmer and F. Schreck. “Reservoir spectroscopy of $5s5p\ ^3P_2$ – $5snd\ ^3D_{1,2,3}$ transitions in strontium”, *Phys. Rev. A* **90**, 022512 (2014) (cit. on p. 42).
- [249] S. Stellmer et al. “Creation of ultracold Sr_2 molecules in the electronic ground state”, *Phys. Rev. Lett.* **109**, 115302 (2012) (cit. on pp. 42, 65, 71).
- [250] T. L. Nicholson et al. “Systematic evaluation of an atomic clock at $2 \cdot 10^{-18}$ total uncertainty”, *Nat. Commun.* **6**, 6896 (2015) (cit. on p. 42).
- [251] S. L. Campbell et al. “A Fermi-degenerate three-dimensional optical lattice clock”, *Science* **358**, 90–94 (2017) (cit. on p. 42).
- [252] L. Sonderhouse et al. “Thermodynamics of a deeply degenerate $\text{SU}(N)$ -symmetric Fermi gas”, *arXiv e-prints*, 2003.02408 (2020) (cit. on p. 43).
- [253] S. Stellmer et al. “Detection and manipulation of nuclear spin states in fermionic strontium”, *Phys. Rev. A* **84**, 043611 (2011) (cit. on p. 43).
- [254] N. R. Newbury et al. “s-wave elastic collisions between cold ground-state ^{87}Rb atoms”, *Phys. Rev. A* **51**, R2680–R2683 (1995) (cit. on p. 43).
- [255] S. Aubin et al. “Rapid sympathetic cooling to Fermi degeneracy on a chip”, *Nat. Phys.* **2**, 384–387 (2006) (cit. on p. 43).
- [256] M. Lara et al. “Ultracold Rb-OH collisions and prospects for sympathetic cooling”, *Phys. Rev. Lett.* **97**, 183201 (2006) (cit. on p. 43).
- [257] S. L. Cornish et al. “Stable ^{85}Rb Bose-Einstein condensates with widely tunable interactions”, *Phys. Rev. Lett.* **85**, 1795–1798 (2000) (cit. on pp. 43, 71).
- [258] C. L. Blackley et al. “Feshbach resonances in ultracold ^{85}Rb ”, *Phys. Rev. A* **87**, 033611 (2013) (cit. on pp. 43, 71).
- [259] R. Guérout et al. “Ground state of the polar alkali-metal-atom–strontium molecules: Potential energy curve and permanent dipole moment”, *Phys. Rev. A* **82**, 042508 (2010) (cit. on pp. 43, 44, 54).
- [260] P. S. Żuchowski et al. “Ultracold RbSr molecules can be formed by magnetoassociation”, *Phys. Rev. Lett.* **105**, 153201 (2010) (cit. on pp. 43, 44, 65, 70).
- [261] E. Wille. “Preparation of an optically trapped Fermi-Fermi mixture of ^6Li and ^{40}K atoms and characterization of the interspecies interactions by Feshbach spectroscopy”. PhD thesis. Innsbruck University (2009) (cit. on pp. 46–49, 55, 77).
- [262] A. Bayerle. “Ultracold strontium and rubidium: mixtures, quantum gases and molecules”. PhD thesis. University of Amsterdam (2017) (cit. on pp. 46, 48, 50, 52, 68, 70).
- [263] C. B. Alcock et al. “Vapour pressure equations for the metallic elements: 298–2500 K”, *Can. Metall. Quart.* **23**, 309–313 (1984) (cit. on p. 46).
- [264] C. A. Stan and W. Ketterle. “Multiple species atom source for laser-cooling experiments”, *Rev. Sci. Instrum.* **76**, 063113 (2005) (cit. on p. 46).
- [265] S. A. Hopkins et al. “A versatile dual-species Zeeman slower for caesium and ytterbium”, *Rev. Sci. Instrum.* **87**, 043109 (2016) (cit. on pp. 46, 47).
- [266] W. Bowden et al. “An adaptable dual species effusive source and Zeeman slower design demonstrated with Rb and Li”, *Rev. Sci. Instrum.* **87**, 043111 (2016) (cit. on p. 46).
- [267] L. Reichsöllner. private communication (2019) (cit. on pp. 49, 70, 72).
- [268] A. Ciamei. “Taming ultracold RbSr and Sr_2 ”. PhD thesis. University of Amsterdam (2018) (cit. on pp. 50, 67).
- [269] R. W. P. Drever et al. “Laser phase and frequency stabilization using an optical resonator”, *Appl. Phys. B* **31**, 97–105 (1983) (cit. on p. 50).

- [270] J. Catani et al. “Entropy exchange in a mixture of ultracold atoms”, *Phys. Rev. Lett.* **103**, 140401 (2009) (cit. on p. 54).
- [271] G. Lamporesi et al. “Scattering in mixed dimensions with ultracold gases”, *Phys. Rev. Lett.* **104**, 153202 (2010) (cit. on p. 54).
- [272] C. Salomon et al., eds. *Many-Body Physics with Ultracold Gases*. Lecture Notes of the Les Houches Summer School: Volume 94, July 2010. North Holland, Amsterdam (2010) (cit. on p. 54).
- [273] O. I. Kartavtsev and A. V. Malykh. “Low-energy three-body dynamics in binary quantum gases”, *J. Phys. B* **40**, 1429 (2007) (cit. on p. 54).
- [274] J. Levinsen et al. “Atom-dimer scattering and long-lived trimers in fermionic mixtures”, *Phys. Rev. Lett.* **103**, 153202 (2009) (cit. on p. 54).
- [275] D. S. Petrov et al. “Crystalline phase of strongly interacting Fermi mixtures”, *Phys. Rev. Lett.* **99**, 130407 (2007) (cit. on p. 54).
- [276] D. S. Jin and J. Ye. “Introduction to ultracold molecules: New frontiers in quantum and chemical physics”, *Chem. Rev.* **112**, 4801–4802 (2012) (cit. on p. 54).
- [277] A. Lercher et al. “Production of a dual-species Bose-Einstein condensate of Rb and Cs atoms”, *Eur. Phys. J. D* **65**, 3–9 (2011) (cit. on p. 54).
- [278] D. McCarron et al. “Dual-species Bose-Einstein condensate of ^{87}Rb and ^{133}Cs ”, *Phys. Rev. A* **84**, 011603 (2011) (cit. on p. 54).
- [279] C.-H. Wu et al. “Strongly interacting isotopic Bose-Fermi mixture immersed in a Fermi sea”, *Phys. Rev. A* **84**, 011601 (2011) (cit. on pp. 54, 78).
- [280] J. W. Park et al. “Quantum degenerate Bose-Fermi mixture of chemically different atomic species with widely tunable interactions”, *Phys. Rev. A* **85**, 051602 (2012) (cit. on p. 54).
- [281] Y. Takasu et al. “Spin-singlet Bose-Einstein condensation of two-electron atoms”, *Phys. Rev. Lett.* **91**, 040404 (2003) (cit. on p. 54).
- [282] S. Kraft et al. “Bose-Einstein condensation of alkaline earth atoms: ^{40}Ca ”, *Phys. Rev. Lett.* **103**, 130401 (2009) (cit. on p. 54).
- [283] Y. N. Martinez de Escobar et al. “Bose-Einstein Condensation of ^{84}Sr ”, *Phys. Rev. Lett.* **103**, 200402 (2009) (cit. on p. 54).
- [284] A. H. Hansen et al. “Quantum degenerate mixture of ytterbium and lithium atoms”, *Phys. Rev. A* **84**, 011606 (2011) (cit. on p. 54).
- [285] B. K. Stuhl et al. “Evaporative cooling of the dipolar hydroxyl radical”, *Nature* **492**, 396–400 (2012) (cit. on p. 54).
- [286] A. O. G. Wallis et al. “Conical intersections in laboratory coordinates with ultracold molecules”, *Phys. Rev. Lett.* **103**, 083201 (2009) (cit. on p. 54).
- [287] J. Pérez-Ríos et al. “External field control of collective spin excitations in an optical lattice of $^2\Sigma$ molecules”, *New J. Phys.* **12**, 103007 (2010) (cit. on p. 54).
- [288] M. Mudrich et al. “Sympathetic cooling with two atomic species in an optical trap”, *Phys. Rev. Lett.* **88**, 253001 (2002) (cit. on pp. 54, 125).
- [289] G. Ferrari et al. “Cooling of Sr to high phase-space density by laser and sympathetic cooling in isotopic mixtures”, *Phys. Rev. A* **73**, 023408 (2006) (cit. on pp. 54, 64).
- [290] G. Modugno et al. “Sub-Doppler laser cooling of fermionic ^{40}K atoms”, *Phys. Rev. A* **60**, R3373–R3376 (1999) (cit. on pp. 55, 78).
- [291] A. Aspect et al. “Laser cooling below the one-photon recoil energy by velocity-selective coherent population trapping”, *Phys. Rev. Lett.* **61**, 826–829 (1988) (cit. on p. 55).
- [292] S. E. Hamann et al. “Resolved-sideband Raman cooling to the ground state of an optical lattice”, *Phys. Rev. Lett.* **80**, 4149–4152 (1998) (cit. on p. 55).

- [293] P. M. Duarte et al. “All-optical production of a lithium quantum gas using narrow-line laser cooling”, *Phys. Rev. A* **84**, 061406 (2011) (cit. on p. 55).
- [294] D.-J. Han et al. “3D Raman sideband cooling of cesium atoms at high density”, *Phys. Rev. Lett.* **85**, 724–727 (2000) (cit. on p. 55).
- [295] T. Ido et al. “Optical-dipole trapping of Sr atoms at a high phase-space density”, *Phys. Rev. A* **61**, 061403 (2000) (cit. on p. 55).
- [296] C. R. Monroe et al. “Measurement of Cs-Cs elastic scattering at $T=30\ \mu\text{K}$ ”, *Phys. Rev. Lett.* **70**, 414–417 (1993) (cit. on p. 58).
- [297] J. Mitroy and M. W. J. Bromley. “Semiempirical calculation of van der Waals coefficients for alkali-metal and alkaline-earth-metal atoms”, *Phys. Rev. A* **68**, 052714 (2003) (cit. on p. 58).
- [298] M. S. Safronova et al. “Frequency-dependent polarizabilities of alkali-metal atoms from ultraviolet through infrared spectral regions”, *Phys. Rev. A* **73**, 022505 (2006) (cit. on p. 58).
- [299] Y. N. Martinez de Escobar et al. “Two-photon photoassociative spectroscopy of ultracold ^{88}Sr ”, *Phys. Rev. A* **78**, 062708 (2008) (cit. on pp. 61, 62).
- [300] A. Stein et al. “Fourier-transform spectroscopy of Sr_2 and revised ground-state potential”, *Phys. Rev. A* **78**, 042508 (2008) (cit. on pp. 61, 62).
- [301] M.-S. Chang et al. “Observation of spinor dynamics in optically trapped ^{87}Rb Bose-Einstein condensates”, *Phys. Rev. Lett.* **92**, 140403 (2004) (cit. on p. 61).
- [302] F. Dalfovo et al. “Theory of Bose-Einstein condensation in trapped gases”, *Rev. Mod. Phys.* **71**, 463–512 (1999) (cit. on p. 61).
- [303] E. A. Donley et al. “Dynamics of Collapsing and Exploding Bose-Einstein Condensates”, *Nature* **412**, 295–299 (2001) (cit. on p. 61).
- [304] P. G. Mickelson et al. “Bose-Einstein condensation of ^{88}Sr through sympathetic cooling with ^{87}Sr ”, *Phys. Rev. A* **81**, 051601 (2010) (cit. on p. 61).
- [305] M. Yan et al. “Controlling condensate collapse and expansion with an optical Feshbach resonance”, *Phys. Rev. Lett.* **110** (2013) (cit. on p. 61).
- [306] N. Poli et al. “Cooling and trapping of ultracold strontium isotopic mixtures”, *Phys. Rev. A* **71**, 061403 (2005) (cit. on p. 61).
- [307] A. H. Hansen et al. “Production of quantum-degenerate mixtures of ytterbium and lithium with controllable interspecies overlap”, *Phys. Rev. A* **87**, 013615 (2013) (cit. on p. 64).
- [308] J. G. Danzl et al. “Quantum gas of deeply bound ground state molecules”, *Science* **321**, 1062–1066 (2008) (cit. on p. 65).
- [309] F. Lang et al. “Ultracold triplet molecules in the rovibrational ground state”, *Phys. Rev. Lett.* **101**, 133005 (2008) (cit. on p. 65).
- [310] A. Devolder et al. “Proposal for the formation of ultracold deeply bound RbSr dipolar molecules by all-optical methods”, *Phys. Rev. A* **98**, 053411 (2018) (cit. on pp. 66, 70).
- [311] F. Lackner et al. “Helium-droplet-assisted preparation of cold RbSr molecules”, *Phys. Rev. Lett.* **113**, 153001 (2014) (cit. on p. 66).
- [312] J. V. Pototschnig et al. “Ab initio study of the RbSr electronic structure: Potential energy curves, transition dipole moments, and permanent electric dipole moments”, *J. Chem. Phys.* **141**, 234309 (2014) (cit. on p. 67).
- [313] P. S. Żuchowski et al. “Ground- and excited-state properties of the polar and paramagnetic RbSr molecule: A comparative study”, *Phys. Rev. A* **90**, 012507 (2014) (cit. on p. 69).
- [314] J. V. Pototschnig et al. “Vibronic transitions in the alkali-metal (Li, Na, K, Rb) – alkaline-earth-metal (Ca, Sr) series: A systematic analysis of de-excitation mechanisms based on the graphical mapping of Frank-Condon integrals”, *Phys. Rev. A* **95**, 022501 (2017) (cit. on p. 69).

- [315] M. Debatin et al. “Molecular spectroscopy for ground-state transfer of ultracold RbCs molecules”, *Phys. Chem. Chem. Phys.* **13**, 18926–18935 (2011) (cit. on p. 69).
- [316] T. Chen et al. “Prospects for transferring $^{87}\text{Rb}^{84}\text{Sr}$ dimers to the rovibrational ground state based on calculated molecular structures”, *Phys. Rev. A* **89**, 063402 (2014) (cit. on p. 69).
- [317] M. Guo et al. “High-resolution molecular spectroscopy for producing ultracold absolute-ground-state $^{23}\text{Na}^{87}\text{Rb}$ molecules”, *Phys. Rev. A* **96**, 052505 (2017) (cit. on p. 69).
- [318] S. A. Moses et al. “Creation of a low-entropy quantum gas of polar molecules in an optical lattice”, *Science* **350**, 659–662 (2015) (cit. on p. 70).
- [319] S. Stellmer et al. “Bose-Einstein condensation of ^{86}Sr ”, *Phys. Rev. A* **82**, 041602 (2010) (cit. on p. 71).
- [320] C. Ravensbergen et al. “Accurate determination of the dynamical polarizability of dysprosium”, *Phys. Rev. Lett.* **120**, 223001 (2018) (cit. on pp. 74, 117, 119–121).
- [321] A. Frisch. “Dipolar quantum gases of erbium”. PhD thesis. University of Innsbruck (2014) (cit. on pp. 75, 87, 92–94, 119).
- [322] K. Baumann et al. “Observation of low-field Fano-Feshbach resonances in ultracold gases of dysprosium”, *Phys. Rev. A* **89**, 020701 (2014) (cit. on pp. 75, 79).
- [323] I. Segal et al. “Isotope ratio measurements of dysprosium by multiple collection inductively coupled plasma mass spectrometry”, *Int.J. Mass Spectrom.* **216**, 177–184 (2002) (cit. on p. 75).
- [324] T. Maier. “Interactions in a quantum gas of dysprosium atoms”. PhD thesis. University of Stuttgart (2015) (cit. on pp. 76, 105, 114–116, 121, 122).
- [325] I. Ferrier-Barbut et al. “Observation of quantum droplets in a strongly dipolar Bose gas”, *Phys. Rev. Lett.* **116**, 215301 (2016) (cit. on p. 76).
- [326] T. Maier et al. “Broad universal Feshbach resonances in the chaotic spectrum of dysprosium atoms”, *Phys. Rev. A* **92**, 060702 (2015) (cit. on pp. 76, 79).
- [327] B. Naylor et al. “Chromium dipolar Fermi sea”, *Phys. Rev. A* **91**, 011603 (2015) (cit. on p. 76).
- [328] G. Unnikrishnan et al. “Sub-Doppler laser cooling of ^{39}K via the $4\text{S}\rightarrow 5\text{P}$ transition”, *SciPost Phys.* **6**, 47 (2019) (cit. on p. 78).
- [329] C. D’Errico et al. “Feshbach resonances in ultracold ^{39}K ”, *New J. Phys.* **9**, 223 (2007) (cit. on p. 78).
- [330] A. Ludewig. “Feshbach resonances in ^{40}K ”. PhD thesis. University of Amsterdam (2012) (cit. on p. 78).
- [331] L. Tanzi et al. “Feshbach resonances in potassium Bose-Bose mixtures”, *Phys. Rev. A* **98**, 062712 (2018) (cit. on p. 78).
- [332] M. S. Safronova et al. “Magic wavelengths for optical cooling and trapping of potassium”, *Phys. Rev. A* **87**, 052504 (2013) (cit. on pp. 78, 120).
- [333] M. Köhl et al. “Fermionic atoms in a three dimensional optical lattice: Observing Fermi surfaces, dynamics, and interactions”, *Phys. Rev. Lett.* **94**, 080403 (2005) (cit. on p. 78).
- [334] L. Tarruell et al. “Creating, moving and merging Dirac points with a Fermi gas in a tunable honeycomb lattice”, *Nature* **483**, 302–305 (2012) (cit. on p. 78).
- [335] B. DeMarco et al. “An enriched ^{40}K source for fermionic atom studies”, *Rev. Sci. Instrum.* **70**, 1967–1969 (1999) (cit. on p. 78).
- [336] Thywissen Lab. *fermionlattice* (2009). URL: <http://fermionlattice.wikidot.com> (cit. on p. 78).
- [337] G. Edge. *40K Dispenser Construction* (2012). URL: fermionlattice.wdfiles.com/local--files/papers/dispensers (cit. on p. 78).

- [338] S. Jochim et al. “Bose-Einstein condensation of molecules”, *Science* **302**, 2101–2103 (2003) (cit. on p. 78).
- [339] C. Chin et al. “Observation of the pairing gap in a strongly interacting Fermi gas”, *Science* **305**, 1128–1130 (2004) (cit. on p. 78).
- [340] M. Bartenstein et al. “Collective excitations of a degenerate gas at the BEC-BCS crossover”, *Phys. Rev. Lett.* **92** (2004) (cit. on p. 78).
- [341] E. Lucioni et al. “Dysprosium dipolar Bose-Einstein condensate with broad Feshbach resonances”, *Phys. Rev. A* **97**, 060701 (2018) (cit. on pp. 79, 122, 133).
- [342] Kimball Physics Inc. *MCF Design Theory and Part Numbering System* () (cit. on p. 83).
- [343] J. F. O’Hanlon. *A user’s guide to vacuum technology*. 3. ed. (2003) (cit. on pp. 84, 88, 93).
- [344] S. Ospelkaus-Schwarzer. “Quantum degenerate Fermi-Bose mixtures of ^{40}K and ^{87}Rb in 3D optical lattices”. PhD thesis. University of Hamburg (2006) (cit. on pp. 84, 113).
- [345] A. Kumar et al. “A study on low magnetic permeability gas tungsten arc weldment of AISI 316LN stainless steel for application in electron accelerator”, *Materials & Design* **53**, 86–92 (2014) (cit. on p. 85).
- [346] F. Schreck. *Control system* (). URL: <http://www.strontiumbec.com/> (cit. on pp. 86, 150).
- [347] A. Ridinger et al. “Large atom number dual-species magneto-optical trap for fermionic ^6Li and ^{40}K atoms”, *Eur. Phys. J. D* **65**, 223–242 (2011) (cit. on pp. 87, 88, 111).
- [348] J.-L. Yang et al. “Enhanced loading of ^{40}K from natural abundance potassium source with a high performance 2D+ MOT”, *Chin. Phys. Lett.* **35**, 033701 (2018) (cit. on p. 89).
- [349] M. Kreyer. “Double-stage magneto-optical trap system for fermionic potassium atoms”. MA thesis. University of Innsbruck (2017) (cit. on pp. 90, 102, 110, 111).
- [350] L. A. Sidorenkov. “Coherence, hydrodynamics and superfluidity of a strongly interacting Fermi gas”. PhD thesis. University of Innsbruck (2013) (cit. on p. 99).
- [351] S. Nakamura. “Nobel Lecture: Background story of the invention of efficient blue InGaN light emitting diodes”, *Rev. Mod. Phys.* **87**, 1139–1151 (2015) (cit. on p. 103).
- [352] A. Wilson et al. “A 750-mW, continuous-wave, solid-state laser source at 313 nm for cooling and manipulating trapped $^9\text{Be}^+$ ions”, *Applied Physics B* **105**, 741–748 (2011) (cit. on p. 105).
- [353] R. B. Diener and M. Randeria. “BCS-BEC crossover with unequal-mass fermions”, *Phys. Rev. A* **81**, 033608 (2010) (cit. on pp. 108, 121).
- [354] G. Modugno et al. “Comparative investigation of ^{39}K and ^{40}K trap loss rates: alternative loss channel at low light intensities”, *Eur. Phys. J. D - Atomic, Molecular, Optical and Plasma Physics* **23**, 409–413 (2003) (cit. on p. 113).
- [355] P. Ilzhöfer et al. “Two-species five-beam magneto-optical trap for erbium and dysprosium”, *Phys. Rev. A* **97**, 023633 (2018) (cit. on pp. 114–116).
- [356] P. Ahmadi et al. “Geometrical effects in the loading of an optical atom trap”, *Phys. Rev. A* **72**, 023411 (2005) (cit. on p. 119).
- [357] M. Schmitt. “A self-bound dilute quantum liquid of dysprosium atoms”. PhD thesis. University of Stuttgart (2017) (cit. on p. 121).
- [358] K. Jachymski and P. S. Julienne. “Analytical model of overlapping Feshbach resonances”, *Phys. Rev. A* **88**, 052701 (2013) (cit. on pp. 126, 127).
- [359] A. D. Lange et al. “Determination of atomic scattering lengths from measurements of molecular binding energies near Feshbach resonances”, *Phys. Rev. A* **79**, 013622 (2009) (cit. on p. 126).
- [360] B. D. Esry et al. “Threshold laws for three-body recombination”, *Phys. Rev. A* **65**, 010705 (2001) (cit. on p. 133).

- [361] D. S. Petrov and F. Werner. “Three-body recombination in heteronuclear mixtures at finite temperature”, *Phys. Rev. A* **92**, 022704 (2015) (cit. on p. 134).
- [362] P. O. Fedichev et al. “Three-body recombination of ultracold atoms to a weakly bound s level”, *Phys. Rev. Lett.* **77**, 2921–2924 (1996) (cit. on p. 134).
- [363] P. F. Bedaque et al. “Three-body recombination in Bose gases with large scattering length”, *Phys. Rev. Lett.* **85**, 908–911 (2000) (cit. on p. 134).
- [364] C. Ravensbergen et al. “Resonantly interacting Fermi-Fermi mixture of ^{161}Dy and ^{40}K ”, *Phys. Rev. Lett.* **124**, 203402 (2020) (cit. on p. 138).
- [365] L. P. Yatsenko et al. “Coherence in the output spectrum of frequency shifted feedback lasers”, *Opt. Commun.* **282**, 300–309 (2009) (cit. on pp. 140, 143, 145).
- [366] H. G. de Chatellus et al. “Generation of ultrahigh and tunable repetition rates in CW injection-seeded frequency-shifted feedback lasers”, *Opt. Express* **21**, 15065–15074 (2013) (cit. on p. 140).
- [367] G. Bonnet et al. “Dynamics and self-modelocking of a titanium-sapphire laser with intracavity frequency shifted feedback”, *Opt. Commun.* **123**, 790–800 (1996) (cit. on p. 140).
- [368] M. W. Phillips et al. “Frequency comb generation and pulsed operation in a Nd:YLF laser with frequency-shifted feedback”, *Opt. Commun.* **100**, 473–478 (1993) (cit. on p. 140).
- [369] K. Nakamura et al. “Optical frequency domain ranging by a frequency-shifted feedback laser”, *IEEE J. Quant. Electron.* **36**, 305–316 (2000) (cit. on p. 140).
- [370] M. Cashen et al. “Optical pumping in ^4He with frequency-shifted feedback amplification of light”, *J. Opt. Soc. Am. B* **17**, 530–533 (2000) (cit. on p. 140).
- [371] J.-P. Pique and S. Farinotti. “Efficient modeless laser for a mesospheric sodium laser guide star”, *J. Opt. Soc. Am. B* **20**, 2093–2101 (2003) (cit. on p. 140).
- [372] J. Ye and S. Cundiff, eds. *Femtosecond optical frequency comb: Principle, operation and applications*. Springer, New York (2005) (cit. on pp. 140, 146).
- [373] J. R. M. Barr et al. “Accurate optical frequency-interval measurement by use of nonresonant frequency comb generation”, *Opt. Lett.* **18**, 1010–1012 (1993) (cit. on p. 140).
- [374] L. C. Foster et al. “Laser mode locking by an external Doppler cell”, *Appl. Phys. Lett.* **6**, 6–8 (1965) (cit. on p. 140).
- [375] D. J. Taylor et al. “Electronic Tuning of a Dye Laser Using the Acousto-Optic Filter”, *Appl. Phys. Lett.* **19**, 269–271 (1971) (cit. on p. 140).
- [376] F. V. Kowalski et al. “Broadband continuous-wave laser”, *Opt. Lett.* **13**, 622–624 (1988) (cit. on p. 140).
- [377] V. V. Ogurtsov et al. “Experimental characterization of an Yb^{3+} -doped fiber ring laser with frequency-shifted feedback”, *Opt. Commun.* **266**, 627–637 (2006) (cit. on pp. 140, 145).
- [378] A. P. Willis et al. “External cavity laser diodes with frequency-shifted feedback”, *Opt. Commun.* **116**, 87–93 (1995) (cit. on p. 140).
- [379] K. A. Shore and D. M. Kane. “Comb generation bandwidth for frequency-shifted feedback semiconductor lasers”, *IEEE J. Quant. Electron.* **35**, 1053–1056 (1999) (cit. on p. 140).
- [380] P. I. Richter and T. W. Hänsch. “Diode lasers in external cavities with frequency-shifted feedback”, *Opt. Commun.* **85**, 414–418 (1991) (cit. on p. 140).
- [381] M. Sellahi et al. “Highly coherent modeless broadband semiconductor laser”, *Opt. Lett.* **40**, 4301–4304 (2015) (cit. on p. 140).
- [382] M. Schiemangk et al. “High-power, micro-integrated diode laser modules at 767 and 780 nm for portable quantum gas experiments”, *Appl. Opt.* **54**, 5332–5338 (2015) (cit. on p. 140).
- [383] M. Lim et al. *Frequency-shifted feedback amplifier for broadband laser cooling*. SAO/NASA ADS Physics Abstract Service, 2014APS..MAR.C1323L (2014) (cit. on p. 140).

- [384] L. Yatsenko et al. “Ranging and interferometry with a frequency shifted feedback laser”, *Opt. Commun.* **242**, 581–598 (2004) (cit. on p. 143).
- [385] A. E. Siegmann, ed. *Lasers*. University Science Books, Mill Valley (1986) (cit. on p. 145).
- [386] D. Hou et al. “Demonstration of a stable erbium-fiber-laser-based frequency comb based on a single rubidium atomic resonator”, *Appl. Phys. Lett.* **102** (2013) (cit. on p. 145).
- [387] A. A. Savchenkov et al. “Tunable optical frequency comb with a crystalline whispering gallery mode resonator”, *Phys. Rev. Lett.* **101**, 093902 (2008) (cit. on p. 146).
- [388] A. Frisch et al. “Hyperfine structure of laser-cooling transitions in fermionic erbium-167”, *Phys. Rev. A* **88**, 032508 (2013) (cit. on p. 149).

Acknowledgments

The PhD was a long journey for me with multiple stops between Innsbruck and Amsterdam and I wish to thank everybody, who supported me through it. I would like to especially thank my supervisors Prof. Rudi Grimm and Prof. Florian Schreck for introducing me to the fascinating world of quantum matter near absolute zero. I deeply appreciate the experience I gathered from Rudi as a researcher and a teacher while being part of the renowned Center for Ultracold Atoms and Quantum Gases. The accumulated know-how between the university and IQOQI is remarkable and I wish to thank the entire ultracold community (atoms and ions) from Innsbruck for the professional and often fun cooperation. I am grateful to the Dy-K team, to the old and new Sr-Rb teams, to the colleagues from the mechanical and electronic workshops, to the indispensable non-scientific staff and to all peers with whom we shared the joy and the troubles of the students' life. The writing of this thesis was the bumpiest part of my trip and I wouldn't have found the right exit without Rianne and my husband Lukas, thank you! Finally, a lot of gratitude goes to my parents, my sister, my family-in-law and my friends for the constant moral support.